University of Cape Town

Faculty of Engineering and Built Environment

Mechanical Engineering/Centre for Materials Engineering

THE INFLUENCE OF PRIOR CREEP DAMAGE ON THE FRACTURE LOCALISATION IN X20CrMoV12-1 CROSS-WELD CREEP TESTS

By

Trisha Rasiawan

Supervisor: Prof. Robert Knutsen

August 2017

A thesis submitted to the Faculty of Engineering and the Built Environment, at the University of Cape Town, in fulfilment of the degree of Master of Science in Engineering

Declaration

I, Trisha Rasiawan know the meaning of plagiarism and declare that all the work in the document, save for that which is properly acknowledged, is my own

Signature: Signature removed

Date: 08 August 2017

Abstract

Eskom's coal fired power plants have an operating age of between 50 000 and 300 000 hours and an average of 170 000 hours and a few operating close to 300 000 hours. Main steam temperatures experienced in a power plant vary between 535-555°C. These operating conditions place main steam pipe components to operate within the creep regime. It is of utmost importance for safety and plant health that these critical components are managed to determine the remaining life and risks associated with high temperature exposure for prolonged periods of time.

Non-destructive testing (NDT) methods are utilised extensively on Eskom power plants to determine the remaining life and replacement strategies for critical components. Surface replication is used as a life assessment tool for creep damage quantification of main steam pipe work. A large part of maintaining plant is repair welding on creep aged material as entire system replacements are impractical and time consuming. By repair welding new material onto creep aged material, mechanical and microstructural properties of the creep aged material deteriorates.

The study of this work is focused on characterising the as-received materials from Eskom power plants and using these creep aged materials to create cross-weld samples with virgin material. The cross-weld samples were creep-rupture tested at high temperature and low stress conditions to determine the fracture location of repair welded cross-weld samples. Once ruptured, the zone of rupture, was identified and created in a larger volume by simulation using Gleeble® thermo-mechanical equipment.

The as-received base materials were subjected to different operating conditions hence contain different degrees of creep damage. The microstructural evaluation of the creep damaged material was conducted using optical microscopy, scanning electron microscopy (SEM), coupled with more advanced electron backscattered diffraction (EBSD). Microhardness and hot tensile testing were included to characterise the mechanical degradation of the as-received material.

The fracture location of the creep-ruptured cross-weld samples were investigated using optical microscopy, SEM and EBSD and occurred on the outer region of the heat affected zone (HAZ) of the creep aged material. The fine grained microstructure with coarse precipitation of this region is characteristic of the fine grain heat affected zone (FGHAZ). The occurrences of voids predominantly occur in this narrow region with very few voids in the adjacent base/weld material. As this zone is of particular interest due to it being the weakest region in repair welded joints, the need to investigate it further is important. A larger testing volume of the FGHAZ was created by applying a weld thermal cycle simulation to the as-received base materials. The impact of this simulation was determined microstructurally by optical microscopy and mechanically by hardness and tensile testing.

The FGHAZ has low creep resistance and is most susceptible to failure due to the small grained microstructure. Due to the numerous small grains, there is a high effective diffusion coefficient (HEDC). The multi axial stresses induced during in service/ creep testing

conditions together with the HEDC causes voids to form at an accelerated rate. Significant void coalescence promotes the formation of micro cracks which in turn lead to macro crack formation and eventually failure.

Acknowledgements

I would like to give thanks to the following people who have contributed to the outcomes of this study:

- My industrial sponsor, Eskom, for affording me the opportunity to pursue this study.
- My supervisors Professor B. Sonderegger, Professor R.D. Knutsen and Dr I. Shuro for their guidance, advice and supervision throughout the course of this study.
- Dr J. Westraadt at the Centre for High Resolution Transmission Electron Microscopy, Nelson Mandela Metropolitan University for his assistance and guidance with SEM and EBSD.
- Dr T. Pete at Eskom's Research and Innovation Centre for assistance with the material acquisition, welding and creep testing.
- Industrial mentors M. Bezuidenhout and P. Doubell for encouragement and advice.
- Staff and fellow students at the Centre for Materials engineering for their lab assistance and continuous motivation.

I would also like to give sincere gratitude to my parents, Krish and Jenny, and my brother, Trinesh, for their heartfelt motivation, encouragement, love and prayers throughout the course of this study. Thanks to my dearest friends Nicolas, Sandy, Julien, Ryan and Karine for their unconditional friendship, support and academic assistance.

Finally, I wish to give gratitude to God for providing me with the strength, courage and resilience to do this research.

Contents

Declaration i
Abstract ii
Acknowledgements iv
Contents v
List of Figures ix
List of Tables xvii
List of Abbreviations xviii
List of Symbols xix
1. Introduction 1
1.1. Subject of Thesis 1
1.2. Background to Thesis 1
1.3. Objectives of Thesis 3
1.4. Scope and Limitations 3
2. Literature Review 5
2.1 Creep Fundamentals 5
2.1.1 Introduction 5
2.1.2 Creep Rate Curves 6
2.2 Diffusion and creep 9
2.2.1 Activation Energies 10
2.2.2 Time-dependant Deformation and Diffusion 10
2.2.3 Influence of Short-circuit Diffusion 11
2.3 Creep Deformation Mechanisms 11
2.4 Creep Fracture Mechanisms 13
2.4.1 Introduction 13
2.4.2 Fracture Mechanisms 13
2.4.3 Rupture 15
2.4.4 Fracture Mechanism Maps 16
2.5 X20 CrMoV12-1 Material Properties and Characteristics 17
2.5.1 Background 17
2.5.2 Chemical Composition 19

2.5.3 Mechanical Properties 20
2.5.4 Hardness of X20CrMoV12-1 21
2.5.5 Microstructure 23
2.5.6 Precipitates in X20CrMoV12-1 24
2.5.7 Heat treatment 26
2.5.7.1 Transformation behaviour 26
2.5.7.2 Final Heat Treatment 28
2.5.7.3 Post Weld Heat Treatments of Welds 28
2.6 Microstructural Evolution in the Heat Affected Zone of 9-12%Cr Steels 30
2.6.1 Introduction 30
2.6.2 The Welding Procedure 30
2.6.3 The Heat Affected Zone of 9-12%Cr Steels 32
2.6.4 Damage Mechanisms in Creep Exposed Welded Joints 34
2.6.5 Type IV Cracking 35
2.7 Fine Grain Heat Affected Zone Simulation 38
2.7.1 Introduction 38
2.7.2 Determination of the weld thermal cycle 39
2.7.3 Gleeble Welding Simulation 40
3. Experimental Investigation 44
3.1 Investigated Materials 44
3.1.1 Sample Designation 45
3.1.2 Chemical Composition 46
3.2 Creep Testing 47
3.2.1 Material Sampling 47
3.2.2 Experimental Set-up 48
3.3 Weld Thermal Cycle Simulation 49
3.3.1 Material Sampling 49
3.3.2 Experimental Set-up 50
3.3.2.1 MatCalc Thermal Equilibrium Simulation 50
3.3.2.2 Dilatometry 53
3.3.3 Gleeble Weld Thermal Cycle Simulation 56
3.3.4 Post Weld Heat Treatment 57

3.4 Microhardness 57
3.5 High Temperature Tensile Testing 58
3.6 Metallographic Investigation 59
3.6.1 Optical Microscopy 60
3.6.2 Scanning Electron Microscopy 61
3.6.3 Electron Backscatter Diffraction 62
4. Results and Discussion 67
4.1 Base Material Characterisation 67
4.1.1 High Temperature Tensile Strength 67
4.1.2 Microhardness Testing 68
4.1.3 Microstructural Analysis of Base Materials 68
4.1.4 Damage Analysis of Base Materials 71
4.1.5 Discussion 74
4.2 Cross Weld Samples after Creep Testing 78
4.2.1 Creep Tests Results 78
4.2.2 Fracture Mechanism of Creep Tests 82
4.2.3 Microstructural Profile of Fractured Samples 83
4.2.4 Microhardness Profile 93
4.2.5 Void Density of Fractured Sample 97
4.2.6 Discussion 102
4.3 Weld Thermal Cycle Simulation Using the Gleeble®3800 107
4.3.1 Weld Thermal Cycle Simulation at a Peak Temperature of 1050˚C 107
4.3.2 General Microstructure 109
4.3.3 High Temperature Tensile Strength 115
4.3.4 Microhardness Profile 116
4.3.5 Discussion 117
5. Conclusion 121
5.1 Summary 121
6. Recommendations 124
7. Appendices 125
Appendix 1 As-received Base Material 125
Appendix 2 Fracture Surfaces 126

Appendix 3 Void Occurrences 131
Appendix 4 Void Density Profile 135
Appendix 5 Creep Strain Curves 150
8. References 152

List of Figures

Figure 1: Eskom power plants: Plant age January 2014*[2]* 1

Figure 2: Typical creep curves[10] 6

Figure 3: Creep curve of a 9-12% Cr steel under constant tensile load and constant temperature[11] 7

Figure 4: (a), (b), (c) creep curves of engineering steels under constant tensile load and constant temperature and (d), (e) and (f) their creep rate as a function of time [7] 9

Figure 7: Schematic deformation mechanism map with contours of constant creep rate[7] ... 12

Figure 8: Representative fracture modes at high temperatures. (a) Brittle intergranular fracture by wedge cracking and diffusion cavity growth, (b) intergranular and transgranular cavity growth due to plastic deformation and (c) rupture after 100% reduction of area[7] 14

Figure 9: Intergranular, creep controlled, fracture. Voids nucleate by grain boundary sliding (a) and (b), grow by diffusion (c)[22] 14

Figure 10: Schematic representation of rupture with dynamic recrystallization[22] 15

Figure 11: Schematic fracture mechanism naps for a) FCC and b) BCC materials[22] 16

Figure 12: Tensile and creep properties of X20CrMoV12-1 as a function of temperature[23] 21

Figure 13: Continuous Cooling Transformation (CCT) diagram of X20CrMoV12-1 [8] 22

Figure 14: Variation of hardness of X20CrMoV12-1 steel as a function of tempering time[28] 23

Figure 15: Tempered martensite microstructure of X20CrMoV12-1 24

Figure 16: Schematic illustration of microstructure of a typical martensite 9-12%Cr creep-resistant steel containing precipitates on the internal interfaces[8] 24

Figure 17: Representation of crystal structure of $Cr_{23}C_6$ carbide with FCC structure[8] 25

Figure 18: Chromium rich $M_{23}C_6$ carbides on a prior austenite and sub grain boundaries 26

Figure 19: Martensitic transformation of X20[23] 27

Figure 20: Heat treatment for welds on X20CrMoV12-1 29

Figure 21: Typical heat treatment for welded joints in P91 steel[36] 31

Figure 22: Schematic representation of welded joint in 9-12% Cr ferritic steel[38] 32

Figure 23: Schematic of the sub-zones of the heat-affected zone and relation to the calculated equilibrium phase diagram of X10CrMoVNb9-1 steel[34] 33

Figure 24: Classification of crack locations[43] 35

Figure 25: Representation of the shortfall in creep strength of a cross-weld specimen compared with a parent or all-weld-metal specimen[44] 36

Figure 26: Development of microstructure in the FGHAZ of typical 9-12% Cr creep resistant steel[50] 37

Figure 27: Coupling of the most influencing factors on the HAZ properties in a logical way[55] 39

Figure 29: Thermocouple welded onto specimen 40

Figure 30: Weld thermal cycles for the coarse-grained zone [52] 41

Figure 31: Typical procedure for Gleeble weldability testing and subsequent property determination[55] 43

Figure 32: Dimensions for the creep damaged pipes used for this research[56] 44

Figure 33: Two weldments used for cross-weld creep testing specimens 47

Figure 34: Specimen with cross weld in the middle[43] 48

Figure 35: Completed cross-weld samples 48

Figure 36: a) Creep testing furnace at Eskom Research and Innovation Centre and b) shows the vacuum chamber which houses the specimen 49

Figure 37: Weld thermal cycle simulation sample 50

Figure 38: X20 CrMoV12-1 MatCalc thermal equilibrium simulation 52

Figure 39: Set-up for dilatometry experiment 53

Figure 40: Simulated weld thermal cycle of X20_ND at a peak temperature of 980˚C 54

Figure 41: Phase transformation temperatures achieved by the weld thermal cycle simulation at a peak temperature of 980˚C on X20_ND 55

Figure 42: Phase transformation temperatures achieved by the weld thermal cycle simulated at a peak temperature of 980°C on X20_ND 55

Figure 43: a) Spot-welded thermocouples on sample, b) sample in the Gleeble 3800 56

Figure 44: Medium damage micro hardness matrix 58

Figure 45: Light micrograph of weldment showing the base material, HAZ and weld material used for microhardness testing 58

Figure 46: Hot tensile testing of base material using the Gleeble® 3800 59

Figure 47: a) Circular specimen mounted for microscopic investigation and b) Scan area of X20_HD for void count 62

Figure 48: Principle components of an EBSD system[59] 64

Figure 49: Graphical representation of lath boundary and prior austenite grain boundary misorientation angles 66

Figure 50: Application of orientation angle prior austenite grain boundaries 66

Figure 51: Optical micrographs of the as-received base materials microstructure showing the prior austenite grain size (left) and tempered martensitic lath structure (right) 69

Figure 52: Backscatter electron SEM images of (a) X20_ND, (b) X20_MD and (c) X20_HD showing the martensitic lath microstructure 70
Figure 53: EBSD All Euler colour image of a) X20_ND, b) X20_MD and c) X20_HD 71
Figure 54: Stitched image of Backscatter SEM micrographs for X20_HD 72
Figure 55: Stitched image of Backscattered SEM micrographs for a) X20_ND and b) X20_MD 72
Figure 56: Threshold image of X20_HD stitched image 73
Figure 57: Graph of the occurrences of voids in relation to their diameter for X20_ND, X20_MD and X20_HD 74
Figure 58: Tensile and creep properties of X20CrMoV12-1 as a function of temperature[23] 75
Figure 59: Surface replica micrograph (left) and SEM image (right) of X20_HD 76
Figure 60: Strings of inclusions in main steam pipe[64] 77
Figure 61: Rupture times for creep tests on weldment 1 (X20_ND to X20_MD) 79
Figure 62: Rupture times for creep tests on weldment 2 (X20_ND to X20_HD) 79
Figure 63: Creep strain curve versus testing time for weldment 1 and 2 at 610°C and 63 MPa 80
Figure 64: Creep strain rate versus testing time for weldment 1 and 2 at 610°C and 63 MPa 81
Figure 65: Creep ruptured sample showing fracture point 82
Figure 66: Fracture surfaces of test 1 A GL at magnifications of 2000x (left) and 5000x (right) 83
Figure 67: Illustration of the heat affected zone showing the location of the sub-zones which make up the heat affected zone[34] 84
Figure 68: Optical micrographs for test 1 A GL (left) and GS (right) 85
Figure 69: Optical micrographs for Test 1 A and B creep ruptured samples 86
Figure 70: Optical micrographs for Test 2 A and B creep ruptured samples 87
Figure 71: Optical micrographs for Test 3 A creep ruptured samples 87
Figure 72: Optical micrographs for Test 4 A and B creep ruptured samples 88
Figure 73: Optical micrographs for Test A creep ruptured samples 88
Figure 74: EBSD map areas for Test 2 A GL (left) and Test 2 A GS (right) 89
Figure 75: EBSD All Euler colour maps for areas A, B and C for sample of Test 2A GL 90
Figure 76: EBSD All Euler colour maps for areas A, B and C for sample of Test 2A GS 90
Figure 77: Test 1A GS (left) GL (right) 91
Figure 78: Test 3A GS (left) GL (right) 92

Figure 79: Test 4B GS (left) GL (right) 92
Figure 80: Test 5A GS (left) GL (right) 92
Figure 81: Optical micrograph of X20_ND weldment 93
Figure 82: Vickers hardness results for the weldment of X20_ND 94
Figure 83: Vickers hardness results for the weldment of X20_MD 94
Figure 84: Vickers hardness results for the weldment of X20_HD 95
Figure 85: EBSD All Euler colour map for the FGHAZ in a) X20_ND HAZ, b) X20_MD HAZ and c) X20_HD HAZ 96
Figure 86: Backscatter SEM images of the rupture surface (left) and base material (right) for test 5A with the black areas indicating voids 98
Figure 87: Optical micrograph of test 1 A GL sample polished cross-section of fracture surface 99
Figure 88: Backscattered electron SEM stitched image of test 1 A GL sample 100
Figure 89: Threshold image for test 1 A GL sample 100
Figure 90: Graph showing the void density as a function of the distance from the fracture surface in sample test 1 A GL 101
Figure 91: Typical optical micrograph of the cross section of creep-ruptured specimen at 650°C and 60 MPa[6] 103
Figure 92: Optical micrograph of weldment 1 creep ruptured specimen at 610°C and 63 MPa 103
Figure 93: Light micrograph showing creep cavitation close to fracture for 10CrMo9 10 cross weld (540° C/95 MPa)[65] 104
Figure 94: SEM images showing creep cavitation close for the fracture surface (610°C/63 MPa) 104
Figure 95: Optical micrograph (left) and EBSD All Euler colour map (right) for the cross-sectional fracture area for Test 2 A GL 105
Figure 96: Optical micrograph (left) and EBSD All Euler colour map (right) for the cross-sectional fracture area for Test 2 A GS 105
Figure 97: Approximate fracture mechanisms for uniaxial cross-weld creep tests for X20CrMoV12-1 weldments[23] 106
Figure 98: EBSD All Euler colour maps of the weld cycle simulated base material at 1050°C for a) X20_NDS, b) X20_MDS and c) X20_HDS 108
Figure 99: EBSD All Euler colour maps of the weld cycle simulated base material at 980°C of a) X20_NDS, b) X20_MDS and c) X20_HDS 110
Figure 100: Optical micrograph of X20_ND base material at magnifications of 50x and 250x (left) and X20_NDS at magnifications of 50x and 250x (right) 111

Figure 101: Optical micrograph of X20_MD base material at magnifications of 50x and 250x (left) and X20_MDS at magnifications of 50x and 250x (right) 112

Figure 102: Optical micrograph of X20_HD base material at magnifications of 50x and 250x (left) and X20_HDS at magnifications of 50x and 250x (right) 113

Figure 103: Test sample for weld thermal cycle simulation at 980°C showing the length of hot zone achieved.....114

Figure 104: Transition between the FGHAZ and the unaffected base material of X20_ND 114

Figure 105: Transition between FGHAZ (left) and base material (right) of weld thermal cycle simulated sample.....115

Figure 106: EBSD All Euler colour maps for a) X20_ND, b) simulated at 1050°C and c) simulated at 980°C.....118

Figure 107: Graphical representation of the impact of weld thermal cycle simulation on hardness.....119

Figure 108: SEM secondary electron image of the microstructure of X20_MD (left) and X20_MDS (right).....120

Figure 109: Graphical representation of the impact of weld thermal cycle simulation on hot tensile strength 120

Figure 110: Base material X20_ND 125

Figure 111: Base material X20_MD.....125

Figure 112: Base material X20_HD 125

Figure 113: Fracture surfaces of test 1 A GS at magnifications of 2000x (left) and 5000x (right) 126

Figure 114: Fracture surfaces of test 1 B GL at magnifications of 2000x (left) and 5000x (right) 126

Figure 115: Fracture surfaces of test 1 B GS at magnifications of 2000x (left) and 5000x (right) 126

Figure 116: Fracture surfaces of test 2 A GL at magnifications of 2000x (left) and 5000x (right) 127

Figure 117: Fracture surfaces of test 2 A GS at magnifications of 2000x (left) and 5000x (right) 127

Figure 118: Fracture surfaces of test 2 B GL at magnifications of 2000x (left) and 5000x (right) 127

Figure 119: Fracture surfaces of test 2 B GS at magnifications of 2000x (left) and 5000x (right) 128

Figure 120: Fracture surfaces of test 3 A GL at magnifications of 2000x (left) and 5000x (right) 128

Figure 121: Fracture surfaces of test 3 A GS at magnifications of 2000x (left) and 5000x (right) 128

Figure 122: Fracture surfaces of test 4 A GL at magnifications of 2000x (left) and 5000x (right) 129

Figure 123: Fracture surfaces of test 4 A GS at magnifications of 2000x (left) and 5000x (right) 129

Figure 124: Fracture surfaces of test 4 B GL at a magnification of 2000x 129

Figure 125: Fracture surfaces of test 4 B GS at a magnification of 2000x 130

Figure 126: Fracture surfaces of test 5 A GL at magnifications of 2000x (left) and 5000x (right) 130

Figure 127: Fracture surfaces of test 5 A GS at a magnification of 2000x 130

Figure 128: Backscatter SEM images of the rupture surface (left) and base/weld material (right) for test 1 A 131

Figure 129: Backscatter SEM images of the rupture surface (left) and base/weld material (right) for test 1 B 131

Figure 130: Backscatter SEM images of the rupture surface (left) and base/weld material (right) for test 2 A 132

Figure 131: Backscatter SEM images of the rupture surface (left) and base/weld material (right) for test 2 B 132

Figure 132: Backscatter SEM images of the rupture surface (left) and base/weld material (right) for test 3 A 133

Figure 133: Backscatter SEM images of the rupture surface (left) and base/weld material (right) for test 4 A 133

Figure 134: Backscatter SEM images of the rupture surface (left) and base/weld material (right) for test 4 B 134

Figure 135: Backscatter SEM stitched image of test 1 A GS sample 135

Figure 136: Graph showing the void density as a function of the distance from the fracture surface in sample test 1 A GS 135

Figure 137: Backscatter SEM stitched image of test 1 B GL sample 136

Figure 138: Graph showing the void density as a function of the distance from the fracture surface in sample test 1 B GL 136

Figure 139: Backscatter SEM stitched image of test 1 B GS sample 137

Figure 140: Graph showing the void density as a function of the distance from the fracture surface in sample test 1 B GS 137

Figure 141: Backscatter SEM stitched image of test 2 A GL sample 138

Figure 142: Graph showing the void density as a function of the distance from the fracture surface in sample test 2 A GL 138

Figure 143: Backscatter SEM stitched image of test 2 A GS sample.....139

Figure 144: Graph showing the void density as a function of the distance from the fracture surface in sample test 2 A GS.....139

Figure 145: Backscatter SEM stitched image of test 2 B GL sample.....140

Figure 146: Graph showing the void density as a function of the distance from the fracture surface in sample test 2 B GL.....140

Figure 147: Backscatter SEM stitched image of test 2 B GS sample.....141

Figure 148: Graph showing the void density as a function of the distance from the fracture surface in sample test 2 B GS.....141

Figure 149: Backscatter SEM stitched image of test 3 A GL sample.....142

Figure 150: Graph showing the void density as a function of the distance from the fracture surface in sample test 3 A GL.....142

Figure 151: Backscatter SEM stitched image of test 3 A GS sampl.....143

Figure 152: Graph showing the void density as a function of the distance from the fracture surface in sample test 3 A GS.....143

Figure 153: Backscatter SEM stitched image of test 4 A GL sample.....144

Figure 154: Graph showing the void density as a function of the distance from the fracture surface in sample test 4 A GL.....144

Figure 155: Backscatter SEM stitched image of test 4 A GS sample.....145

Figure 156: Graph showing the void density as a function of the distance from the fracture surface in sample test 4 A GS.....145

Figure 157: Backscatter SEM stitched image of test 4 B GL sample.....146

Figure 158: Graph showing the void density as a function of the distance from the fracture surface in sample test 4 B GL.....146

Figure 159: Backscatter SEM stitched image of test 4 B GS sample.....147

Figure 160: Graph showing the void density as a function of the distance from the fracture surface in sample test 4 B GS.....147

Figure 161: Backscatter SEM stitched image of test 5 A GL sample.....148

Figure 162: Graph showing the void density as a function of the distance from the fracture surface in sample test 5 A GL.....148

Figure 163: Backscatter SEM stitched image of test 5 A GS sample.....149

Figure 164: Graph showing the void density as a function of the distance from the fracture surface in sample test 5 A GL.....149

Figure 165: Creep strain curve versus testing time for weldment 1 and 2 at 610°C and 80 MPa.....150

Figure 166: Creep strain rate versus testing time for weldment 1 and 2 at 610°C and 80 MPa 150
Figure 167: Creep strain curve versus testing time for weldment 1 and 2 at 610°C and 90 MPa 151
Figure 168: Creep strain rate versus testing time for weldment 1 and 2 at 610°C and 90 MPa 151

List of Tables

Table 1: Stress exponent n, grain size exponent p and diffusion coefficient D for each creep mechanism[20] 11

Table 2: Material specifications for X20 CrMoV12-1 martensitic steels[23] 18

Table 3: Chemical requirements of X20 and X22 steels and equivalent materials according to several standards[23] 19

Table 4: Room temperature mechanical and fracture properties of X20 CrMoV12-1[26] 20

Table 5: Phase transformation temperatures for X20[23] 27

Table 6: Heat treatment temperatures for X20CrMoV12-1[23] 28

Table 7: Minimum information required for HAZ simulation[43] 38

Table 8: Operating and design conditions for as received X20CrMoV12-1 material 44

Table 9: Sample designation of as-received material 45

Table 10: Sample designation of weldments 45

Table 11: Sample designation for weld thermal cycle simulated and PWHT base material 45

Table 12: Chemical analysis (in weight %) for the X20 CrMoV12-1 samples used in this research [56] 46

Table 13: Chemical composition input for MatCalc simulation 51

Table 14: Weld thermal cycle properties 54

Table 15: Summary of phase transformation temperatures for the as-received base material 56

Table 16: Post weld heat treatment conditions conducted on weld thermal cycle simulated samples 57

Table 17: Polishing and grinding steps using the Struers Tegramin-25 60

Table 18: High temperature tensile strength for base materials 67

Table 19: Vicker's Hardness measurements for as received base material 68

Table 20: Comparison of void density measurements between surface replica and SEM 77

Table 21: Creep rupture test results 78

Table 22: Summary of calculated grain size for the FGHAZ of weldments 1 and 2 95

Table 23: Void density comparison between fracture surface and base/weld material 102

Table 24: Weld thermal cycle simulation on the Gleeble® 3800 at 1050°C 107

Table 25: Weld thermal cycle simulation on the Gleeble® 3800 at 980°C 109

Table 26: Summary of grain size calculation for weld thermal cycle simulation at 980°C 109

Table 27: Hot tensile strength of the weld thermal cycle simulation at 980°C base material 116

Table 28: Vickers Hardness measurements for weld thermal cycle simulated base material 117

List of Abbreviations

X20- DIN 17175 X20 CrMoV12-1

NDT – Non-destructive testing

SEM- Scanning Electron Microscopy

EBSD- Electron Backscattered Diffraction

HAZ- Heat Affected Zone

FGHAZ- Fine Grained Heat Affected Zone

ICHAZ- Intercritical Heat Affected Zone

HEDC- High Effective Diffusion Coefficient

Weldment- fusion welding of two materials to create a single component

ERIC- Eskom Research and Innovation Centre

UCT- University of Cape Town

USC- Ultra Super Critical

TTP- Time-Temperature Parameter

TTT- Time Transformation Temperature

CCT- Continuous Cooling Transformation

FCC- Face-centre Cubic

BCC- Body-centre Cubic

BIF- Brittle Intergranular Fracture

PAGB- Prior Austenite Grain Boundary

GTAW- Gas Tungsten Arc Welding

MMAW- Manual Metal Arc Welding

FCAW- Flux Core Arc Welding

SAW- Submerged Arc Welding

PWHT- Post Weld Heat Treatment

CSEF- Creep Strength Enhanced Ferritic

FL- Fusion Line

List of Symbols

T_m- Absolute Melting Temperature

T_P- Peak Temperature

$\dot{\varepsilon}$- Creep rate

ε_r- Rupture strain

t_r- Time to rupture

$\dot{\varepsilon}_{min}$- Minimum creep rate

A_{c1} - Starting temperature for Austenite formation

A_{c2} - Curie temperature (Ferromagnetic- Paramagnetic)

A_{c3} - Austenite completion temperature

M_s - Starting temperature for Martensite formation

M_F - Martensite completion temperature

γ- Austenite

δ- Delta Ferrite

1. Introduction

1.1. Subject of Thesis

The subject of this research involves the characterisation of creep damage in ex-serviced X20 CrMoV12-1 materials received from power plants. Weldments created from the creep aged material will be used to investigate the impact of prior creep damage on the localisation of failure during creep testing. This will help identify the weakest point in the microstructure for creep-damaged weldments which are most susceptible to failure in in-service conditions.

1.2. Background to Thesis

Eskom is the largest electricity producing utility in South Africa with an installed generating capacity of approximately 40 gigawatts. Approximately 90% of this capacity is generated by coal fired power plants. For coal fired power stations, increasing efficiency is essential to reduce pollution and operational costs[1]. The average age of plant components in various Eskom power plants are in excess of the contracted design life with some coal fired power plants operating in excess of 300 000 hours. Figure 1 shows a summary of the contracted design life, maximum operating life and the percentage used life of all the coal fired power plants within the Eskom fleet. The maximum operating life of the power plants has exceeded the contracted design life.

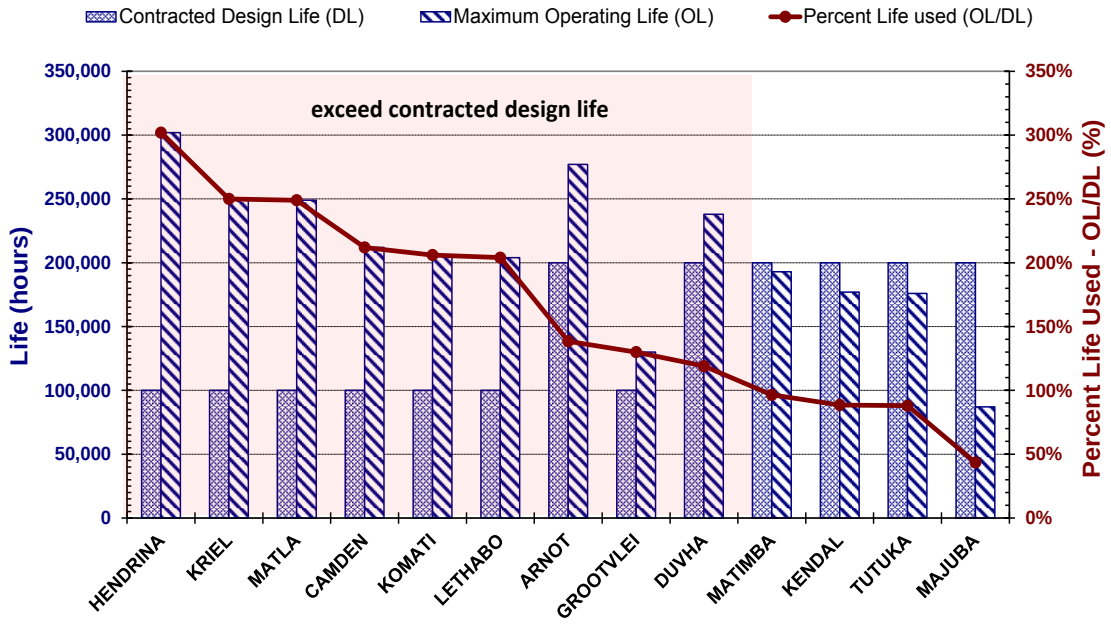

Figure 1: Eskom power plants: Plant age January 2014*[2]*

Power generation at high temperatures requires development of more reliable materials and assessment of degradation of components which operate at these temperatures[1].Due to the current strain on the national supply grid, maintenance and repair schedules are compromised

in efforts to provide a constant supply of electricity to the consumer. Current life management strategies are constantly being revised with outcomes affecting maintenance and repairs on power plant components. Plant components operating under high temperatures are characterised as running in the creep regime ($0.4T_m°C$) and require frequent monitoring and maintenance. In terms of steam delivery in coal fired power stations, steam temperatures and pressures can be as high as 555 °C and 17 MPa respectively. The risk of operating power plants at these high temperatures without interim inspection and repairs can lead to detrimental consequences. Catastrophic failures can occur without warning resulting in injuries, fatalities as well as loss in production[3]. Due to this, many countries and utilities have introduced regulations to govern the inspection and replacement of components operating in the creep regime. The majority of work performed on equipment operating in the creep regime is focused on life extension management of these high temperature and high pressure piping, i.e. main steam and hot reheat piping[4].

Creep life management of pipe work in Eskom is performed by means of various non-destructive evaluation techniques, strain measurement techniques as well as material creep property degradation parameters acquired from both experimental and literature based sources [3]. Eskom utilises the surface replica technique as a non-destructive method to determine the material degradation of the pipework systems, in conjunction with magnetic particle inspections, ultrasonic inspections and hardness testing. This risk based inspection method has yielded a database of about a million replicas, which was used for life assessment of the pipework, and the creep models were optimised for CrMoV – and X20CrMoV12-1 materials[4].

Many of Eskom's power plants make use of X20 CrMoV12-1 creep resistant steel as pipework for conveying saturated steam from the boiler to the inlet of the high pressure turbine. The current maintenance and repair philosophy involves the abovementioned non-destructive techniques as well as replacing like-for-like components. Life management is determined by the formation and occurrences of voids, which Eskom uses in its creep models[3]. These creep models are implemented to facilitate how many useful years are remaining on the high pressure pipework. In the event that a section of pipework has outlived its operational life, it has to be replaced by welding a new X20 CrMoV12-1 pipe onto an existing X20 CrMoV12-1 creep aged pipe. Welding on the creep aged pipe consumes a significant amount of remaining operational life of that material. In many cases welded joints show creep aging relatively early, often before the design life has been reached[5].

Extensive studies have been focused on the base material X20 CrMoV12-1. However very few have reported on the behaviour of creep aged X20 CrMoV12-1 under the influence of welding and the creep properties associated with continuing power plant operations on these creep aged repair welded materials. This study aims to investigate how creep aged X20 CrMoV12-1 behaves in high temperature, low stress conditions after repair welding. Another important area in this research involves the investigation of the fusion zone created by welding onto the creep aged pipework as research has evidently identified the heat affected zone as the region most susceptible to failure in real life applications[6]. By understanding the behaviour of X20 CrMoV12-1 in repair welded conditions, life estimation and life management models can be established to provide reliable and efficient estimates for parameters to consider in welding on creep aged components.

1.3. Objectives of Thesis

The objectives of this research will be achieved by:

- Characterisation of the microstructural and mechanical behaviour in X20 CrMov12-1 exposed to different in-service conditions
- Investigating the zone of the rupture during creep testing of welded joints between new and creep aged X20 CrMoV12-1
- Investigating the precursor to cracking in welded joints
- Creating welding simulations of the zone of fracture in weldments using the Gleeble®3800
- Measuring the impact of welding simulations on the as-received base material in terms of mechanical properties
- Correlation of microscopic methods to conventional Non-destructive Testing (NDT) methods to investigate the damage in ex-serviced X20 CrMoV12-1

1.4. Scope and Limitations

Eskom's Research and Innovation Centre (ERIC) supplied the three classes of X20 CrMoV12-1 chosen for this study. The materials studied, vary in hours of operation at Eskom's power plants and exposure to temperature ant stress conditions. The welds created for the creep experiments are also derived for the supplied material. The weldments would be subjected to varying stresses at a specific temperature in a vacuum furnace until rupture. The ruptured specimens would provide information regarding the evolution of the microstructure at different stresses. The location of the rupture in the creep tested samples would also feed the research with direction into investigating the area most susceptible to failure in welded joints. By gathering valuable information regarding the zone of fracture, this zone can be simulated in greater volume for further investigations. Microscopic methods such as Electron Backscatter Diffraction (EBSD), Scanning Electron Microscopy (SEM) and optical microscopy will be used to characterise the as-received material and investigate creep tested samples.

The limitations of this research involve the use of creep furnaces at ERIC and the University of Cape Town (UCT). ERIC has 10 newly installed creep furnaces in its creep testing facility. These furnaces have only recently been commissioned. Creep testing on X20 CrMoV12-1 weldments or base materials have not been carried out prior to the commencement of this research. Upon the commencement of creep testing of the X20 CrMoV12-1 weldments, numerous problems arose. Problems included insufficient furnace cooling which lead to limited operation of furnaces- only 2 furnaces could operate at any given time. This imposed a huge limitation on the number of samples that could be tested. Upon writing this report, the problems associated with cooling of the furnaces had not yet been resolved.

The next limitation is also related to creep furnaces available for creep testing at UCT. UCT has two creep furnaces. These furnaces were designed and built as a research project done by Michael J Dollman in 2003. The technology and components were modified and updated to

meet the requirements for testing of this research project. However, due to the recent implementation of load shedding, the use of these furnaces for creep testing of the base material became impossible. The effects of a drop in temperature during heating and cooling almost daily could not be quantified during the course of this project.

2. Literature Review

2.1 Creep Fundamentals

2.1.1 Introduction

Plastic deformation is irreversible. It consists of time-dependant and time-independent components. In general, creep refers to the time-dependant component of plastic deformation. This means that creep is a slow and continuous plastic deformation of materials over extended periods under load. Although creep can take place at all temperatures above absolute zero Kelvin, traditionally creep has been associated with time-dependant plastic deformation at elevated temperatures, often higher than roughly $0.4T_m$, where T_m is the absolute melting temperature (°C), because diffusion can assist creep at elevated temperatures[7][8][9][10].

The use of metals at elevated temperatures introduces the possibility of failure in service by this mechanism known as creep[11].Creep resistant steels that can be used for a long time at elevated temperature is the key to the construction of thermal and nuclear power plants, chemical plants and petroleum plants. During the last decade, great progress has been made in developing creep-resistant steels of high strength and good corrosion resistance at ever increasing temperatures and in evaluating the steels in terms of weld characteristics, creep strength and corrosion resistance necessary for constructing plants[12].

Previously, in the field of thermal power generation, the maximum allowable temperature was about 565°C (approximately 50%T_m) for conventional low alloy ferritic steels. However, progress in recent years has led to the development of high-strength 9-12% Cr ferric steels capable of operating in ultra super critical (USC) power plants at metal temperatures approaching 650°C. Recent research on enhancing the creep strength of 9-12Cr steels for 650°C operation has revealed that the microstructural evolution near the grain boundary weakens the material and promotes local creep deformation resulting in premature fracture. It is therefore important to take into account microstructural evolution phenomena during creep such as precipitation and coarsening of carbonitrides and intermetallic compounds, dynamic recovery and dynamic recrystallization, in the matrix as well as in the vicinity of grain boundaries[12]. The formation of some phases can have deleterious effects on the materials creep resistance properties.

Recently, some high-strength 9-12Cr steels have been found to suffer premature loss of creep strength at 550°C or higher often after prolonged use up to relevant times. Therefore, efforts have been made to clarify the mechanisms of creep strength loss, using modern transmission electron microscopy analysis. Extrapolations of short duration laboratory data using time-temperature parameter (TTP) methods, such as the Larson-Miller parameter, have been used widely in the past to predict long-term life. However, it has now become clear that conventional TTP methods tend to over-predict the long term strength because of microstructural degradation phenomena. [12]

2.1.2 Creep Rate Curves

At relatively high temperatures creep appears to occur at all stress levels, but the creep rate increases with increasing stress at a given temperature. Figure 2 curve a shows the characteristics of a typical creep curve. Following the instantaneous strain caused by the sudden application of the load, the creep process may be divided into three stages[10]:

- Primary or transient creep
- Secondary or steady state creep
- Tertiary or accelerated creep

The characteristics of the creep curve often vary, however, and the tertiary stage of creep may be more advanced or retarded depending on temperature and stress at which the test is carried out as shown in curves b and c in Figure 2 [10].

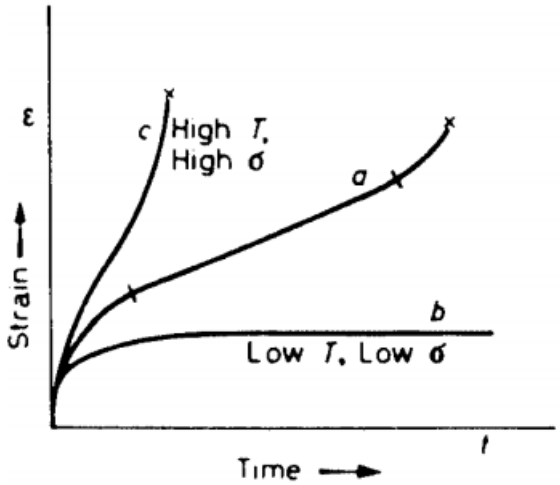

Figure 2: Typical creep curves[10]

In an experimental setup, creep is often tested by measuring the elongation of a specimen as a function of time and in certain instances, it might be necessary to rupture the specimen. Creep tests on engineering materials are most frequently conducted at a constant tensile load and temperature. The results of creep tests are plotted as creep curves which graphically represent the time dependence of strain measured over a reference or gauge length[8]. Figure 3 shows a more detailed schematic representation of a typical creep curve indicating the three stages of creep.

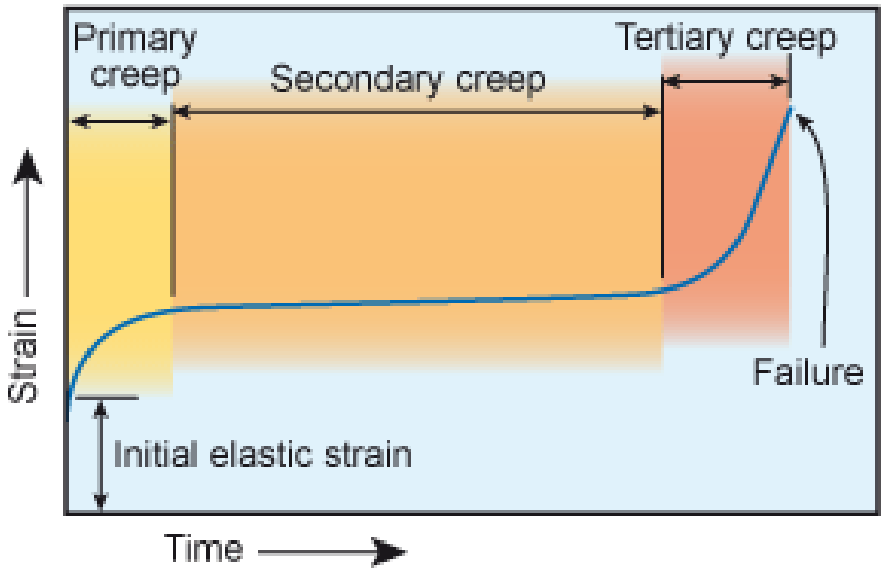

Figure 3: Creep curve of a 9-12% Cr steel under constant tensile load and constant temperature[11]

Figure 4 shows the three types of creep curves under constant tensile load and constant temperature conditions and also their creep rates. The creep rate is given by the equation below:

$$\dot{\varepsilon} = d\varepsilon/dt \qquad \text{Equation 1[7]}$$

Where ε is the strain and t the time as a function of time. The instantaneous strain, $\varepsilon 0$, occurs immediately on application of load, and may contain both elastic and plastic deformations. In the primary creep stage between $\varepsilon 0$ and $\varepsilon 1$, the creep rate,$\dot{\varepsilon}$, decreases with time as shown in Figure 4 (d). The decreased creep rate in the primary creep stage has been attributed to strain hardening or to a decrease in free mobile dislocations.

In the secondary creep stage between $\varepsilon_1$and ε_2, the creep strain remains constant as the effect of strain hardening is counter balanced by a recovery influence. This creep rate,$\dot{\varepsilon}_s$, is given by:

$$\dot{\varepsilon}_s = (\varepsilon_2 - \varepsilon_1)/(t_2 - t_1) \qquad \text{Equation 2[7]}$$

There is a state of balance between the rate of generation of dislocations contributing to hardening and the rate of recovery contributing to softening. At high homologous temperatures, solid state diffusion is dominant and diffusional creep occurs. This is because solid state diffusion processes are enhanced significantly at high temperatures. Since atomic movements are directly related to microstructural reorganization processes it is then natural to expect that creep phenomena will be directly related to solid state diffusion phenomena, particularly, at the highest temperatures.. There will be the first appearance of isolated inter-granular cavities forming in the later part of the secondary stage[3].

In the tertiary creep stage, the creep rates starts to increase with time until rupture at time t_r and strain ε_r . At this stage the cavities become numerous and begin to line up along discreet sections of the grain boundaries resulting in a rapid increase of the creep strain rate. With the passage of time, and part way through this tertiary stage, cavities begin to coalesce forming micro-cracks which in turn transforms to macro-cracks leading to resulting in complete material failure[3]. During testing under constant load, the stress continuously increases as creep proceeds or as the cross-section decreases and a pronounced effect of increase in stress on the creep rate appears in the tertiary stage. Necking of the specimens before rupture causes a significant increase in stress. The increase in creep rate with time in the tertiary creep stage can be a result of increasing stress or from microstructural evolution including damage evolution taking place during creep. Microstructural evolution usually consists of dynamic recovery, dynamic recrystallization, coarsening of precipitates and other phenomena which results in a decrease in creep resistance[10].

Under certain conditions, the secondary creep stage may be absent. This results in the tertiary creep stage starting immediately after the primary creep stage at T_m as shown in Figure 4 (b) and (e). In this case, the minimum creep rate, $\dot{\varepsilon}_{min}$, can be defined instead of the steady-state creep rate, $\dot{\varepsilon}_s$. The stress dependence of steady state creep rate is usually expressed by a power law:

$$\dot{\varepsilon}_{min} \; or \; \dot{\varepsilon}_s = A\sigma^n \qquad \text{Equation 3[7]}$$

$$A = A' \exp(-Q_c / RT) \qquad \text{Equation 4[7]}$$

Where n is the stress exponent, Q_c the activation energy for creep, R the gas constant and T the absolute temperature. The parameter A' includes microstructure parameters such as grain size etc. Equation 4 is referred to a Norton's law[7].

It is well known that the minimum or steady-state creep rate is inversely proportional to the time to rupture t_r as:

$$\dot{\varepsilon}_{min} \; or \; \dot{\varepsilon}_s = C/(t_r)^m = A'\sigma^n \exp(-Q_c/RT) \qquad \text{Equation 5[7]}$$

Where C is a constant dependant on total elongation during creep and m is a constant often nearly equal to 1. Equation 5 is referred to as the Monkman-Grant relationship which has been experimentally confirmed not only for simple metals and alloys but also for a number of engineering creep resistant steels and alloys[7].

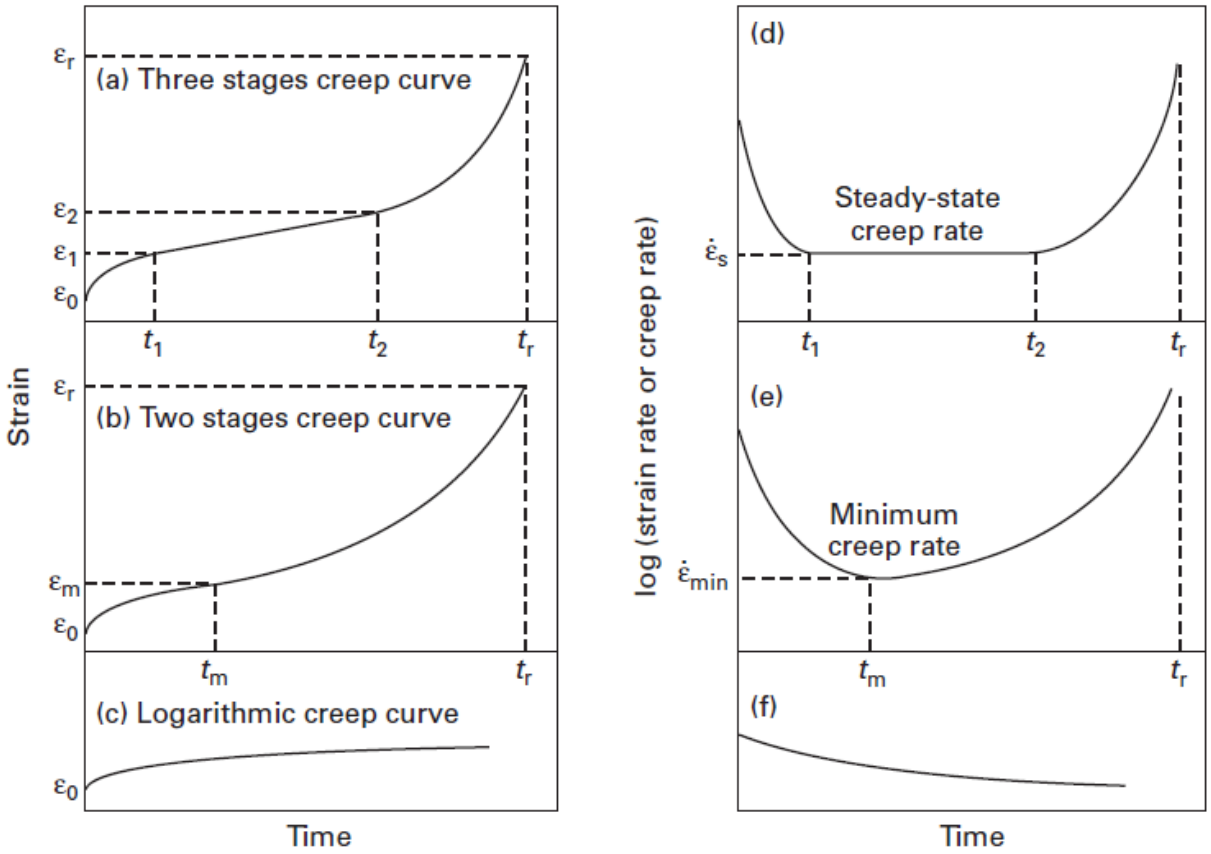

Figure 4: (a), (b), (c) creep curves of engineering steels under constant tensile load and constant temperature and (d), (e) and (f) their creep rate as a function of time [7]

2.2 Diffusion and creep

Diffusion is one of the most fundamental processes governing creep deformation. In the early 1950s, researchers analysed creep data and diffusion data of several metals and claimed that the temperature dependence of both is similar. Nowadays, it is almost certain that the temperature dependence of creep at high homologous temperatures is similar to that of diffusion in pure metals[18].

During creep in of complex alloys such as steels, significant changes occur. At the very first stage of creep, a significant change in dislocation configuration occurs, followed by slow changes, not only in dislocation structures, but also in the kind, shape, size and amount of precipitates. Diffusion of the solute plays an important role in the formation of a new phase and precipitates. When the solute atoms combine to form precipitates, it is known as de-homogenization. In the event whereby the solute element is consumed from the matrix to make different phases as precipitates, the concentration of the solute causing drag resistance decreases, leading to a weakened material by precipitation formation. In the early stage of precipitation, the size of the newly precipitated phase is very small but the number of precipitates is very large. Precipitate strengthening may occur at this stage and some of the weakening by solute consumption may be cancelled. Towards the later stage of precipitation formation, the size of the precipitates increases in volume while the quantity decreases.

During this stage of precipitate coarsening, the diffusion of precipitate constituent atoms must be taken into account. For this process, the average concentration of solute remains unchanged, however, the strength of the material decreases because of the pinning force of precipitates on dislocations[18].

2.2.1 Activation Energies

There is an essential difference in the physical meaning of temperature dependence of creep and of diffusion, although the temperature dependence of these two phenomena are close to each other under the same conditions. Diffusion in simple metals can be recognised as a thermally activated process, where the activation energy is the sum of the formation energy and the migration energy of vacancies. The pre-exponential (or frequency) term is essentially the number of lattice sites in the system and not a function of temperature[18].

Creep is a time-dependent deformation process which is a result of complex dislocation behaviour, its temperature dependence is influenced by many factors which may have their own temperature dependence. The so-called activation energy of creep is a temperature dependence of the steady-state (or minimum) creep rate under a given stress, derived on the assumption that one thermally activated process occurs in the phenomenon. Therefore, the activation energy of creep is an apparent one in the sense of rigorous thermal activation rate theory. It must be noted that during discussions of creep mechanisms that the pre-exponential term in the form of a thermally activated rate equation contains many factors which might depend on temperature even under constant stress [18].

2.2.2 Time-dependant Deformation and Diffusion

Creep deformation is time-dependant straining under a constant applied stress, or under a given load in many cases. At very high temperatures under very low stress, ‘diffusional creep’ occurs in pure metals. Under these conditions, creep strain arises directly from the movement of atoms. The temperature dependence (activation energy) of creep is the same as that of vacancy diffusion [18].

At temperatures higher than about a half of the melting temperature, $0.4T_m$, and under ordinal creep conditions, the temperature dependence of creep (strain rate) is similar to that of diffusion. This similarity, however, does not mean that creep strain arises from the movement of atoms. Rather, the similarity indicates that the rate-controlling step of ‘so-called’ high-temperature creep is a kind of restoration process relating intimately to diffusion. When steady-state creep rates and/or minimum creep rates are taken as the parameter of a creep process, a similarity in the temperature dependence between creep and diffusion can be observed. Correlation between diffusion and creep behaviour of practical alloys under practical creep conditions is not simple, as in the care of pure metals and solid solution alloys at high temperatures. In these conditions temperature is usually less than $0.5T_m$, significant structure changes occur in the matrix and the influence of surrounding atmosphere becomes obvious with time. These factors strongly affect the creep behaviour of material and any simple relation between creep and diffusion is difficult to observe [18].

2.2.3 Influence of Short-circuit Diffusion

In creep of metals and alloys, the essential rate-determining stage is a kind of restoration process which is governed by diffusion of vacancies and/or alloying elements. At temperatures higher than about $0.4T_m$, diffusion of vacancies/atoms through nearly perfect crystal lattice governs creep process and the temperature dependence of creep rate is similar to that of the lattice diffusion of vacancies/atoms. At temperatures lower than about $0.5T_m$, however, the effects of short-circuit diffusion becomes obvious in many cases. The absolute values of short-circuit diffusion coefficients are always larger than the lattice diffusion coefficients, but the net effect of these types of diffusion is not always large, because their cross-sectional areas are small. In some cases, a change in the activation energy of creep is observed at temperatures below $0.5T_m$. This change in activation energy can be explained not by a change in creep mechanisms, but simply by the effect of short-circuit diffusion [18].

2.3 Creep Deformation Mechanisms

Ashby[19] proposed the concept of a deformation mechanism map, based on the assumption that all deformation mechanisms concerned are mutually independent and operate in a parallel way. According to Maruyama[20], the main deformations include:

- Diffusion creep controlled by volume diffusion (Nabarro-Herring)
- Grain boundary diffusion (Coble creep)
- Dislocation creep controlled by volume diffusion (high temperature power law creep)
- Pipe diffusion (low temperature power law creep)

The creep rates of all the mechanisms are represented by the equation:

$$\dot{\varepsilon} = \dot{\varepsilon}_0(\sigma/G)^n d^p D \qquad \text{Equation6[20][7][7]}$$

Where $\dot{\varepsilon}_0$ is a material constant characteristic of the mechanism and material, σ is the shear stress, d is the grain size, p in the grain size exponent, G is the shear modulus, D is the diffusion coefficient relevant to the mechanism, σ is the shear stress and n is the stress exponent which is usually greater than 3. The values for n, p and D are typical of each creep mechanism and are given in Table 1. D_1, D_p, and D_{gb} are the diffusion coefficient of lattice, dislocation pipe and grain boundary diffusion respectively[20].

Table 1: Stress exponent n, grain size exponent p and diffusion coefficient D for each creep mechanism[20]

Deformation mechanism	n	p	D
Dislocation creep			
Low temperature power law creep	5–7	0	D_p
High temperature power law creep	3–5	0	D_l
Diffusion creep			
Coble creep	1	3	D_{gb}
Nabarro–Herring creep	1	2	D_l

Figure 5 shows a schematic representation of the deformation mechanism map with axes of normalised stress (σ/G) and the homologous temperature ($T/T_{m)}$. The map is divided into fields. Within each field, one mechanism is dominant. This means that it supplies a greater strain rate than any other mechanism. The upper limit of the boundary is set by a theoretical or ideal strength of roughly G/20 or G/30. At stresses lower than yield stress, dislocation creep can take place with the aid of diffusion. Dislocation creep is further divided into two fields: low- and high- temperature dislocation creep fields. At low stresses, volume diffusion creep (Nabarro-Herring creep) and grain boundary diffusion creep (Coble creep) dominate. The boundaries between adjacent fields in the creep region indicate the conditions under which two mechanisms contribute equally to the overall creep rate[7].

The creep rates which govern the boundaries can be calculated by using appropriate constitutive equations for creep rates as functions of temperature and stress. Figure 5 shows these boundaries for the different fields for constant creep rates. The locations of the boundaries between adjacent creep fields differ for different materials and also depend on microstructure parameters such as grain size.

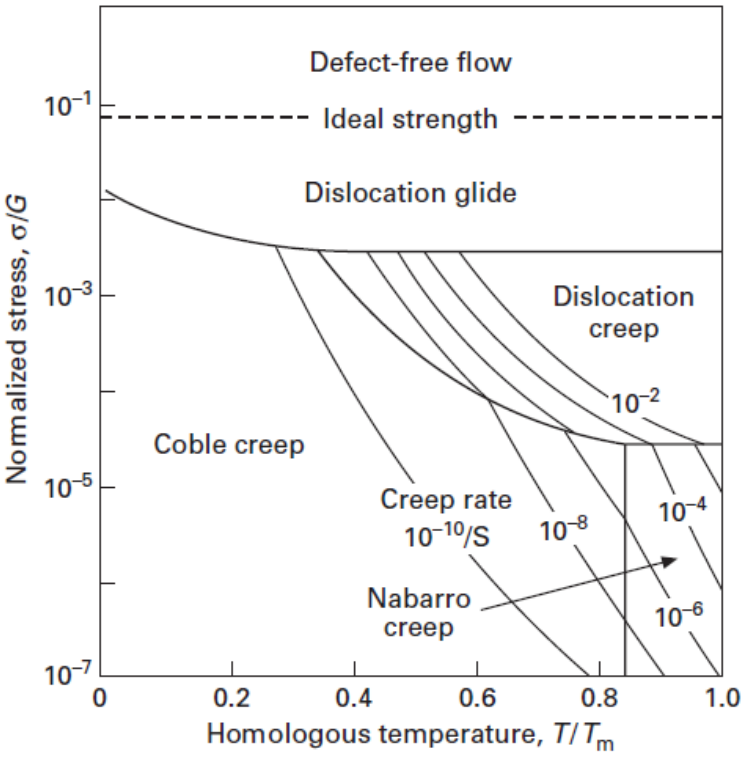

Figure 5: Schematic deformation mechanism map with contours of constant creep rate[7]

2.4 Creep Fracture Mechanisms

2.4.1 Introduction

At elevated temperatures metallic alloys deform continuously even under a constant stress and finally break after a certain time. This is the consequence of creep deformation and creep fracture. Creep fracture in uniaxial tension under constant stress has been described by the Monkman-Grant relation as given by Equation 5 which states that the fracture of creep-deforming materials is controlled by steady-state creep rate, $\dot{\varepsilon}_s$ [21]. The time-dependent deformation and fracture are characteristics of high temperature deformation. The creep fracture mechanism often changes from transgranular fracture in short-term creep to intergranular in long-term creep. The changes in fracture mechanisms are summarized in fracture mechanism maps. The transition of fracture modes is often accompanied by a decrease in stress exponent and activation energy, namely the breakdown of creep strength[20].

2.4.2 Fracture Mechanisms

A material exhibits several modes of fracture depending on creep testing conditions such as temperature and stress. Fracture modes for creep testing are classified into three types as shown in Figure 6 as:

a) Brittle intergranular fracture
b) Intergranular or trangranular fracture with some ductility
c) Rupture after 100% reduction in area

The fracture ductility changes substantially with the fracture mechanisms. There are two types of brittle intergranular creep fracture. One is brought about by the coalescence of cavities formed on grain boundaries aligned perpendicular to the applied stress. The other is wedge cracking formed at triple grain boundary junctions by stress concentration created by grain boundary sliding. The intragranular creep cavities are nucleated at inclusions (solid circles) as shown in Figure 6 (b) and their coalescence by deformation brings about the final fracture. Recrystallization occurs in the necking part during the rupture in Figure 6 (c)[20].

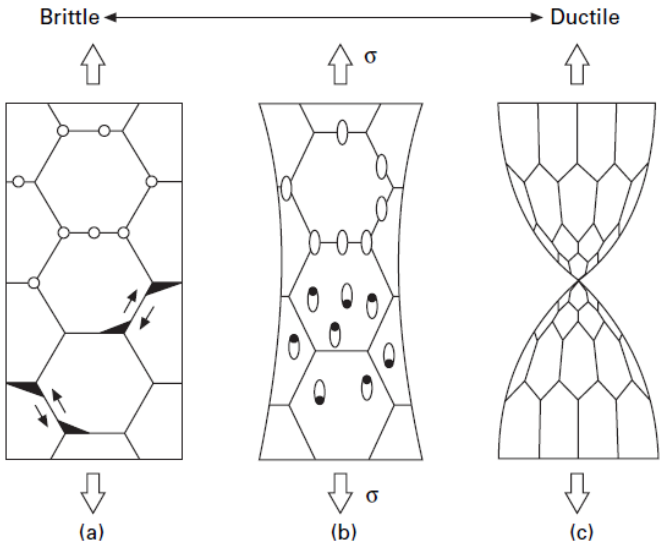

Figure 6: Representative fracture modes at high temperatures. (a) Brittle intergranular fracture by wedge cracking and diffusion cavity growth, (b) intergranular and transgranular cavity growth due to plastic deformation and (c) rupture after 100% reduction of area[7]

Since creep occurs above $0.3T_m$ with a creep rate given by Equation 5, ductile failure of a transgranular nature can occur. This is similar to the ductile failure found commonly at low temperatures when voids nucleated at inclusions within the grains, grow during creep deformation and coalesce to produce fracture. However, because these three processes are occurring at $T \approx 0.3T_m$, local recovery is taking place and this delays both the onset of void nucleation and void coalescence. At lower stresses and longer times-to-fracture, intergranular rather than transgranular fracture is observed. In this situation grain boundary sliding leads to the formation of either wedge cracks of voids on those grain boundaries normal to the tensile axis as shown in Figure 7 (b)[22].

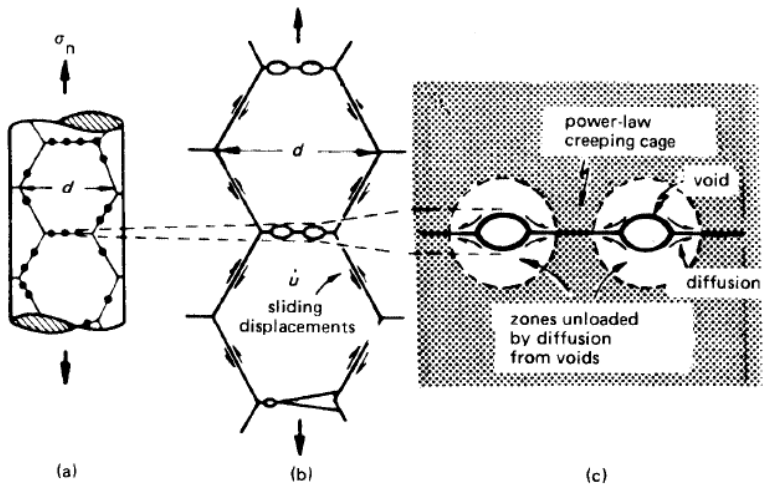

Figure 7: Intergranular, creep controlled, fracture. Voids nucleate by grain boundary sliding (a) and (b), grow by diffusion (c)[22]

2.4.3 Rupture

Ductile rupture, Figure 8, occurs as a result of ductile fracture mechanisms (as mentioned above) is inhibited. Specimens deformed in tension ultimately each a stage of mechanical instability when the deformation is localised with in a neck or in a shear band. With continued straining the cross-section reduces to zero and the specimen ruptures. The strain-to-rupture depends on the amount of strain before and after localization. These strains are influenced by the work-hardening behaviour and strain-rate sensitivity. Rupture is favoured when void nucleation and/or growth is inhibited. This will occur if:

- Second phase particles are removed by zone-refining or dissolution at high temperatures,
- The matrix/particle interface is strong,
- The stress state minimises plastic constraint and plane conditions,
- The work-hardening rate and strain rate sensitivity is high as for superplastic materials and,
- There is stress relief at particles by recovery or dynamic recrystallization. Rupture is observed in most FCC materials. This is usually associated with dynamic recrystallization[17].

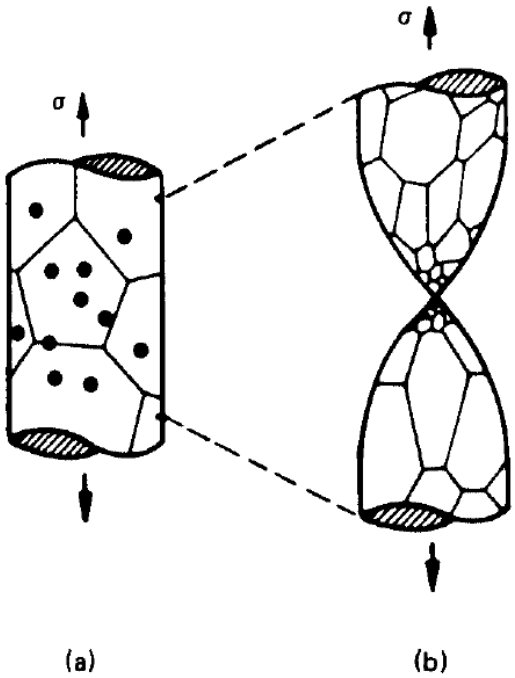

Figure 8: Schematic representation of rupture with dynamic recrystallization[22]

2.4.4 Fracture Mechanism Maps

The fracture behaviour of a metal or alloy in different stress or temperature regimes can be summarised conveniently by displaying the dominant mechanisms on a fracture mechanism map. There are seven fracture mechanisms which have been identified. These include three for the brittle behaviour including cleavage and intergranular brittle fracture and four ductile fracture mechanisms. Figure 9 shows schematic maps for FCC and BCC materials respectively. Fracture regimes exhibited by an FCC material can exclude certain mechanisms and certain ductile processes can be inhibited by altering metallurgical variables. In the BCC metals, brittle behaviour is seperated into three fields; a brittle failure from a pre-existing crack, well below general yield point (cleavage 1) or brittle intergranular fracture (BIF1), depending on the fracture path. An almost totally brittle failure from a crack nucleated by slip or twinning, below the general yield, is called cleavage 2 or BIF2. A cleavege or brittle boundary failure after general yield with a measurable strain-to-failure is called cleavage 3 of BIF3[22].

In many cases, mixed transgranular and intergranular fractures are observed, as a result of small changes in impurity content, texture or temperature. These changes can cause the crack to deviate from one path to another where no distinction is made between cleavage and BIF. While fracture mechanism maps for two structures are shown in Figure 9, it is evident that as bonding changes from metallic to ionic and covalent, the fracture mechanism fiels will move from left to right [22].

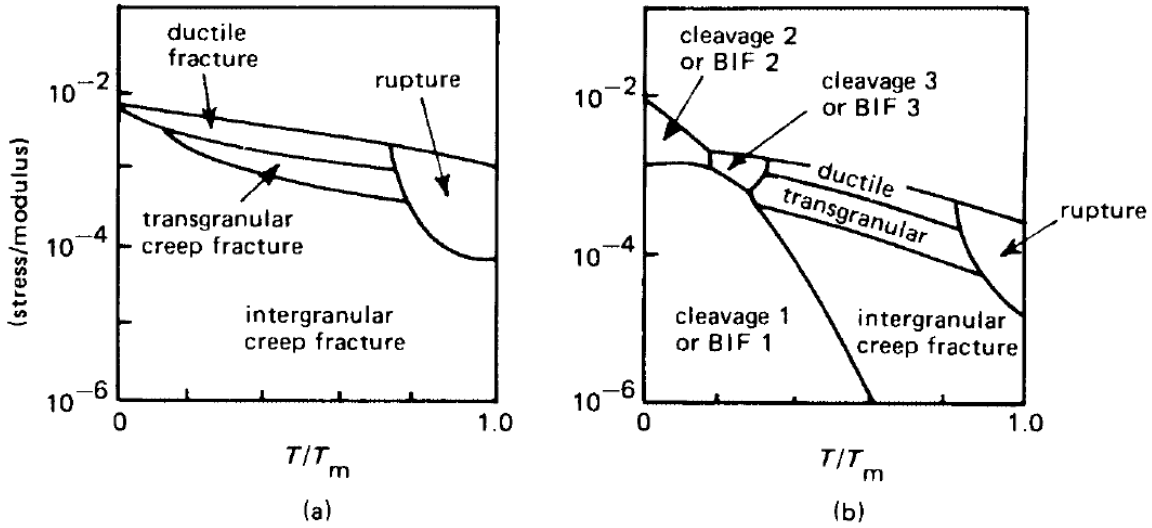

Figure 9: Schematic fracture mechanism naps for a) FCC and b) BCC materials[22]

2.5 X20 CrMoV12-1 Material Properties and Characteristics

2.5.1 Background

The X20 CrMoV12-1 (X20) steel is a high chromium (12%) ferritic steel which has been in service since the early 1960s. The first recorded application of X20 dates back to 1963 in a steam plant in Germany. The high creep strength of the steel allowed for the construction of larger power plants with more advanced steam parameters. It later became favourable for components in thermal, power generation, and chemical plants. Plant components include superheater, reheater tubes, main steam pipes, boilers, turbine casings and blades, and other high-temperature services where high creep strength, corrosion, and oxidation resistance are desired[23][6][1].

The grade X20 CrMoV12-1 is developed based on the corrosion-resistant 12% Cr high-temperature steels containing up to 0.25% C in a tempered condition. These high-temperature steels were used in structures as early as early 1920s for turbine blades and corrosion resistant machine elements[24]. However, due to the problems associated with weldability, material development concentrated on austenitic steels[23]. The expected breakthrough in welding of X20 in manufacturing crack-free welds facilitated its application in boilers and turbine piping with steam temperatures of 560°C and service pressures of 21.28 MPa as early as 1959[25]

The 12CrMoV steels were then standardized for use in steam pipes under the DIN designation X20CrMoV12-1 (X20) as shown in Table 2.

Table 2: Material specifications for X20 CrMoV12-1 martensitic steels[23]

Country	Symbol	Standard
Germany	X20CrMoV12-1	DIN17175 (05/79) DIN17176 (11/90)
Germany	X20CrMoV12-1	DIN EN 10302
European Standard	X20CrMoV11-1	EN10216-2 (05/2002) EN10222-2 (02/2000)
European Standard	X20CrMoV11-1	EN10222-2 (02/2000
European Standard	X20CrMoV12-1	EN10302 (05/2002)
Great Britain	762	BS 3059 Part 1-1987, Part 2-1990
Great Britain	762	BS 3604 Part 1-1990
Hungary	12Cr10MoVNi70.47	MSZ4747 (1985)
Italy	X20CrMoNi12 01 KG;KW	UNI7660 (1977) withdrawn
Poland	20H12M1F	PN84024 (1975)
Rumania	20VNiMoCr120	STAS11523 (1987)
Sweden	2317	SS142317
Czechia/Slovakia	422916	CSN/STN422916 (1973
International (ISO)	X20CrMoNiV11-1-1	ISO9329-2 (1997)
China	S47220	GB T 1221
Japan	SUH 616	JIS G 4311
USA	422	ASTM A 176-99

2.5.2 Chemical Composition

Table 3 provides the chemical composition for X20 in various national and international standards.

Table 3: Chemical requirements of X20 and X22 steels and equivalent materials according to several standards[23]

Standard	Designation	Chemical Composition (wt %)								
		C	Si	Mn	P	S	Cr	Mo	Ni	V
DIN 17175	X20CrMoV12-1	0.17	≤0.50	≤1.00	≤0.030	≤0.030	10	0.8	0.3	0.25
		0.23					12.50	1.20	0.80	0.35
ISO 9327	X20CrMoV11-1	0.17	≤0.04	0.30	≤0.035	≤0.030	10.00	0.80	0.30	0.25
		0.23		1.00			12.50	1.20	0.80	0.35
EN 10222-2	X20CrMoV11-1	0.17	≤0.04	0.30	≤0.025	≤0.015	10.00	0.80	0.30	0.25
		0.23		1.00			12.50	1.20	0.80	0.35
UNI 7660	X20CrMoNi1201 KG;KW	0.20	0.15	0.30	≤0.040	≤0.030	11.50	0.70	0.30	0.20
		0.26	0.40	1.00			12.50	1.20	1.00	0.35
SS 142317	2317	0.18	0.10	0.30	≤0.035	≤0.035	11.50	0.80	0.30	0.25
		0.24	0.50	0.80			12.50	1.20	0.80	0.35
PN/H 84024	20H112M1F	0.17	0.10	0.30	≤0.035	≤0.035	11.00	0.80	0.30	0.25
		0.23	0.50	0.80			12.50	1.20	0.80	0.35
STAS/SR* 11523-87	20VNiMoCr120	0.17	0.10	≤1.20	≤0.035	≤0.035	10.00	0.80	0.30	0.25
		0.23	0.50				12.50	1.20	0.80	0.35
CSN/STN** 422916	422916	0.16	0.10	0.40	≤0.035	≤0.030	10.20	0.90	0.20	0.20
		0.22	0.40	0.70			11.80	1.20	0.60	0.35
B.S 3059 Part 1	762	0.17	≤0.50	≤1.00	≤0.030	≤0.030	10.00	0.80	0.30	0.25
		0.23					12.50	1.20	0.80	0.35
B.S 3604*** Part 1	762	0.17	≤0.50	≤1.00	≤0.030	≤0.030	10.00	0.80	0.30	0.25
		0.23					12.50	1.20	0.80	0.35
MSZ 4747	12Cr10MoVNi70.47	0.17	≤0.50	≤1.00	≤0.030	≤0.030	10.00	0.80	0.30	0.25
		0.23					12.50	1.20	0.80	0.35
DIN 17240+****	X22CrmoV12-1	0.18	0.10	0.30	≤0.035	≤0.035	11.0	0.80	0.30	0.25
		0.24	0.50	0.80			12.5	1.20	0.80	0.35

Note: * STAS/SR 11523-87 Romania) includes more: 0.30% Cu

** According to standard P+S 0.050

*** B.S.3604 Part 1 (UK) includes more: 0.030% Sn, 0.25% Cu, 0.020% Al

**** Added for comparison purposes[23]

2.5.3 Mechanical Properties

The materials engineering properties are determined following standards for testing and analysis of data in order to obtain information for component design and service assessment[23].

Table 4: Room temperature mechanical and fracture properties of X20 CrMoV12-1[26]

Standard	Designation/steel number	Mechanical Properties at ambient temperature						
		Thickness (mm)	Yield stress (MPa)	Tensile strength (MPa)	Fracture Elongation (%)		Charpy Impact Energy (J)	
					L	T	L	T
DIN 17175	X20 CrMoV12-1 1.4922	≥16, ≤60	490	690-840	≥17	≥14	≥48	≥34
EN 10222-2	X20 CrMoV12-1 1.4922	≤100	500	700-850	≥16	≥16	≥39	
		>100, ≤200					≥31	
		>250, ≤300				≥14	≥27	
ISO 9327		≤100	500	700-850	≥16	≥14	≥39	
		>100, ≤200					≥31	
		>250, ≤300					≥27	
ISO 9329-2	X20 CrMoNiV11-1	≥16, ≤60	490	Not listed	≥17	≥14	≥27	≥35
DIN 17240	X22CrMoV12-1 1.4923	≤250	600	800-950	≥14		≥27	

Figure 10 shows the tensile and creep properties of X20 as a function of temperature. There is an inverse relationship between the applied stress and the testing temperature for the tensile and creep properties of X20.

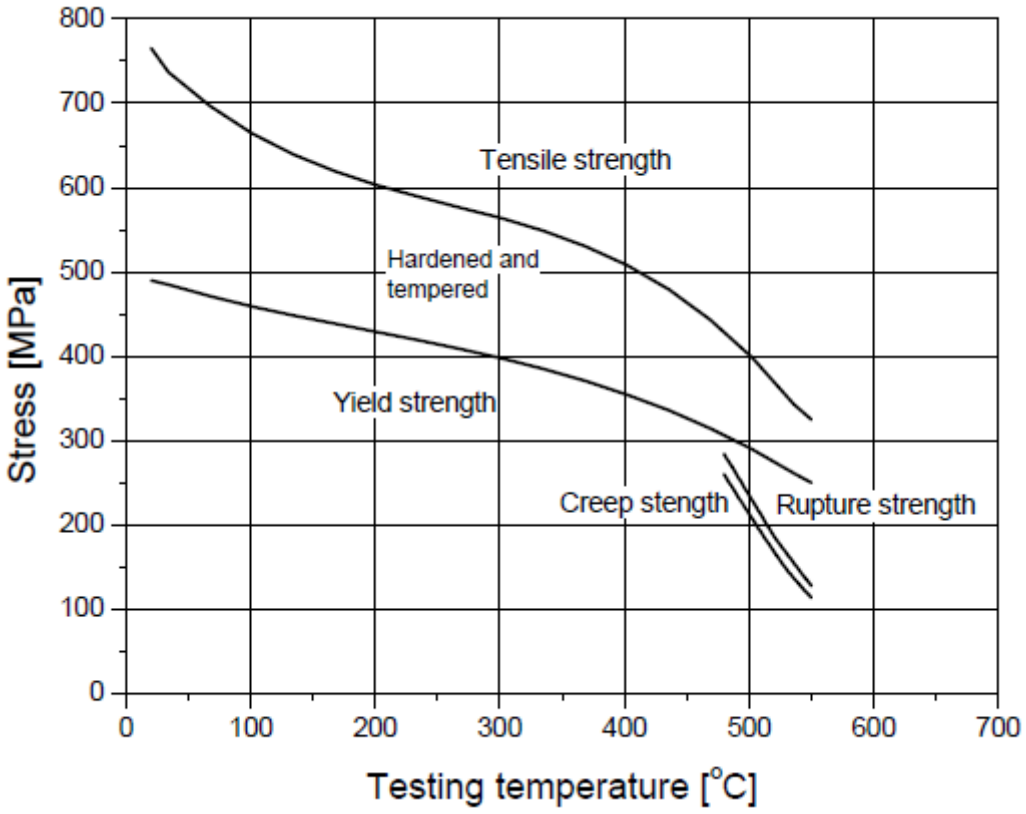

Figure 10: Tensile and creep properties of X20CrMoV12-1 as a function of temperature[23]

2.5.4 Hardness of X20CrMoV12-1

One of the prerequisites for steels is the amount of C and alloy content of the steel. Hardening heat treatment is often applied to increase the strength and wear resistance of steels. The hardness of X20 can be attributed to the heat treatment cycle applied which results in a specific microstructure. The alloy austenitization is at 1050°C. This is followed by air cooling as seen in the CCT diagram in Figure 11.

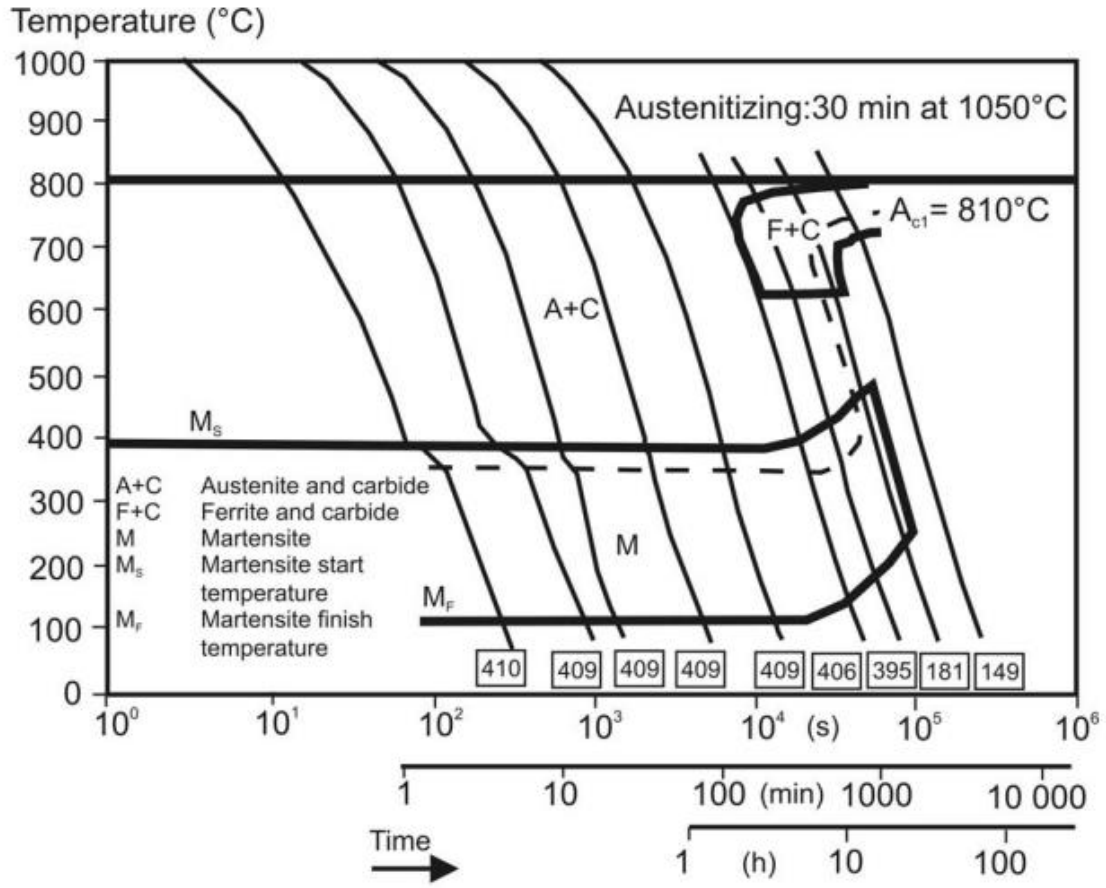

Figure 11: Continuous Cooling Transformation (CCT) diagram of X20CrMoV12-1 [8]

Hardness of X20 can be reduced even in the fully transformed martensitic steel if the C and N content is not sufficient to compensate for the C depletion due to the precipitate growth on the subgrain boundaries[23]. In efforts to increase the hardenability of X20, the related risk of cracking in large components and large wall thicknesses must also be taken into consideration. In addition to hard cracking, hardened components are also sensitive to intercrystalline stress corrosion cracking when exposed to steam or water. Therefore, the hardened small components such as boilers pipes and seam welded pipes with martensitic structure in welds should not be stored in air atmosphere. They must be tempered immediately after the martensite transformation[27].

The variation of Vicker's hardness, with a load of 35kgF, of X20 as a function of tempering temperature of 750°C after austenitizing at 1050°C for 1 hour followed by air cooling can be seen in Figure 12[28].

The heat treatment involved the following three states:

- State 1: the as-received steel heat treatment: homogenised at 1050°C for 1 hour followed by air cooling then tempered at 750°C for 4 hours followed by air cooling

- State 2: X20 in its martensitic state after annealing at 1050°C for 1 hour followed by air cooling and tempering for 10 minutes at 750°C
- State 3: X20 in its martensitic state after annealing at 1050°C for 1 hour and air cooling

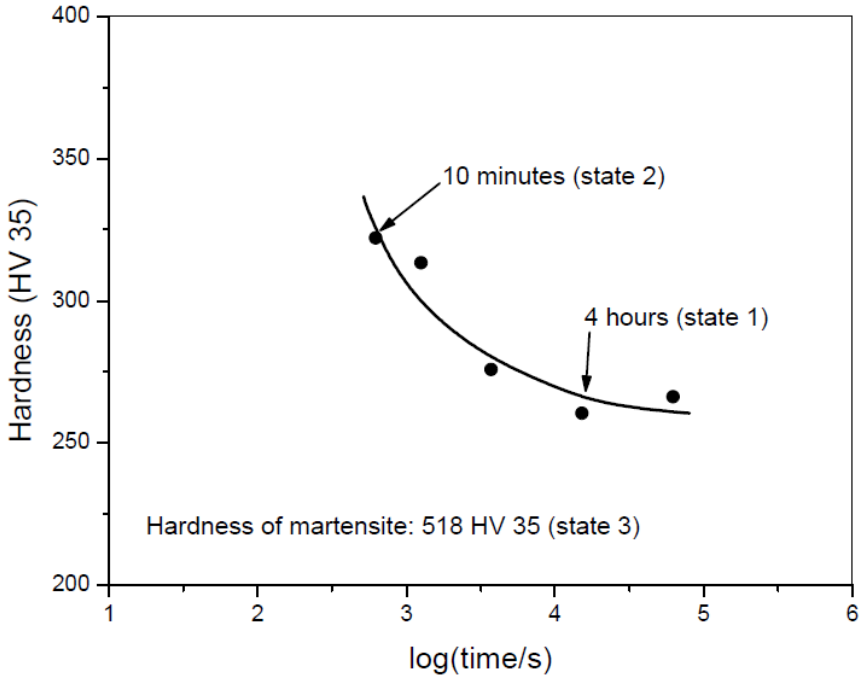

Figure 12: Variation of hardness of X20CrMoV12-1 steel as a function of tempering time[28]

2.5.5 Microstructure

The microstructure of X20 is that of a tempered martensite formed during a final normalizing and tempering heat treatment as seen in Figure 13[23]. The final microstructure for X20 is determined by the cooling rate in the heat treatment. The peak temperature and hold temperature influences the initial austenite grain size.

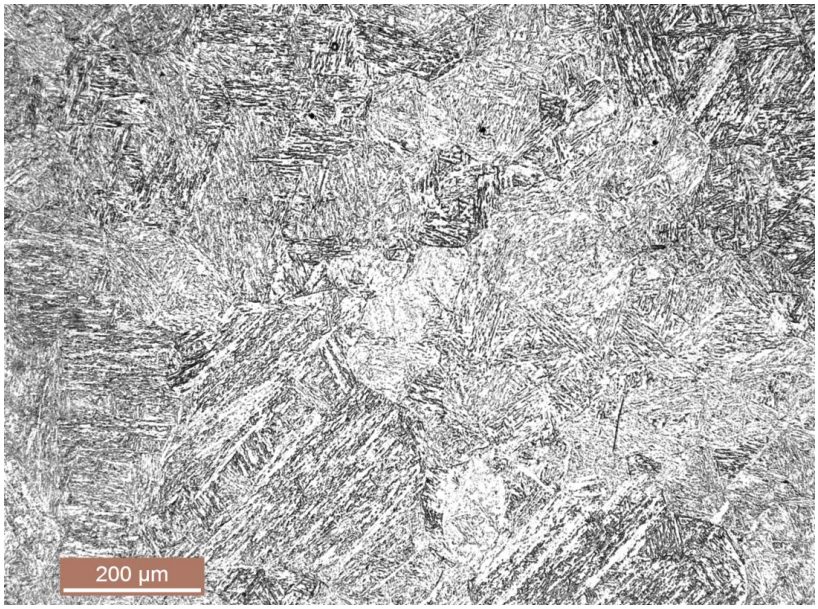

Figure 13: Tempered martensite microstructure of X20CrMoV12-1

In austenitizing at temperatures above A_{C1}, ferrite (BCC) transforms to austenite (FCC). During cooling from the austenitizing temperature to room temperature, a martensitic microstructure forms. Tempering results in a ferritic sub-grain microstructure with carbides and carbonitrides forming at prior austenite grain boundaries (PAGB), sub-grain boundaries and dislocations within the grains as shown in Figure 14 [8].

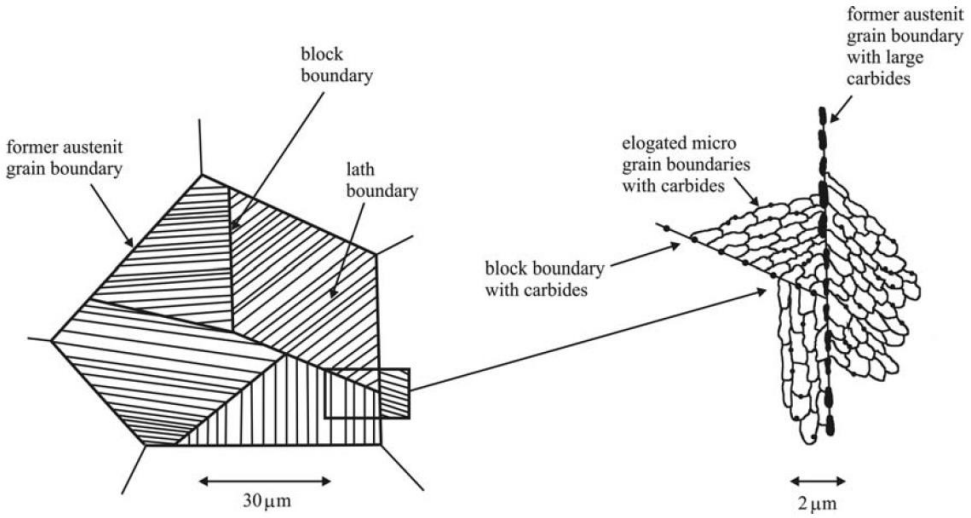

Figure 14: Schematic illustration of microstructure of a typical martensite 9-12%Cr creep-resistant steel containing precipitates on the internal interfaces[8]

2.5.6 Precipitates in X20CrMoV12-1

The fine distribution and high thermal stability of precipitates in X20 is the main characteristic in governing the high creep strength of the alloy[23]. The creep strength of the

material is strongly dependant on the amount, size and dispersion of precipitates [8]. The types of precipitates formed depend on various factors such as composition, temperature history during fabrication and time and temperature of service exposure. The main precipitate found in 9-12% Cr steels is $M_{23}C_6$ carbide consisting of Cr, Fe, Mo, W and C. This precipitate produces the basic creep strength of X20 by precipitating on sub-grain boundaries during tempering at 730-780˚C. The $M_{23}C_6$ precipitates increase the creep strength of X20 by retarding sub-grain growth which is a great contributor to the creep strain of these steels. The thermal stability of $M_{23}C_6$ is relatively high [29]. $M_{23}C_6$ carbides are found in the early stages of tempering because they nucleate easily on the internal interfaces [8]. Figure 15 shows a schematic of the crystal structure of a typical $Cr_{23}C_6$ carbide with an FCC structure.

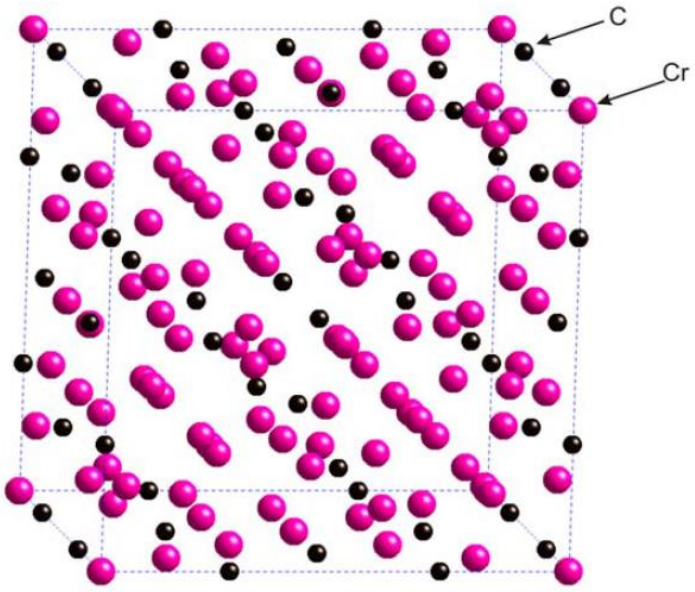

Figure 15: Representation of crystal structure of $Cr_{23}C_6$ carbide with FCC structure[8]

The MX precipitates in X20 consist mainly of V, Nb and N. These precipitates occur within the sub-grains by pinning down dislocations thus resulting in the increases creep strength of the steel. The high thermal stability of $M_{23}C_6$ and MX precipitates also contribute to the high creep strength of X20 [23][29]. Equilibrium calculations carried out on X20 also suggest the occurrence of VN (vanadium nitrides). These precipitates also contribute to the high creep strength of the steel. This is quite interesting as nitrogen is not a specified alloying element in X20. However, it does contribute to the overall high strength of X20[30] .

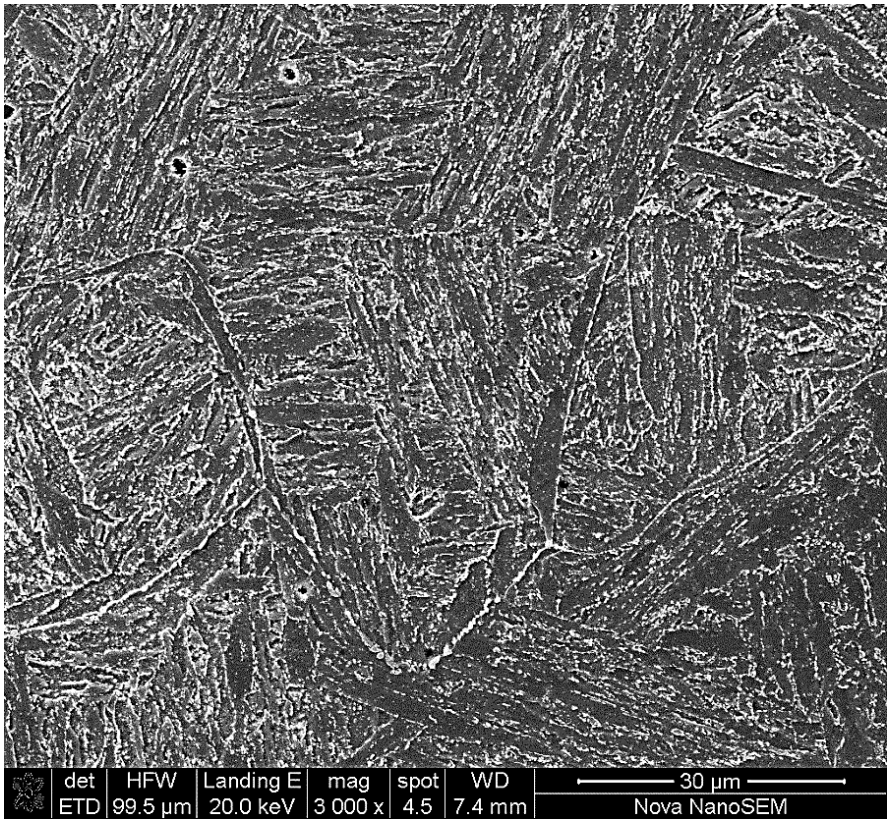

Figure 16: Chromium rich $M_{23}C_6$ carbides on a prior austenite and sub grain boundaries

2.5.7 Heat treatment

The mechanical, creep and fracture properties of X20 steels depend strongly on the microstructure, which in turn depends on the chemical composition, casting and cooling processes. It may be further modified by heat treatment and thermo-mechanical treatment of cast and/or wrought structure[23].

2.5.7.1 Transformation behaviour

The transformation behaviour of X20 is best described using phase transformation diagrams. The microstructure of the material can be predicted for different temperatures using a Time Temperature Transformation (TTT) diagram. The TTT diagrams are used to indicate the microstructural changes as a function of cooling time and heating rate between 500-800°C. Phase changes of X20 occur at specific transformation temperatures. These temperatures indicate the limiting transformation range that can occur in the microstructure[23].

The transformation temperatures for X20 are shown as follows in Table 5.

Table 5: Phase transformation temperatures for X20[23]

Phase	Temperature (°C)
A_{c1}: Austenite begins to form during heating	820
A_{c3}: Transformation of ferrite to austenite is completed during heating	851
A_{r1}: Transformation of austenite to ferrite plus cementite is completed during cooling	600-650
A_{r3}: Transformation of austenite to ferrite plus cementite is during cooling	650-750
M_s: Transformation of austenite to martensite starts during cooling	300
M_f: Transformation of martensite is completed during cooling	

Martensite transformation starts at 300°C in fast cooling, whereas in slower cooling, the precipitation of $M_{23}C_6$ carbides causes martensite transformation over longer times increased to 400°C. The ferrite-carbide transformation start temperature is dependent on the carbon and nitrogen content of the X20 steel[31]. The X20 steels which are used for their creep resistant properties contain transformed martensite. The transformation occurs during air cooling of thick walled components. Figure 17 shows a higher transformation of martensite between 200-275°C and it reaches approximately 90% transformation at 100°C[23].

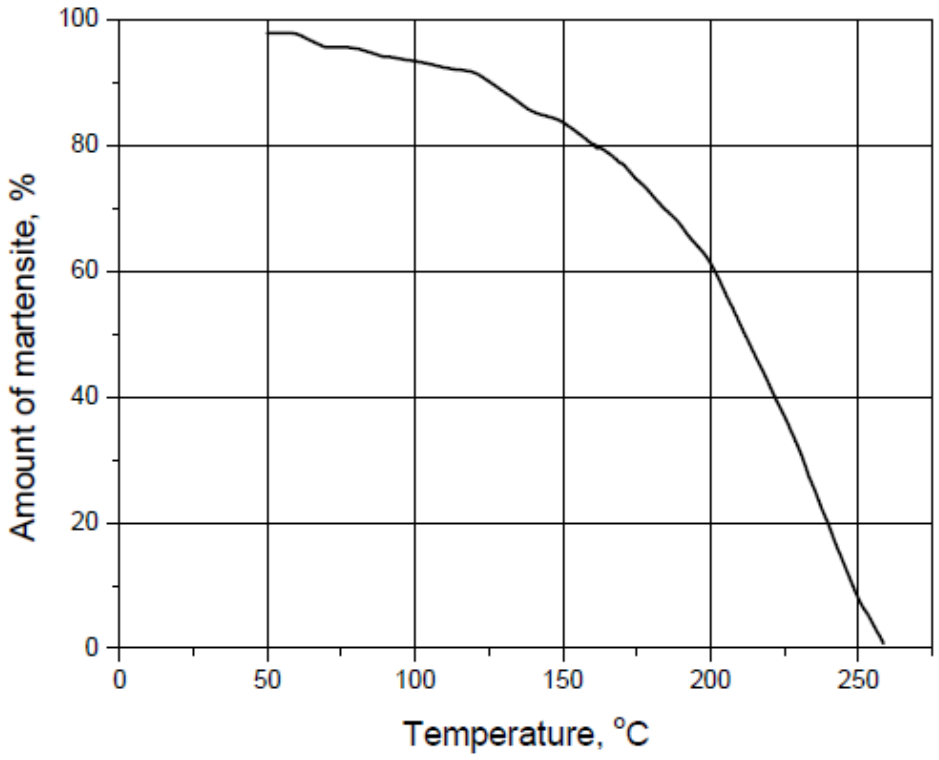

Figure 17: Martensitic transformation of X20[23]

The microstructural changes of X20 can also be identified using a Continuous Cooling Transformation (CCT) diagram. The CCT curves are used to develop the required microstructural changes through the control of applied thermal cycles for a number of different manufacturing processes. Slower cooling rates which occur closer to equilibrium generally result in the formation of ferrite. Bainite and martensite are more frequently formed under more rapid cooling conditions. The welding process is mainly responsible for the fast cooling rates, especially in the weld metal and the HAZ[23].

2.5.7.2 Final Heat Treatment

The heat treatment process of X20 involves controlled heating to austenitiizing temperature and cooling at various rates to manipulate the physical and mechanical properties without changing the product shape. The heat treatment is associated with increasing the strength of the material; however it is also often used to alter certain manufacturability (machinability, formability, ductility) properties of the material[23]. Table 6 provides the temperature range for the various stages of heat treatment for X20. Thick-walled components must undergo intermediate cooling in the range on 100-150°C to promote complete martensitic transformation.

Table 6: Heat treatment temperatures for X20CrMoV12-1[23]

Hot working temperature (°C)	Annealing temperature (°C)	Quenching and tempering	
		Quench hardening temperature (°C)	Tempering temperature(°C)
850-1100	750-780	1020-1070	730-780

2.5.7.3 Post Weld Heat Treatments of Welds

The heat treatment for welds done on X20 is done following specified guidelines. The guidelines for Eskom related welds are governed by the British Standard (BS EN 13480-4:2012): Metallic industrial piping - Part 4: Fabrication and installation[32]. These guidelines include:

- Preheating temperature of 250°C at a heating rate of 50°C/hour
- The root and hot pass at 250°C
- The filler and cap is done at 400°C (after a temperature increase of 50°C/hour until the temperature reaches 400°C)
- After the welding is complete the temperature is decreased at a rate of 50°C/hour to 150°C to promote complete martensitic transformation. The temperature is kept at 150°C for 120 minutes
- Once complete martensitic transformation is complete, the temperature is increased to 750C° also at a rate of 50°C/hour for 120 minutes for annealing

- After annealing is complete, the temperature is dropped to 100°C at a rate of 50°C/hour. Once the temperature of the material reaches 100°C, the post weld heat treatment is complete

Figure 18 shows a schematic representation of the heat treatment for a weld. The heat treatment includes the pre-welding and post welding heat treatment. The weld is a cast structure joining wrought structures which results in a difference in homogeneity.

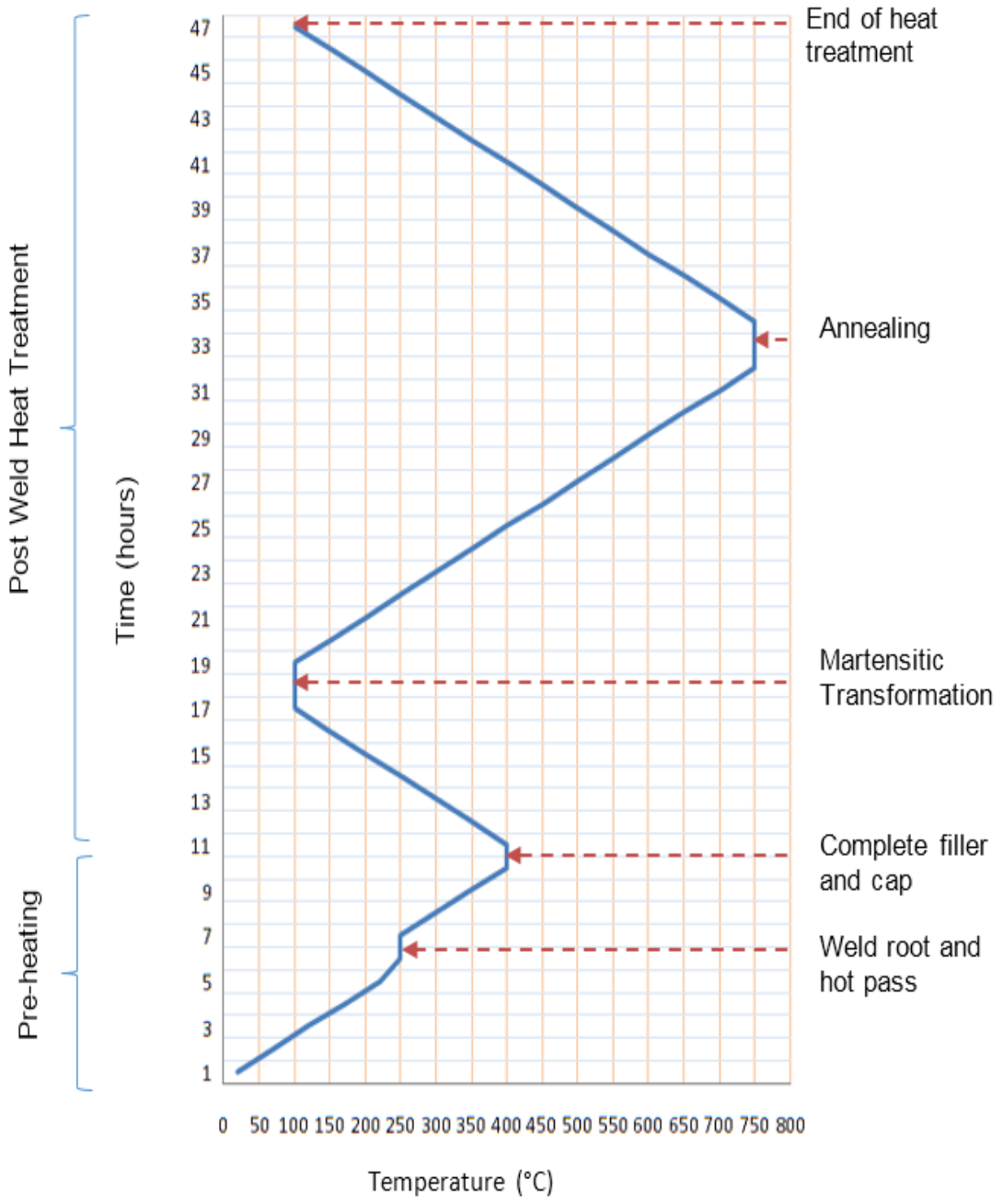

Figure 18: Heat treatment for welds on X20CrMoV12-1

2.6 Microstructural Evolution in the Heat Affected Zone of 9-12%Cr Steels

2.6.1 Introduction

The repair philosophies of main steam pipework in power plant environments rely on fusion welding. Fusion welding is seen as the most important joining process for these steels and strongly affects the properties of power plant components[33]. The fusion process does not only involve the addition of a new material, but it also includes the weld metal which is deposited between the connected parts. The properties of the base material are altered by a local and very inhomogeneous heat treatment as a result of the weld thermal cycle[34]. The variations in the microstructural characteristics of each region of a typical steel weld gives rise to marked variations in creep properties. This mismatch in creep properties leads to highly complex mechanical and material behaviour[35].

This section focuses on the microstructural changes taking place within the weld heat HAZ of ferritic heat resistant steels. The base material microstructure and properties designed through accurate melting techniques, exact production process control and proper heat treatment by the base material manufacturer are changed completely within the HAZ by the application of the weld thermal cycle. Internal stresses generated during the rapid cooling, which are in the order of the yield strength of the material, sum up with external stresses later on in service[34]. Due to the gradients of microstructure in the HAZ, there are corresponding gradients in creep properties. If the creep resistance reaches a minimum at some location then complex constraint effects are expected during cross-weld loading, which may intensify local damage[36].

The high creep strength of martensitic grade steels is based on a tempered martensitic microstructure with finely dispersed carbides and nitrides (M23C6, MX) which hinder dislocation movement during creep exposure. When theses martensitic steels are welded, the HAZ exhibits a reduced creep strength and premature failures compared to the base material[12]. This is due to fine grained structures without lath-martensite formed in the HAZ during weld thermal cycle [37].

2.6.2 The Welding Procedure

Ferritic 9-12% Cr power plant steels are generally supplied in a normalised and tempered condition. Tempering is recommended following welding, to reproduce as far as possible, a tempered martensite microstructure and to relieve some of the stresses induced by welding. The base material is frequently preheated to avoid cold cracking, followed by natural cooling to ambient temperature which is slightly below the martensite finish temperature. A typical heat treatment for a P91 welded joint is shown in Figure 19[36].

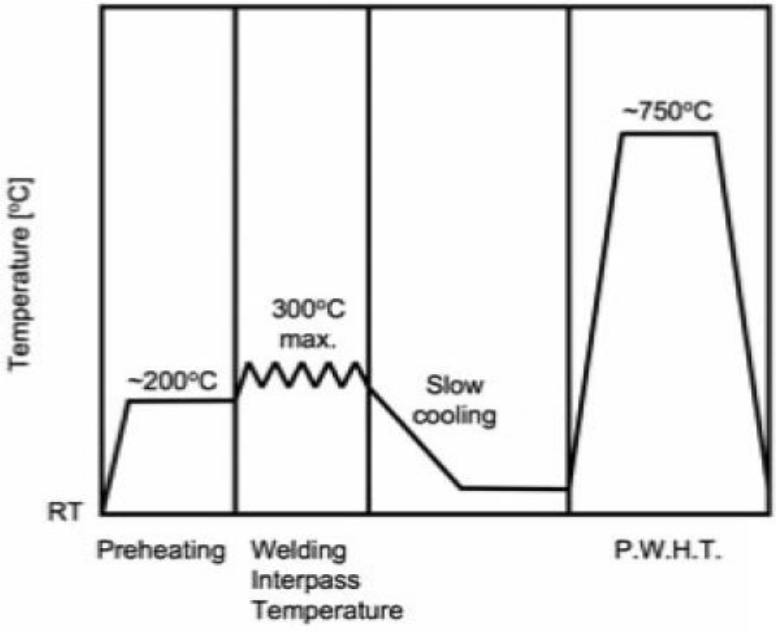

Figure 19: Typical heat treatment for welded joints in P91 steel[36]

Gas tungsten arc welding (GTAW) is often used to complete the root pass (Figure 20) given its ability to make high quality welds. It is essential to have a strong root pass as this is the first physical connection between the base materials and is particularly vulnerable to contraction strains. The same process can be used to complete the joint but manual metal arc welding (MMAW) is often used in complex joints, or high productivity processes such as flux cored arc welding (FCAW) and submerged arc welding (SAW) for deep welds[36]. Filler materials for 9-12% Cr steels are required to match the creep strength of the parent material in service. Ideally, they would also have matching toughness at ambient temperatures since welded joints are exposed to transient stresses during shut down periods[36][38]. Commercial filler metals tend to have similar composition to the parent material, with matching creep strength but lower toughness[36].

Figure 20 shows the root pass as “A”. Pre-determined groove angles depend on the thickness and application of the materials being welded. Special machining preparations are done to create groove angles with equivalent dimensions for the root pass and filler material. Once the root pass is completed by GTAW, filling passes (“B”) are carried out. The process of completing the filling passes involves following the groove angles initially created.

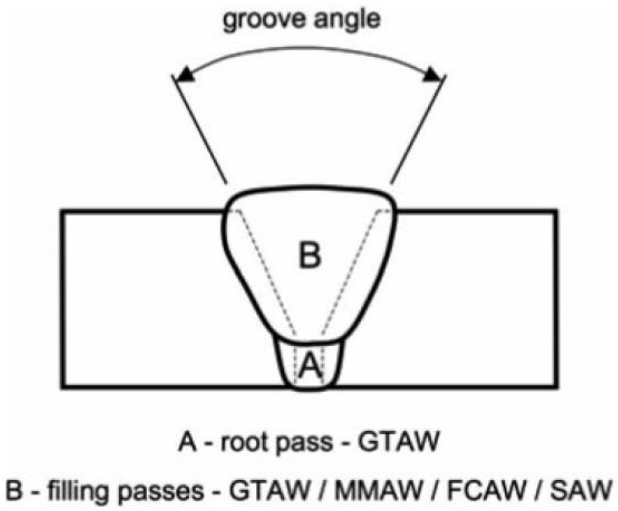

Figure 20: Schematic representation of welded joint in 9-12% Cr ferritic steel[38]

2.6.3 The Heat Affected Zone of 9-12%Cr Steels

The basic influences of the welding process on the metallurgy in the HAZ are shown in Figure 21. In addition to these influences, they are compared to the calculated equilibrium phase diagram of X10CrMoVNb9-1 (P91) steel. The microstructure of the base material, next to the weld, is dependent on the selected welding process and changes depending on the selected welding process. According to Palo et al[23] and Mayr [39], the resulting microstructure of the HAZ is governed by the following factors :

- weld thermal cycle;
- peak temperature (T_P);
- dwell time;
- cooling rate;
- effects of multilayer welding and
- post weld heat treatment (PWHT)

The heating rates in arc welding processes can be as high as hundreds of Ks^{-1}. As a result of the high heating rates, the transformation temperatures are shifted significantly higher than those predicted in the equilibrium phase diagram (T_0). The higher heating rate also shifts the solution temperature of precipitates to a higher temperature. The heating rate also affects the recrystallization temperature, solution temperature of carbides and nitrides and grain growth[34].

Three scenarios could be considered when welding precipitation strengthened creep resistant steels. These include[34]:

- T_P is too low to have any noticeable effect on precipitates
- Particles partially dissolve during the weld thermal cycle but eventually coarsening of favoured particles occur and

- Particles dissolve completely during the thermal cycle and omission of grain boundary pinning causes excessive grain growth.

Besides precipitate strengthening, grain size control is also very important as grain size control is a key factor for good mechanical properties and the susceptibility of the alloy to several damage mechanisms such as cold cracking, reheat cracking or Type IV cracking[34].

In 9-12% Cr steels, the equilibrium phase diagram (Figure 21) shows that austenite (γ) starts to transform to delta ferrite (δ) at high peak temperatures (T>1100˚C). The nucleation of delta ferrite grains at austenite grain boundaries reduces the grain size again. Whereas the lower solubility of carbon and other austenite stabilising elements in the ferrite results in an escape of these elements out of the delta ferrite into the remaining austenite regions, ferrite formers, such as chromium, are enriched in the ferritic region. Therefore, segregated regions differ locally in chemical composition and austenite transformation on cooling can be incomplete, resulting in retained delta ferrite or retained austenite[34].

As previously mentioned, the welding process strongly influences the microstructure and properties of the base material. As a result of severe thermal cycles caused by the welding process, the original microstructure is altered and a so-called HAZ is formed[34]. Experience with welded components shows that creep or creep fatigue damage appear during long exposure times in the HAZ[40],[41]. The HAZ can be divided into a different sub-zones, however the distinct borderline between the different sub-zones is not recognisable[34]. The sub-zones include the coarse grain zone (CGHAZ), fine grain zone (FGHAZ), intercritical zone (ICHAZ) and the over-tempered zone. Each zone is represented by its unique microstructure and properties.

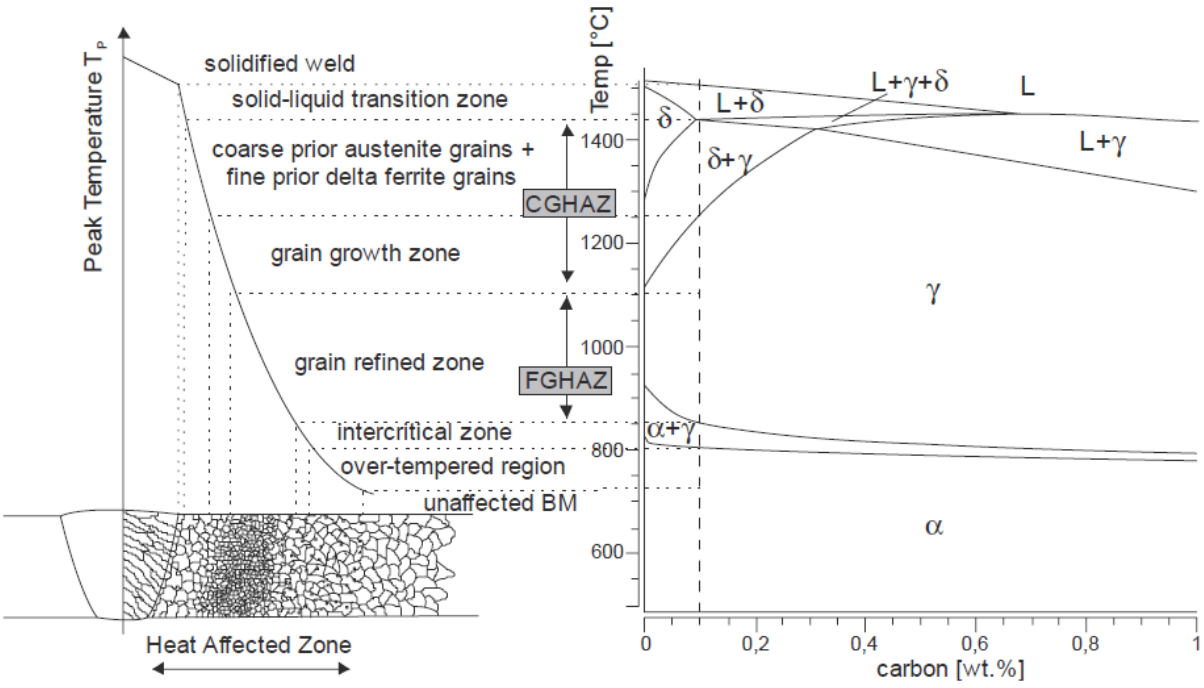

Figure 21: Schematic of the sub-zones of the heat-affected zone and relation to the calculated equilibrium phase diagram of X10CrMoVNb9-1 steel[34]

a) The CGHAZ: the grain growth zone ($T_P >> A_{c3}$)

The CGHAZ is the closest to the fusion line and experiences temperatures well above the A_{c3} temperature. At these temperatures the austenite is the stable phase. Any precipitates which obstruct growth of the austenite grains at lower temperatures dissolve, resulting in the coarse grains of austenite. The CGHAZ features the highest hardness and generally the low toughness values[34][36][41] .

b) The FGHAZ: the grain-refined zone ($T_P > A_{c3}$)

The FGHAZ forms at lower peak temperatures of about 1100°C (just above the A_{c3} temperature). This region comprises of small grains of austenite. Due to the peak temperature not being sufficiently high, the precipitates such as M23C6 and Laves phase do not completely dissolve, limiting grain growth. The FGHAZ is regarded as the weakest zone in the weldments during creep service. This is as a result of precipitates like M23C6 and Laves phase coarsening quickest in this region than in the base material during creep. Due to the high number of small grain boundaries, the diffusional creep rate increases. At longer service times and lower stress levels, most weldments of creep resistant ferritic steels fail within this region by a mechanism known as Type IV cracking [1][36][41].

c) The ICHAZ: the partially transformed zone ($A_{c1}<T_P < A_{c3}$)

The ICHAZ forms at temperatures between A_{c1} and A_{c3} as a result of partial transformation of α into γ on heating. New austenite grains normally nucleate at favoured positions such as prior austenite grain boundaries or martensite lath boundaries. In the case of the ICHAZ, the untransformed tempered martensite microstructure is tempered for a second time by the weld thermal cycle. Partial dissolution of precipitates can occur in conjunction with precipitate coarsening especially subsequent to PWHT[34][36][41].

d) The Over-tempered Region

The peak temperature of this region is below A_{c1} and the microstructure does not undergo any phase transformation. However, the original microstructure is locally tempered at a higher temperature compared to that of the PWHT base material. This results in the coarsening of precipitates being enhanced by a higher coefficient of diffusion at this temperature[34][36].

2.6.4 Damage Mechanisms in Creep Exposed Welded Joints

The types of cracks observed in weldments of heat resistant were first classified by Schüller et al[42] in 1974. Cracks were classified depending on their location and orientation within the weldments. Type I and II cracks occur in the deposited weld metal and develop in the longitudinal or transverse direction. Type I cracks remain in the weld metal but the Type II cracks can propagate into the HAZ and base material. Type III cracks form in the CGHAZ close to the fusion line and can prolong in this zone as well as into the base material. Type IV

cracks occur in the IC/FGHAZ and the base material. The location of the different cracks can be seen in Figure 22 [34], [36].

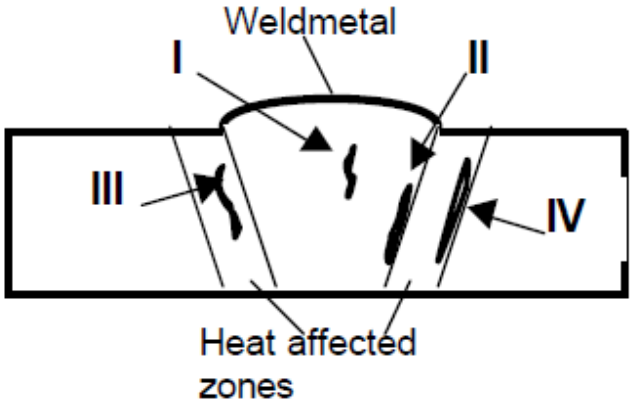

Figure 22: Classification of crack locations[43]

By characterisation of the microstructure local to such cracks and by studying the creep rupture strength of homogenous simulated HAZ specimens, investigators have identified the Type IV region as the ICHAZ, or more commonly, the FGHAZ [44][45][46][47][48]. Therefore for the purpose of this report, emphasis will be made on Type IV cracking as this type of cracking is relevant in the presentation of this work.

2.6.5 Type IV Cracking

Welding in all its variations is the major joining and repair technology for 9-12% Cr steels in power plant operations[34]. The poor cross-weld strength of welded joints compared with that of parent material has become a major concern for power plant operators who have installed creep strength enhanced ferritic (CSEF) steels without adequate provision for the lower creep strength in welded joints[44]. Several years of in-service experience and long-term creep testing data of cross-welds of various grades of martensitic steels have revealed the IC/FGHAZ of the HAZ as the weakest part of such weldments. Reduced creep strength of cross-welds is related to an enhanced microstructural degradation of the HAZ[34].

Type IV cracking is defined as the formation and propagation of failures in the FGHAZ and the ICHAZ region of the HAZ. For Type IV cracking to be characterised, cracking is located towards the outer edge of the visible HAZ[44]. A strict differentiation between the FGHAZ and the ICHAZ is generally difficult because of very similar microstructural features in both regions. Type IV cracking is considered as the major “end of life” failure mechanism for ferritic creep resistant steel weldments in the power generating industry[34], [36]. Therefore, this failure mechanism is of great interest and many researchers have investigated this life limiting phenomenon in welded joints. Creep failures in ferritic weldments at high stress levels take place in the base material, weld metal or the HAZ, whereas fracture location of

weldments exposed to lower stress levels shifted into the very narrow FGHAZ/ICHAZ [12],[18],[34]. This outcome is shown in Figure 25.

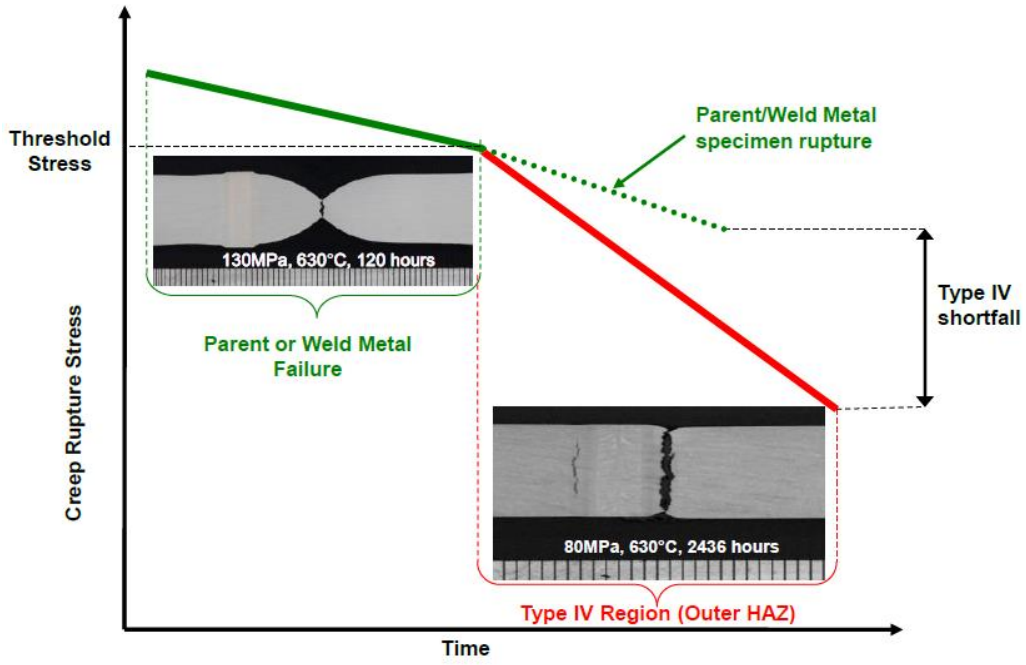

Figure 23: Representation of the shortfall in creep strength of a cross-weld specimen compared with a parent or all-weld-metal specimen[44]

In the FGHAZ, the thermal cycle peak temperature is above A_{c1} and A_{c3} respectively[44]. The mechanism occurs as a result of enhanced void formation in the IC/FGHAZ leading to early failure when compared with creep tests on unwelded steel[36]. Creep voids generally initiate sub-surface and grow in a diffusive manner. Preferred nucleation sites for voids are particle/matrix interfaces associated with inclusions or second phase particles[49]. In the IC/FGHAZ region of weldments, carbides only partially dissolve by the applied weld thermal cycle. This allows re-austenisation at the peak temperatures without complete dissolution of the boundary precipitates, despite the temperature being above the thermodynamic dissolution temperature for $M_{23}C_6$. This results in a microstructure consisting of precipitates at old boundary positions and at newly-formed boundaries without any such precipitates or strengthening (Figure 24). The new boundaries are considered weak, allowing recovery, sub-grain growth and softening to occur at a faster rate[15],[50],[51],[52].

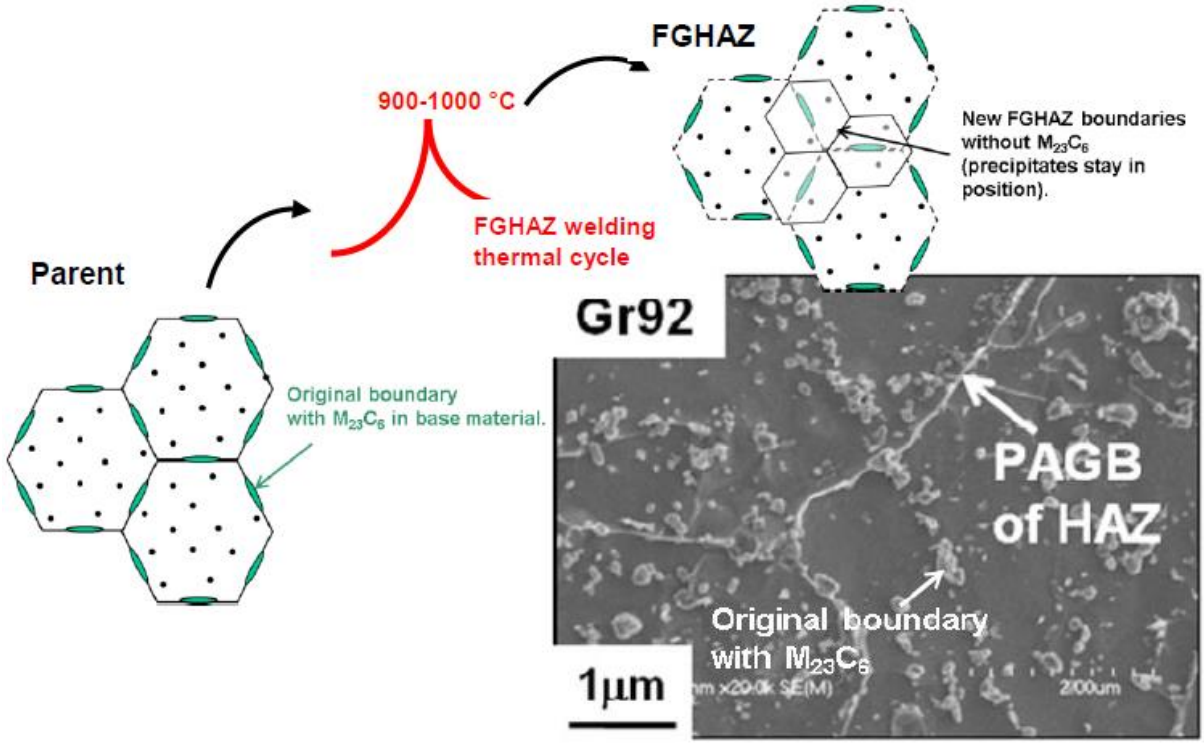

Figure 24: Development of microstructure in the FGHAZ of typical 9-12% Cr creep resistant steel[50]

Precipitation of retained carbides on retained large particles such as $M_{23}C_6$, is favoured instead of the fine re-precipitation on grain boundaries in order to decrease the interfacial energy of the microstructure[53]. Therefore, retained carbides coarsen more rapidly than those in the base material or weld material during PWHT and are preferred nucleation sites for creep voids. All these microstructural changes take place faster in the IC/FGHAZ and contribute to the continuous weakening of this specific region, finally leading to breakdown in creep strength [34]. The total strain in the FGHAZ is also low, contributing to failure[44].

The role of constraint on the creep weak IC/FGHAZ region from adjacent stronger CGHAZ and base material is a key factor for clarification of Type IV cracking mechanism. By tensile loading of the dissimilar regions of the HAZ in series, the weakest region tries to deform transversely under high strains. If this region is sufficiently thin, it is constrained from doing so by the adjacent stronger material. As a result, a triaxial stress state predominates and prevents the weaker region from yielding[34][44]. Consequently, when cross-weld samples are subjected to uniaxial load, if there is a weak creep zone constrained by stronger material, the weak zone is subjected to a multiaxial stress state. A common feature of Type IV failure is that the macroscopic failure strain of a cross-weld is low and appears brittle[35].

2.7 Fine Grain Heat Affected Zone Simulation

2.7.1 Introduction

In order to characterise the creep behaviour of individual zones with the HAZ, HAZ simulation procedures are applied to the base material. The intended purpose of a HAZ simulation is to apply the time-temperature history as experienced in a distinct sub-region of the HAZ to the base material. The gradual changes in the creep behaviour of the HAZ can be determined as a result of the replication of a larger volume of the specific sub-zone of the HAZ[54]. The production of a larger volume ensures a lower scatter of the test results. So the main objective for simulating a HAZ is to apply a weld thermal cycle as measurable in a distant sub-region of the HAZ to a sample with larger testing volume. The temperature of the weld thermal cycle can be measured either by thermocouples or numerical prediction as described in the German code SEW-088. The different methods used for the industrial application of the weld thermal cycle include[43]:

a) Induction heating and hold at peak temperature with subsequent cooling in an oil bath
b) Heating in a hot salt bath until the peak temperature is reached, immediately followed by cooling in a salt bath at about 100°C and
c) HAZ simulation using a Gleeble thermo-mechanical machine

HAZ simulation provides the closest similarity to the actual weld thermal cycle as it is more flexible with the capacity for a larger range of heat inputs. The length of constant microstructure is however limited to approximately 10 mm which has consequences with respect to the gauge length. Methods a) and b) provide a uniform microstructure along the whole specimen length, the heating rate is however much slower and the applicable cooling time is quite restricted [43]. Table 7 gives the minimum information required for parameters which need to be controlled for the HAZ simulation.

Table 7: Minimum information required for HAZ simulation[43]

Category	**Minimum information required**
HAZ simulation	• Method used (induction heating and oil cooling, or salt bath heating and cooling, or Gleeble HAZ simulation
Weld thermal cycle	• Peak temperature • Heating rate or heating time to peak temperature • Holding time at peak temperature • Cooling time between 800 and 500°C • Details of multipass HAZ simulation (second peak temperature and cooling time)
Homogeneity of simulated sample	• Length of uniform microstructure
Heat treatment	• Postweld heat treatment used

The mechanical properties as well as the creep properties of a weldment depend on various influencing parameters which need to be considered in the assessment of creep testing and data acquisition. The basic idea of HAZ simulation is to take into account the most important parameters. In order to investigate the influence of the most important welding parameters on the mechanical properties, the principle route is followed as shown in Figure 25. There is a direct correlation between the mechanical properties and the HAZ microstructure, which depends on the cooling rate and the material dependant transformation kinetics. The transformation kinetics is greatly influenced by the austenitic grain size. The austenite grain size is characterised by the peak temperature and the distance from the fusion line. The weld thermal cycle is characterised by the cooling time between 800°C and 500°C and the peak temperature. The cooling time is dependent on the plate thickness, the welding process (thermal efficiency), joint type, welding parameters (current, voltage, travel speed, heat input) and the preheating temperature[55].

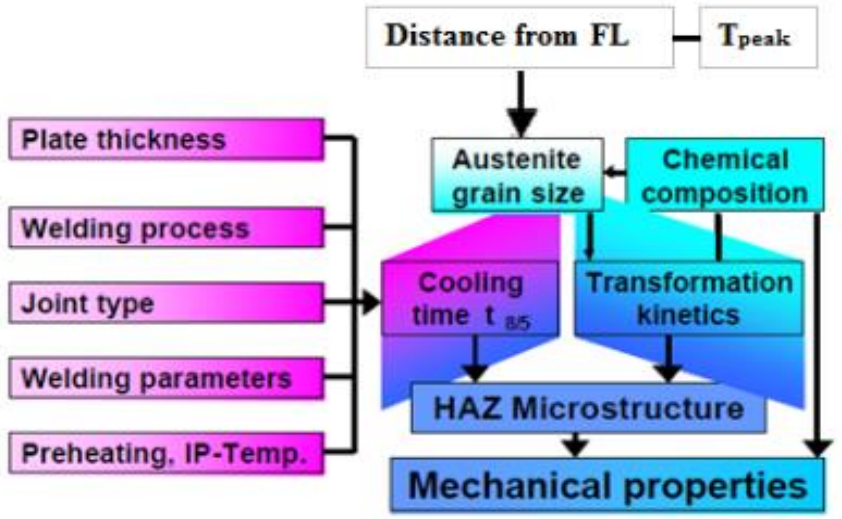

Figure 25: Coupling of the most influencing factors on the HAZ properties in a logical way[55]

2.7.2 Determination of the weld thermal cycle

The most widely used procedure to predict the weld thermal cycle is the standardised cooling time concept according to the German standard SWE 088, which is based on the analytical solution derived by Rosenthal. The principle focuses mainly on two cases[55]:

1. Two dimensional heat flow (thin sheet)
2. Three dimensional heat flow (thick plate)

The cooling time can be predicted from various sets of information such as[55]:

- arc voltage,
- welding current and welding speed,

- preheating temperature, plate thickness,
- electrode diameter and runout time and
- electrode diameter and fused area

By the application of a single temperature-time cycle, one particular subzone in the HAZ under given welding conditions can be simulated. Usually, there can be variations made for the heat input, cooling time and peak temperature.

2.7.3 Gleeble Welding Simulation

By the controlled application of the thermal and/or thermo-mechanical cycles according to a particular weldment geometry and welding parameters, nearly every position in the weldment can be produced representatively and the microstructure can be investigated using conventional or sophisticated skilful techniques [55].

The Gleeble system is a fully interfaced system, readily programmed to provide reference signals for closed loop control of both thermal and mechanical operations. Heating is accomplished by the flow of low-frequency alternating current in the specimen with heating rates of up to 1000K/s. The feedback signal necessary for closed-loop control is normally obtained from a fine wire thermocouple percussion welded to the specimen surface as shown in Figure 26[55].

Figure 26: Thermocouple welded onto specimen

In order to determine a specific property (in this case creep) of a particular region in the HAZ, the weld thermal cycle is fed in the control computer and a cylindrical sample is heated up very rapidly to the desired peak temperature by direct current flow with up to 6000A. The cooling is provided by heat flow through the copper/stainless steel jaws which hold the specimen in position. At slow cooling rates, the given T-t curve in Figure 27 is very well controlled. Faster cooling rates can be achieved by reducing the distance between the jaws, air quenching or external gas cooling. The weld thermal cycles shown in Figure 27 are generally applied for weldability tests of 9-12% chromium steels regarding the likelihood of type IV cracking [55].

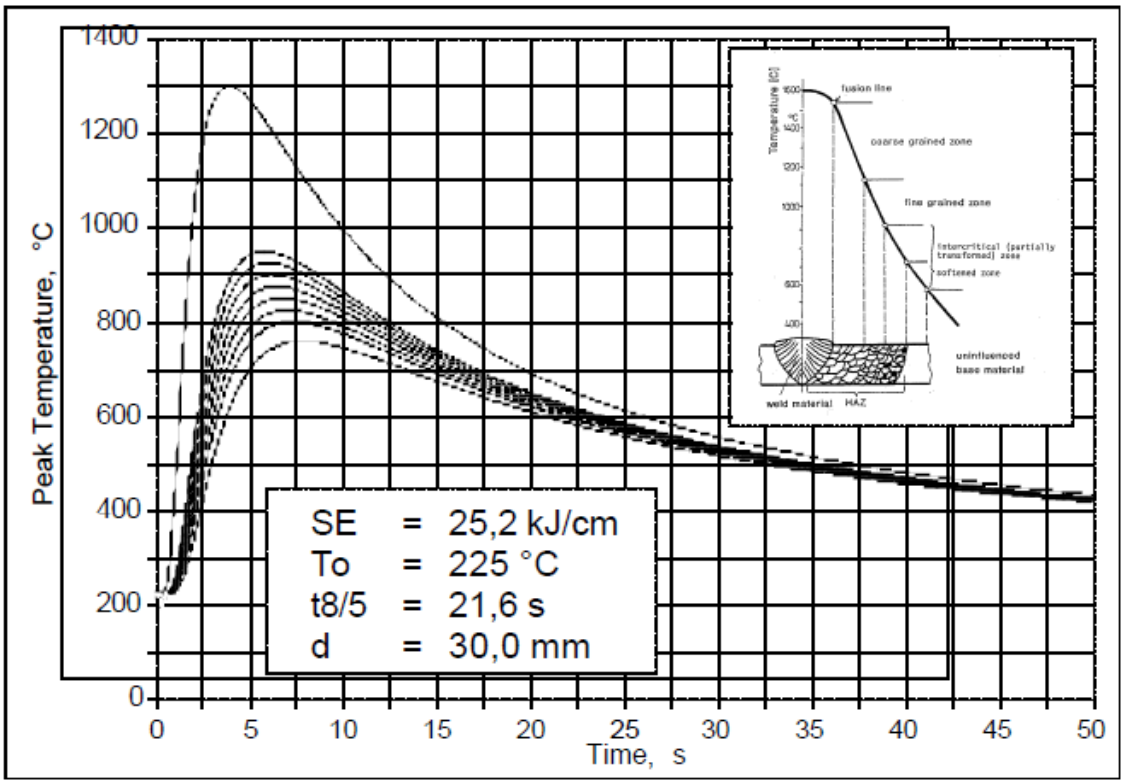

Figure 27: Weld thermal cycles for the coarse-grained zone [52]

The advantages of Gleeble weldability testing are[55]:

- Accurate application and measurement of the thermal cycle for a predefined location in the HAZ
- After simulation, an enlarged volume for further metallographic investigations or mechanical tests is available compared to the limited size in a real weldment
- Due to the larger volume and higher homogeneity of the simulated microstructures, there is a reduced scatter of the HAZ properties
- Phase transformations during welding can be measured by thermal analysis or dilatometric measurement of the C-strain
- In addition, mechanical stresses during the cooling phase can be superimposed in order to simulate any contradiction of the surrounding material
- The mechanical material properties during cooling from high temperatures can be directly measured for input in finite element calculations
- Other combined thermo-mechanical test can be applied such as reheating relaxation test, hot ductility test, partly melting and afterwards cooling to simulated the behaviour of the weld metal

The disadvantages of Gleeble weldability testing are [55]:

- The temperature profile in longitudinal direction causes some experimental problems

- Effects of local gradients in microstructure, properties and residual stresses are not taken into account when using the HAZ simulation technique.

Figure 28 shows the systematic approach in using a Gleeble device for a HAZ simulation. This is a summary of the process followed to create a HAZ simulation using a Gleeble device. Initially the parameters for the simulation must be decided. These include the peak temperature and the cooling rate and can be determined by HAZ-calculators or Gleeble programming. Most HAZ simulations using a Gleeble device are done on cylindrical specimens. Once the HAZ-simulation has been completed, the sample has to undergo PWHT to reduce and redistribute the residual stresses induced by the HAZ-simulation. Thermo-mechanical and metallography testing is often done on the samples once the HAZ simulation and PWHT have been complete.

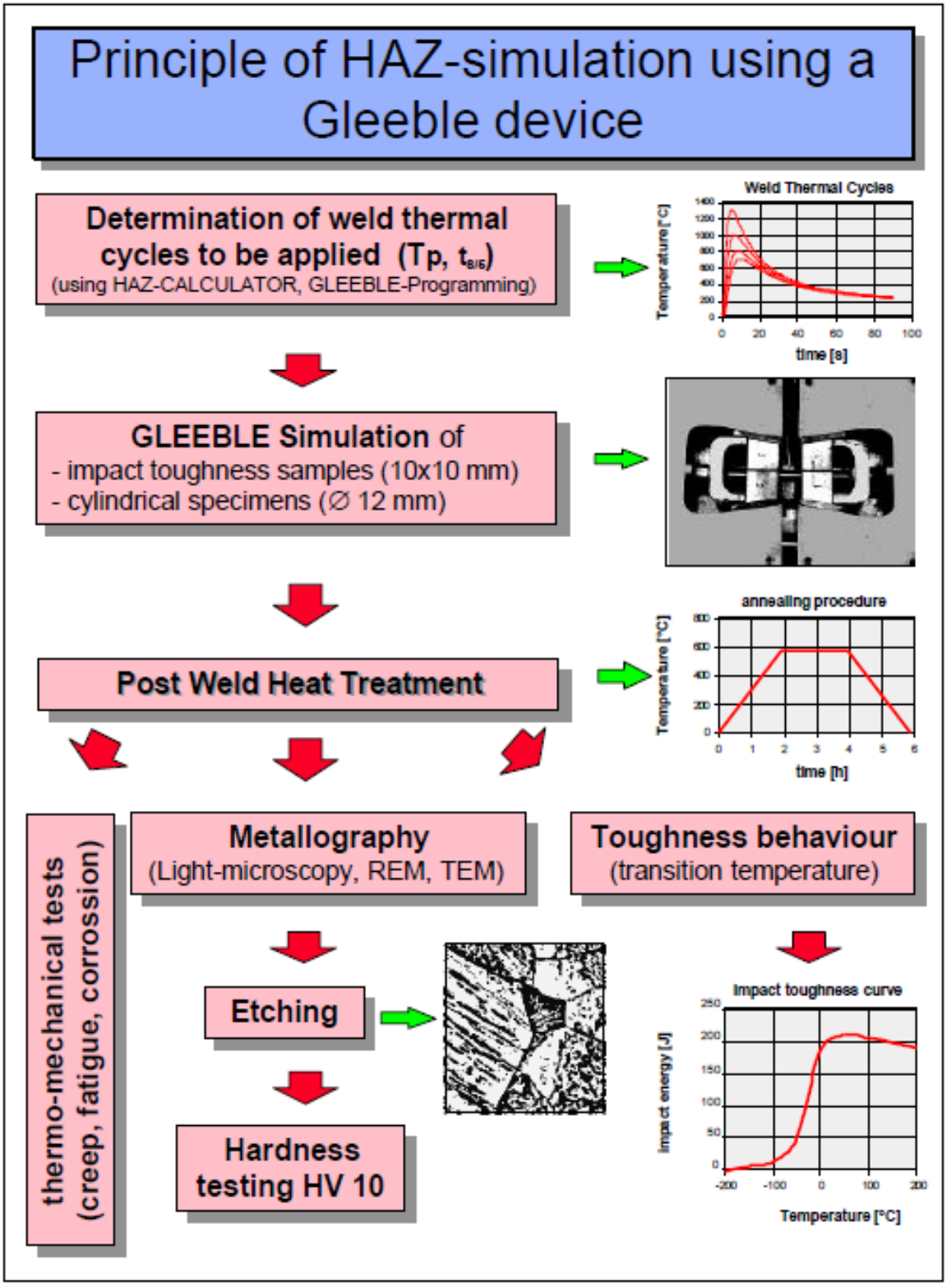

Figure 28: Typical procedure for Gleeble weldability testing and subsequent property determination[55]

3. Experimental Investigation

3.1 Investigated Materials

Three samples of X20 CrMoV12-1 were received from Eskom's Research and Innovation Centre (ERIC). Two samples of X20 were ex-service (creep damaged) material and the third sample was new (no creep aging). The two samples of creep-damaged material were chosen based on the creep damage measurements of the materials. Creep damage measurements are done by extracting surface replicas from surface of the pipework[56]. Table 8 shows the samples of creep-damaged material as well as the sample identification, which will be used for the rest of the report. Design and operating parameters for each material are also shown in the table. The dimensions for the pipe used in this research are given in Figure 29. The pipe has an internal diameter of 255mm±5mm and a wall thickness of 35mm±5mm. The areas, which were surface replicated, are also shown in Figure 29.

Table 8: Operating and design conditions for as received X20CrMoV12-1 material

Eskom Power station	**Eskom Creep Classification**	**Design temp. (° C)**	**Operating temp. (° C)**	**Operating pressure (MPa)**	**Design pressure (MPa)**	**Operating hours**
New material	No damage	545	0	0	19.4	0
Power station 1	Medium damaged	545	540	17.5	19.4	208302
Power station 2	High damaged	545	555	17.5	19.4	129801

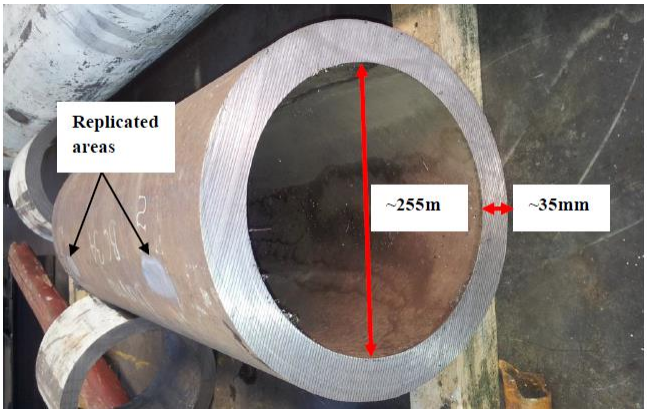

Figure 29: Dimensions for the creep damaged pipes used for this research[56]

3.1.1 Sample Designation

The three samples of creep aged base materials were labelled according to the damage characterisation provided by ERIC. The base materials were investigated in their as-received normalised and tempered condition. Table 9 shows the base materials together with their sample identification and creep damage. The sample identification for the as-received base materials, given in Table 9, is used as such for the rest of this dissertation.

Table 9: Sample designation of as-received material

Eskom Power station	**Eskom Creep Classification**	**Sample Identification**	**Creep damage (voids/mm^2)**
New material	No damage	X20_ND	No damage
Power station 1	Medium damaged	X20_MD	130-200
Power station 2	High damaged	X20_HD	340-485

The base materials are also investigated in a welded state as shown in Table 10. The weldments are created using Manual Metal Arc Welding (MMAW). Weldment 1 consists of X20_ND and X20_MD and weldment 2 consists of X20_ND and X20_HD.

Table 10: Sample designation of weldments

Weldment material	**Sample Identification**
X20_ND to X20_MD	Weldment 1
X20_ND to X20_HD	Weldment 2

Samples of the base materials which have undergone weld thermal cycle simulations and PWHT are named as shown in Table 11:

Table 11: Sample designation for weld thermal cycle simulated and PWHT base material

Original base material	**After weld thermal cycle simulation and PWHT**
X20_ND	X20_NDS
X20_MD	X20_MDS
X20_HD	X20_HDS

3.1.2 Chemical Composition

The chemical composition analysis for all three grades of material were carried out during the project of Teboho Molokwane[56]. Eskom follows the chemical composition standard prescribed by DIN 17175 for the acceptability of X20 CrMoV12-1 grade material in main steam lines. Table 12 gives the chemical composition analysis carried out on the three base materials. The chemical composition in weight percentage is given in comparison to the chemical composition prescribed by DIN 17175. The chemical composition of the materials used in this research complies with the range specified by DIN 17175.

Table 12: Chemical analysis (in weight %) for the X20 CrMoV12-1 samples used in this research [56]

Element	**X20 CrMoV12-1 (DIN 17175)**	**X20_ND**	**X20_MD**	**X20_HD**
C	0.17-0.23	0.19	0.21	0.2
Mn	≤1.00	0.35	0.41	0.46
S	≤0.030	≤0.005	≤0.005	≤0.005
P	≤0.030	0.012	0.006	0.015
Si	≤0.50	0.15	0.31	0.31
Cr	10.00-12.50	10	10.8	11.1
Mo	0.80-1.2	0.86	0.84	0.88
Ni	0.30-0.80	0.48	0.52	0.50
Cu		0.12	0.11	0.14
Al		0.025	0.036	0.038
V		0.24	0.28	0.26
Nb		≤0.005	≤0.005	≤0.005
Ti		≤0.005	≤0.005	≤0.005
B		≤0.001	≤0.001	≤0.001
W		≤0.005	≤0.005	≤0.005
Sn		≤0.002	≤0.002	≤0.002
As		0.0096	0.0086	0.0157
Sb		≤0.005	≤0.005	≤0.005
N		676 ppm	530 ppm	547 ppm
Fe	Matrix	Matrix	Matrix	Matrix

3.2Creep Testing

3.2.1 Material Sampling

The cross-weld creep test samples were machined at Eskom's Research and Innovation Centre (ERIC). Two weldments were created using Manual Metal Arc Welding (MMAW). The first weldment was a weld of X20_ND and X20_MD (weldment 1) and the second was a weldment of X20_ND and X20_HD (weldment 2).

Figure 30: Two weldments used for cross-weld creep testing specimens

The cross-weld samples were machined to include both base materials and weld for weldments 1 and 2. The specimens were machined following the European Creep Collaborative Committee (ECCC) recommendations[43]. The minimum diameter for the cross weld specimen had to be 8mm in order to ensure that the specimen deformation behaviour was representative of the welded joint. If the minimum required diameter of 8mm still could not be achieved due to limited material thickness and the consequent ratio of the FGHAZ-width to diameter is large, different necking effects may cause different stress enhancement or stress redistribution and hence influence the rupture time[43].

A minimum length of at least five times the outer diameter is required to ensure that there is no influence on the stress rupture time. In order to cater for the possibility of failure in the parent metal, the test piece gauge length must contain a considerable length of parent metal. High deformation in the FGHAZ may cause stress redistribution in the parent metal in the direct vicinity of the HAZ. It is therefore recommended that the length of the unaffected parent metal should not be less than 2.5 times the outer diameter. This is achieved by ensuring that the fusion line lays mid length of the gauge length. Figure 31 shows the drawing of the sample geometry which had to include the two base materials and the weld metal. The final cross-weld samples are shown in Figure 32.

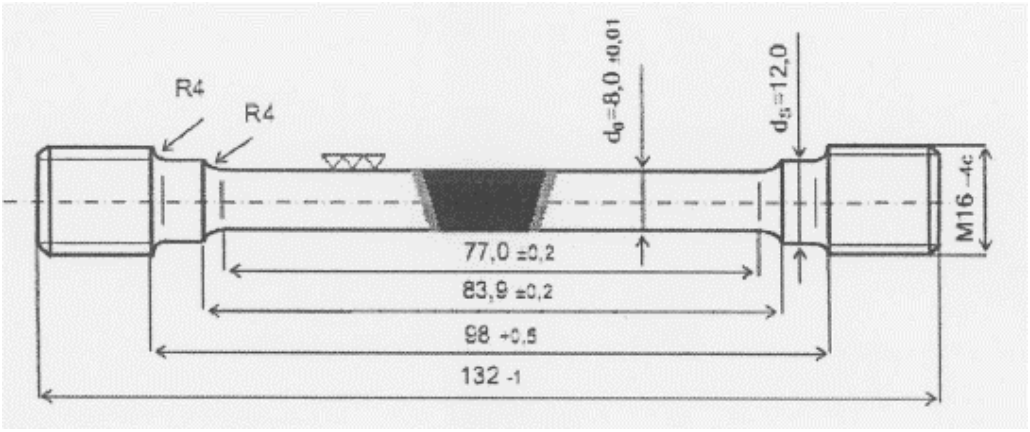

Figure 31: Specimen with cross weld in the middle[43]

Figure 32: Completed cross-weld samples

3.2.2 Experimental Set-up

Creep rupture tests were conducted at ERIC. The tests were carried out at a constant temperature of 610°C with varied loads. The reference stress for the initial test is based on a derivation made by Teboho Molokwane [56]. The reference load, σ_R, of 63 MPa was based on the Von Mises equation [3]:

$$\sigma_R = P\frac{\sqrt{3}}{2}\left[ln\frac{R_o}{R_i}\right]^{-1} \qquad \text{Equation 7}$$

Where P is the operating pressure

R_o is the outer radius of the pipe

R_i is the inner radius of the pipe

Stresses of 63, 80 and 90 MPa were applied to the samples. Furnaces made and installed by Applied Test Systems (ATS) were used for the creep testing. Figure 33 a) shows one of the furnaces used. The furnace is a split tube furnace. The creep tests were conducted in an argon filled chamber as shown in Figure 33 b). Temperature was monitored at three points: both ends on the sample and the centre of the sample by type K thermocouples. The ends of the

samples were fitted with extensometers to measure the displacement as a function of time under the constant load. This practice was applied to all samples at all loads. The tests were terminated when the samples ruptured.

Figure 33: a) Creep testing furnace at Eskom Research and Innovation Centre and b) shows the vacuum chamber which houses the specimen

3.3 Weld Thermal Cycle Simulation

The basic idea of HAZ simulation was to take into account the most significant parameters, whilst varying parameters were eliminated as far as possible. There is a direct correlation between mechanical properties and HAZ microstructure, which depends on the cooling rate and the material transformation kinetics, which itself is influenced by the austenite grain size. The austenite grain size is given by the peak temperature or by the distance from the fusion line, respectively [55].

3.3.1 Material Sampling

The as-received base materials were also used for weld thermal cycle simulations on the Gleeble®3800. The simulations were carried out to replicate the microstructure of the FGHAZ by using thermo-mechanical means. Further investigations included the impact of welding on material and mechanical properties of the as-received base material. The set-up of the Gleeble® required the use of 6mm diameter rod samples with lengths of 120mm for the weld thermal cycle simulation. Due to the nature of the clamping mechanisms of the Gleeble®, the ends of the rods had to be machined with M6 threads. Figure 34 shows the samples which were used for the FGHAZ simulation in the Gleeble®.

Figure 34: Weld thermal cycle simulation sample

3.3.2 Experimental Set-up

The parameters for the simulation depended on the transformation temperatures of the material. The model for the simulation was adopted from research conducted by Molokwane[2] and Mayr[34]. The time-temperature profile for the simulation is dependent on the A_{C3} (temperature at which ferrite to austenite is completed during heating) and A_{C1} (temperature at which austenite begins to form during heating). This can be found in section 2.6. These temperatures were material specific; hence investigations were conducted to determine these critical parameters for the simulation model.

The A_{C3} and A_{C1} were investigated in 2 ways:

- Equilibrium calculations for X20 using MatCalc and
- Dilatometry testing using the Gleeble®3800

3.3.2.1 MatCalc Thermal Equilibrium Simulation

MatCalc software was used to predict the equilibrium transformation temperature for the materials. The thermodynamic foundation for MatCalc is the CALPHAD (Computer Coupling of Phase Diagrams and Thermochemistry). CALPHAD is based on the promotion of computational thermodynamics through development of models to represent thermodynamic properties for various phases which permit prediction of properties of multicomponent systems[57]. The software uses data from its impressive database for steels. The user inputs required for the phase transformation of the material are the chemical composition and the temperature at which simulation must be calculated. The temperature used in this simulation corresponded to that used for the creep test (610°C). The MatCalc simulation is carried out using the chemical composition of X20_ND which is given in Table 13.

Table 13: Chemical composition input for MatCalc simulation

	C	Cr	Cu	Mn	N	Nb	Si	V	Ni	Mo
Weight %	0.19	10	0.12	0.35	0.03	0.005	0.15	0.24	0.48	0.86

The equilibrium simulation was conducted at 610°C. The phase fraction in relation as a function of temperature is shown in Figure 35. The simulation shows that the A_{C3} temperature is approximately 820°C. This temperature is vital in establishing the simulation model for the weld thermal cycle as the FGHAZ exists at the A_{C3} temperature. Another important finding in this simulation was the temperature at which the $M_{23}C_6$ precipitates completely dissolve. The $M_{23}C_6$ precipitates were completely dissolved in the FGHAZ and recovered after the PWHT. Therefore the peak temperature for the simulation of the weld thermal cycle had to be higher than the temperature at which the $M_{23}C_6$ precipitates dissolve. This temperature is given as approximately 940°C according to the MatCalc simulation. At the equilibrium temperature of 610°C, the simulation did not show the development of Laves phase or Z-phase. Other precipitates which do occur at the equilibrium temperature were MX and VN. These precipitates were present until temperatures of approximately 940°C. At temperatures above 940°C these precipitates completely dissolved into the matrix.

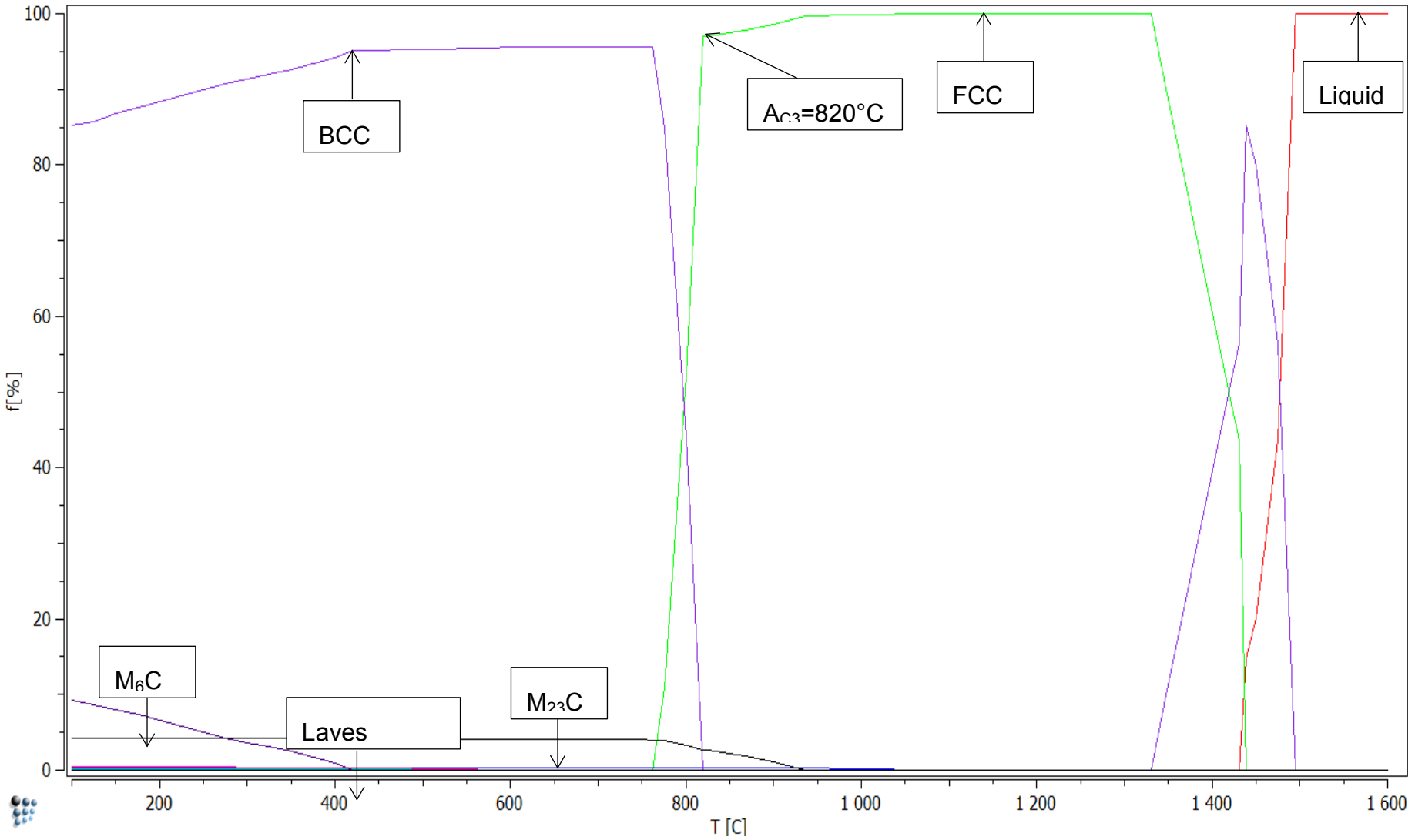

Figure 35: X20 CrMoV12-1 MatCalc thermal equilibrium simulation

3.3.2.2 Dilatometry

Dilatometry is the measurement of volume change of a material during a physical or chemical process. In a thermo-mechanical process, a dilatometer measures the expansion or shrinkage of a material over a certain temperature range. During phase transformations the specific volume changes due to the change of the lattice structure and this enables to receive transformation temperatures [41]. In this experiment, dilatometry was used to determine the non-equilibrium phase transformation temperatures of the base material, in particular A_{C3}. The Gleeble 3800 is equipped with a quenching dilatometer and measured the change in diameter of the sample.

The set-up for the dilatometry experiment was carried out in the following steps:

a) The 6mm diameter, 120mm long rods were spot welded with thermocouples (highlighted by red). The rods were then fastened by end plates to ensure that they remained in place during the simulation (Figure 36 a)) and placed inside the Gleeble®
b) The rod was then placed between copper grips. The grips were used as a medium for the thermal load to be applied to the rod specimen (Figure 36 b))
c) The dilatometer was placed on the sample at the point of temperature measurement as shown in Figure 36 c) to measure the change in diameter of the sample during the simulation. The dilatometer was used to verify the commencement and completion of the phase transformations.

Figure 36: Set-up for dilatometry experiment

The specimens were put through a thermal cycle as shown in Table 14. This time-temperature profile was used in the study conducted by Molokwane [56] to replicate the FGHAZ and had been used in this investigation for dilatometry experiments. The data acquired from the dilatometry measurements made it possible to know the A_{C1}, A_{C2}, A_{C3}, M_S and M_F temperatures of the material. A summary of the results for the dilatometry are shown in Table 15. The FGHAZ occurs at temperatures just above the A_{C3} temperature of the base material. By the use of dilatometry, this can be achieved from the relative expansion of the base material through the weld thermal cycle.

Table 14: Weld thermal cycle properties

Temperature (°C)	Time (s)	Holding time(s)	Heating rate (°C/s)	Cooling rate (°C/s)
25	0	0		
250	5		45	
250	25	20		
1050	29		200	
1050	33	4		
100	59.4			26.4
100	79.4	20		

3.3.2.3 Dilatometry for X20_ND

Figure 37 is the dilatometry curve generated from weld thermal cycle simulation conducted on X20_ND at a peak temperature of 980°C. The relative expansion of the sample is determined by the expansion/contraction of the sample in relation to the initial diameter during the weld thermal cycle simulation. The dilatometry curve can be divided into two separate curves. The heating part of the curve provides information about A_{C1}, A_{C2} and A_{C3}. The cooling part of the curve provides information about M_S and M_F.

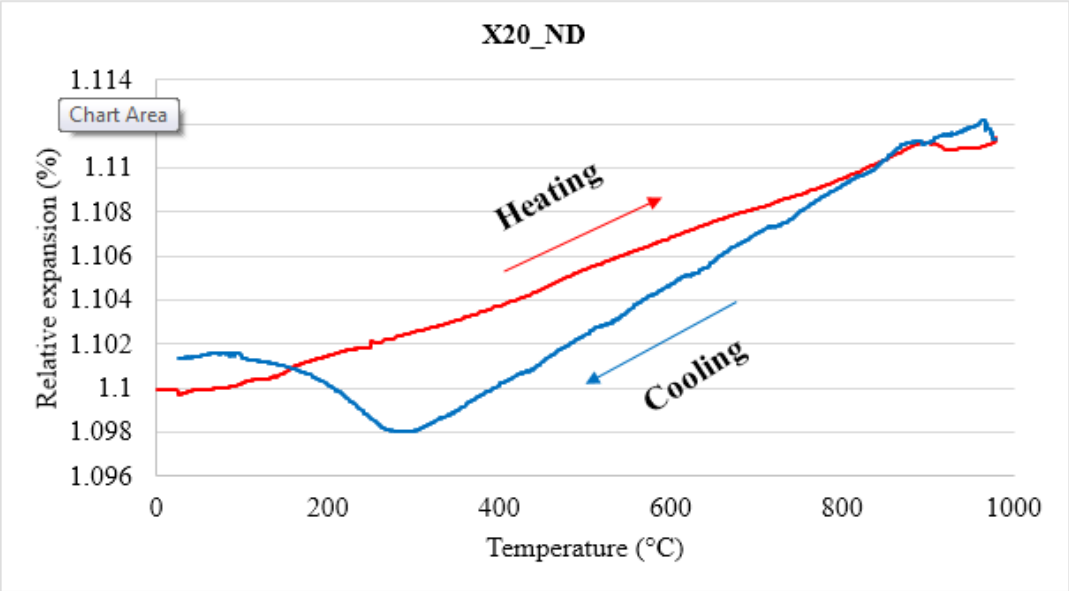

Figure 37: Simulated weld thermal cycle of X20_ND at a peak temperature of 980°C

The first phase change transformation occurs by the change of ferromagnetic to paramagnetic. This occurs at A_{C2} (750°C) shown in Figure 38 and is known as the Curie temperature. The A_{C1} temperature (896°C) indicates the start of the transformation into

austenite. This phase change brings about volume changes as a result of the heating cycle. Complete austenite transformation temperature is given as A_{C3} (966˚C). These transformation temperatures can be seen graphically in Figure 38 by the relative expansion of X20_ND during the weld thermal cycle simulation.

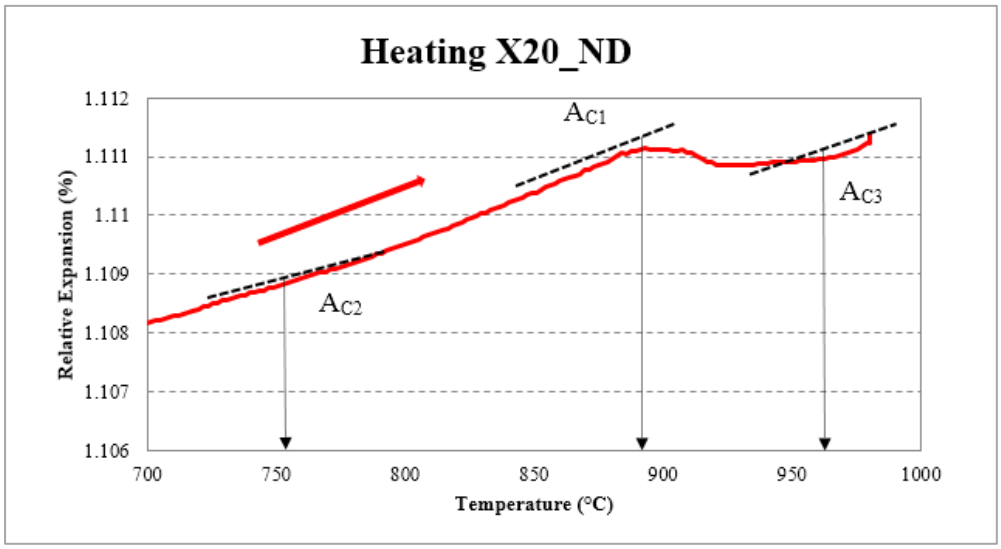

Figure 38: Phase transformation temperatures achieved by the weld thermal cycle simulation at a peak temperature of 980˚C on X20_ND

After being held at a peak temperature of 980˚C for 4 seconds, the sample is air quenched to transform austenite into martensite. This phase transformation from the face-centred cubic austenite into the body-centred tetragonal martensite begins at M_S (310˚C). This transformation is complete at M_F (86˚C). At M_F, there is almost complete martensite transformation. However, from practice, small volume fractions of austenite remain. Figure 39 shows the graphical representation of the cooling process of the dilatometry curve adapted from the weld thermal cycle simulation.

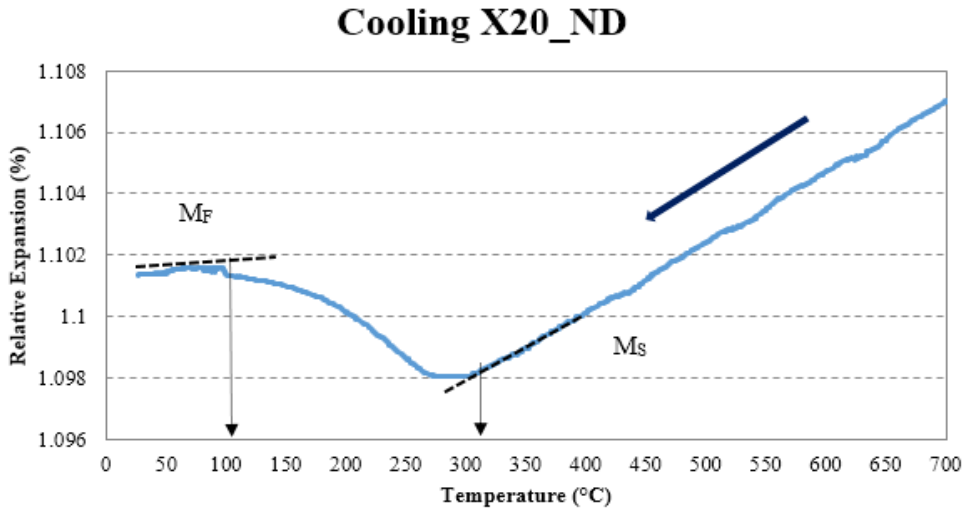

Figure 39: Phase transformation temperatures achieved by the weld thermal cycle simulated at a peak temperature of 980˚C on X20_ND

The analysis shown in Figure 38 and Figure 39 are done for X20_MD and X20_HD. These results are shown in Table 15.

Table 15: Summary of phase transformation temperatures for the as-received base material

Base Material	**Peak temperature (°C)**	**A_{C1} (°C)**	**A_{C2} (°C)**	**A_{C3} (°C)**	**M_S (°C)**	**M_F (°C)**
X20_ND	980	896	750	966	310	86
X20_MD	980	890	751	940	360	86
X20_HD	980	893	741	935	308	86

3.3.3 Gleeble Weld Thermal Cycle Simulation

The equilibrium and non-equilibrium calculations yielded A_{C3} temperatures of 820°C and approximately 950°C. Since all non-equilibrium temperatures occur similarly, an A_{C3} temperature of 980°C was selected for the simulation. The addition of ≈30°C to the non-equilibrium A_{C3} temperature is to accommodate for the complete dissolution of precipitates in the matrix. The same time-temperature profile used for the dilatometry experiments was used for the FGHAZ weld thermal cycle simulation. However, the peak temperature used for the FGHAZ simulation was set to 980°C.

The first few simulation tests were conducted by measuring the temperature gradient between 3 points of measurement. The first thermocouple, the temperature control thermocouple, was spot-welded at the centre of the sample. A second and third set were welded on either side of the first thermocouple at a distance of 5mm as shown. The placements of the thermocouples are highlighted by red in Figure 40 a). The sample was held in place by copper grips and fixed into position by C-grips as highlighted by red arrows in Figure 40 b). Due to the application of a minimal preload, the sample did not have to be accommodated in the longitudinal direction.

a)

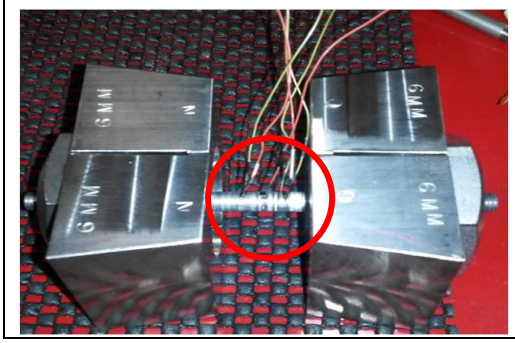

b)

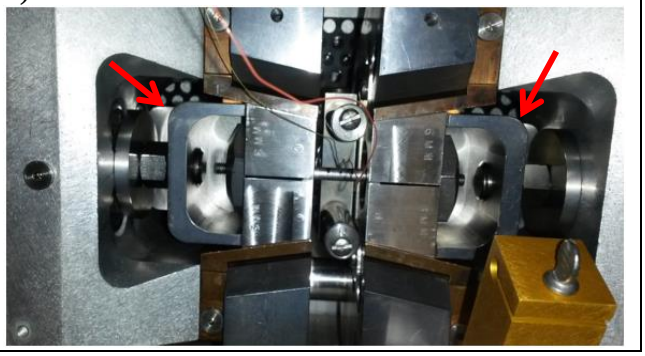

Figure 40: a) Spot-welded thermocouples on sample, b) sample in the Gleeble 3800

The weld thermal cycle is used to mimic the conditions of a single pass weld. The heat cycle involves a heating rate of 45°C/s from ambient temperature to 250°C. This temperature is maintained for 20 seconds. The heating rate increases to 200°C/s to raise the temperature to the peak temperature of 980°C. This temperature is maintained for 4 seconds before being air quenched to 100°C at a cooling rate of 26.4°C/s.

3.3.4 Post Weld Heat Treatment

All completed weld thermal cycle simulation samples were followed by a post-weld heat treatment. The post-weld heat treatment was carried out according to the British Standard: BS EN 13480-4:2012- Metallic industrial piping Part 4: Fabrication and installation. Prior to PWHT, the samples were coated with a mixture of Isomol 100 and methanol. This was done to prevent oxidation of the material during the PWHT. The samples were placed in a furnace with thermocouples placed on the samples for accurate temperature measurements. The samples were heated to a peak temperature of 740°C at a heating rate of 100°C/hr. The samples were held at peak temperature for 30 minutes thereafter cooled to ambient temperature at a cooling rate of 100°C/hr. The conditions for the heat treatment are given in Table 16.

Table 16: Post weld heat treatment conditions conducted on weld thermal cycle simulated samples

Initial Temperature (°C)	Heating rate (°C/hr)	Peak Temperature (°C)	Holding time (hr)	Cooling Rate (°C/hr)	Final Temperature (°C)
23	100	740	0.5	100	23

3.4 Microhardness

Microhardness testing was carried out with a testing load of 300gf on the Zwick Roell ZHV1 micro Vickers hardness tester. Testing was done on all three base materials to determine the possible mechanical property degradation after different durations of creep aging. The standard used for assistance in the micro hardness testing is the ASTM E384-11. A matrix of 3x3 was indented on the base material with a distance of 10mm between consecutive points. Figure 41 shows the indents on the samples of X20_MD base material. The same test method was applied to the simulated FGHAZ samples as well.

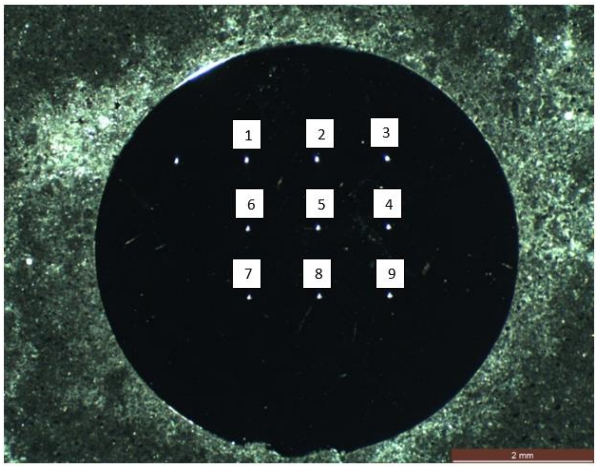

Figure 41: Medium damage micro hardness matrix

Microhardness tests are conducted on weldment 1 and 2 across the HAZ. Three lines of micro hardness tests were done for each HAZ. The length of the HAZ, indicated between the white solid lines in Figure 42, was approximately 2.5 mm. Due to the HAZ been so short in length, the indent spacing used for the microhardness tests are 0.25 mm between each indent. The purpose for microhardness testing along the profile of the HAZ was to identify the regions of varying hardness. According to research conducted by Koukal et al[58], the FGHAZ/ICHAZ possess the lowest hardness value. Also, by identifying the regions of different hardness, these areas were used to carry out EBSD analysis of the specific FGHAZ.

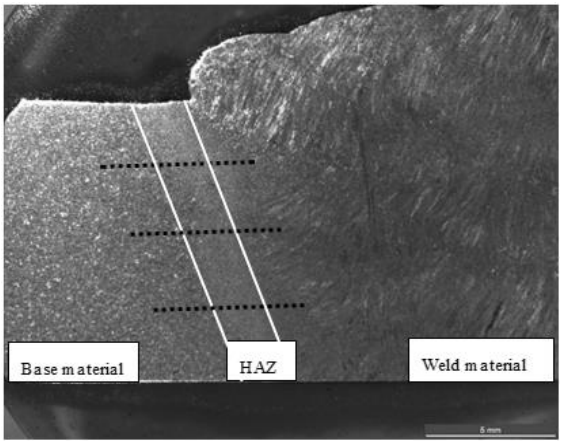

Figure 42: Light micrograph of weldment showing the base material, HAZ and weld material used for microhardness testing

3.5 High Temperature Tensile Testing

Hot tensile testing provides vital information regarding the mechanical properties of the material. Due to the different amount of creep damage induced in the base materials, understanding the possible difference in tensile properties adds value to the characterisation of the creep damage. Also, by applying weld thermal cycles onto the base materials by

simulation, the possibility for a change in the tensile strength is present. The three base materials and simulated weld thermal cycle samples were hot tensile tested, firstly, to establish the effect of creep damage on the tensile strength of the base material and ,secondly, to determine the effect of a weld thermal cycle on the hot tensile strength of the base material.

The hot tensile tests were conducted using the Gleeble® 3800. Five samples, with the same geometry as the simulation samples, of each base material and 5 samples of each weld thermal cycle simulated base material were hot tensile tested. Prior to testing each sample was measured for its initial length and cross-sectional diameter. Temperature control was provided by type-K thermocouples which were welded onto the centre of the length of the sample. Figure 43 shows the sample being pulled in the Gleeble®. The heat cycle used for the hot tensile tests involved heating the samples to 610°C in 30 seconds. This temperature was maintained for 20 seconds after which a strain rate of $10^{-3}s^{-1}$ was applied to the samples. Precaution had to be taken once the samples begin necking. The current supplied through the sample caused intense sparking once the sample began to break apart. Therefore most of the tensile tests were immediately stopped as soon as the rupture occurred.

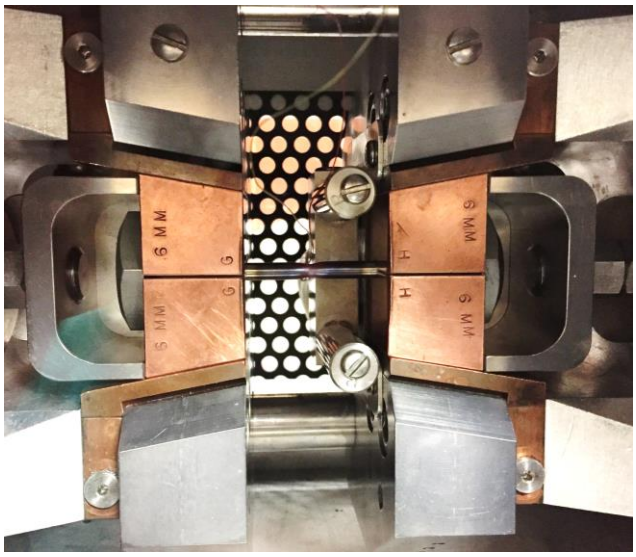

Figure 43: Hot tensile testing of base material using the Gleeble® 3800

3.6Metallographic Investigation

In order to prepare specimens for light and electron microscopy examinations, preparations were performed according to the procedure shown in Table 17 Planar grinding was performed by means of silicon carbide (SIC) paper and the Struers Tegramin-25 automatic polisher.

Table 17: Polishing and grinding steps using the Struers Tegramin-25

Grinding/Polishing step	Surface	Suspension/ lubricant	Polishing time (minutes)	Force (N)	Rotational speed (Rpm)
800 SIC grit paper		water	5	30	300
1200 SIC grit paper		water	10	30	300
3µm	MD-Dur	DiaDuo-2 3µm	25	10	150
1µm	MD-Nap	DiaDuo-2 1µm	25	10	150
Colloidal Silica	MD-Chem	OP-S	10	10	150

After each grinding and polishing step, the samples were washed with ethanol and placed in an ultrasonic bath for 10 minutes to remove excess grit, dirt and residue polishing and grinding compound from the polishing and grinding steps. The samples were further viewed under the optical microscope to ensure that the sample surface was perfectly clean for microscopic analysis.

The surfaces of the ground and polished samples were etched using Villela's reagent (1 gram Picric acid, 5 ml hydrochloric acid and 100ml ethanol). The reagent has a distinctive neon yellow colour and was swabbed onto the samples using cotton wool for 40 seconds before being washed thoroughly with ethanol. The application of the reagent enabled microstructural features of the samples to be analysed using optical and scanning electron microscopy.

3.6.1 Optical Microscopy

Qualitative characterisation of the microstructure at different magnifications (50x, 100x and 500x) were conducted using a Nikon Eclipse MA200 optical microscope to view microstructural features such as prior austenite grain boundaries, precipitation and void dispersion in the base materials. Each base material was investigated in various regions to report an overall conclusion of the microstructure. This microscope was also used to identify differences between the base material and Gleeble simulated FGHAZ samples. The fracture surface cross-sections of the creep-ruptured samples were also investigated.

The Leica EZ4D and Leica DME microscopes at Nelson Mandela Metropolitan University (NMMU) are used to investigate the creep ruptured samples as well as the Gleeble simulated FGHAZ samples. The Leica EZ4D was used to determine the length of uniform microstructure achieved by the Gleeble simulation and also to identify the location of fracture in the creep-ruptured samples.

3.6.2 Scanning Electron Microscopy

The SEM investigations were carried out using two microscopes. The first microscope is the Nova NanoSEM 230 and is housed at the Electron Microscope Unit (EMU) at the University of Cape Town. The second microscope is the JEOL7001F housed at the Centre for High Resolution Transmission Electron Microscopy (CHRTEM) at the Nelson Mandela Metropolitan University. The main reason for the use of two microscopes was due to the Nova NanoSEM 230 not being available due to breakdown during the course of this study.

Parameters for SEM operation included using an accelerating voltage of 20.0 kV with a spot size of 5 all analysis. The working distance between the pole piece and sample surface varied between 4mm and 12mm, depending on the depth of focus required for microstructural requirements. Fracture surface analyses required a less depth of focus as compared to the analyses of the cross-sectional areas. In instances were secondary electron detection was insufficient to reveal certain microstructural features, backscattered electron detection was used.

3.6.2.1 Evaluation of Damage in Base Materials

The focus of this work was on the secondary electron and backscatter imaging of the base material to quantify the occurrence of voids. Base material characterisation was done at magnifications of 1500x. A 1mm by 1mm area is outlined my microhardness indents out for the void count of X20_ND, X20_MD and X20_HD. Figure 44 a) highlights the area mapped out (red square) by SEM. Each image has an area of approximately 200µm x 170µm. Figure 44 b) is a backscattered electron image taken showing the occurrence of voids used in the void count analysis of the base material. Typical voids used in the analysis are outlined by red circles.

a)

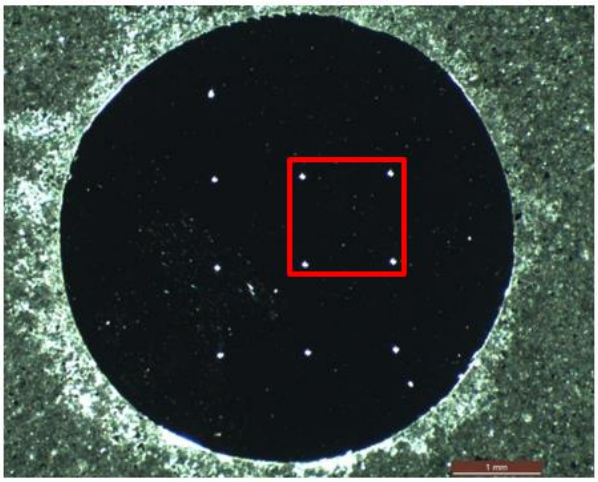

b)

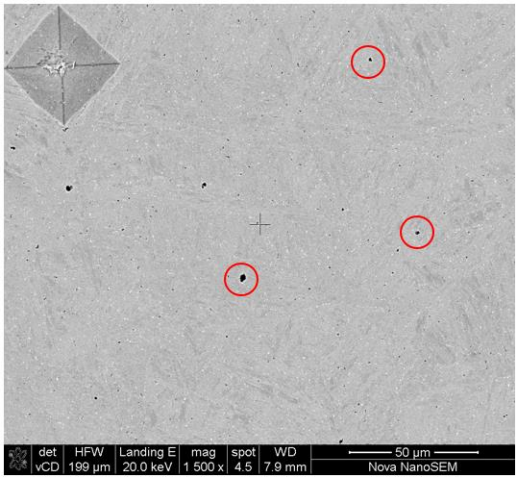

Figure 44: a) Circular specimen mounted for microscopic investigation and b) Scan area of X20_HD for void count

3.6.2.2 Creep-ruptured Samples

SEM was used to observe the fracture location and fracture surface of the creep-tested samples. The main contribution of SEM to the analysis of the creep-ruptured cross-sectioned samples was the comparison of microstructure between the base material and the regions close to the fracture surface. Cross-sectional analysis was used to investigate the behaviour of the samples as one proceeds from the crack surface to the unaffected base materials. Secondary electron and backscattered electron SEM was used on the fracture surface to characterise the type of fracture for the creep-ruptured samples.

3.6.3 Electron Backscatter Diffraction

Electron Backscatter Diffraction (EBSD) is a scanning electron microscope (SEM) based technique which is mainly for the characterization of phase distributions, grain and sub-grain structures and textures[59][60]. The first backscattered electron Kikuchi patterns were observed more than 50 years ago before the development of the SEM[4]. It provides crystallographic information about the microstructure of the material. In EBSD, a stationary electron beam interacts with a tilted crystalline sample and the diffracted electrons form a pattern that can be detected with a fluorescent screen[59]. The diffraction pattern is characteristic of the crystal structure and orientation in the sample region where it is generated. This allows the pattern to be used to determine the crystal orientation, discriminate between crystallographic different phases, characterise grain boundaries and provide information about the local crystalline perfection[59]. When the electron beam is scanned in a grid across a polycrystalline sample and the crystal orientation is measured at each point, the resulting map reveals the grain morphology, orientations and boundaries. Thus a complete and quantitative representation of the microstructure of a material can be obtained by EBSD. Sample preparation is critical in order to obtain good EBSD results. A deformation-free

surface is required to yield good EBSD patterns[59]. The diffraction pattern is generated from the surface layer of the sample; therefore the surface has to be electro polished or at least mechanically polished for hard materials for good EBSD results[60].

3.6.3.1 EBSD Setup

The analyses of all samples were carried out on unetched, scratch-free, clean surfaces. Two SEMs are used for the investigation (as mentioned in section 3.6.2). Once the sample was placed in the SEM, the stage was tilted to 70° and the sample area of interest was centered and focused. Figure 45 shows the basic set up for the sample analysis. An accelerating voltage of 20 kV and spot size of 5 was used for the base material, simulated FGHAZ material and creep-ruptured samples. The working distance was changed to a value where the EBSD software is calibrated to work. The HKL Technology Nordlys EBSD detector is setup to obtain the maximum amount of EBSPs and the Kikuchi bands are indexed properly for the body centered cubic (BCC)[4].

The setup of an EBSD system comprises of [59]:

- A crystalline sample tilted 70° from the horizontal by the use of the SEM stage or a pre-tilted holder.
- A phosphor screen which is fluoresced by the electrons scattered from the sample.
- A sensitive camera together with optics for viewing the patterned formed on the phosphor screen.
- An insertion mechanism, which accurately controls the position of the detector when it is in use, and retracts the detector to a safe position when it is not in use to prevent interference with SEM operation.
- Electronics to control the SEM, including the beam and stage movements.
- A computer to control the EBSD experiments, collects and analyse the diffraction patterns, and display the results.
- Optional forescatter diodes (FSD) mounted around the phosphor screen, which are used to generate microstructure images of the sample before collecting EBSD data.

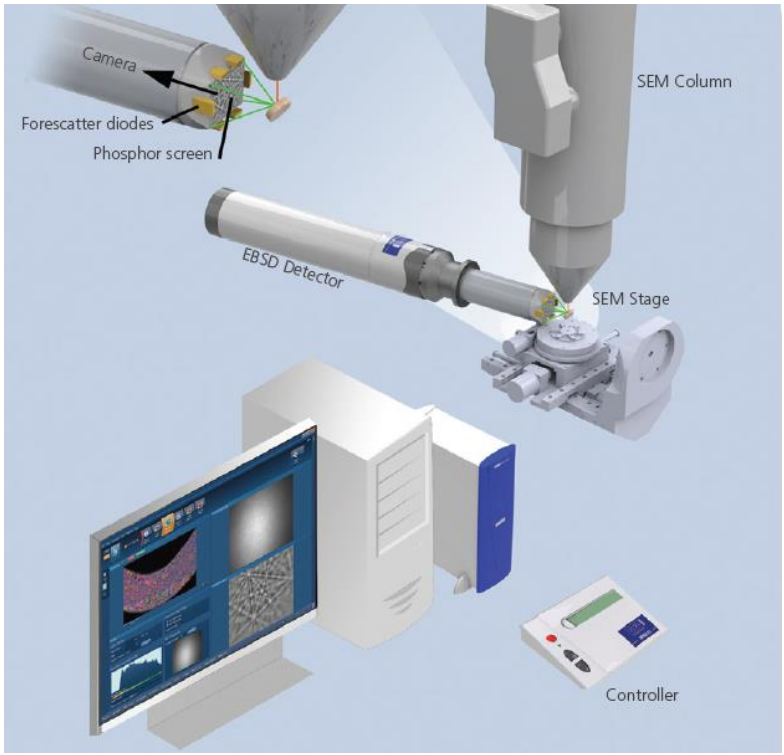

Figure 45: Principle components of an EBSD system[59]

Analysis of the EBSD data was carried out using software package, Channel 5. Channel 5 is the proprietary software package supplied with the HKL Technology Nordlys detector. The EBSD data is cleaned with 3 nearest neighbours in Channel 5. In this report, EBSD data is represented by Euler angles which show the orientation of the grains acquired by EBSD scanning. The data is extracted by Channel 5 and referred to as Euler maps. The misorientation angle distributions were acquired using Channel 5.

EBSD analysis was conducted on:

- Base material (X20_ND, X20_MD and X20_HD)
- Simulated FGHAZ (X20_ND, X20_MD and X20_HD)
- Creep-ruptured samples

3.6.3.2 Base Material

EBSD analysis was conducted in order to reveal the state of the microstructure of the base material in its as-received state. Important features, which were analysed in the base material, included the size of prior austenite grain boundaries (PAGB) and the martensitic structure differences between the different creep- aged materials. EBSD scans were done either at NMMU and UCT depending on the availability and operability of the microscopes at UCT. Step sizes of 0.2-0.6 µm were used. Each map required approximately 8 hours of scanning time to acquire sufficient data points for low and high angle grain sizes. The pattern solution

rate for all maps scanned on the base material have been greater than 93% indicating very good pattern acquisition and reliable EBSD data.

3.6.3.3 Creep-ruptured Samples

All creep-ruptured samples failed in the HAZ of the creep aged material. The HAZ length in most ruptured samples is approximately 3-5mm. Identification of a specific sub-zone is difficult to characterise using optical microscopy and SEM as these sub-zones are between 1-2mm in length. EBSD was used to determine the zone of fracture by relating the size of actual weldment grains for each sub-zone to those of the ruptured samples. After analysis of all the creep-ruptured samples using optical microscopy, a decision was taken to proceed with EBSD scans for samples of each test condition as optical microscopy provided insufficient evidence to conclude on the location of fracture. Optical microscopy is more available and significantly less expensive than EBSD data acquisition. The samples scanned with EBSD were done on both ends of the ruptured samples.

3.6.3.4 Simulated FGHAZ Material

The influence of the weld thermal cycle on the base material was characterised by means of EBSD. EBSD maps taken of the simulated material was used to determine the change in PAGB size after the base material had undergone a weld thermal cycle and post weld heat treatment (PWHT). EBSD maps were taken from the point of temperature measurement on the simulated samples. The samples were cross-sectioned at the point of temperature measurement when surface prepared. The scans were also done at UCT and NMMU. The data acquisition time for the simulated FGHAZ samples were approximately the same as that for the base material scans. Spot sizes of 0.2-0.6 µm were used. The pattern solution rates were also greater than 93% for these scans.

3.6.3.5 EBSD Data Analysis

The post-processing of the EBSD data was carried out using HKL Channel 5 software. All EBSD maps are cleaned with 3 nearest neighbouring pixels. The first step taken in post-processing is the noise reduction of the map. The application of noise reduction is completed by cleaning the map with iteration of the 3 nearest neighbouring pixels.

3.6.3.6 Automated Prior Austenite Grain Re-construction in HKL Channel 5

A grain is a three-dimensional crystalline volume within a sample that differs in crystallographic orientation from its surroundings but internally has little variation. In order to determine the grains within a sample, a critical misorientation angle must be defined. The critical misorientation angle is defined as the angle where all boundary segments with an angle higher than the defined critical angles are to be considered as grain boundaries. It is also possible to identify the boundaries enclosing the individual grains by measuring the misorientation between all pixel pairs. By combining the information gathered from grain

boundaries and phase transformation, it becomes possible to determine the grain size distributions from different phases within the sample[59].

Typically, grain boundaries with a misorientation angle between 2-15° are considered sub-grain or low-angle grain boundaries. Boundaries with misorientations >15° are considered random high angle grain boundaries[61]. Martensitic lath boundaries have a specific misorientation angle, which cannot be changed. These include low angle (2-15°) and high angle (45-60°) grain boundaries. PAGB, however, have random misorientation angles between 10 and 60°. Due to this overlap, shown by the red rectangles in Figure 46, for low angle and high angle misorientation between lath boundaries and PAGBs, the software cannot distinguish between the differences. Hence, grains are not completely re-constructed using automatic grain re-construction as shown in Figure 47. Grains have to be outlined manually after automatic re-construction before the mean line intercept method can be applied.

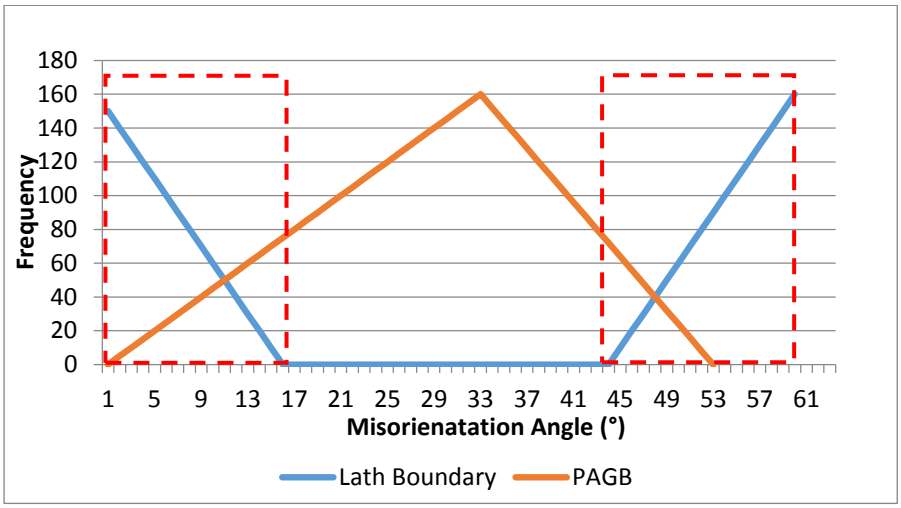

Figure 46: Graphical representation of lath boundary and prior austenite grain boundary misorientation angles

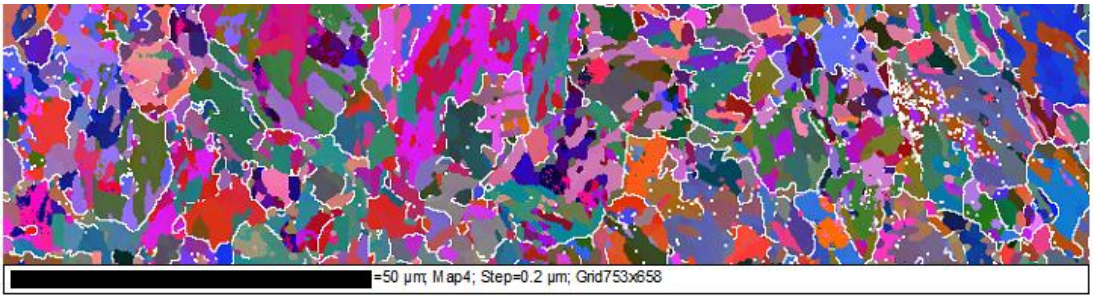

Figure 47: Application of orientation angle prior austenite grain boundaries

4. Results and Discussion

4.1Base Material Characterisation

4.1.1 High Temperature Tensile Strength

Five samples of each base material were tensile tested at 610°C with a strain rate of $10^{-3}s^{-1}$. The yield strength and ultimate tensile strength (UTS) results for each test are provided in Table 18. The similarity in yield strength and UTS can be seen for individual tests for X20_ND and X20_MD. The decrease of yield strength and UTS is noticeable between X20_ND/X20_MD and X20_HD. The creep damage induced in X20_HD has an impact on the hot tensile properties of the material. The higher the amount of creep damage in the material, the lower is its tensile properties.

Table 18: High temperature tensile strength for base materials

	Test number	**Yield strength (MPa)**	**Ultimate tensile strength (MPa)**	**Elongation (%)**
X20_ND	1	297	376	4.28
	2	319	377	4.11
	3	323	375	3.77
	4	274	376	3.55
	5	324	399	4.03
Average		**307**	**381**	**3.95**
X20_MD	1	309	385	4.18
	2	309	375	4.32
	3	292	381	4.08
	4	290	365	4.98
	5	336	385	3.94
Average		**307**	**378**	**4.30**
X20_HD	1	228	328	4.95
	2	251	323	5.50
	3	266	330	4.78
	4	245	308	5.35
	5	227	291	3.17
Average		**243**	**316**	**4.75**

4.1.2 Microhardness Testing

Microhardness testing was performed on all as-received base materials. A Vickers microhardness testing machine was used with a testing load of 0.3kgf. The microhardness testing was conducted on the cross-sectional area of the rods created for Gleeble testing. Table 19 gives a summary of the Vickers hardness for all three as received classes of material. It is evident from the microhardness testing of the as-received base materials, X20_ND, X20_MD and X20_HD that the hardness values decrease with the amount of creep damage of the material. It must be noted though that hardness is measured at room temperature whereas the tensile tests were performed at 610°C. Nevertheless, the trends are similar although it could be argued that there is a slightly greater difference in the hardness of X20_ND and X20_MD compared to their tensile properties.

Table 19: Vicker's Hardness measurements for as received base material

Matrix Position	**Vicker's Hardness (HV0.3)**		
	X20_ND	**X20_MD**	**X20_HD**
1	262	246	213
2	269	250	208
3	260	245	204
4	254	237	209
5	257	238	210
6	258	241	215
7	261	234	208
8	260	239	211
9	268	243	211
Average	**256**	**241**	**210**
Standard Deviation	**4.95**	**4.86**	**3.21**

4.1.3 Microstructural Analysis of Base Materials

All base materials exhibit a tempered martensite microstructure as a result of the normalised and tempering heat treatment carried out prior to the materials being placed in service. These microstructures are shown in Figure 48 where the prior austenite grain boundaries (PAGBs) can also be identified as superimposed on the lath martensite grain structure. Large sections of the base materials are considered in the observations of the microstructure.

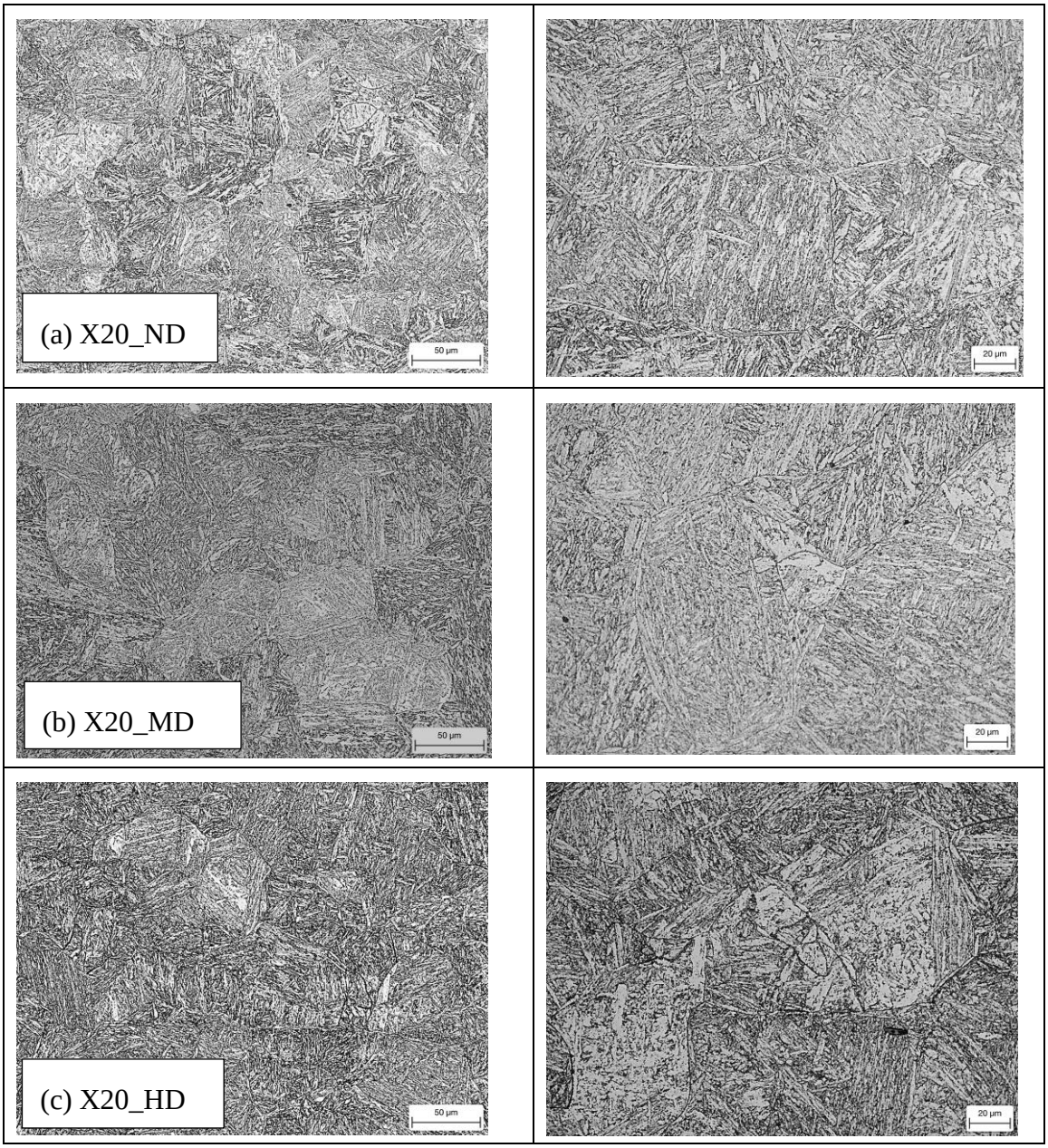

Figure 48: Optical micrographs of the as-received base materials microstructure showing the prior austenite grain size (left) and tempered martensitic lath structure (right)

Scanning electron microscopy further supports the tempered martensitic microstructure at higher magnifications as shown in Figure 49. The topographical orientation of the surface of the base materials show the needle-like lath microstructure in all base materials examined. Instances in X20_HD which make the boundaries appear thicker could be as a result of precipitate coarsening.

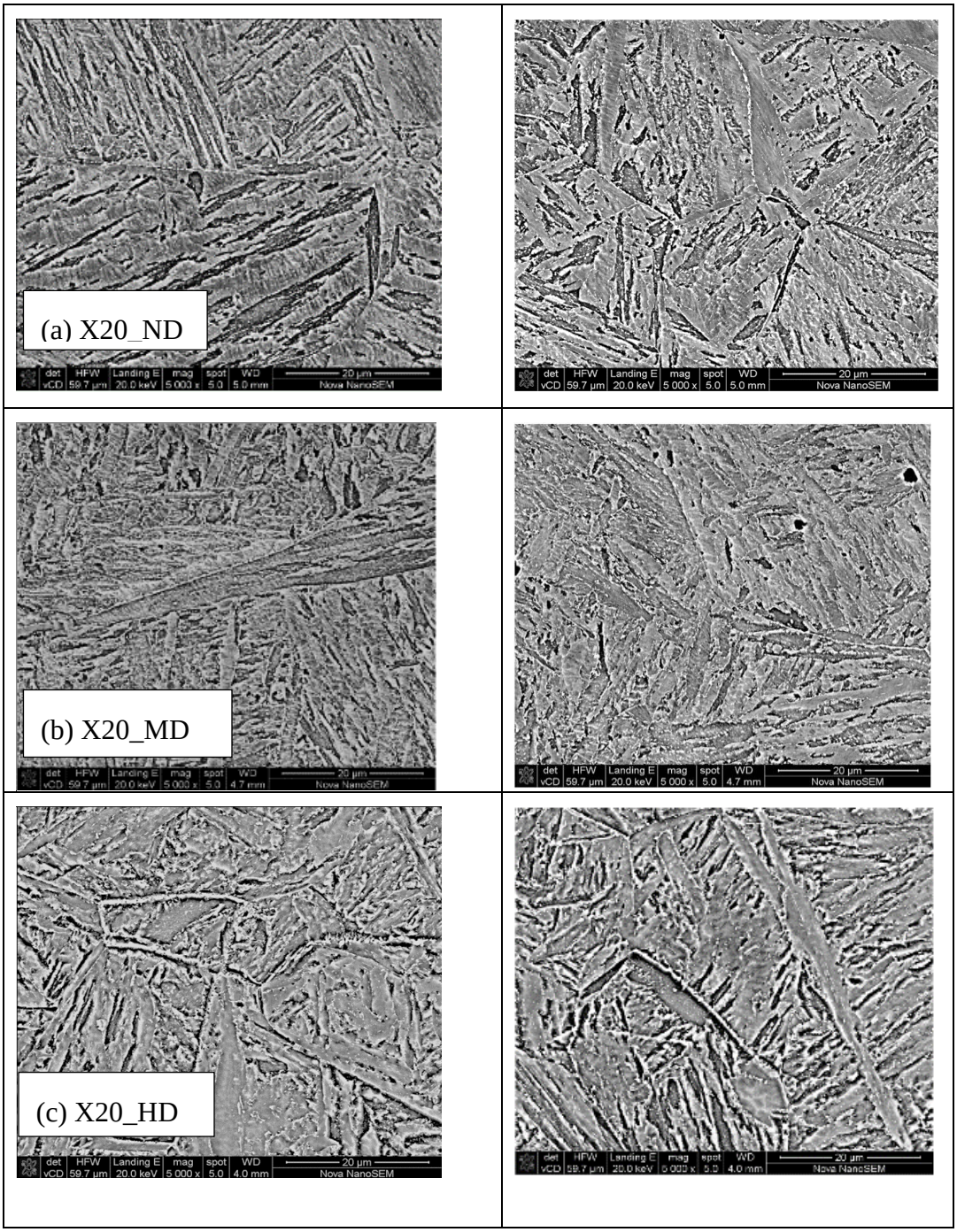

Figure 49: Backscatter electron SEM images of (a) X20_ND, (b) X20_MD and (c) X20_HD showing the martensitic lath microstructure

Figure 50 shows the All Euler colour maps obtained from EBSD scans on the base material showing the typical martensitic laths and lath packages for X20_ND, X20_MD and X20_HD. PAGBs are outlined in white and detected using a detection tool in HKL Channel 5. The PAGBs with misorientation angles between 15° and 45° were detected. The tempered martensitic microstructure can be seen as the needle-like laths. Figure 50 shows the microstructure for the base materials with partially detected PAGBs. It is generally accepted

that the low angle grain boundaries (LAGB), which represent sub-grain boundaries are found between misorientations of 2 and 15 degrees as the minimum detection limit is 2°. High angle grain boundaries (HAGB), which have misorientations greater than 15 degrees, are known to represent grain boundaries and PAGBs. The martensite lath grain boundaries have been excluded from the analysis.

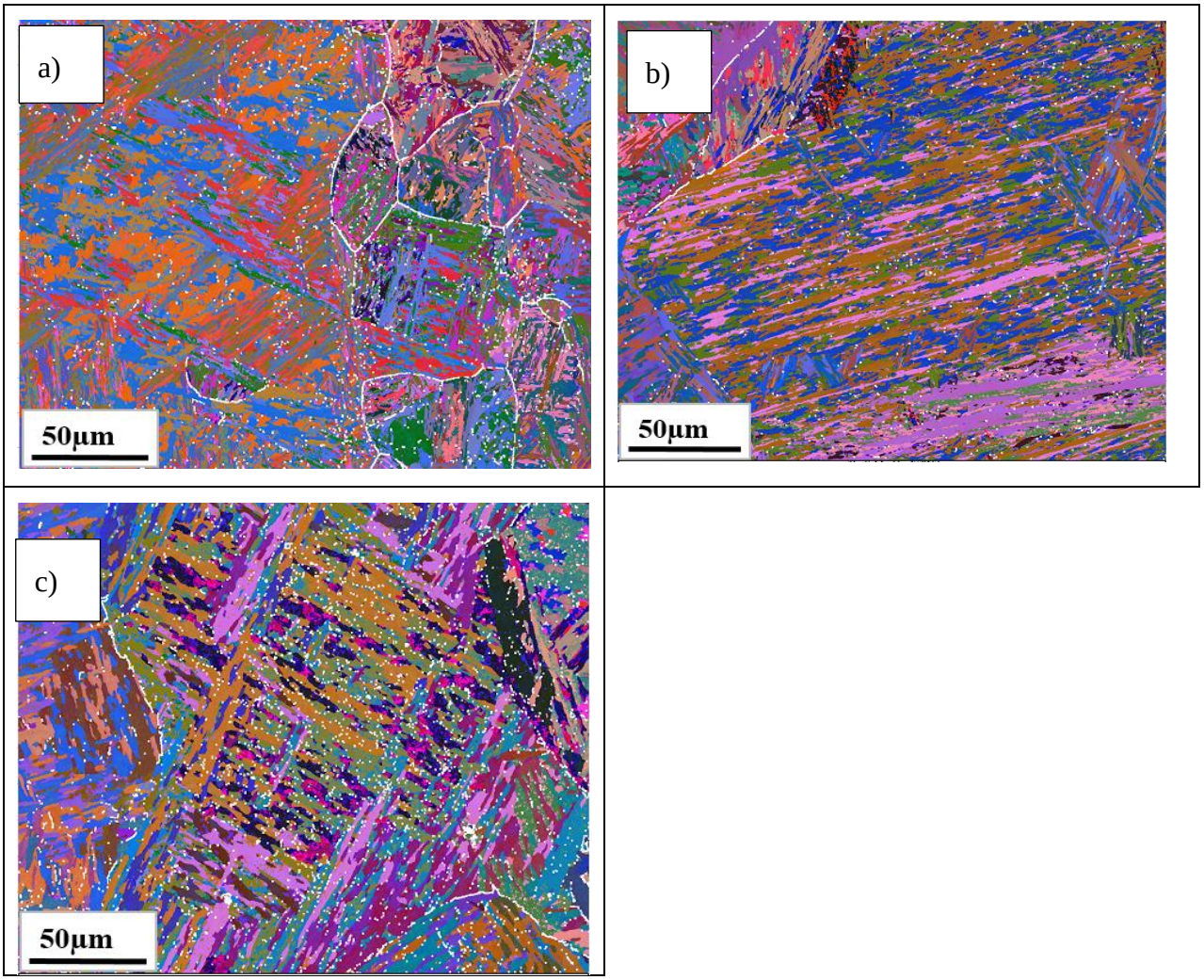

Figure 50: EBSD All Euler colour image of a) X20_ND, b) X20_MD and c) X20_HD

4.1.4 Damage Analysis of Base Materials

Figure 51 shows a compilation of backscattered electron SEM micrographs for the area used in damage analysis of the base materials. Analyses of the micrographs were done using ImageJ which is an open source image processing program designed for scientific images[62]. The process for this analysis involved adjusting the scale of the stitched image to correspond to the scale function in ImageJ. Measuring the scale bar of the stitched image does this and represents this measured length as a function of the measurement in the program. Once the measurement function has been assigned to the image, the image is

threshold to identify specified objects on the image. For this analysis, the program was set up to detect shape threshold occurrences on the map. Boundary conditions can be imposed to detect predefined sizes of voids (circular objects with diameters less than 10µm). The black outlined objects on Figure 51 are examples of voids detected on the image. Figure 52 show the stitched images for a) X20_ND and b) X20_MD.

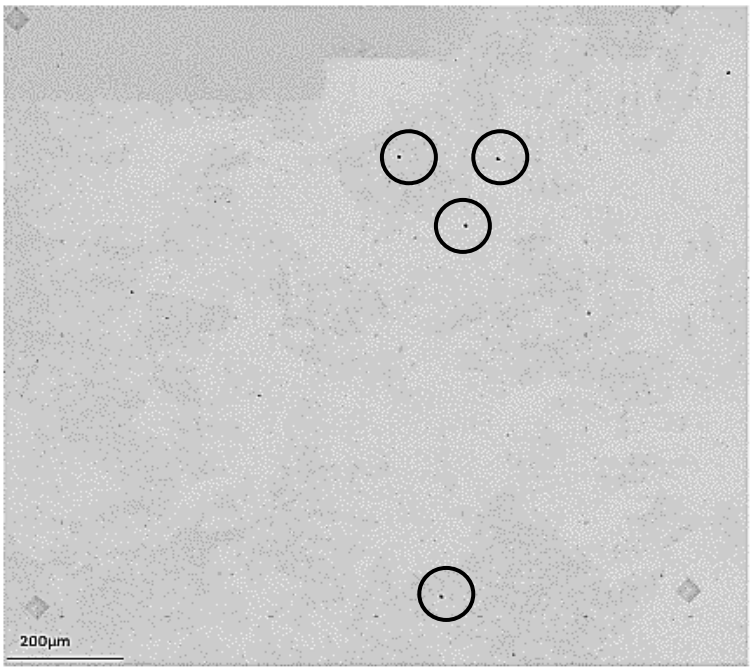

Figure 51: Stitched image of Backscatter SEM micrographs for X20_HD

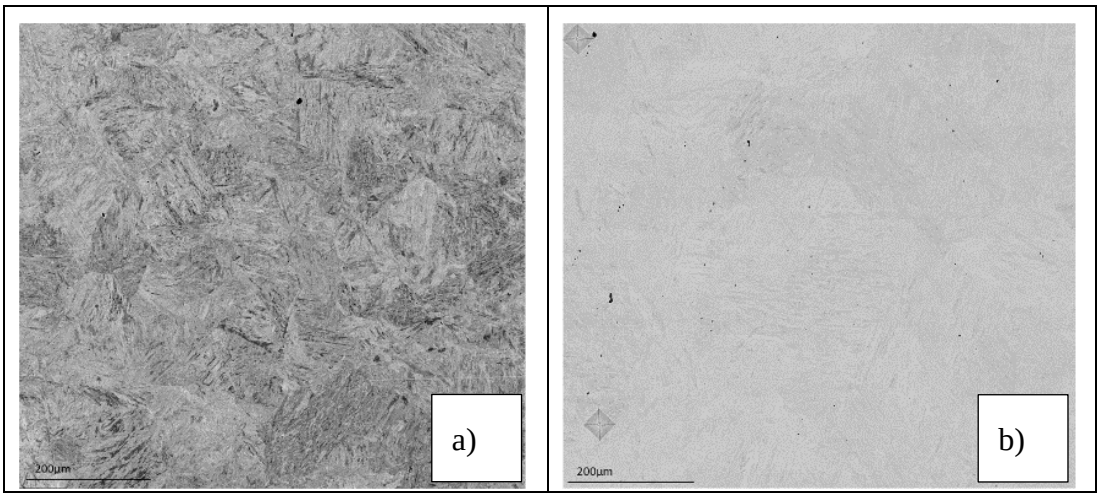

Figure 52: Stitched image of Backscattered SEM micrographs for a) X20_ND and b) X20_MD

After the boundary conditions have been implemented into the programme, the image is threshold to detect the voids (circular objects with diameters less than 10mm). Figure 53

shows the threshold image. The analysis for the void detection included the area of each void, the standard deviation and the minimum and maximum areas.

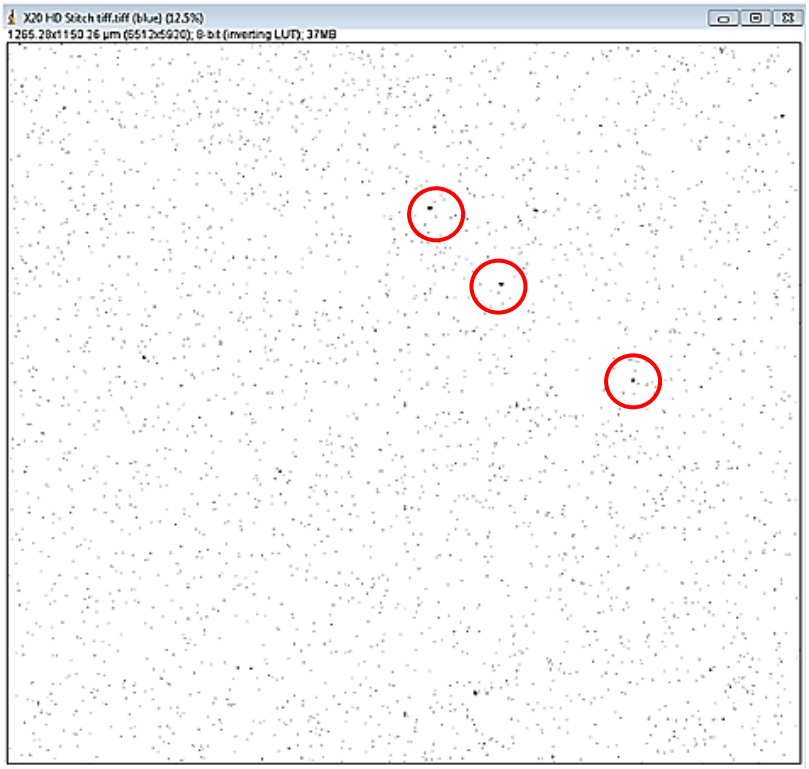

Figure 53: Threshold image of X20_HD stitched image

The equivalent circle diameter (d) of each void was determined from the area (A) of the void obtained from the particle analysis. The assumption used for this analysis is that all voids are circular in shape. Hence from Equation 8, d can be determined as shown by:

$$d = \sqrt[2]{\frac{4 * A}{\pi}}$$

Equation 8

A summary of the void distribution can be seen in Figure 54. The graph shows the number of voids/mm^2 per each diameter size.

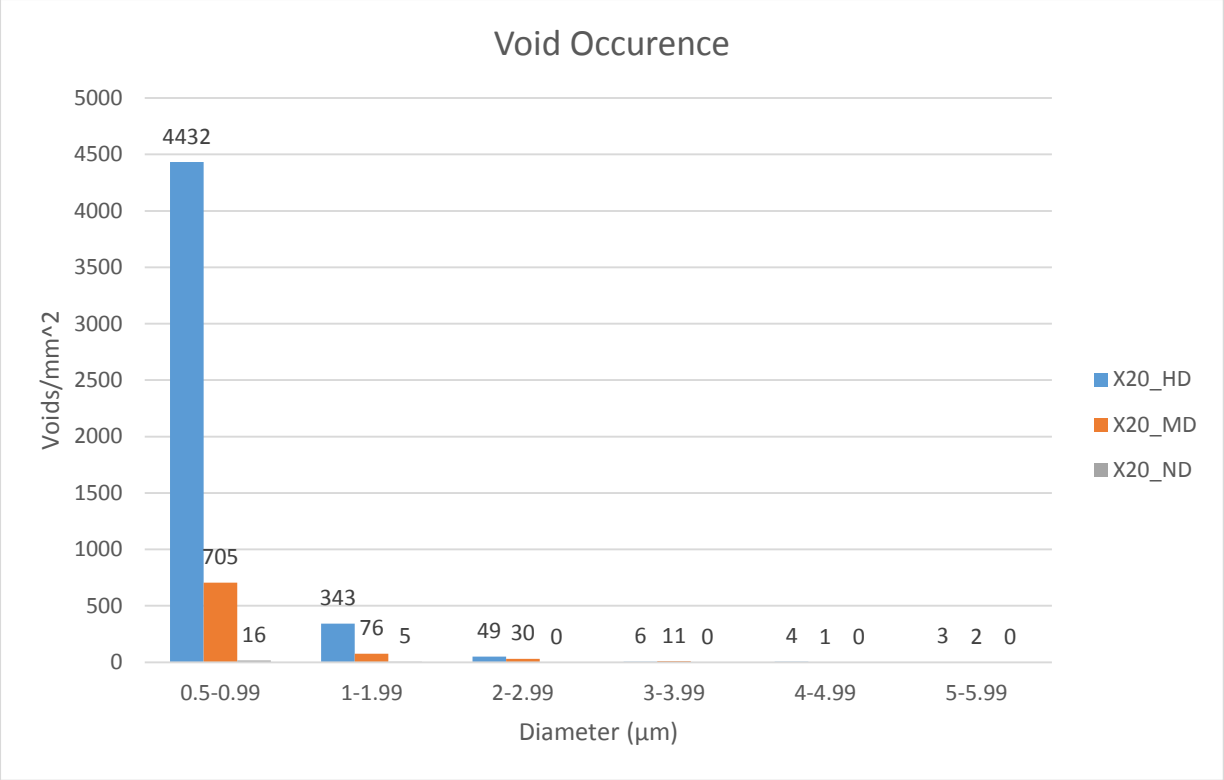

Figure 54: Graph of the occurrences of voids in relation to their diameter for X20_ND, X20_MD and X20_HD

4.1.5 Discussion

Optical microscope imaging showed the tempered martensitic microstructures of the base material. Needle-like lath boundaries contained in prior austenite grains occurred in X20_ND, X20_MD and X20_HD. Appendix 1 shows further details of this microstructure for all three as-received base materials. SEM analysis conducted on the as-received base materials showed further clarification of the martensitic microstructure. EBSD of the as-received base materials confirmed that X20_HD had indeed undergone the most microstructural degradation compared to X20_MD. This is evident by the bigger sub-grain sizes in X20_HD. This could possibly be due to the enhanced dislocation movement caused by the high operating temperatures.

Microhardness and hot tensile mechanical testing show the degradation in mechanical properties by the decrease in hardness and hot tensile strength in accordance to creep damage. X20_HD had a hardness reduction of 18% in comparison to X20_ND which has no creep damage. The hardness of X20_MD is reduced by 6%. The decrease in ultimate tensile strength for X20_MD and X20_HD are 1 and 17% respectively relative to the no damage X20_ND. The occurrence of creep voids being greater in X20_HD impacts the mechanical properties of the material as well. The relation of creep voids to the mechanical properties of

the base materials is evident by the occurrence of voids and the decreased mechanical properties. Evidently, X20_HD was found to have the most creep voids/mm^2 together with the greatest reduction in mechanical properties. Figure 10 shows data supplied by EPRI[23] for the tensile properties of X20. There is an obvious dependence of tensile strength on the testing temperature. With this regard, the results obtained for the base material hot tensile tests conducted at 610°C are well below the range indicated in Figure 10.

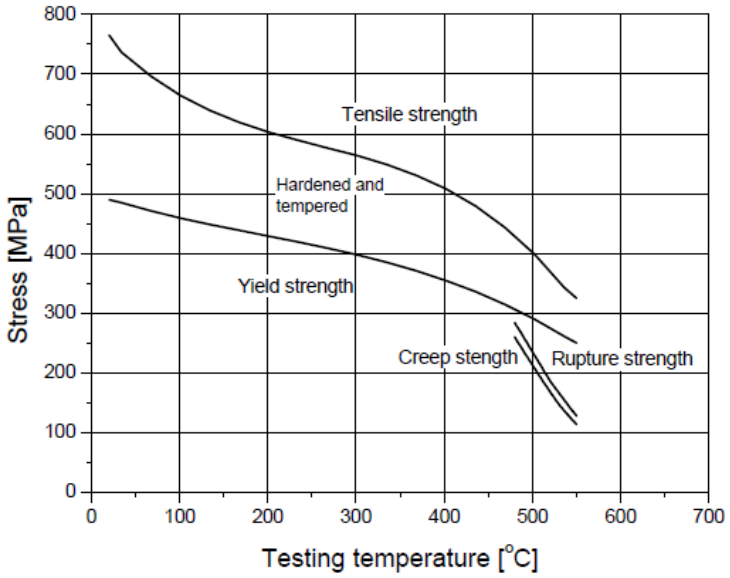

Figure 55: Tensile and creep properties of X20CrMoV12-1 as a function of temperature[23]

The quantification of voids for the three as-received base materials concluded that the occurrence and size of voids increases with exposure to creep conditions. More specifically, X20_HD was operated at higher temperatures (555°C) for a shorter duration (130 000 hours) than X20_MD (540°C for 208 000 hours) and resulted in having a higher occurrence of creep voids than X20_MD. From this evidence, increased operational temperature has a greater influence on creep degradation than operational time. The higher operating temperatures which X20_HD was subjected to accelerated void formation.

Creep defects cause the majority of failures in power plants components operating under stress and thermal load, and the surface replica method is suitable for these defects. Therefore, the replica tool has become an especially important tool in the determination of remaining life in such components as boiler tubes, steam piping and turbine effects. Creep defects begin as small cavities at grain boundaries and second phases. When subjected to stress and temperature over time, these cavities can link up and form cracks that eventually lead to failure of the component[63].

Eskom uses surface replication to determine the creep void occurrence in creep aged components. An objective of this project was to compare the results obtained from the surface replication method to a more advance microscopic method to determine the

occurrence of creep voids. Surface replicas were examined under optical microscope. The detection of voids at 500x magnification proved difficult due to the low resolution of the optical microscope. Hence, the examining and reporting of the void density measurements were subjective to the optical microscope operator. Figure 56 shows a surface replica micrograph (left) and a SEM image (right) of the same sample but in the case of the SEM image, the actual sample is examined rather than the replicated surface only. SEM allows for much high magnifications and better resolutions. However, the process requires sufficient sample preparation and is less cost effective than optical microscopy.

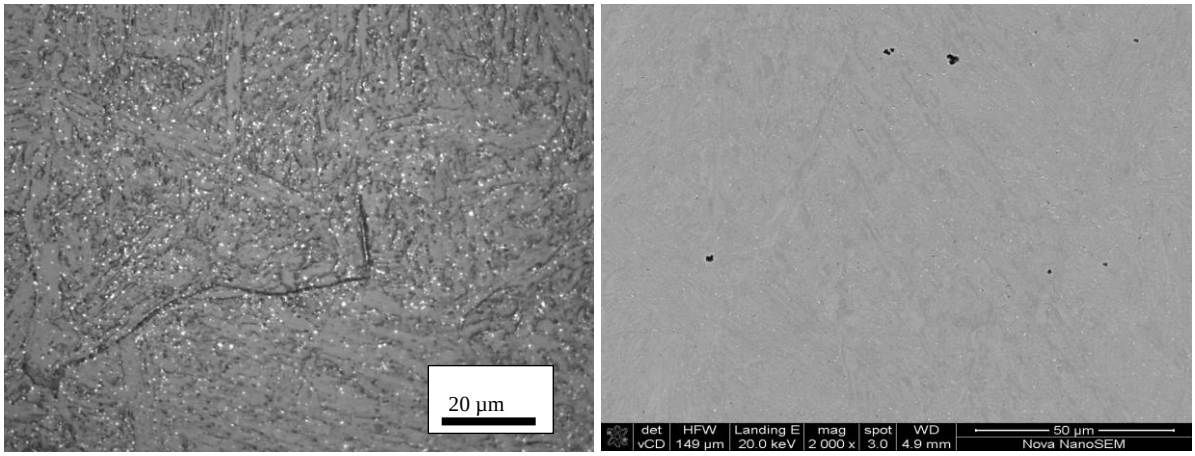

Figure 56: Surface replica micrograph (left) and SEM image (right) of X20_HD

ERIC (Eskom Research and Innovation Centre) provided the author with surface replication data for the base materials X20_ND, X20_MD and X20_HD at the commencement of this research study in a challenge to verify whether or not advanced microscopic techniques such as SEM could provide similar/different results for void density measurements. Table 20 provides the comparison of creep voids for the base materials using surface replication and SEM. The reported void density provided by ERIC measured voids greater than 1µm in diameter. Therefore, for comparison reasons, all voids smaller than 1µm detected by SEM were neglected. X20_ND was reported to contain no voids. However SEM analysis identified 5 voids/mm^2 present in the sample examined. This is possibly due to defects and inclusions, which arise in the manufacturing and heat treatment process. Studies conducted by van Zyl *et al* [64] also concluded that fabrication methods and heat treatments lead to a large degree of void scatter in new material. Inclusions, and clusters of inclusions is also dependent on the wall thickness and system loads [64].
Figure 57 shows virgin X20 main steam pipe with inclusions found in studies done by van Zyl *et al*[64]. These findings provide reasoning for the inclusions found on X20_ND (Figure 107 found in Appendix 1).

a)

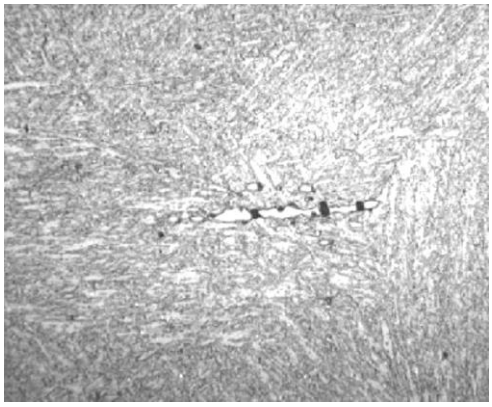

b)

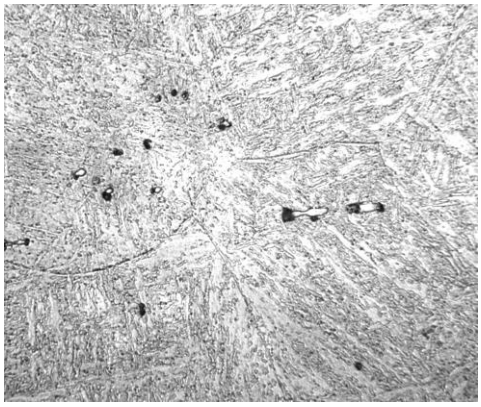

Figure 57: Strings of inclusions in main steam pipe[64]

The reported void density measurement for X20_MD, as per the replication approach, lies in a range of 130- 200 voids/mm^2. The void density determined by SEM is below that range (120 voids/mm^2). The reported void density measurement for X20_HD lies in the range of 340 - 485 voids/mm^2 and the void density confirmed by SEM falls within that range (405 voids/mm^2).

Table 20: Comparison of void density measurements between surface replica and SEM

Sample Identification	**Surface Replica Creep damage (voids/mm^2)**	**SEM creep damage (voids/mm^2)**
X20_ND	No damage	5
X20_MD	130-200	120
X20_HD	340-485	405

The reported values for the void density measurements obtained from surface replication are not greatly different to the void density measurements obtained from SEM. Although not a highly sophisticated method, surface replication provides reasonable data for the assessment of creep void density measurements and as a NDT approach. Also, surface replication is a cost effective and time efficient method for non-destructive testing *in situ*. The need to assess the condition of power plant components on a large scale is ideal for the application of surface replication as investigations conducted in this study show that the results obtained from surface replication are comparable to results obtained from more advanced methods (SEM) of determining creep void density measurements.

4.2Cross Weld Samples after Creep Testing

4.2.1 Creep Tests Results

Creep tests for cross-weld samples extracted from weldment 1 (X20_ND to X20_MD) and 2 (X20_ND to X20_HD) at stresses of 63, 80 and 90 MPa were carried out at 610˚C. Table 21 provides the test numbers and the stresses at which the tests were conducted, together with the rupture times for the tests. Each stress condition was tested twice in order to provide some degree of repeatability.

Table 21: Creep rupture test results

	Test number	**Stress (MPa)**	**$t_{rupture}$ (hours)**
Weldment 1	Test 1 A	63	2226
	Test 1 B		903
	Test 2 A	80	340
	Test 2 B		1092
	Test 3 A	90	86
	Test 3 B		104
Weldment 2	Test 4 A	63	581
	Test 4 B		791
	Test 5 A	80	274
	Test 5 B		102

Figure 58 and Figure 59 show graphical representation of the rupture times for the creep tests on weldment 1 and 2 respectively. At lower stresses of 63 and 80 MPa, both weldments show a significant difference in rupture times for the repeated test. The rupture time for test 1 A is in excess of 40% longer than test 1 B. Similarly, the rupture time for test 2 A is significantly shorter than the repeated test 2 B. Test 3 A and B carried out at 90 MPa for weldment 1 show a much smaller difference in ruptures times; however, the rupture times for creep tests carried out at 90 MPa are very short and are possible representative of a hot tensile test.

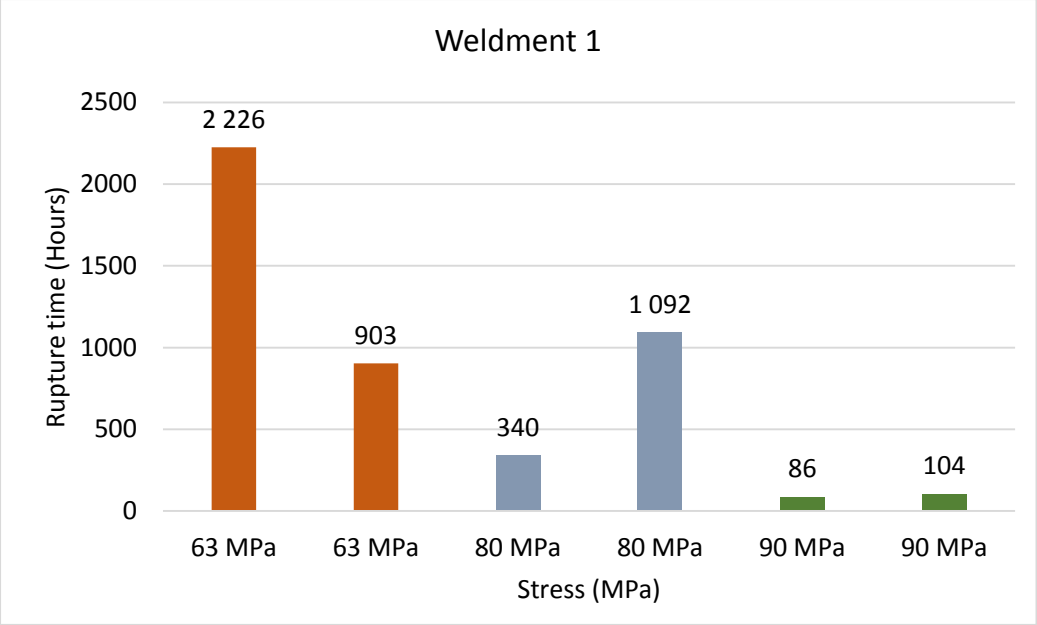

Figure 58: Rupture times for creep tests on weldment 1 (X20_ND to X20_MD)

After the rupture times for test 3 A and B were observed to be very short, creep tests on weldment 2 at 90 MPa were not considered as these could yield results too short to be considered as creep tests. Test 4 A and B of weldment 2 have a smaller difference in rupture times as compared to test 1 A and B of weldment 2; however, the overall rupture times for test 4 are lower than test 1. Test 5 A and B produced rupture times of 274 and 102 hours respectively.

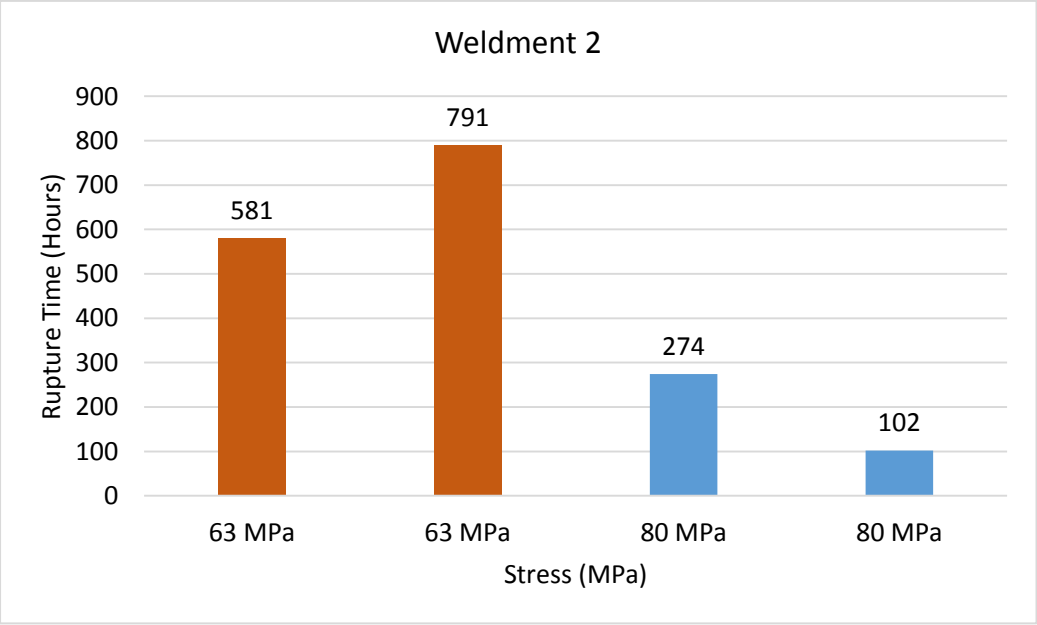

Figure 59: Rupture times for creep tests on weldment 2 (X20_ND to X20_HD)

Due to the rupture times for the creep tests being short (less than 10 000 hours), one could argue whether the creep cavitation seen in the FGHAZ is as a result of actual creep deformation or plastic deformation due to the high stress induced accelerated strain rate which perhaps promotes plastic (dislocation intense) deformation as opposed to void formation due to creep. By analysing the creep strain and strain rates, it became more evident that these curves display characteristics of typical creep strain and strain rate curves. Figure 60 shows the creep strain curves for weldment 1 and 2 at 610°C/63 MPa. The three stages of creep can be seen more obviously for Test 1 A. The primary creep stage ended at a strain of <0.1%. The secondary creep stage seemed to continue for the most of the duration of the test until a rapid increase in strain brought about the tertiary stage and eventually failure.

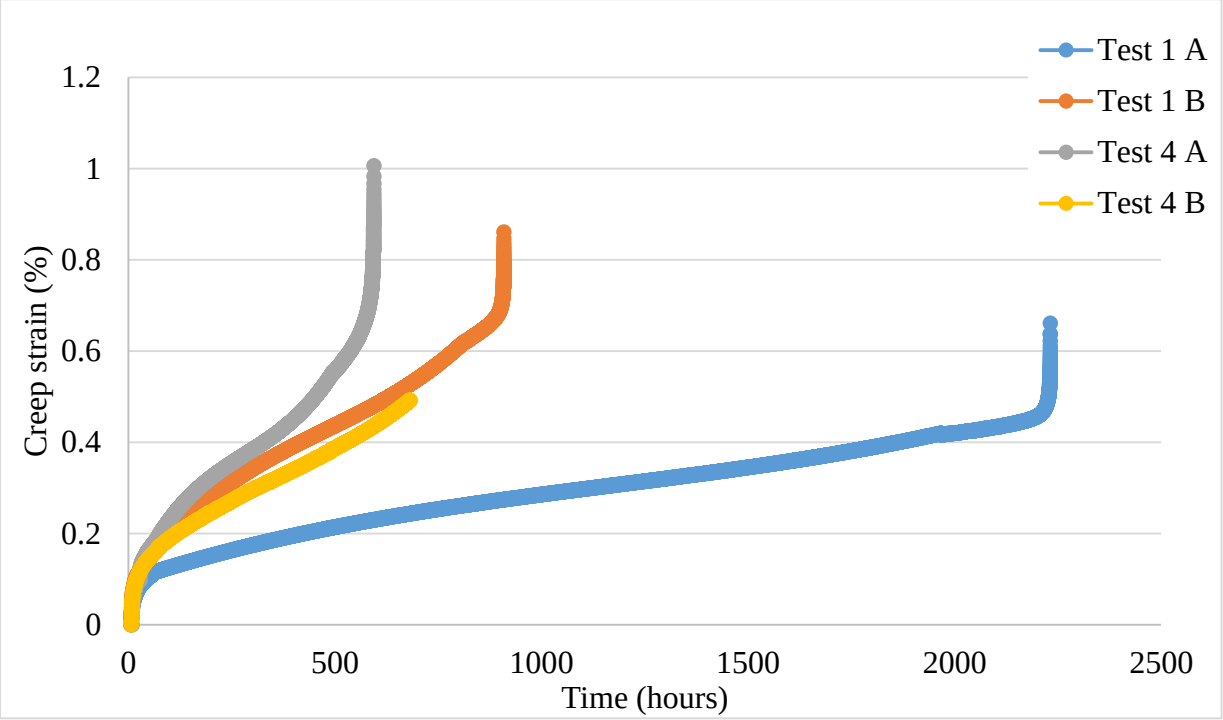

Figure 60: Creep strain curve versus testing time for weldment 1 and 2 at 610°C and 63 MPa

The longer durations for weldment 1 could be linked to the lower creep damage and consequently, better mechanical properties. Creep strain curves for weldment 1 and 2 at 610°C/80 MPa can be seen in Appendix 5. Once again, the performance of weldment 1 exceeds that of weldment 2 based on duration of the tests before rupture. Test 2 A and B ran longer than Test 5 A. The longer running times for weldment 1 were an indication of greater ductility of X20_MD as compared to X20_HD. In support of this, the higher Vicker's hardness and hot tensile properties of X20_MD (section 4.1.1 and 4.1.2) justify the greater creep strength of X20_MD relative to that of X20_HD.

The creep rate curves for weldment 1 and 2 at 610°C/63MPa are shown in Figure 61. The creep rate remains at a constant in the secondary stage. This is attributed to a state of balance between the rate of generation of dislocations contributing to hardening and the rate of recovery contributing to softening. At high homologous temperatures, creep mainly involves diffusion and hence the recovery rate is high enough to balance the strain hardening and results in the appearance of the secondary stage. In the tertiary creep stage, the creep rate increases with time until rupture. It should be remembered that under constant tensile load, the stress continuously increases as creep proceeds or as cross-section decreases and a pronounced effect of increase in stress on the creep rate appears in the tertiary creep stage.

Necking of the specimens before rupture causes a significant increase in stress. The increase in creep rate with time in the tertiary creep stage can follow increasing stress or microstructure evolution including damage evolution taking place during creep. Microstructure evolution usually consists of dynamic recovery, dynamic recrystallization, coarsening of precipitates and other phenomena, which cause softening and result in a decrease in resistance to creep. The onset of the tertiary creep stage can also be identified by the minimal necking of the test samples which can be seen in Figure 62.

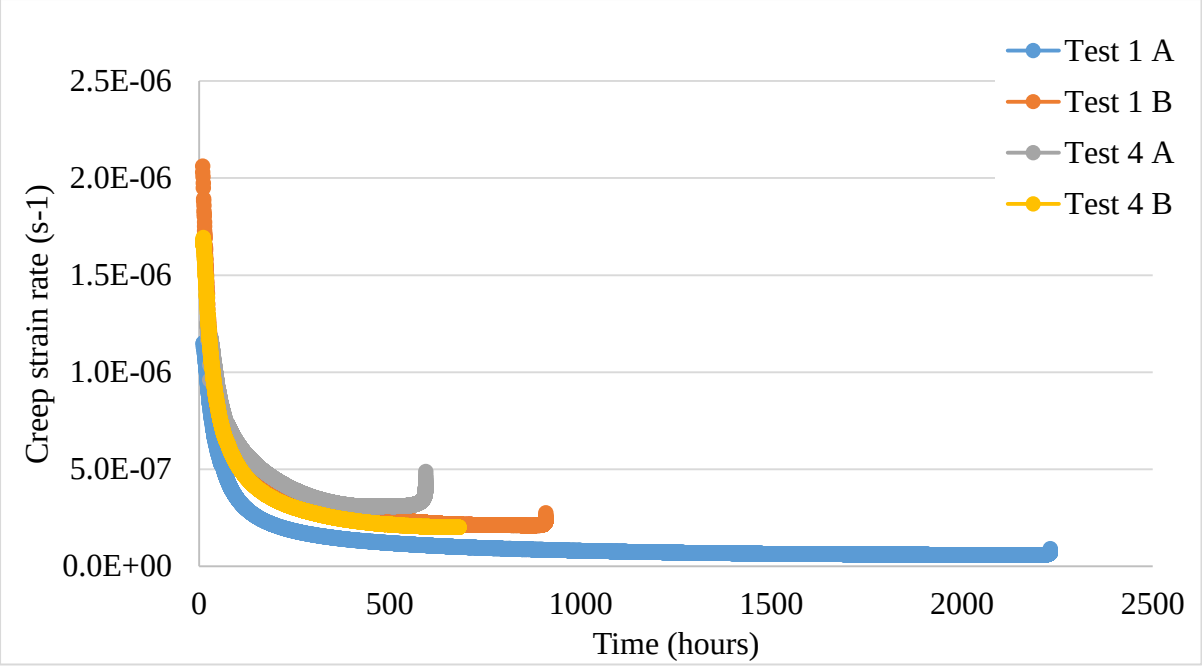

Figure 61: Creep strain rate versus testing time for weldment 1 and 2 at 610°C and 63 MPa

4.2.2 Fracture Mechanism of Creep Tests

In order to determine the location for the fracture in all creep tested samples, these samples were examined at under an optical microscope. The creep-ruptured samples were cut along the white dotted line and investigated on either side of the rupture. Figure 62 shows a creep-ruptured sample with the fracture area highlighted by the red ring. The long side of the ruptured sample for all tests contains the weld and X20_ND and will be indicated by GL. The short side of the ruptured samples contain the creep aged X20_MD/X20_HD (GS).

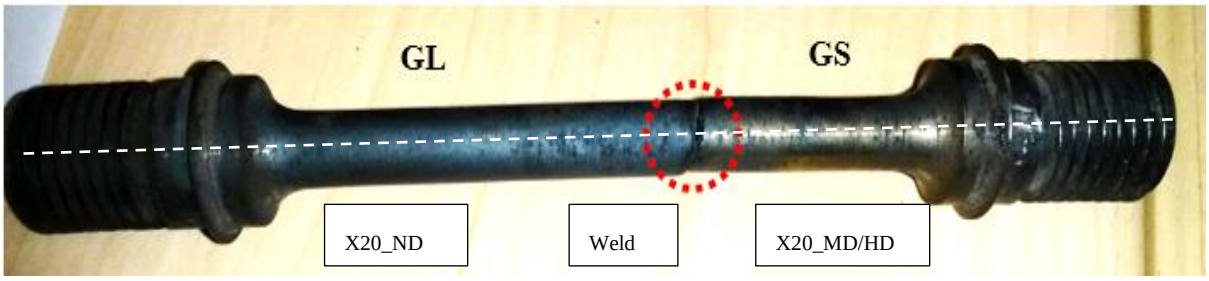

Figure 62: Creep ruptured sample showing fracture point

The fracture surfaces of all creep tested samples were examined using secondary electron SEM to identify the type of fracture which occurred on the samples. Due to fracture of the samples at high temperature, the fracture surface oxidised. The samples were placed in an acetone solution and an ultrasonic cleaner for 30 minutes. The debris on the fracture surface has been removed to a certain extent; however, the surface still possesses an extra layer of debris. Figure 63 shows the fracture surface of test 1 A GL with a magnification of 2000x on the left and 5000x on the right. SEM images, taken at 2000x magnification, show attributes of a ductile fracture which is characteristic of a dimple-like structure. SEM images show particles at the bottom of the dimples as indicted by the black outlines in Figure 63. The white outlines indicate micro voids at the bottom of the dimples. Images for the rest of the test samples can be found in Appendix 2.

The figures in Appendix 2 also show dimple-like appearances on the fracture surfaces. Exanimation of the fracture surface of both ends of the fracture provides evidence of the zone of fracture for the creep tested samples. Figure 122, Figure 123 and Figure 124 show the oxide layer that has formed on the fracture surface.

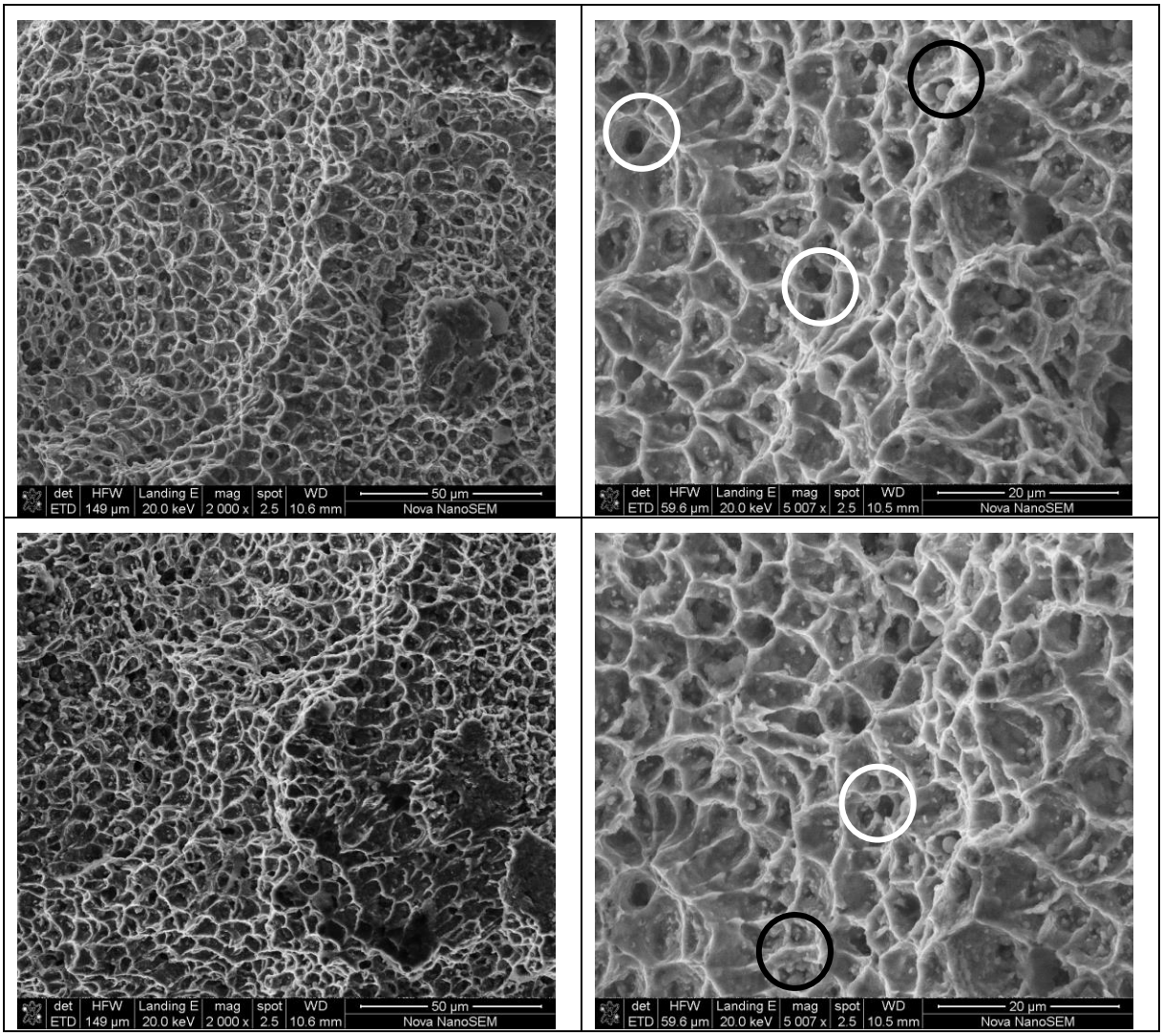

Figure 63: Fracture surfaces of test 1 A GL at magnifications of 2000x (left) and 5000x (right)

4.2.3 Microstructural Profile of Fractured Samples

4.2.3.1 General Microstructure

According to Figure 64, the FG/ICHAZ lies on the outer side of the HAZ closer to base material. With reference to the location of the FGHAZ in Figure 64, the location of fracture can be identified by the analysis of optical micrographs in Figure 65. Figure 65 a), b), c) and d) show areas at the rupture surface for samples of test 1 A. Bands of a finer microstructure can be observed next to the weld metal in a) and base material in b)

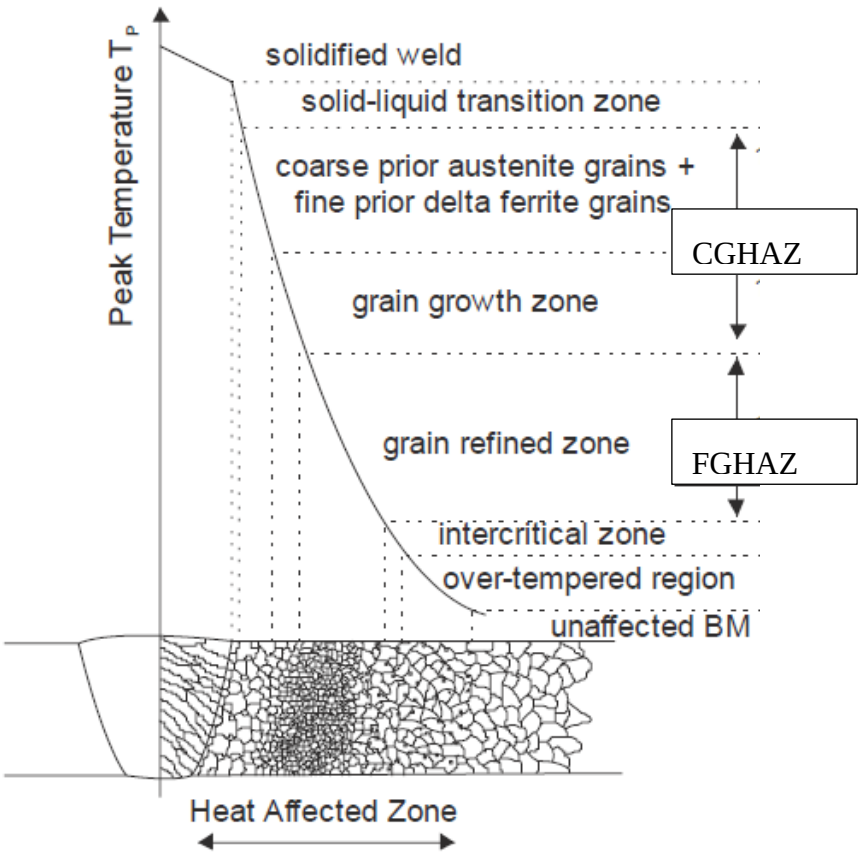

Figure 64: Illustration of the heat affected zone showing the location of the sub-zones which make up the heat affected zone[34]

Figure 65 a), b), c) and d) show distinctions in microstructure between the weld metal and base material respectively. The HAZ is located between the red dashed line and the fracture surface. Figure 65 e) and f) show the fine grain microstructure close to the rupture surface in more detail. The region had an abundance of voids and few micro-cracks.

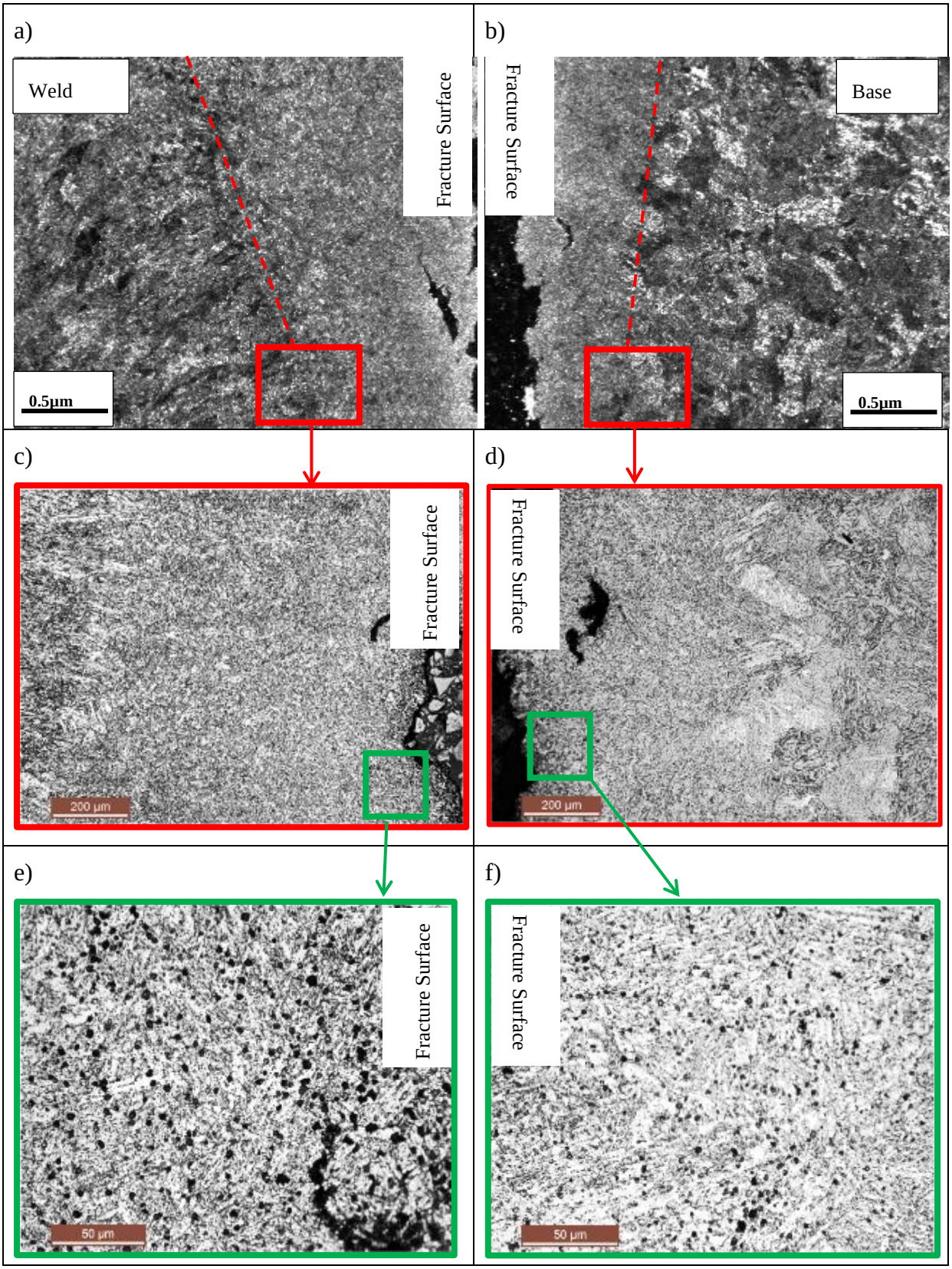

Figure 65: Optical micrographs for test 1 A GL (left) and GS (right)

All weldments exhibited the similar location for fracture. Optical micrographs for test 1 B, 2 A, 2 B, 3 A, 4 A, 4 B and 5 A can be found in Figure 66, Figure 67, Figure 68, Figure 69 and Figure 70. The images convincingly show in all cases that fracture occurred in the HAZ corresponding to the parent material that has been exposed to prior creep damage (X20_Md and X20_HD). The sample for test 3 B had to be discarded due to errors in the machining after creep testing.

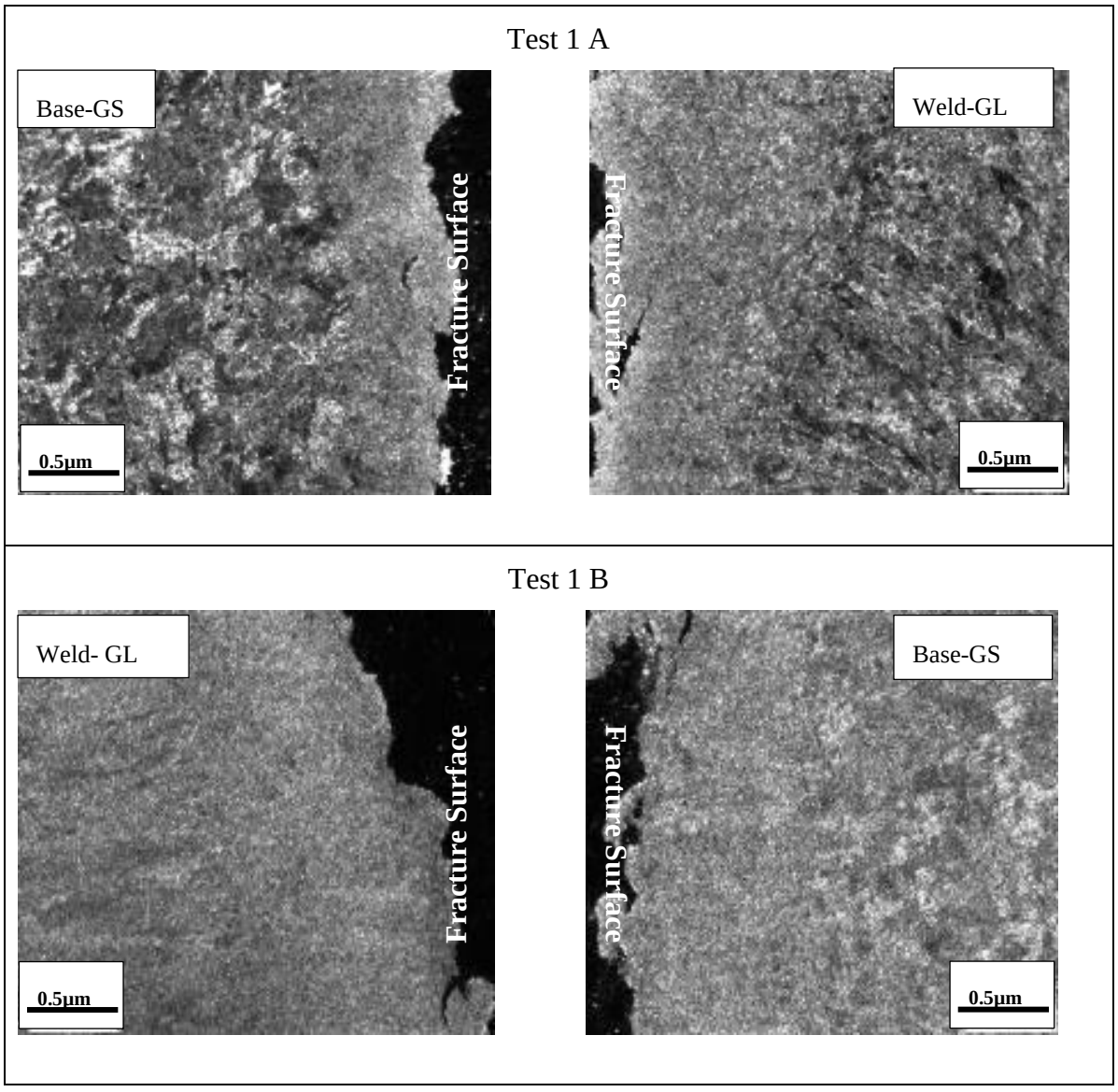

Figure 66: Optical micrographs for Test 1 A and B creep ruptured samples

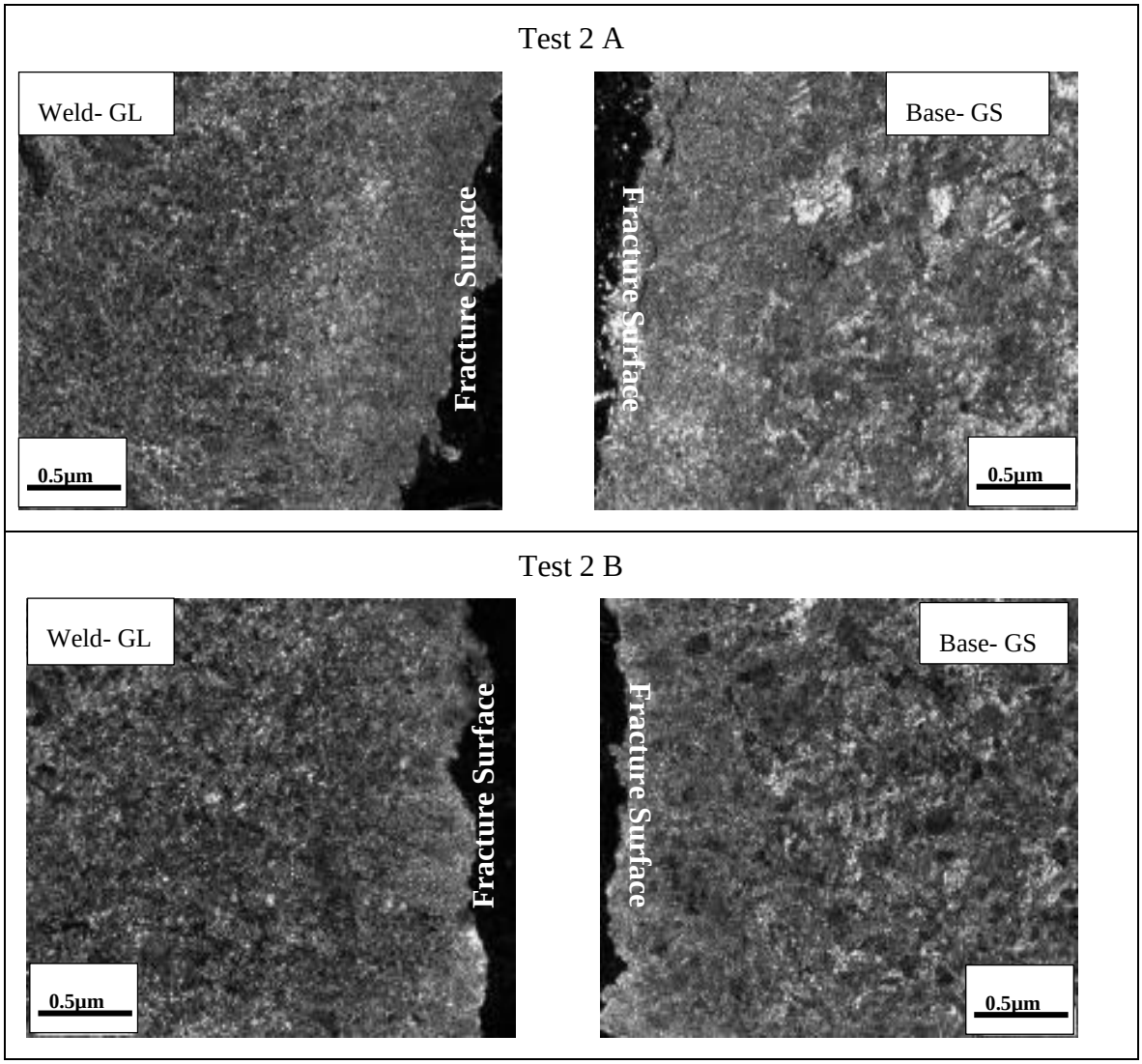

Figure 67: Optical micrographs for Test 2 A and B creep ruptured samples

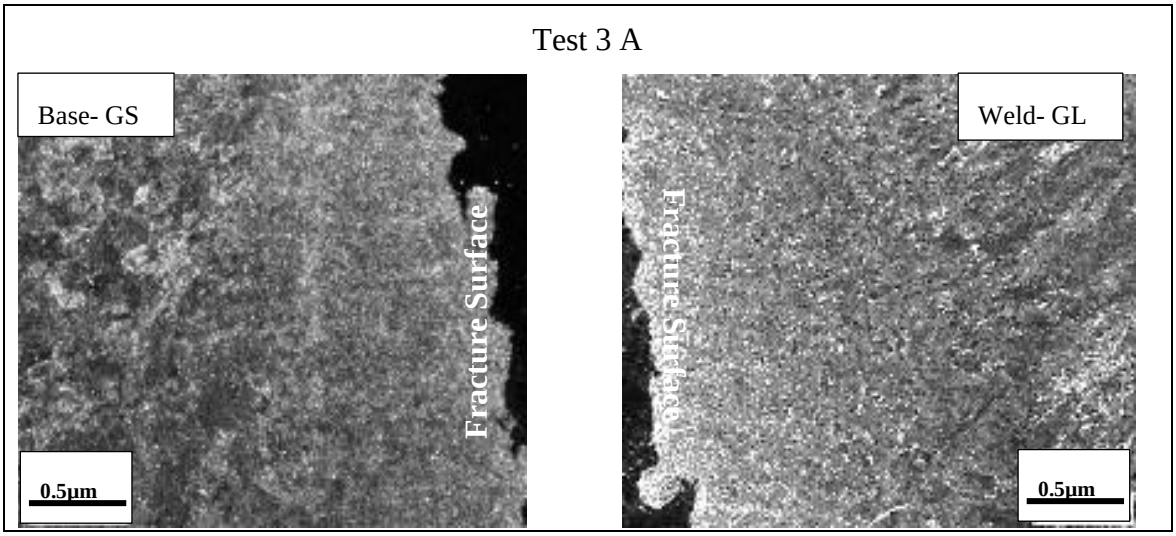

Figure 68: Optical micrographs for Test 3 A creep ruptured samples

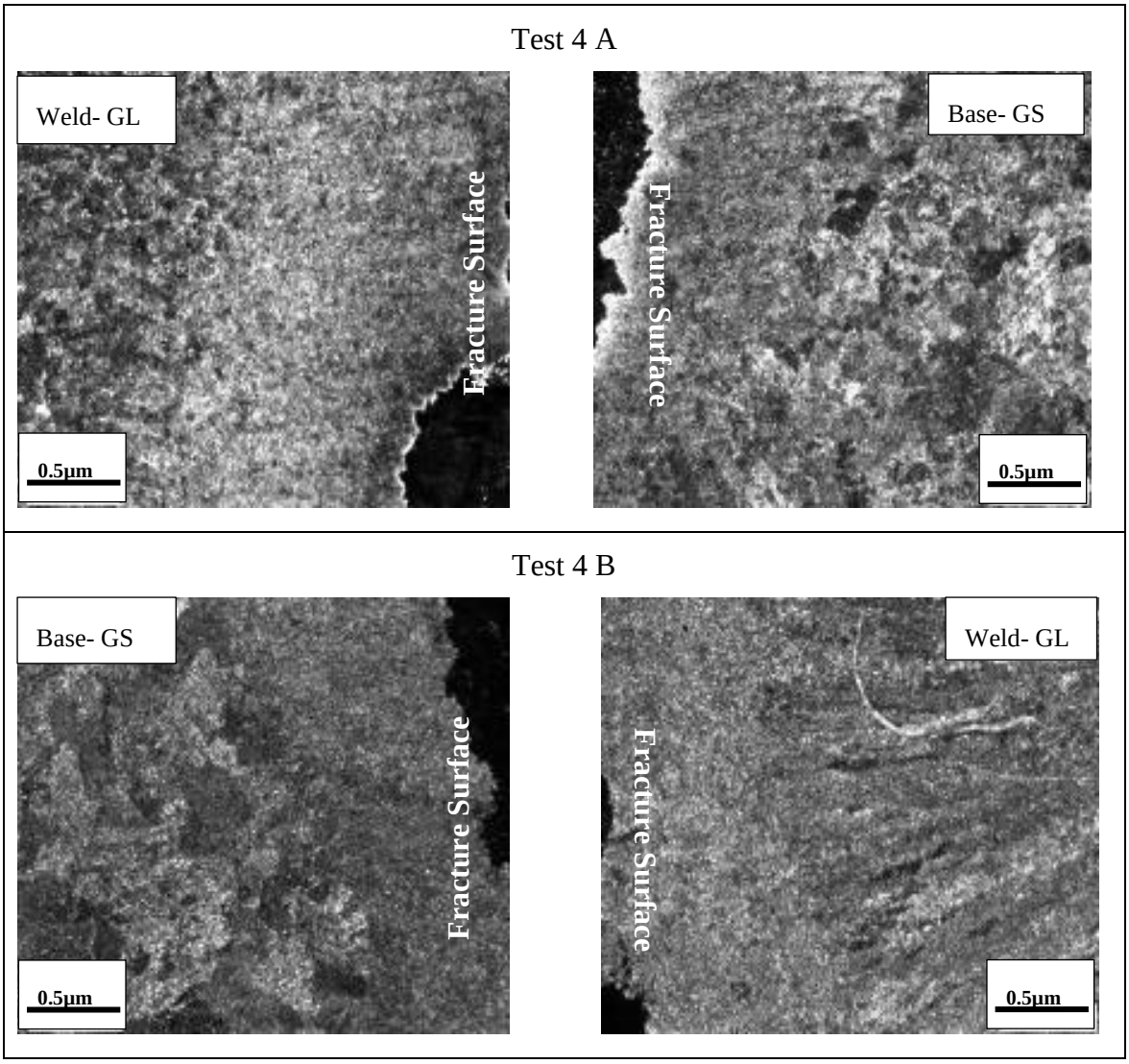

Figure 69: Optical micrographs for Test 4 A and B creep ruptured samples

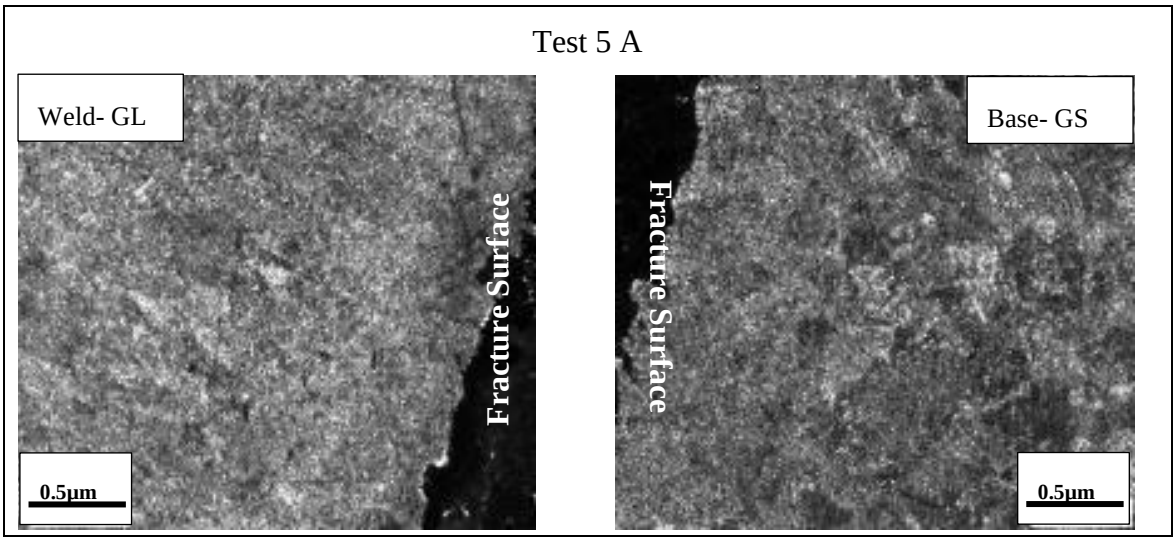

Figure 70: Optical micrographs for Test A creep ruptured samples

In order to determine, more specifically, the microstructure at the area of fracture, EBSD maps were acquired at areas A, B and C for both ends of the fractured sample as shown in Figure 71. Area A is mapped at 500x magnification with a step size of 0.2µm, while areas B and C are mapped at a magnification of 250x with a step size of 0.5µm. Area A contains details of the fracture and key microstructural features of location of fracture, hence a higher magnification and smaller step size were required. Areas B and C provide details of the microstructure neighbouring the fracture, and hence were acquired with lower magnifications and step size.

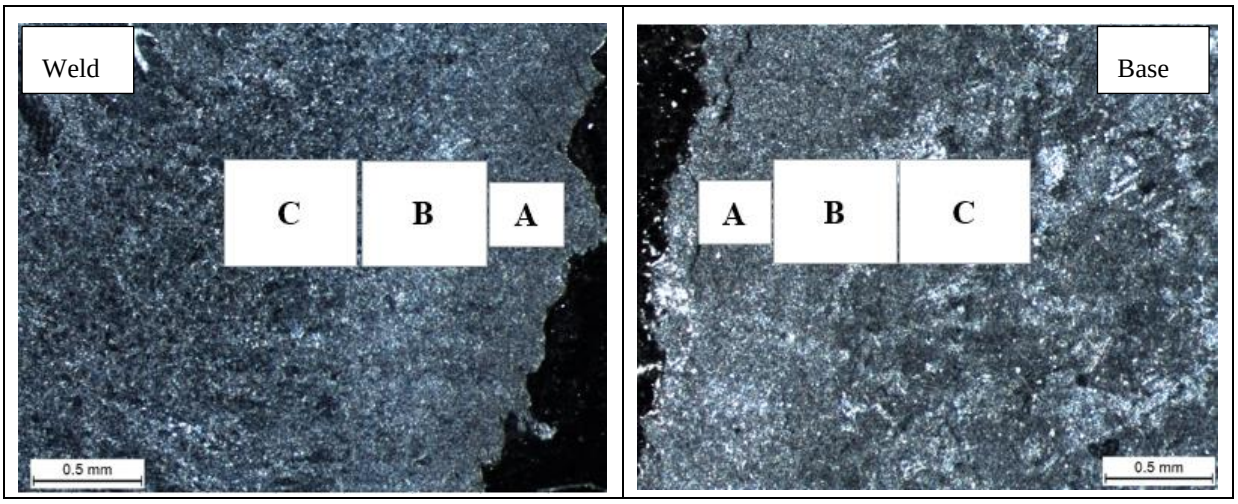

Figure 71: EBSD map areas for Test 2 A GL (left) and Test 2 A GS (right)

Figure 72 shows EBSD All Euler colour maps for areas A, B and C of sample Test 2A GL. Area A showed a fine grained microstructure at the region near the fracture surface. As one proceeded away from the fracture to areas B and C, a noticeable difference can be seen between areas B and C. Area C possesses the largest prior austenite grain size microstructure which could possibly represent the CGHAZ. Figure 73 shows the EBSD All Euler colour maps for areas A, B and C of sample Test 2A GS. Again, with this sample, the microstructure changed from fine prior austenite grains in area B to a much larger prior austenite grain size on the right in area C. This area to the right in area C could possibly represent the over-tempered region of the HAZ.

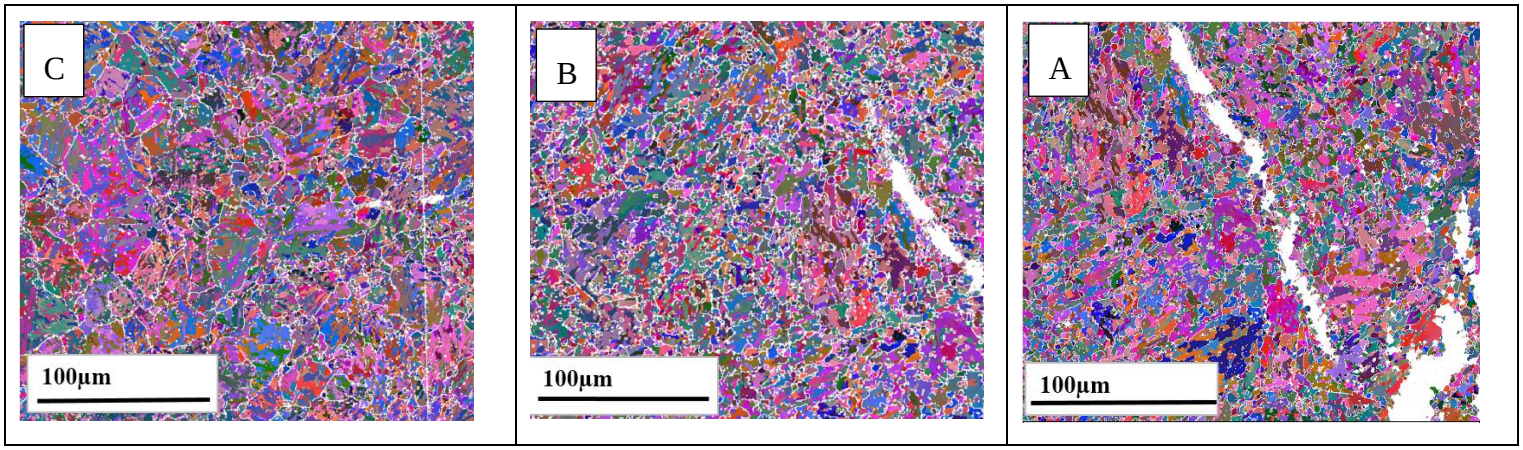

Figure 72: EBSD All Euler colour maps for areas A, B and C for sample of Test 2A GL

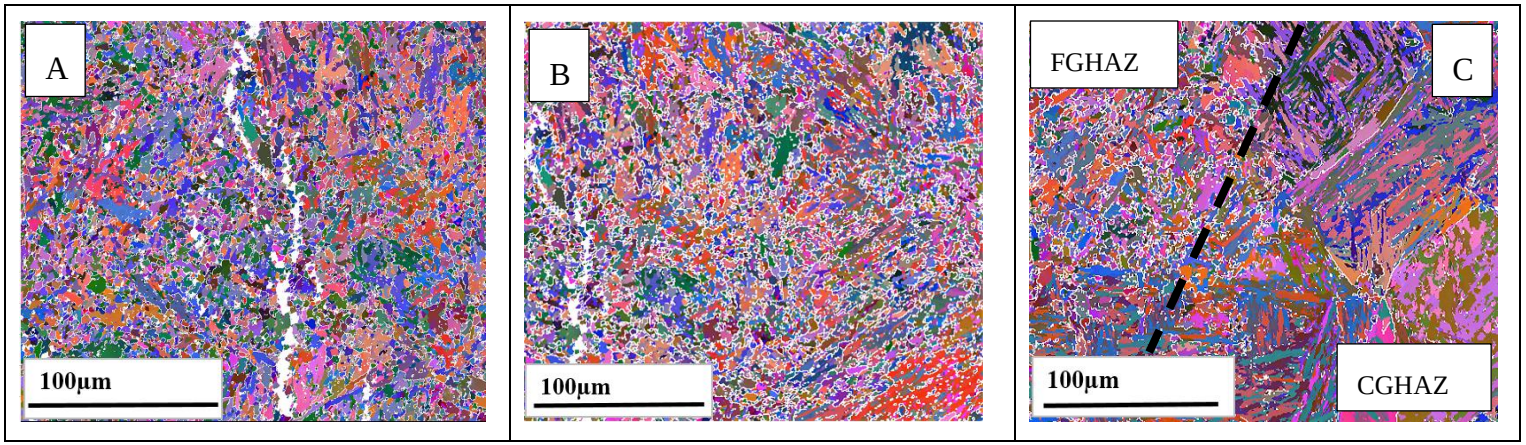

Figure 73: EBSD All Euler colour maps for areas A, B and C for sample of Test 2A GS

Samples for each weldment and stress condition were analysed using EBSD. Test 1A, 3A, 4B and 5A samples were analysed at UCT using the Nova NanoSEM 230. Due to time constraints and equipment availability, a higher step size (0.5µm) and magnification (2000x) were used to generate EBSD maps for these samples. Each map required a minimum of 8 hours to solve. The All Euler colour maps were taken very close to the fracture surface hence indexing was not optimal due to the numerous voids present. These maps can be seen below in Figure 74, Figure 75, Figure 76 and Figure 77. The All Euler colour maps show very small grains representative of the FGHAZ. The white boundaries on the All Euler maps below were detected using the automated detection of prior austenite grain boundaries as previously mentioned.

Figure 74 shows All Euler colour maps for Test 1 A on either side of the fracture surface. The fine grain microstructure can be seen more evidently in Test 1 A GL. A small area of fine grained microstructure can be seen at the bottom of Test 1 GS map. This is as a result of the map being taken further away from the fracture surface due to excessive void cavitation. Figure 75 shows the microstructure on either side of the fracture for Test 3 A. The fine grained microstructure is evident in both All Euler colour maps (GS and GL). Figure 76 and Figure 77 exhibit slightly larger grains. This is also as a result of the All Euler colour maps being scanned further away from the fracture surface due to the excessive cavitation.

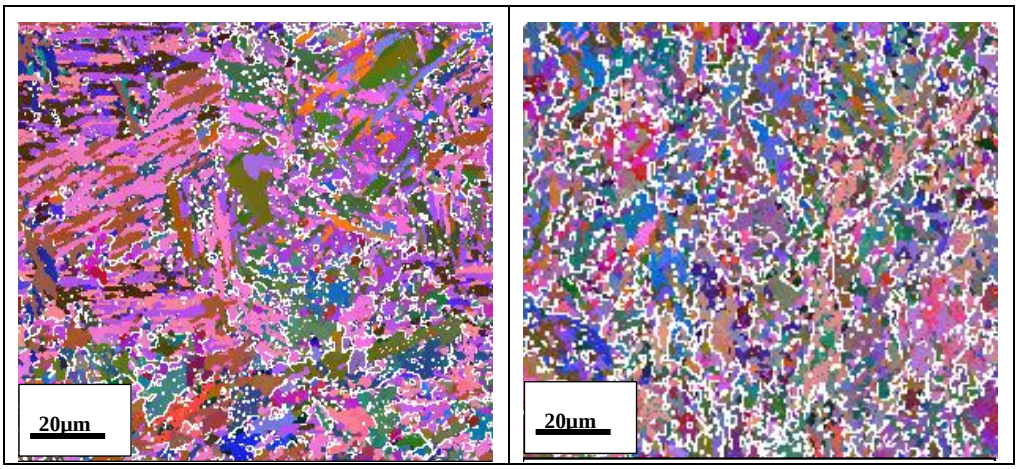

Figure 74: Test 1A GS (left) GL (right)

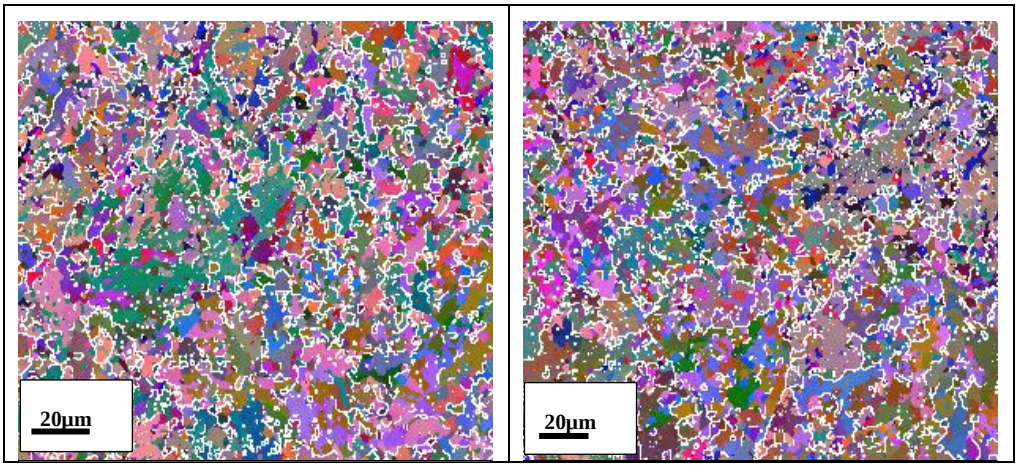

Figure 75: Test 3A GS (left) GL (right)

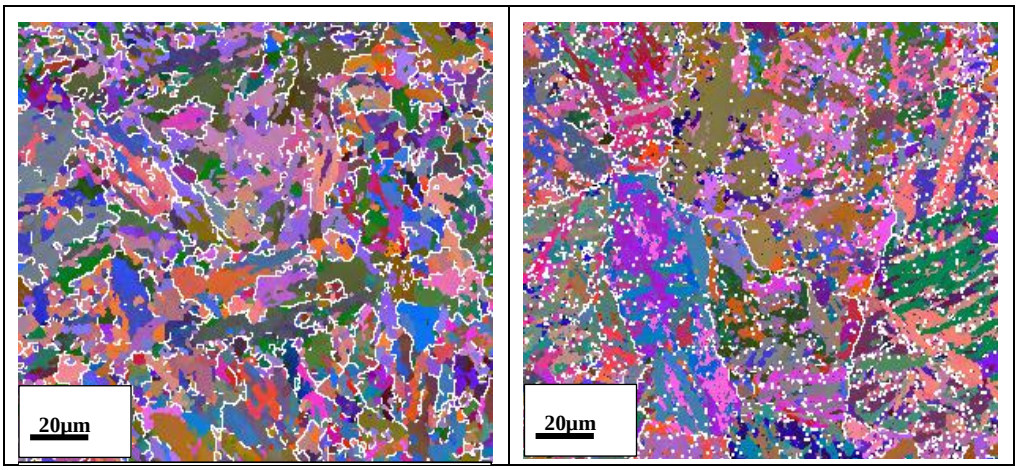

Figure 76: Test 4B GS (left) GL (right)

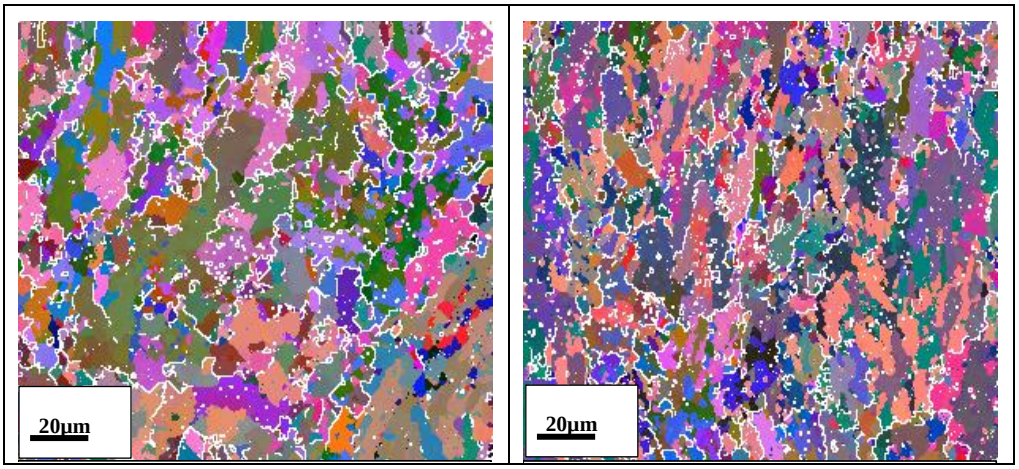

Figure 77: Test 5A GS (left) GL (right)

Evidence from optical microscopy and EBSD confirmed that fracture of the creep tested samples occurred in the HAZ on the creep damaged X20_MD/X20_HD. The region within the HAZ, more specially, consists of a fine grained microstructure. In order to determine, with greater confidence, the exact region which exhibits this behaviour, the fracture confirmation was combined with investigations that were conducted on the weldments prior to creep testing. The microstructure of the FGHAZ was acquired from the weldments by first testing the hardness across the HAZ.

4.2.4 Microhardness Profile

The hardness values for weldments 1 and 2 were determined by Vickers microhardness testing along the width (black, dashed lines) of the HAZ (white, dashed lines) as shown in Figure 78. Small intervals of 0.25mm were used as the transition between the various sub-zones of the HAZ were in very close proximity to the neighbouring sub-zones.

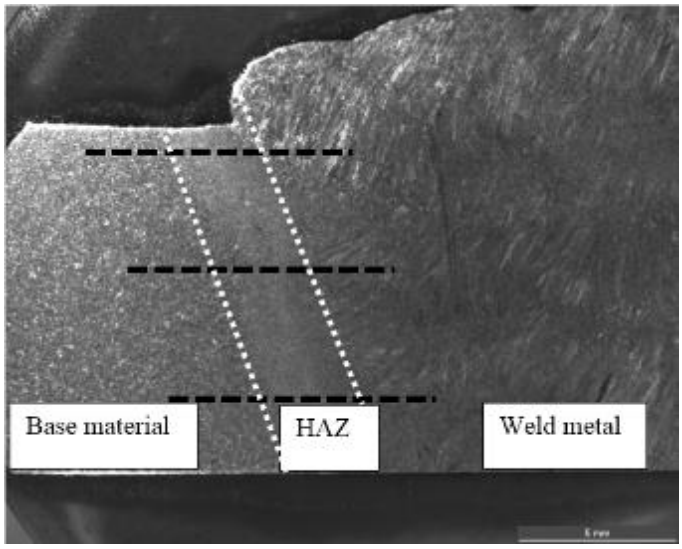

Figure 78: Optical micrograph of X20_ND weldment

Figure 79 shows the Vickers microhardness test results for the top, middle and bottom of the HAZ of the X20_ND weldment. The sub-zones are identified by the values yielded from the microhardness testing. The ICHAZ possesses the lowest hardness while the CGHAZ has the highest hardness value. The FGHAZ lies between the ICHAZ and the CGHAZ. Indicators have been added to Figure 79 to distinguish the hardness's of each sub-zone. Figure 79, Figure 80, and Figure 81 show the hardness values for the top, middle and bottom of the HAZ, together with the average hardness.

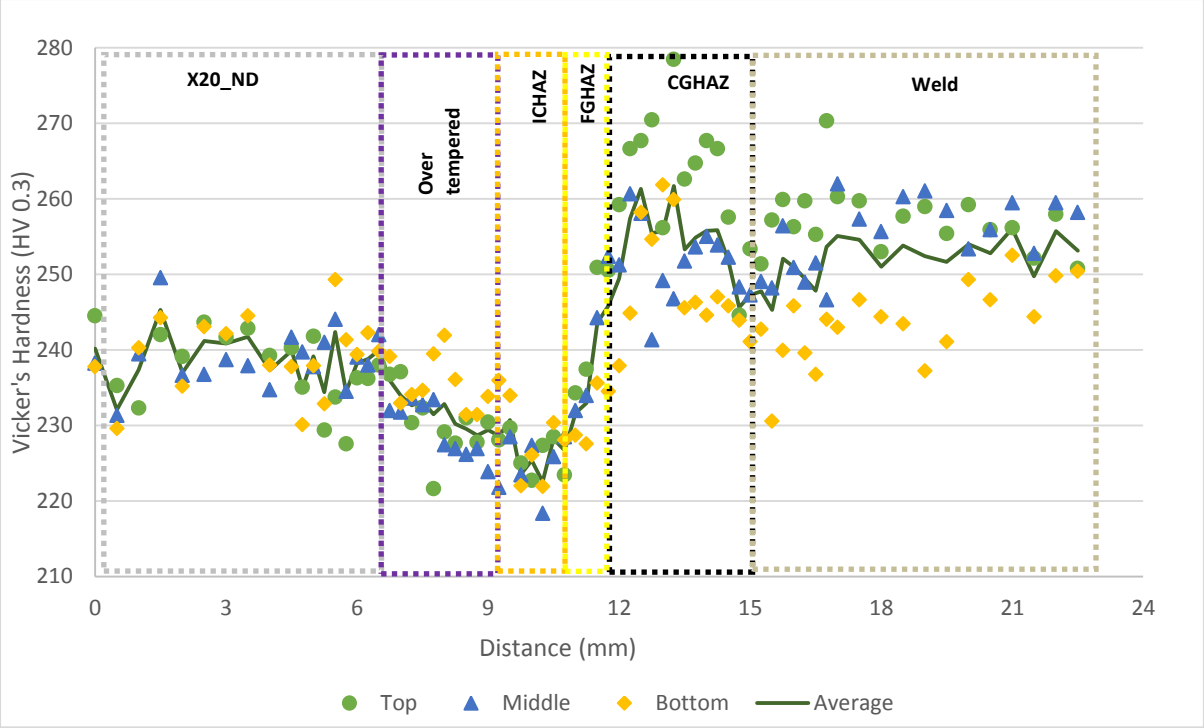

Figure 79: Vickers hardness results for the weldment of X20_ND

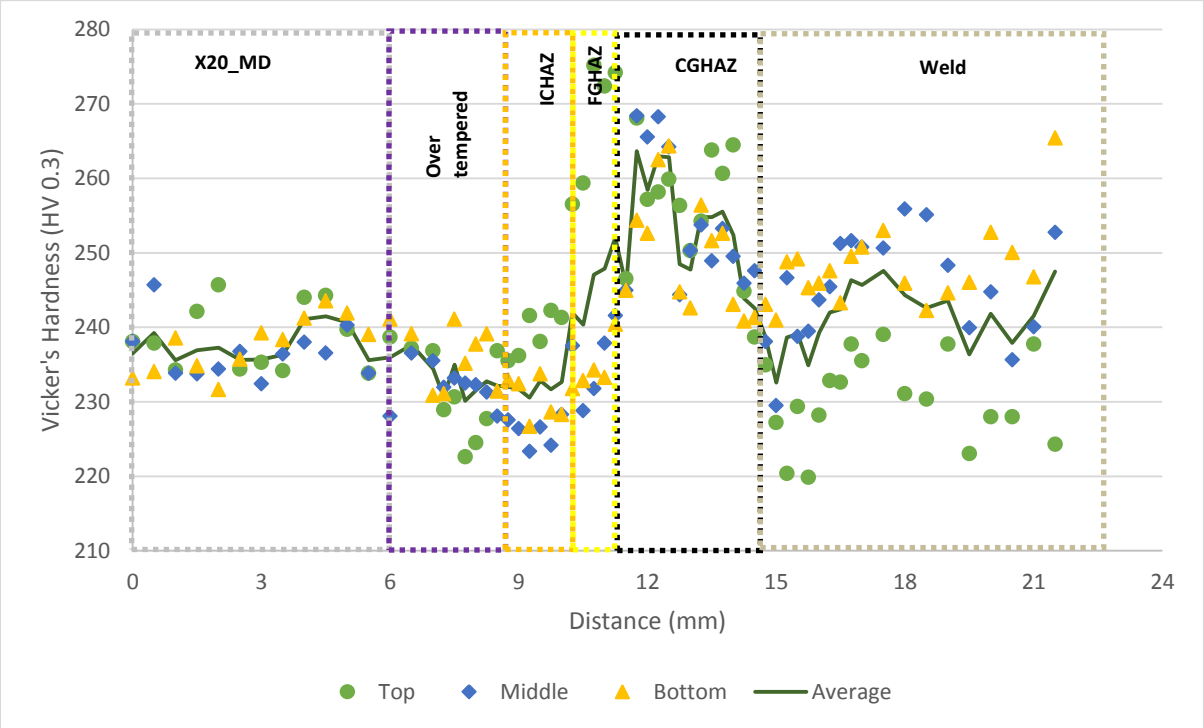

Figure 80: Vickers hardness results for the weldment of X20_MD

Figure 81: Vickers hardness results for the weldment of X20_HD

Once the location of the FGHAZ was determined by microhardness testing, EBSD maps were acquired from the three HAZ of weldment 1 and 2. Figure 82 shows the All Euler colour maps of the FGHAZ for X20_ND, X20_MD and X20_HD respectively. The prior austenite grain sizes for each map were calculated using the mean linear intercept method. PAGBs were determined by detecting grains with misorientation angles between 10 and 60°. A summary of the calculated grain size is shown in Table 22.

Table 22: Summary of calculated grain size for the FGHAZ of weldments 1 and 2

	X20_ND	X20_MD	X20_HD
Horizontal intercept grain size (µm)	9	4.9	14
Vertical intercept grain size (µm)	11	3.7	16.9
Average grain size (µm)	10	4.2	15.8

The main purpose for acquiring the microstructure of the FGHAZ for the different base materials is to be able to compare the 'ideal" representation of the FGHAZ adapted from an actual weldment to:

- The region of failure in the creep ruptured zone and
- The simulated weld thermal cycle base material

By identifying the microstructure of the FGHAZ of actual weldments, one could easily compare the microstructures of the creep-rupture/simulated weld thermal cycle samples are in relation to the FGHAZ of the actual weldment. The prior austenite grain boundaries for the FGHAZ were detected using misorientation angles between 10 and 60°. Tests 1A, 2A and 3 A shows very fine grained microstructure which is evidently comparable to the fine grained microstructure of the FGHAZ of X20_MD. The grain size for Tests 4B and 5A are also fine-grained but larger and more comparable to the FGHAZ acquired from the HAZ of X20_HD.

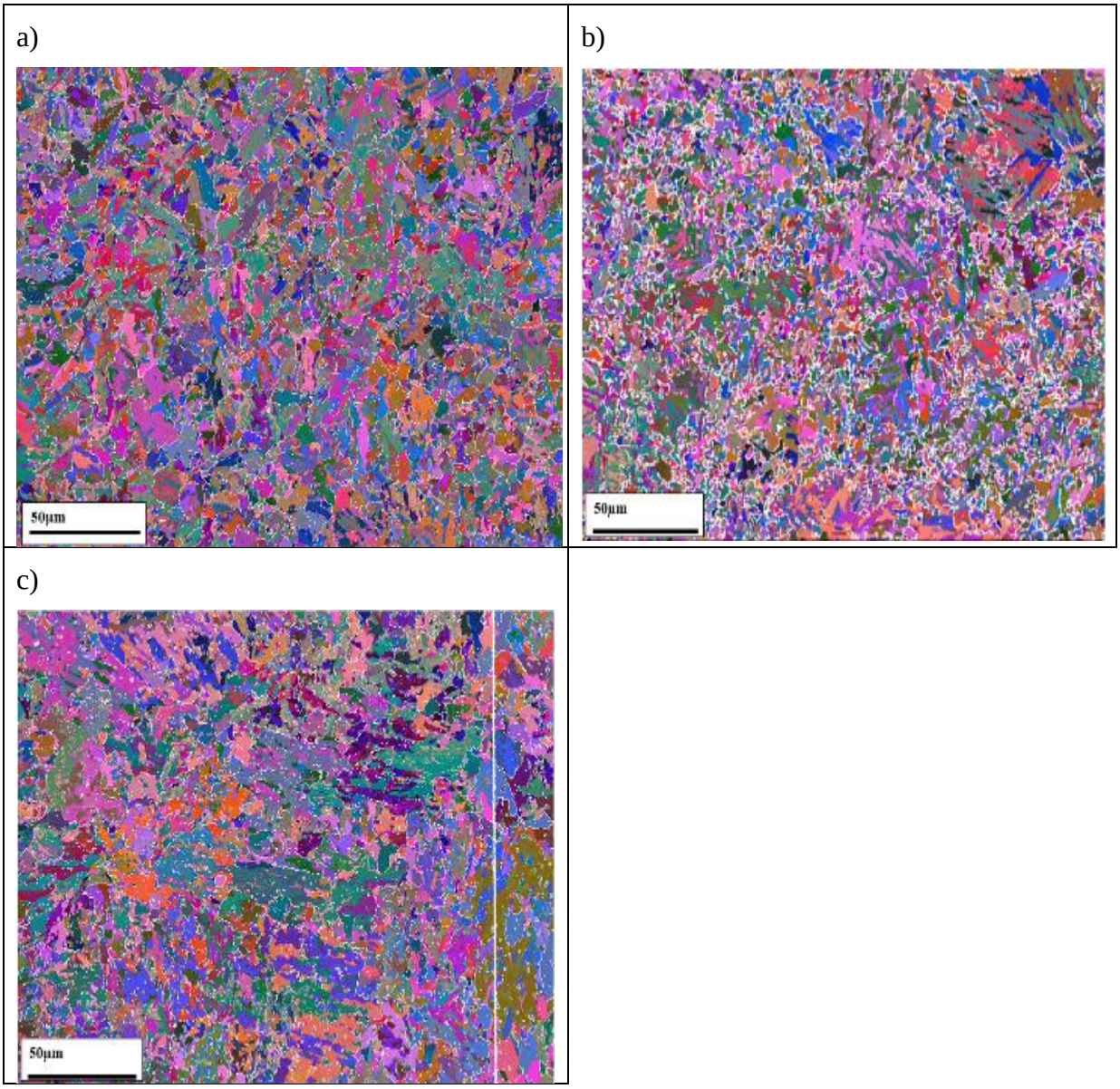

Figure 82: EBSD All Euler colour map for the FGHAZ in a) X20_ND HAZ, b) X20_MD HAZ and c) X20_HD HAZ

4.2.5 Void Density of Fractured Sample

SEM is used to investigate three properties of the creep-ruptured samples:

- Comparison of microstructure between the cross-sectional surface of fracture and unaffected base/weld material
- Void density of the fractured sample
- Fracture surface analysis to identify type of fracture mechanism

The areas of fracture for the creep-ruptured samples are investigated to identify any microstructural similarities or differences to the unaffected base or weld material. **Figure** 83 shows the cross-sectional fracture area on the left and the base material on the right for test 5 A. The cross-sectional fracture surfaces show a fine recrystallized microstructure with the presence of voids. Images on the right in Figure 83 show the typical martensitic lath microstructure. Needle-like laths are present with precipitation on lath and prior austenite grain boundaries. The occurrence of voids is less noticeable in the base material as compared to the fracture area.

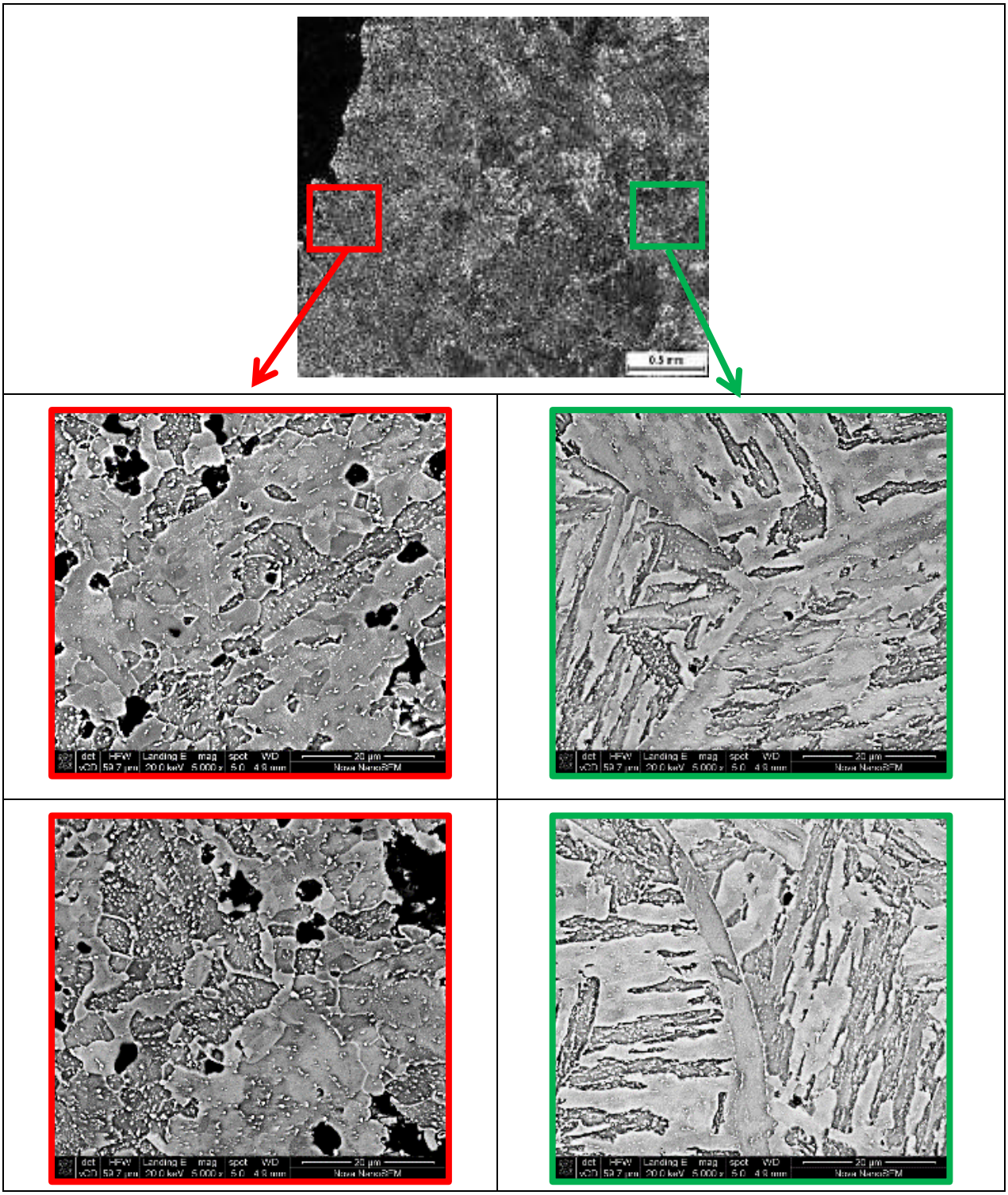

Figure 83: Backscatter SEM images of the rupture surface (left) and base material (right) for test 5A with the black areas indicating voids

Appendix 3 contains the SEM images for the rest of the tests. Figure 125 to Figure 131 show the comparison of voids in size and quantity between the fracture area and the unaffected base/weld metal. Figure 125, Figure 128, Figure 129, Figure 130 and Figure 131 also show the difference in microstructure between the fracture area and the unaffected base/weld metal. Once again, the fracture areas contain several larger voids. The unaffected base material/weld metal microstructure is similar for most of the samples. Figure 126 and Figure 130 do not show detail of the microstructure as clearly as the others; however, the amount and size of voids can be seen. The microstructures are representative of the entire fracture area and unaffected base/weld metal. SEM images were taken along the length of the fracture area as well as over large areas of the base/weld metal.

Backscattered electron SEM images were acquired from the fracture surface cross-section into the base/weld material at a magnification of 1500x as shown by the directional arrow in Figure 84. This was done to determine how the microstructure and void density changes from the fracture surface to unaffected base/weld material.

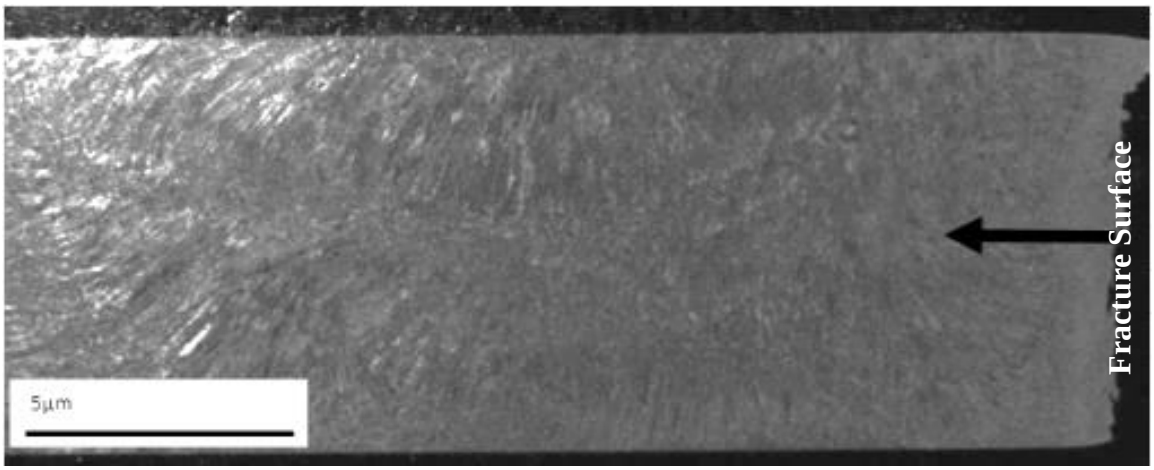

Figure 84: Optical micrograph of test 1 A GL sample polished cross-section of fracture surface

Each image is approximately 200µm x170µm in size. An average of 5 to 6 images was stitched together using Microsoft ICE to represent a continuous, single image as shown in Figure 85. This is sufficient to notice the change in microstructure and void density from the fracture surface to the base/weld material. It is evident from Figure 85 that as one progresses away from the fracture, the frequency of void occurrence decreases significantly. In order to quantify the change in accumulation of voids as one moves away from the fracture surface, ImageJ is used to threshold the appearance of voids. Figure 86 is the threshold image for test 1 A GL sample.

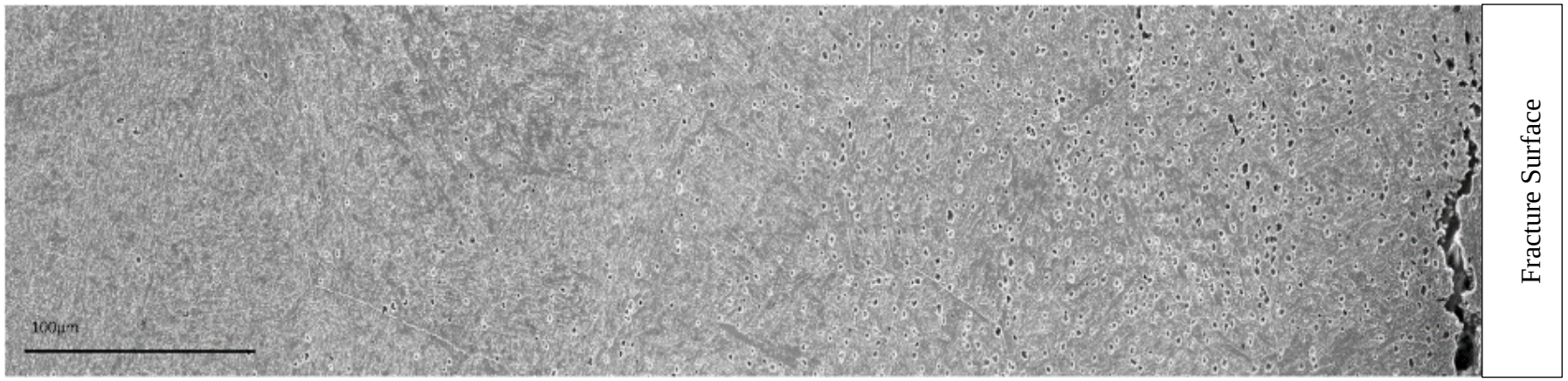

Figure 85: Backscattered electron SEM stitched image of test 1 A GL sample

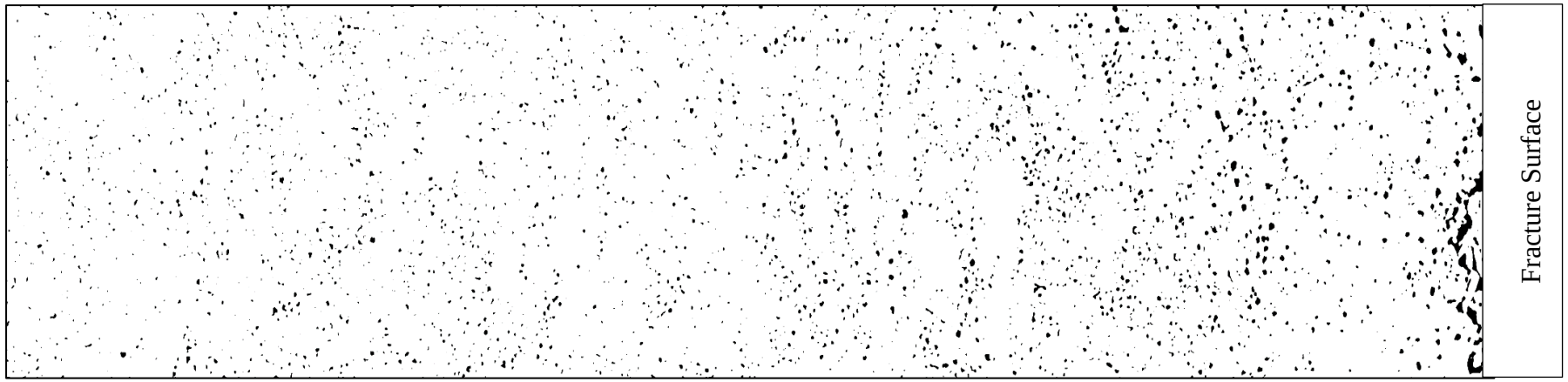

Figure 86: Threshold image for test 1 A GL sample

The number of voids were counted along the length of the map and plotted against the distance as one moves away from the fracture. Figure 87 shows the relationship of number of voids in relation to the distance from the fracture surface. There in an inverse relation between number of voids present and the distance from fracture. The number of voids is 9 times higher in the region closest to the crack as opposed to the base/weld material.

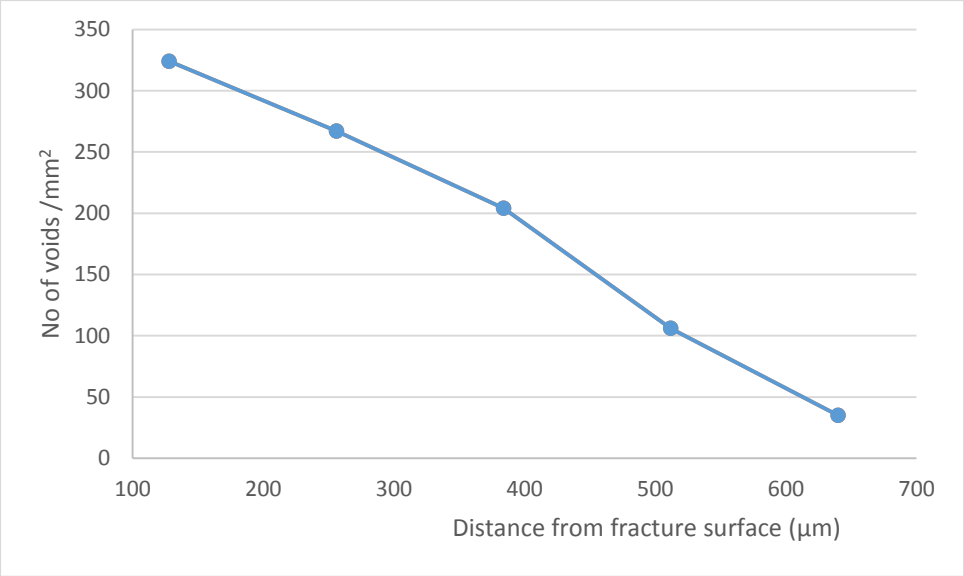

Figure 87: Graph showing the void density as a function of the distance from the fracture surface in sample test 1 A GL

Table 23 provides a summary for the void density ratio for all creep tested samples. The stitched images for the remaining tests, together with their void density profile can be found in Appendix 4. The SEM images show an increase in size and quantity of voids as one approaches the fracture area. The difference in microstructure is noted based on the fine-grained region at the fracture and the large grained region away from the fracture. By using both ends of the fractured sample, it is observed that the concentration of voids occurs in a very narrow region (≈ 300µm) on each side of the fracture. Figure 134 and Figure 136 provide evidence of this occurence. Test 1 B GL and GS both show similar void density profiles on either side of the fracture. It can also be seen that the size of the voids decreases as one moves away from the fracture.

Table 23: Void density comparison between fracture surface and base/weld material

Weldment	Test number	Sample	No. of voids at fracture area/mm^2	No. of voids in unaffected base/ weld area/mm^2	Ratio of voids at fracture area: base/weld area
Weldment 1	Test 1A	GL	324	35	9:1
		GS	257	28	9:1
	Test 1 B	GL	307	28	11:1
		GS	273	30	9:1
	Test 2 A	GL	308	2	154:1
		GS	262	32	8:1
	Test 2 B	GL	134	8	17:1
		GS	143	39	4:1
	Test 3 A	GL	313	66	5:1
		GS	126	25	5:1
Weldment 2	Test 4 A	GL	312	8	39:1
		GS	221	18	12:1
	Test 4 B	GL	112	21	5:1
		GS	97	17	6:1
	Test 5 A	GL	102	6	17:1
		GS	125	24	5:1

4.2.6 Discussion

Microscopic investigations using light, SEM and EBSD microscopy has shown that failure in the FGHAZ is caused by creep cavitation in the narrow transition between the weld and base metal. The intensively damaged area by creep cavitation was the transition region from the FGHAZ to the unaffected base material. The FGHAZ has small PAGBs and they occur numerously in this specific zone. Due to the numerous PAGBs, the diffusion coefficient is very high. The multi axial stresses induced into the material coupled with the high effective diffusion coefficient caused high formation of voids at PAGBs. As voids become prominent in number, they begin to coalesce. Eventually the coalescence of voids leads to micro crack formation and eventually macro crack formation.

Investigations conducted by Chung et al[6] confirmed fracture at the transition area from the FGHAZ to unaffected base material using optical microscopy. Figure 88 shows the optical micrograph of an X20 cross weld tested at 650°C and 60 MPa. The sub-zones of the HAZ are characterised by the governing microstructure.

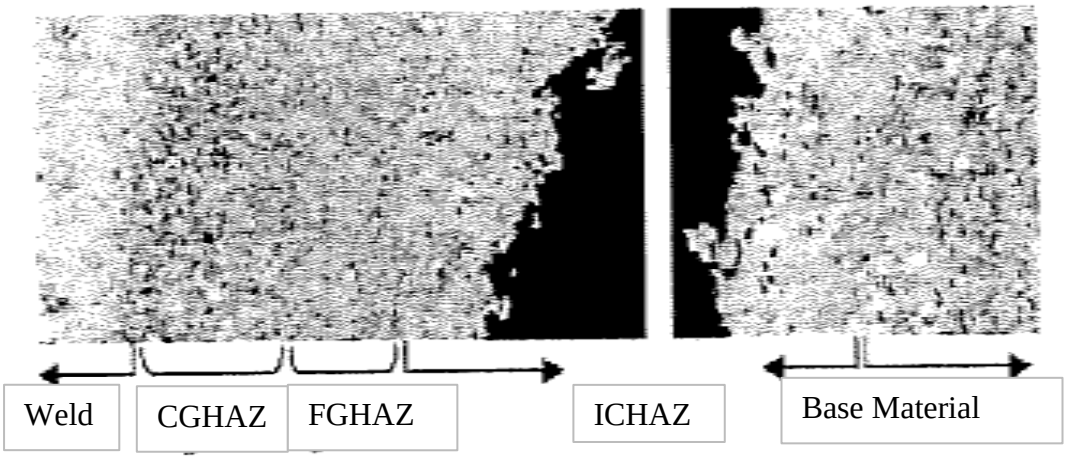

Figure 88: Typical optical micrograph of the cross section of creep-ruptured specimen at 650°C and 60 MPa[6]

Optical micrographs taken of the creep ruptured specimen of weldment 1 at 610°C and 63 MPa in Figure 89 shows that it has similar fracture location as that shown in Figure 88. The exact sub-zone at fracture is better shown as the FGHAZ using EBSD as explained later in this chapter.

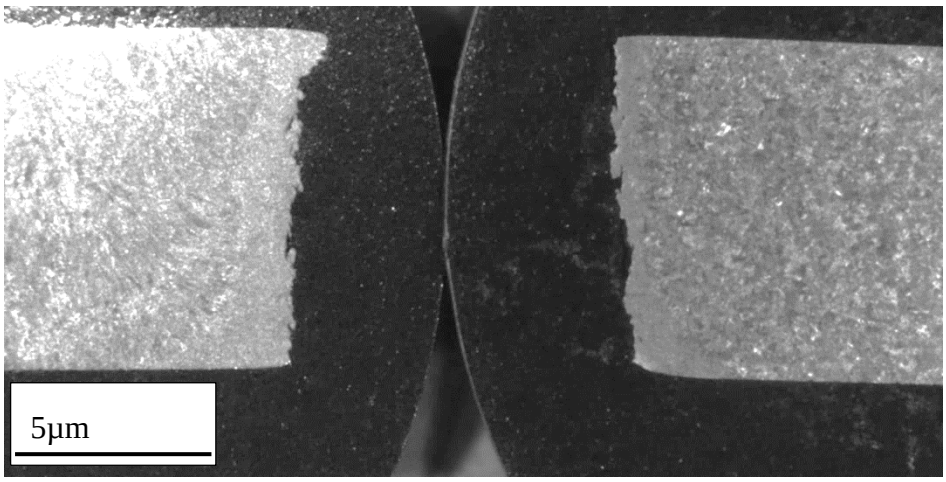

Figure 89: Optical micrograph of weldment 1 creep ruptured specimen at 610°C and 63 MPa

Creep tests conducted by Rui et al[65] on ex service 10CrMo9 10 cross welds at 540°C and 95 MPa show that the contributing reason for failure is the creep cavitation very close to the fracture surface (Figure 90). Enhanced multi axial stresses as a result of overmatched welds may develop in the HAZ, leading to premature failure. Highly mis-matched welds, where creep strength in the weld metal is much higher than that in the base metal, or where the creep rate in weld metal is much lower than that of the base metal results in premature failure.

The higher degree of mis-matching, the higher the risk of failure in the HAZ and the shorter creep lifetime of a weld as a whole[65]. The shorter creep life of weldment 2 (X20_ND to X20_HD) can be further highlighted by the results of the tensile tests. The X20_HD is much weaker than X20_MD and X20_ND and hence it is anticipated that the weld HAZ of the X20_HD material is much weaker.

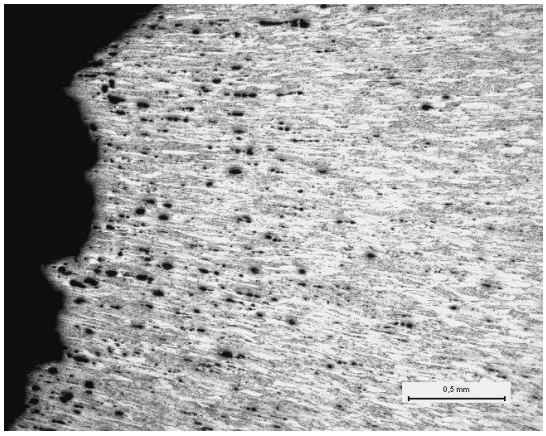

Figure 90: Light micrograph showing creep cavitation close to fracture for 10CrMo9 10 cross weld (540° C/95 MPa)[65]

Similarly, SEM images taken for Test 1A samples also revealed extensive damage close to the region of fracture. Creep cavitation and micro cracks can be seen in Figure 91. The sizes of the voids appear larger at closer proximity to the fracture as compared to voids about 150µm away from the fracture (Figure 91 (left)). A higher magnification image at 3000x (Figure 91 (right)) reveals micro cracks which could possibly be as a result of the coalescence of voids.

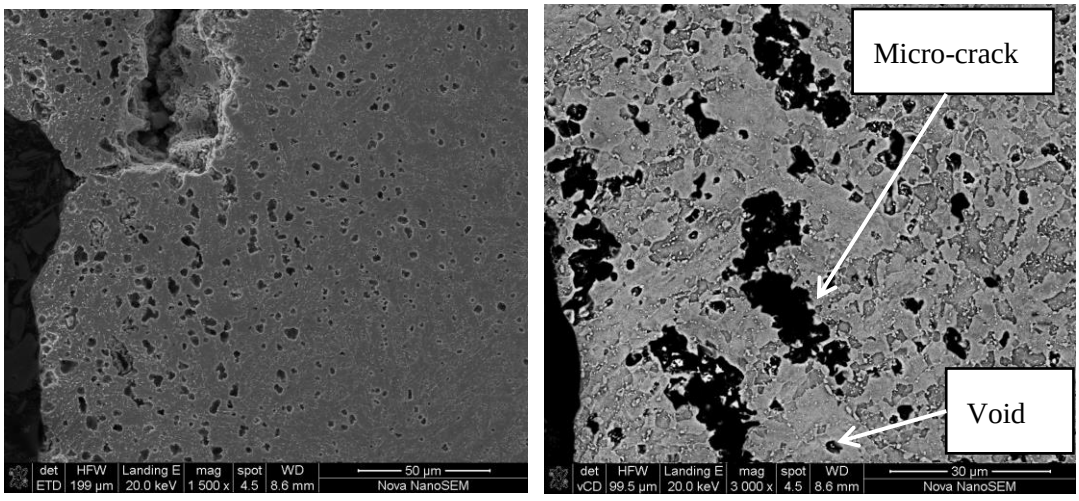

Figure 91: SEM images showing creep cavitation close for the fracture surface (610°C/63 MPa)

The presence of creep cavities is not only on the PAGBs but also occur within the martensitic matrix. This observation implies that the areas between the precipitates in the matrix, the matrix and PAGBs act as possible sites for cavity nucleation.

The use of EBSD and optical microscopy conclude that:

1. The region close to fracture is indeed damaged by creep cavitation (Figure 92 (left) and Figure 93 (left). Micro cracks can be seen surrounded by voids.
2. The region close to fracture possesses a fine-grained microstructure with PAGB sizes as small as 5µm (Figure 92 (right) and Figure 93 (right)). The comparison of PAGB size of the FGHAZ extracted from weldments to that of the fracture area suggests that the region of failure in welded joints is the FGHAZ.

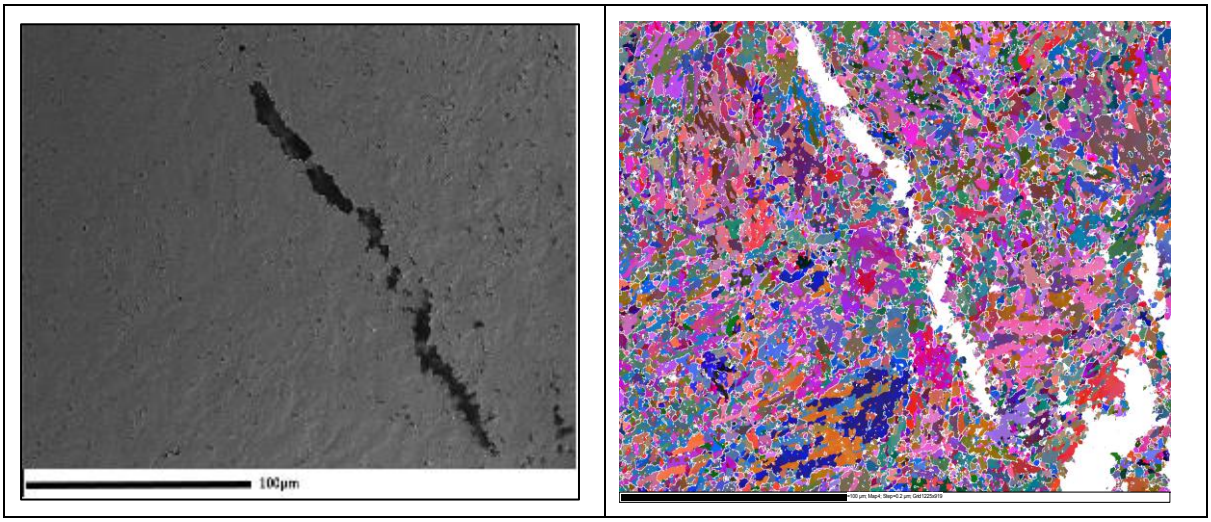

Figure 92: Optical micrograph (left) and EBSD All Euler colour map (right) for the cross-sectional fracture area for Test 2 A GL

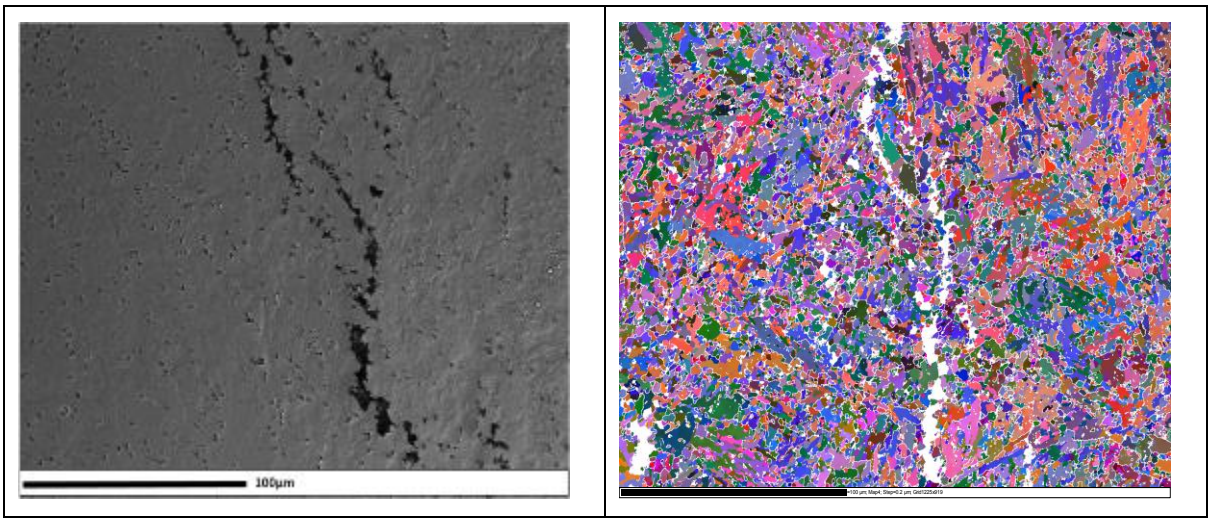

Figure 93: Optical micrograph (left) and EBSD All Euler colour map (right) for the cross-sectional fracture area for Test 2 A GS

Information regarding fracture mechanisms for uniaxial cross weld creep tests provided by EPRI[23] show that the type of fracture for cross weld creep tests are sensitive to temperature and stress. The three types of fracture areas (transgranular base metal, transgranular HAZ and intergranular HAZ) are defined by the creep testing conditions. Based on the creep testing conditions done in this research, the fracture of the cross weld samples should be an intergranular HAZ fracture according to Figure 94.

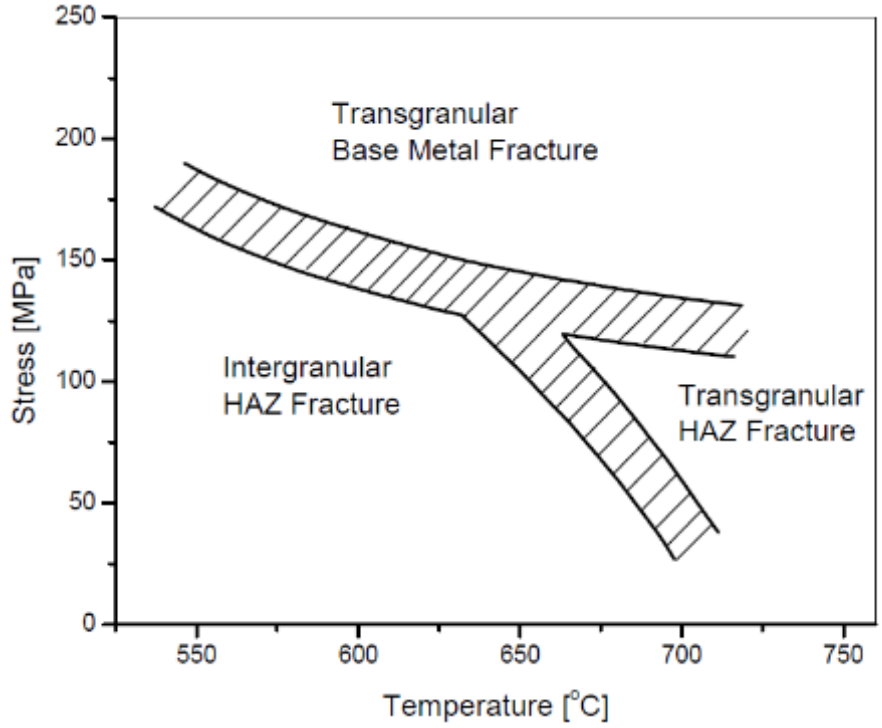

Figure 94: Approximate fracture mechanisms for uniaxial cross-weld creep tests for X20CrMoV12-1 weldments[23]

Results from fracture surface analysis using SEM show that the fracture surface exhibits a typical ductile failure. This is characterised by the "dimple" appearance of the fracture surface. Creep usually takes place above $0.4T_m$ and under such conditions ductile failure of a transgranular nature. This process is similar to a ductile failure at low temperatures when voids nucleate at inclusions within grains, grow during creep deformation and coalesce to produce fracture. However, because these three processes are occurring at $0.3T_m$, local recovery is taking place and this delays both the onset of void nucleation and void coalescence. More commonly at lower stresses and longer times-to-fracture, intergranular rather than transgranular fracture is observed[10]. This is the typical case demonstrated by the fracture mechanism noted for the cross weld samples tested in this research

4.3 Weld Thermal Cycle Simulation Using the Gleeble®3800

4.3.1 Weld Thermal Cycle Simulation at a Peak Temperature of 1050°C

The first attempt at simulating the FGHAZ using the Gleeble® 3800 is conducted using information obtained from the MatCalc thermal equilibrium software. A key parameter in the simulation is the peak temperature. By using the A_{C3} temperature of 940°C derived from the thermal equilibrium calculation and an extra 110°C to ensure complete dissolution of precipitates, the peak temperature for the first weld thermal cycle simulation is set at 1050°C. Table 24 provides the temperature profile used to create the weld thermal cycle simulation on base material.

Table 24: Weld thermal cycle simulation on the Gleeble® 3800 at 1050°C

Temperature (°C)	Time lapsed (s)	Holding time (s)	Heating rate (°C/s)	Cooling rate (°C/s)
25	0	0		
250	5		45	
250	25	20		
1050	29		200	
1050	33	4		
100	59.4			26.4
100	79.4	20		

The EBSD All Euler colour maps for the FGHAZ achieved from the weld thermal cycle simulation is shown in Figure 95. By comparing the FGHAZ taken from a weldment to the FGHAZ created by the weld thermal cycle simulation, one can see that the microstructure created by the weld thermal cycle simulation is not similar to that of the FGHAZ of a weldment (Figure 82). The PAGB size for the FGHAZ of the actual weldment is smaller when compared to that of the weld thermal cycle simulated PAGB size. The microstructure obtained from the weld thermal cycle simulation at 1050°C could possibly represent the microstructure of the CGHAZ. Hence no further analysis was carried out on the base material that had undergone the weld thermal cycle simulation at 1050°C as described in Table 24. The first set of weld thermal cycle simulations carried out at 1050°C yielded a possible CGHAZ microstructure, therefore it is evident that 1050°C is much higher than the actual A_{C3} temperature of the material. Since the microstructure of the sub-zones of the HAZ was temperature dependent, dilatometry was used to determine the exact A_{C3} temperatures of the base material.

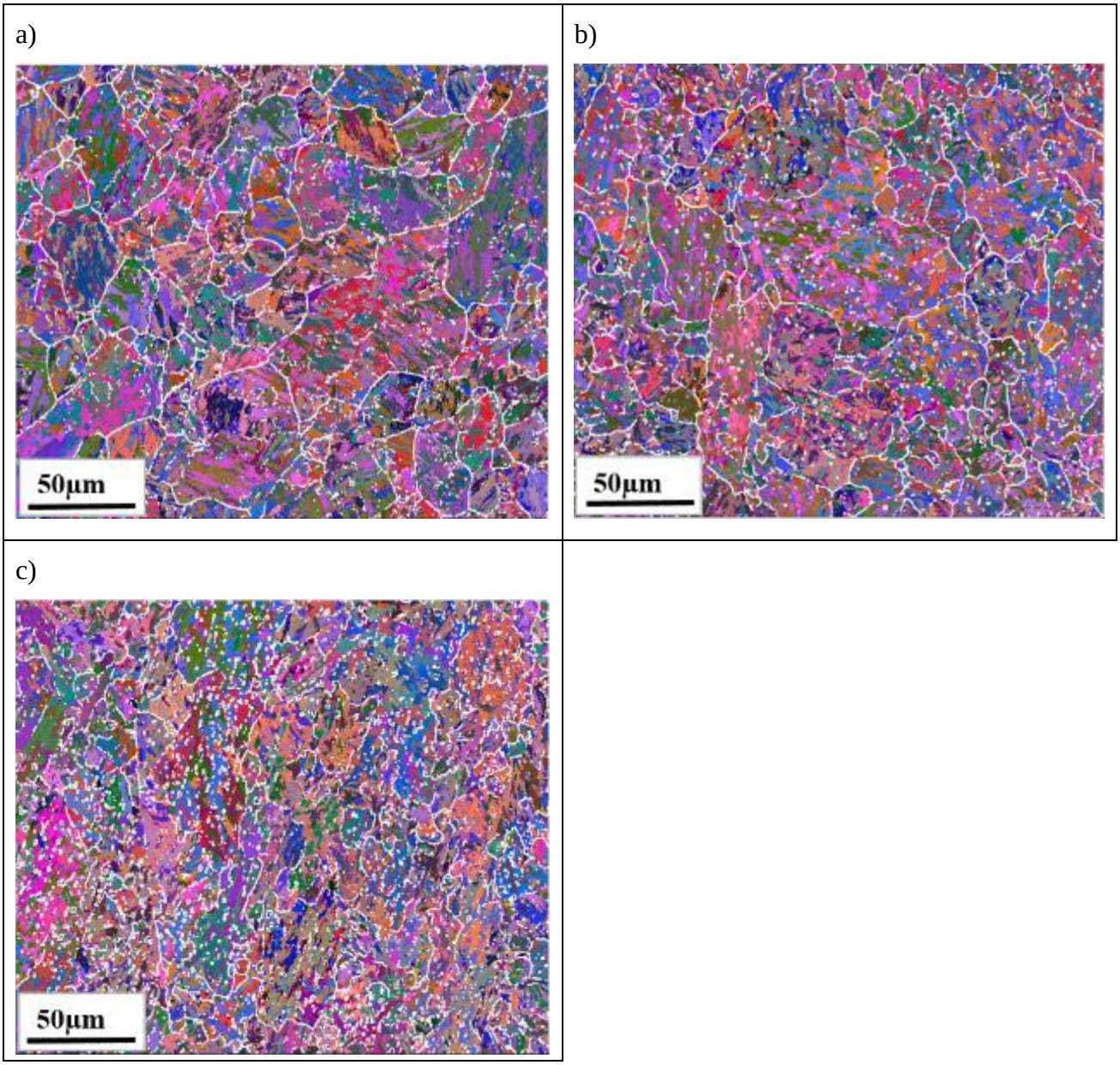

Figure 95: EBSD All Euler colour maps of the weld cycle simulated base material at 1050˚C for a) X20_NDS, b) X20_MDS and c) X20_HDS

4.3.1.1 Weld Thermal Cycle Simulation at a Peak Temperature of 980°C

The second attempt at the weld thermal cycle simulation is based on the dilatometry results obtained with a trial simulation at 1050˚C. Table 25 provides the heat treatment temperature profile used for the weld thermal cycle simulation at a peak temperature of 980˚C. The holding time, heating and cooling rate are the same as those used in the weld thermal cycle simulation at a peak temperature of 1050˚C.

Table 25: Weld thermal cycle simulation on the Gleeble® 3800 at 980°C

Temperature (°C)	Time lapsed (s)	Holding time (s)	Heating rate (°C/s)	Cooling rate (°C/s)
25	0	0		
250	5		45	
250	25	20		
980	29		200	
980	33	4		
100	59.4			26.4
100	79.4	20		

4.3.2 General Microstructure

The EBSD All Euler colour maps for the samples simulated at 980°C are shown in Figure 96. The microstructure obtained from the weld thermal cycle simulation at 980°C possesses similar grain structure as the FGHAZ extracted from weldments for X20_ND, X20_MD and X20_HD. Mean linear intercept method was used once again to determine the PAGB of the microstructure obtained from the simulation. Table 26 provides the average PAGB for X20_ND, X20_NDS, X20_MD, X20_MDS, X20_HD and X20_HDS.

Comparison of the PAGB size of the simulated sample to that of the FGHAZ of the weldments shows a slight difference in grain size. The PAGB of the X20_ND FGHAZ is 1µm smaller than the simulated FGHAZ for X20_ND. Similarly, the difference in PAGB size for X20_MD and X20_MDS is 1.3 µm. The largest difference in PAGB size yields from the comparison between X20_HD and X20_HDS which is 3.5µm.

Table 26: Summary of grain size calculation for weld thermal cycle simulation at 980°C

	Horizontal intercept grain size (µm)	Vertical intercept grain size (µm)	Average grain size (µm)
X20_ND	9	11	**10**
X20_NDS	10.5	11.8	**11.2**
X20_MD	4	3.7	**3.9**
X20-MDS	5	5.4	**5.2**
X20_HD	14	16.9	**15.5**
X20_HDS	12	12	**12**

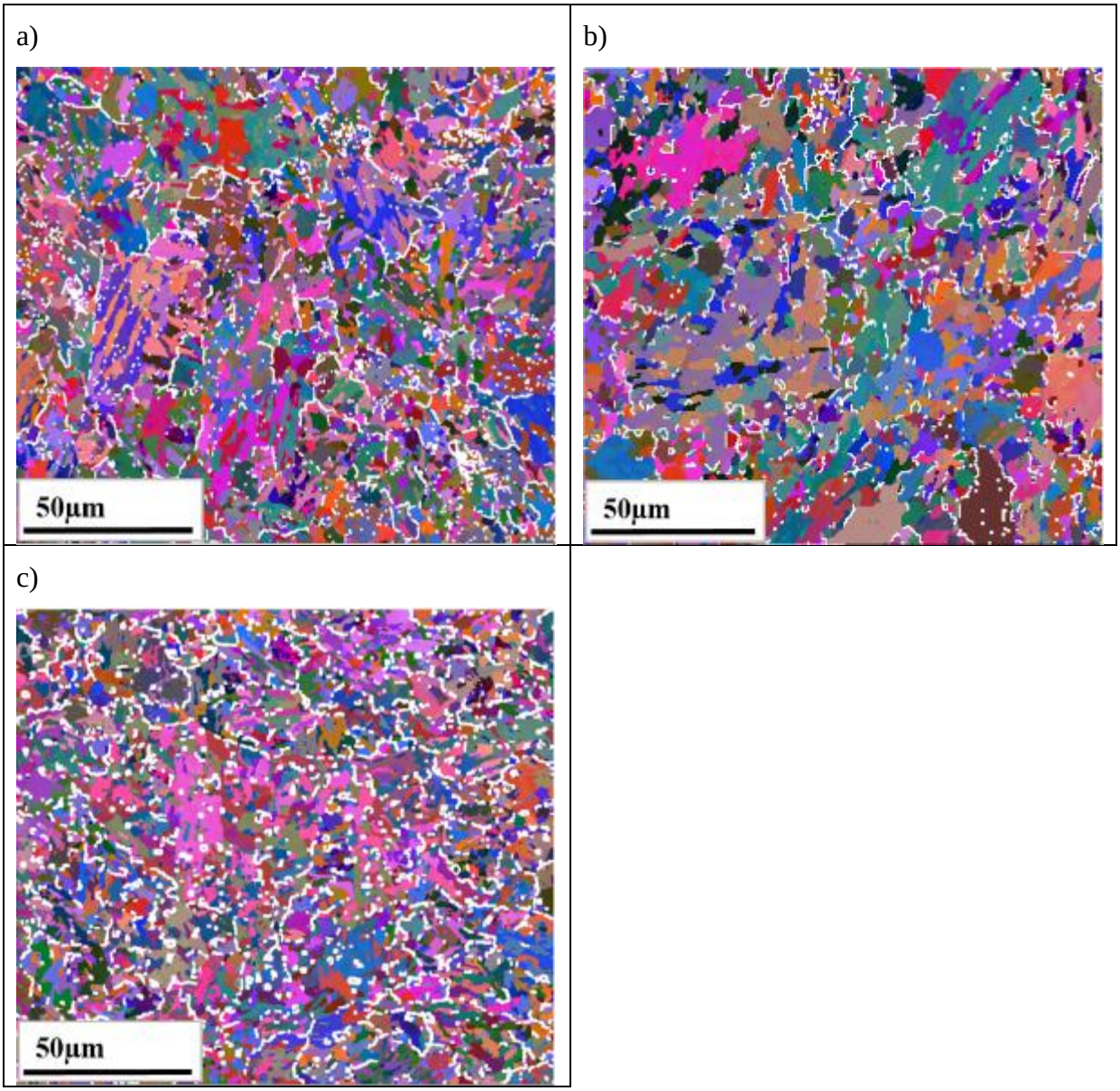

Figure 96: EBSD All Euler colour maps of the weld cycle simulated base material at 980˚C of a) X20_NDS, b) X20_MDS and c) X20_HDS

Figure 97, Figure 98and Figure 99 and show the microstructure of the as-received base material (left) and the microstructure after the weld thermal cycle simulation at 980˚C (right). As described in section 4.1.1, the base materials for X20_ND, X20_MD and X20_HD exhibit a typical tempered martensitic lath microstructure. The characteristics of this microstructure is highlighted by the ferritic sub-grain microstructure with carbides and carbonitrides forming at PAGBs and sub-grain boundaries[8]. This can be seen on the left in Figure 97, Figure 98 and Figure 99.

After the weld thermal cycle simulation of 980˚C and PWHT, the X20_NDS, X20_MDS and X20_HDS samples show a complete refinement of its microstructure. At a magnification of 50x, the microstructure shows very little similarity to the as-received base material. The

distinctive needle-like martensitic microstructure of X20 seems absent after the application of the weld thermal cycle simulation and PWHT[39].

At a magnification of 250x, the microstructure of the weld thermal cycle simulated base material shows evidence of the refined prior austenite grain boundaries (PAGBs). This is most visible for X20_NDS. X20_MDS and X20_HDS exhibit less of these features. The microstructure consists of very small grains.

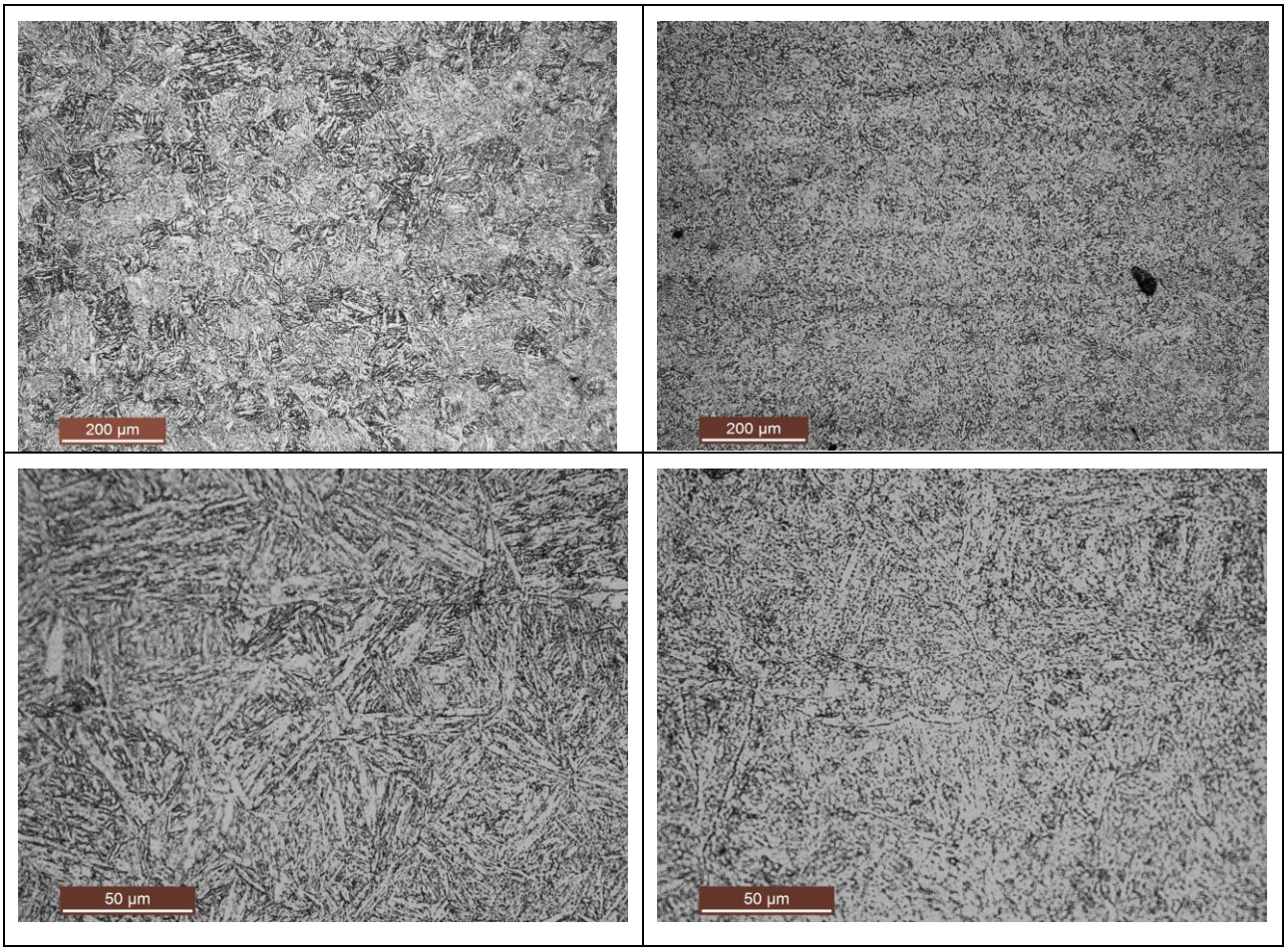

Figure 97: Optical micrograph of X20_ND base material at magnifications of 50x and 250x (left) and X20_NDS at magnifications of 50x and 250x (right)

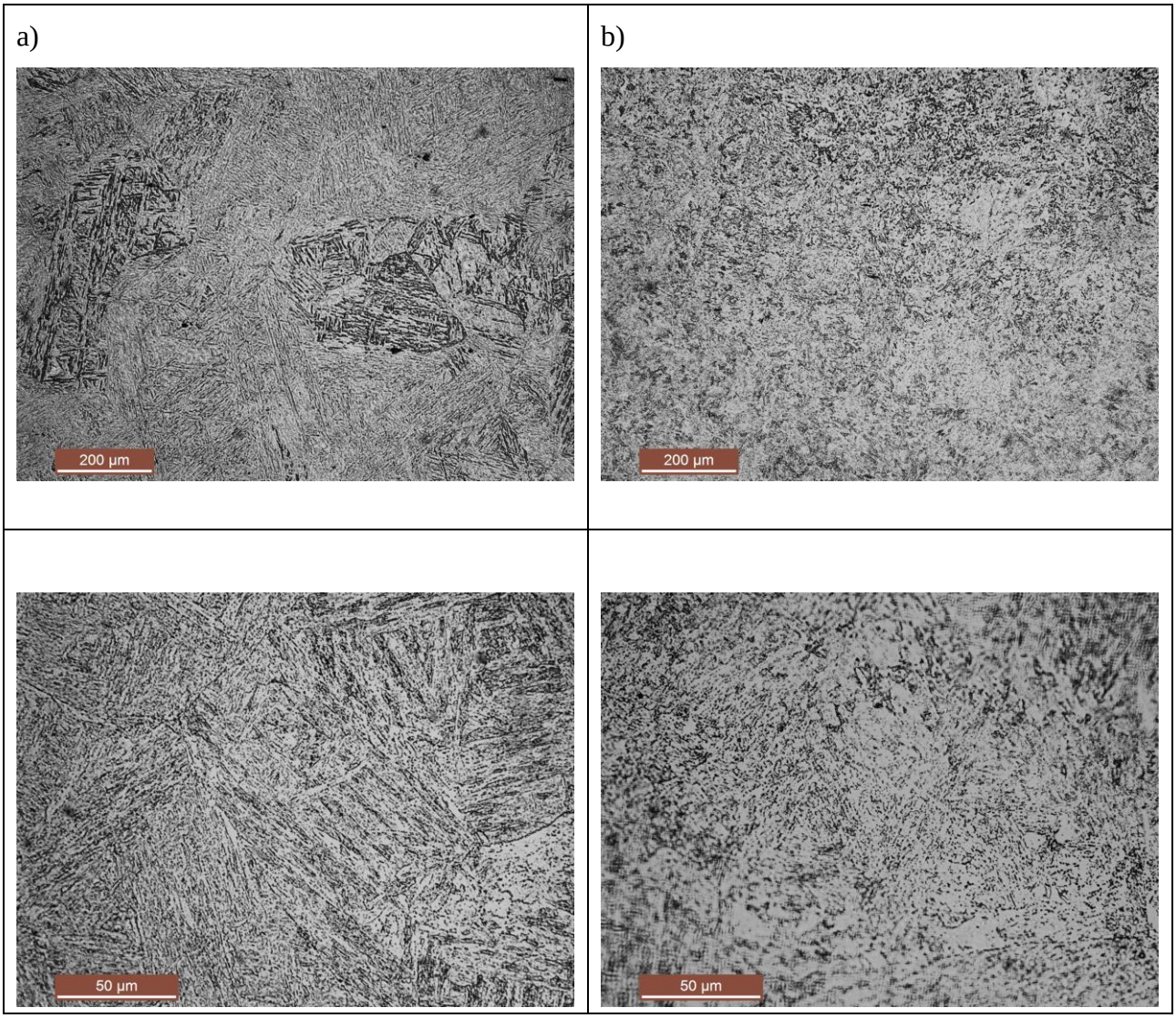

Figure 98: Optical micrograph of X20_MD base material at magnifications of 50x and 250x (left) and X20_MDS at magnifications of 50x and 250x (right)

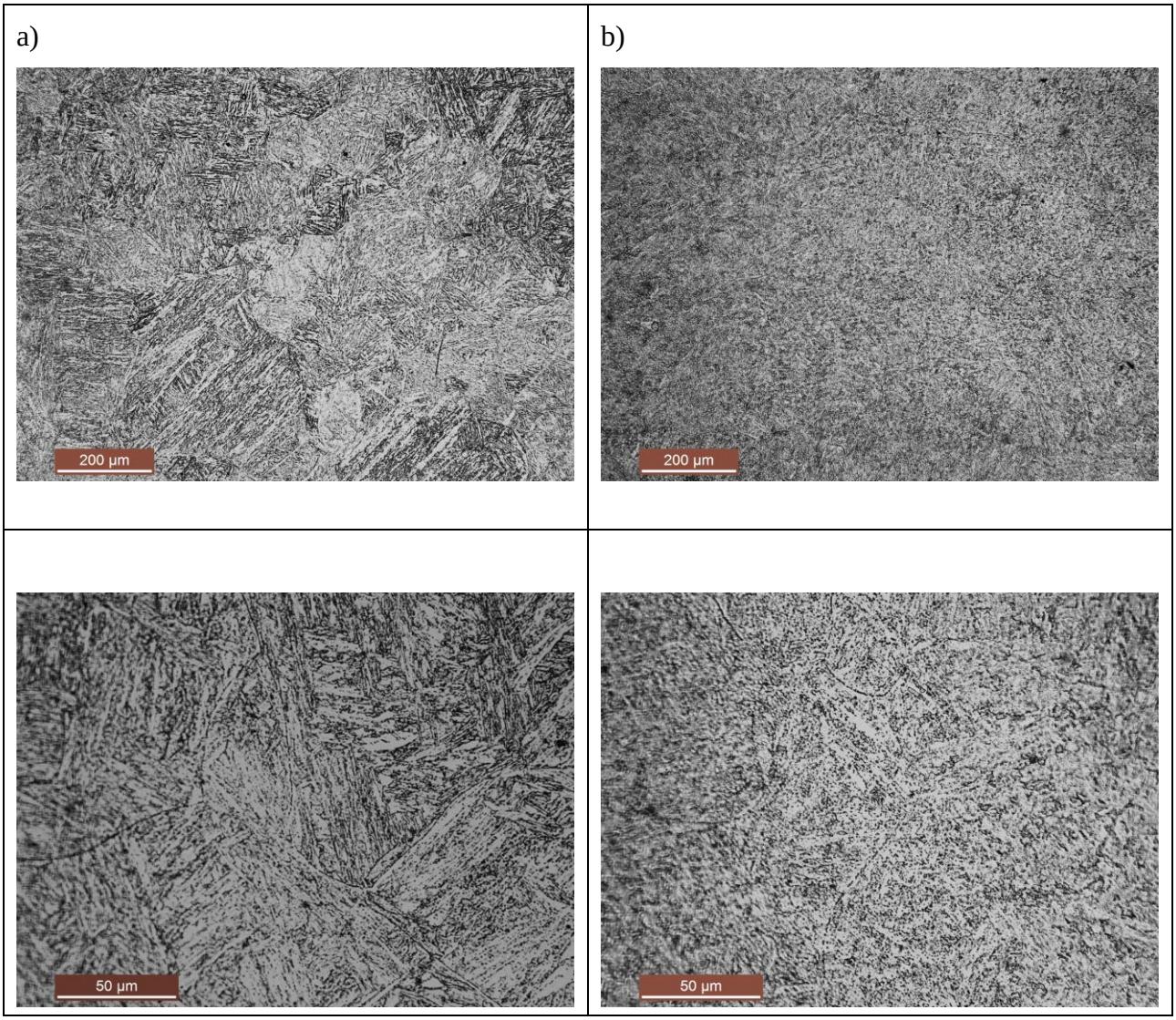

Figure 99: Optical micrograph of X20_HD base material at magnifications of 50x and 250x (left) and X20_HDS at magnifications of 50x and 250x (right)

4.3.2.1 Distribution of Uniform Microstructure in Simulated Weld Specimen

The quantification of the creep behaviour of weldments is much more challenging compared to the base material because of the heterogeneity of the microstructure in the weld metal, HAZ and adjacent base material in a narrow range[55]. A main reason for simulating the FGHAZ using the Gleeble®3800 is to produce a larger volume of the microstructure which exists in weldments. By producing a larger testing volume, the influence of the surrounding zones and therefore scatter would be reduced.

The hot zone created by the weld thermal cycle simulation at 980°C can be seen between the dashed black lines in Figure 100. The length of the hot zone is approximately 25 mm. Temperature control of the simulation is achieved by type K thermocouples. These have been placed in the middle of the length as indicated by the red dashed line. Microscopic analyses

are carried out on half of the sample based on the assumption that the temperature gradient is consistent on either side of the thermocouples

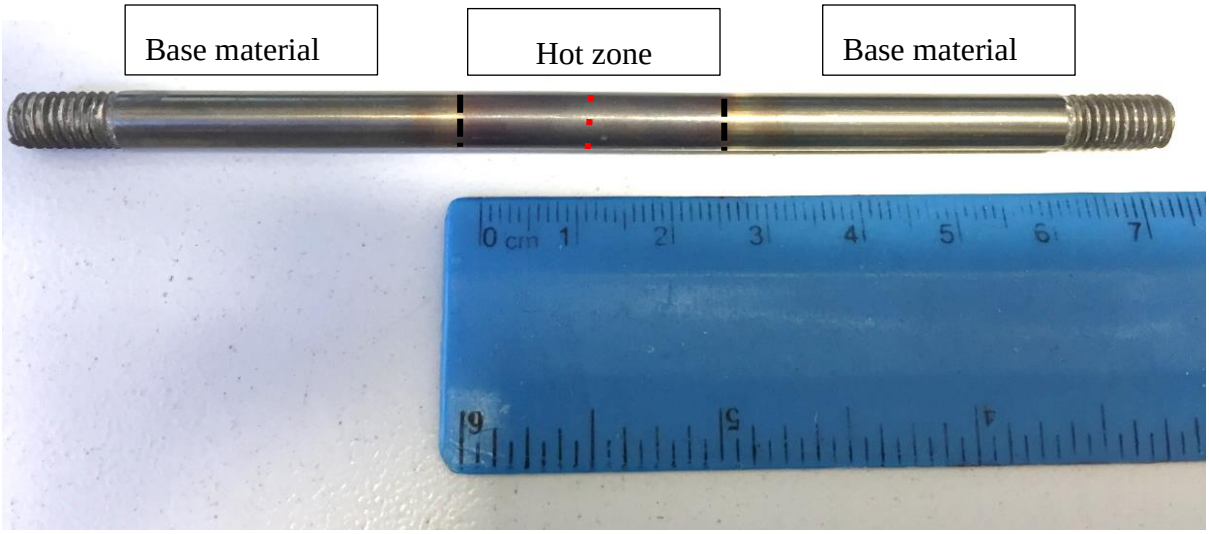

Figure 100: Test sample for weld thermal cycle simulation at 980°C showing the length of hot zone achieved

Figure 101 shows the area between the point of temperature measurement (red line), end of hot zone (black line) and the unaffected base material. Left of the black line in the micrograph shows the refined grain structure created by the weld thermal cycle simulation. Right of the black line is the unaffected base material. A clear distinction in appearance of microstructure can be seen between the FGHAZ created by the weld thermal cycle simulation and the unaffected base material.

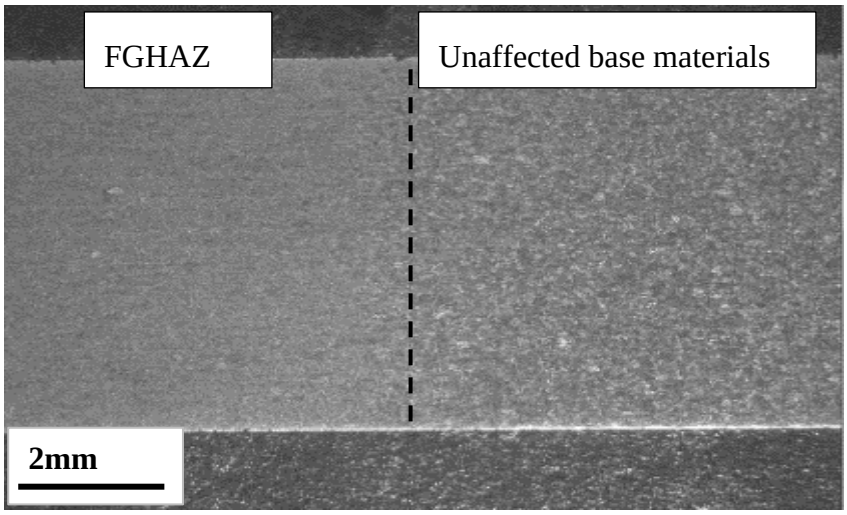

Figure 101: Transition between the FGHAZ and the unaffected base material of X20_ND

The FGHAZ is differentiated from the base material by the transition as shown in Figure 102. The refined microstructure of the FGHAZ can be seen on the left with the black dashed line representing the transition. The unaffected base material can be seen on the right of the dashed line.

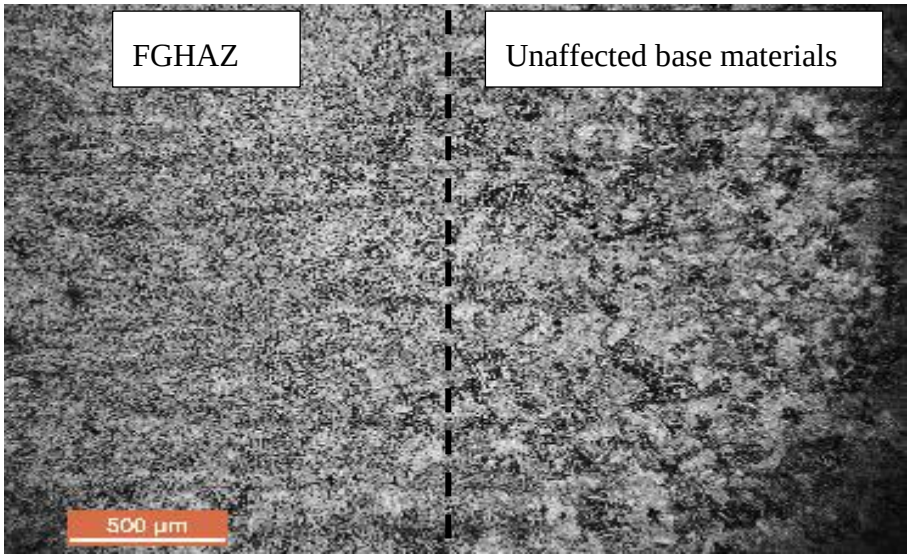

Figure 102: Transition between FGHAZ (left) and base material (right) of weld thermal cycle simulated sample

Estimations regarding the length of uniform microstructure (approximately 20mm) have been made using micrographs taken with the Leica EZ4D microscope. X20_NDS, X20_MDS and X20_HDS are analysed using the same method as all three materials have undergone the same weld thermal cycle simulation.

4.3.3 High Temperature Tensile Strength

Five samples of each base material were tensile tested at 610°C at a strain rate of $10^{-3}s^{-1}$. The yield strength and ultimate tensile strength results for each test are provided in Table 27. The values obtained for the yield and ultimate tensile strengths have a small scatter for each weld thermal cycle simulated base material. However due to this small scatter, the results seem representative for the yield and ultimate tensile strengths. The ultimate tensile strength for X20_NDS is slightly higher than that for X20_MDS; however, X20_HDS possesses the lowest ultimate tensile strength.

Table 27: Hot tensile strength of the weld thermal cycle simulation at 980°C base material

	Test Number	Yield Stress (MPa)	Ultimate Tensile Stress (MPa)
X20_NDS	1	169	210
	2	172	215
	3	195	221
	4	168	206
	5	180	230
Average		**176**	**216**
X20_MDS	1	165	208
	2	162	215
	3	130	153
	4	154	191
	5	156	236
Average		**153**	**200**
X20_HDS	1	156	204
	2	147	208
	3	135	
	4	127	155
	5	136	205
Average		**140**	**193**

4.3.4 Microhardness Profile

Microhardness tests were performed on weld thermal cycle simulated base material. A Vicker's microhardness testing machine was used with a testing load of 0.3kgf. The micro indentation location is exactly the same as that for the as-received base material. The values for the hardness are given below in Table 28. Within the specific region of the FGHAZ, the hardness was found to be uniform for each sample. It is evident that the hardness of the weld thermal cycle simulated material decreases with degree of the creep damage of the material. X20_NDS, as expected, possesses the highest hardness values followed by X20_MDS and X20_HDS.

Table 28: Vickers Hardness measurements for weld thermal cycle simulated base material

Matrix Position	**Vickers Hardness (HV0.3)**		
	X20_NDS	X20_MDS	X20_HDS
1	223	210	192
2	219	201	186
3	221	206	189
4	219	207	182
5	222	203	185
6	226	203	185
7	223	208	187
8	220	202	188
9	226	201	187
Average	222	205	187
Standard deviation	2.79	3.23	2.70

4.3.5 Discussion

Two sets of weld thermal cycle simulations were carried out. The first simulation was performed using a peak temperature of 1050°C. The peak temperature was derived from MatCalc simulations using the chemical composition and equilibrium conditions for the calculations. A key characteristic for the FGHAZ is the partial dissolution of precipitates and small grains of austenite. Hence, in achieving a peak temperature for the simulation, temperatures should be just above the A_{c3} temperature. The A_{c3} temperature is representative of the temperature at which the transformation of ferrite to austenite is complete. The MatCalc calculation yielded an A_{c3} temperature of 820°C. In conjunction with obtaining an A_{c3}, considerations had to be taken into account for the dissolution of $M_{23}C_6$ precipitates as well. The MatCalc calculation yielded 940°C for the dissolution of $M_{23}C_6$ into the matrix. Therefore, the final peak temperature for the first weld thermal cycle simulation was set at 1050°C. This took the A_{c3} temperature and precipitate dissolution temperature into account.

The single cycle simulation was carried out with a dilatometer attached to the sample during the test. This was carried out to verify the A_{c3} temperature achieved by the MatCalc calculation. A key outcome from the first simulation at 1050°C concluded that the A_{c3} temperature from the MatCalc calculation was too low. Dilatometry results showed that the A_{c3} temperatures for X20_ND, X20_MD and X20_HD were 966°C, 940°C and 935°C respectively. Secondly, EBSD analysis of the microstructure revealed that the PAGB size obtained from the simulation did not correspond to that of the FGHAZ microstructure extracted from the weldments. The microstructure was refined slightly as seen by comparison of the base material in Figure 103 a) to Figure 103 b). The refined microstructure with PAGB

sizes > 50µm could possibly represent the CGHAZ. Therefore the peak temperature was too high as the CGHAZ exists at temperatures much higher than the A_{c3}. These two findings provided sufficient evidence that the first simulation at 1050°C did not succeed in producing the FGHAZ microstructure.

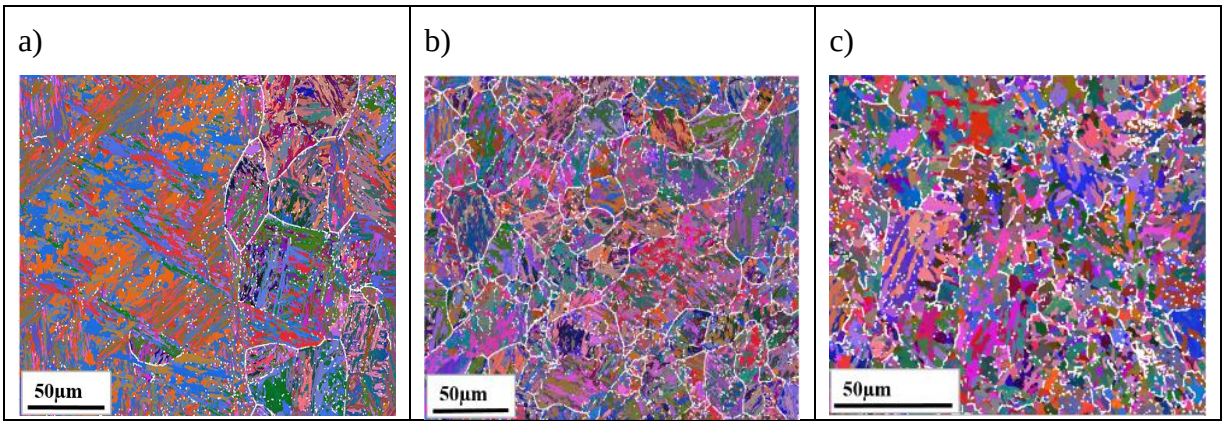

Figure 103: EBSD All Euler colour maps for a) X20_ND, b) simulated at 1050°C and c) simulated at 980°C

The second simulation peak temperature had to be below 1050°C yet above the A_{C3} temperatures obtained from the dilatometry experiments. By taking a temperature slightly higher that the highest A_{c3} obtained from the dilatomety results, the next peak temperature was set at 980°C. EBSD analysis carried out on the samples simulated at 980°C showed much more refinement of the microstructure (Figure 103 c)). Comparison of PAGB size of the simulated microstructure to that of the extracted FGHAZ for the weldment showed that the microstructure obtained from simulation is very comparable to that of the FGHAZ for the weldment. PAGB sizes for the simulation are as small at 5µm corresponding to the PAGB size of the FGHAZ in the weldment (4 µm).

In addition to achieving a microstructure similar in PAGB size by Gleeble simulation to that of an actual FGHAZ for a weldment, the length of uniform microstructure created by the simulation is also to be noted. The FGHAZ in a weldment can be as narrow as 1.5mm. This width is insufficient for creep testing and further experimental work as the area is constrained by the CGHAZ and base material. Hence, simulation allows for a larger volume of the FGHAZ microstructure to be produced. The European Creep Collaborative Committee [43] stated that the length of uniform microstructure achieved by Gleeble simulation is about 10mm. Optical microscopy was used to investigate the length of uniform microstructure achieved by the simulation. The “hot zone” is the section of sample which lies between the grips during the simulation in the Gleeble. The volume of the FGHAZ lies within the hot zone. A cross-section of the rod sample revealed that the fine microstructure representative of the FGHAZ is approximately 20mm long. Therefore, by a weld thermal cycle simulation, a length of uniform microstructure was produced and approximately 13 times greater in volume than the FGHAZ of a weldment.

Klenk et al [12] suggested that the influencing effects on the behaviour of a weld in a component are:

- Differences in strength between base and weld material
- Different microstructures in the HAZ
- Development of zones near the fusion line with change in chemical composition due to diffusion
- Additional thermal stresses due to different dilation coefficients
- Stress enhancement due to different creep rates in constituent materials and
- Residual stresses due to the welding and manufacturing processes

Along with the effects mentioned above, the effects of welding can be seen in microstructural and mechanical properties of the material. Vickers hardness measurements were conducted on the base material before and after the weld thermal cycle simulation and PWHT. The load used was 0.3kgF along the cross-section of the sample. Figure 104 shows the hardness of the base material in its as-received state and after the weld thermal cycle simulation and PWHT. The hardness of X20_ND decreased by an average of 15% after the application of the weld thermal cycle simulation and PWHT. X20_MD and X20_HD decreased in hardness by 15% and 11% respectively.

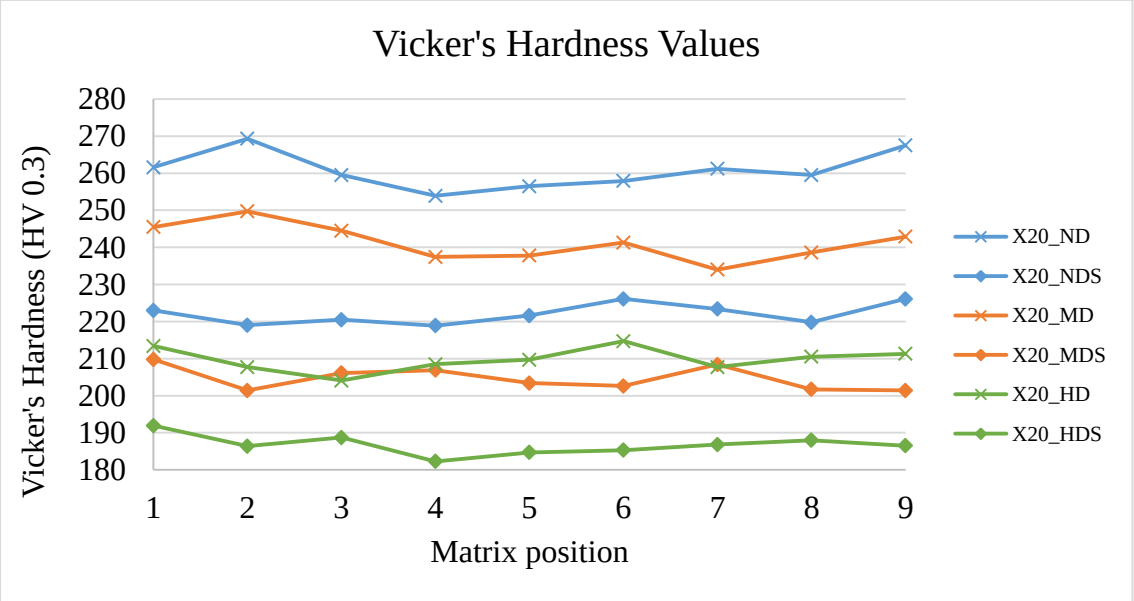

Figure 104: Graphical representation of the impact of weld thermal cycle simulation on hardness

As hardness of the material is the resistance to plastic deformation, a decrease in hardness could possibly imply that the ability of the base materials after simulation to resist plastic deformation has also decreased. The microstructure of weld thermal cycle simulation sample possesses very small PAGBs as shown in Figure 105 (right). This characteristic makes it unfavourable for creep resistance as the PAGBs occur numerously. The effect of numerous small PAGBs results in a very high diffusion coefficient. The nature of creep testing or

consequently, in service conditions, induce multi axial stresses in the weldment. The combination of a high diffusion coefficient and effects of multi axial stresses causes the rate of void formation to increase. This phenomenon is not favourable for the creep resistance of the material; hence a decrease in hardness can be observed.

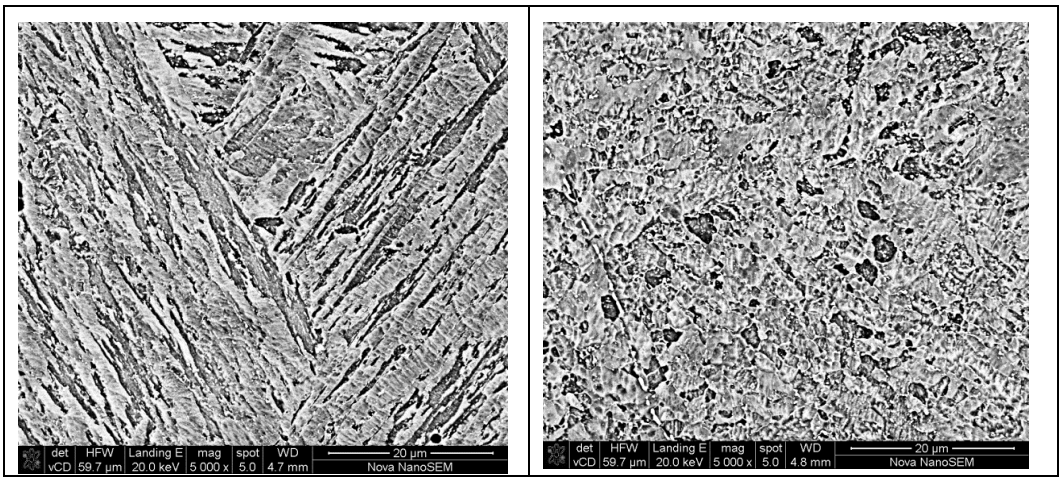

Figure 105: SEM secondary electron image of the microstructure of X20_MD (left) and X20_MDS (right)

The effect of the weld thermal cycle simulation on the hot tensile properties of the base materials is shown in Figure 106. Once again, it can be seen that the hot tensile strength of X20_ND and X20_MD are similar. The application of the weld thermal cycle and PWHT reduced the hot tensile strength of X20_NDS, X20_MDS and X20_HDS by 45%, 47% and 38% respectively. This impact is significant as a large percentage of remaining life of the material is consumed by the application of a weld thermal cycle. The significant decrease in hot tensile properties of the as-received base material after a weld thermal cycle simulation can be seen.

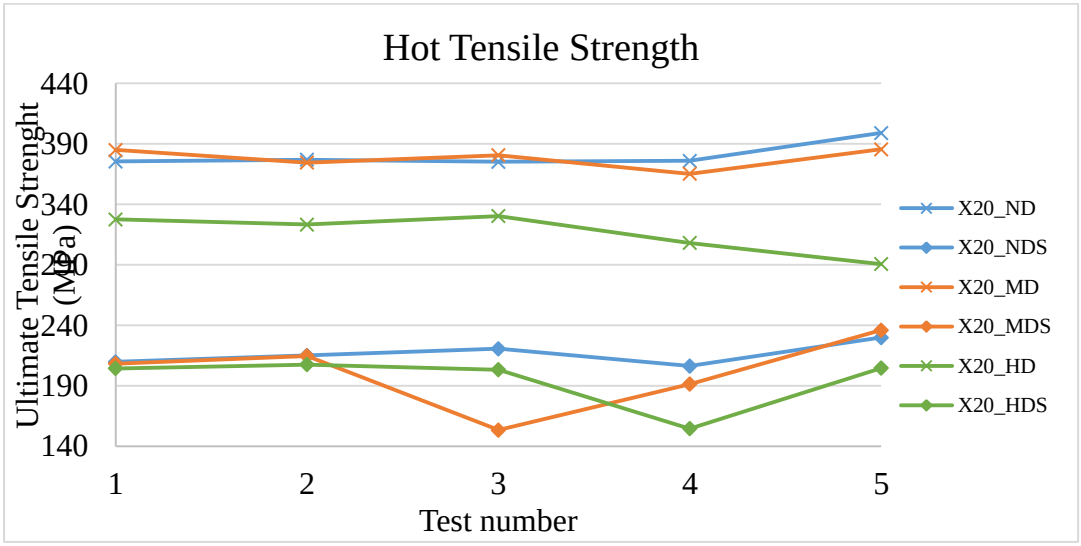

Figure 106: Graphical representation of the impact of weld thermal cycle simulation on hot tensile strength

5. Conclusion

5.1Summary

ERIC (Eskom Research and Innovation Centre) provided three base materials (X20_ND, X20_MD and X20_HD). Of the three base materials, two weldments were created (X20_ND to X20_MD and X20_ND to X20_HD). The amount of creep exposure in the base materials were first classified at ERIC by the surface replication method. In order to verify the surface replication method with more advanced microscopic and mechanical methods, the base material was examined for microstructural and mechanical properties in the course of this study. The key finding for the base materials are that the mechanical properties decrease with increased operational temperature with which the material is exposed to for the in-service period. This finding was determined by microhardness testing and hot tensile strength testing. Also, by microstructural observations, the amount of creep voids increased with increased temperature exposure for the in-service period.

The weldments were creep tested at a constant temperature and different stresses. Weldment 1 (X20_ND to X20_MD) performed better in terms of test duration than weldment 2(X20_ND to X20_HD). A key finding in the creep tests was that all samples failed in the creep exposed material (X20_MD and X20_HD) on the existing creep side. The areas of failure in the creep test specimens were the fine grain heat affected zones (FGHAZ). As the FGHAZ of creep exposed weldments was most susceptible to failure in this study, this microstructural zone was replicated in greater volume using the Gleeble®3800. This was done to investigate the impact of welding on prior creep exposed material, as well as to establish larger microstructural volumes of the FGHAZ for further testing and research.

The following points below provide more detailed findings for this study:

- Optical microscopy and SEM have been successfully used to determine the microstructural properties of the as-received base materials for degrees of creep exposure. The assessment of creep void density in virgin X20 and X20 exposed to 128 000 hours and 208 000 hours of in service operation show that creep voids are dependent on temperature rather than hours of service,
- The use of more advanced SEM provides validation of the creep damage reported by surface replication and optical microscopy studies conducted at ERIC. However, SEM analysis provides greater detail with regards to the size of creep voids present in the as-received base material,
- Vicker's micro hardness and hot tensile testing assist is classifying the creep damaged state of as-received base material. The comparison of hardness and tensile strength of

virgin X20_ND to that of creep exposed X20_MD and X20_HD show the reduction of these properties with exposure to temperature.

- The combination of microstructural analysis and mechanical testing confirm that X20_ND and X20_MD have similar microstructural features and mechanical properties. However, high operating temperatures have impacted on X20_HD which has significantly deteriorated microstructural and mechanical properties.

- Creep testing of weldments made from X20_ND and X20_MD (weldment 1) and X20_ND and X20_HD (weldment 2) show failure in the HAZ of the creep exposed material when subjected to 610˚C and 63, 80 and 90MPa.

- The creep testing performance of weldment 1 exceeded that of weldment 2. The creep rupture times for both welds confirm that the amount of prior creep damage does impact the duration of creep exposure. Weldment 2, containing X20_HD, failed sooner than weldment 1. Both welds confirm that prior damaged X20 subjected to the heat cycling of welding will cause failure in the weakest region when tested at elevated temperatures.

- Optical microscopy has been successfully used to identify failure in the HAZ of the creep exposed material. The fracture surface lies closer to the base material confirming failure in the ICHAZ or FGHAZ.

- Investigations done on the fracture surface also add to the evidence for location of fracture. SEM imaging highlight the small grains and cup-and-cone features associated with a ductile fracture. The large amount of voids found at the bottom of the dimples also confirm that the failures are as a result of creep cavitation

- SEM and optical microscopy have been used to show void coalescence and extensive void damage closest to the area of failure. SEM shows the difference between the fine-grained, void accumulated fracture area and the unaffected base/weld material. The size and quantity of voids at the fracture area are greater than in base/weld metal. Analysis of every test specimen for these microstructural features provide a great level of confidence in the localisation and reasons for failure.

- EBSD mapping done on the weldments before creep testing helped acquire the microstructure for the FGHAZ by hardness testing. EBSD mapping thereafter, was completed close to the fracture surface of the creep tested samples to conclude that the samples did fracture in the FGHAZ by comparison of microstructure to the FGHAZ acquired from the weldments.

- The evidence provided by optical microscopy, SEM and EBSD conclude that mis-matched creep strength material (strong weld metal and weaker prior creep damaged material) will result in type IV cracking when subjected to accelerated creep testing conditions.

- By weld thermal cycle simulation, the FGHAZ was replicated in larger volume for further testing. Thermo-mechanical Gleeble 3800 provided the means for carrying out the simulation.
- The refinement of the microstructure required to simulate the FGHAZ is dependent on the peak temperature. In turn, the peak temperature is dependent on the A_{C3} temperature of the material. Dilatometry and MatCalc thermal equilibrium simulation were successful in determining the A_{C3} of all the as-received material.
- The refinement of grain structure was carried out in two steps. First at T_P = 1050°C and then at T_P=980°C. Successful simulation was achieved by T_P = 980°C
- By using the Gleeble®3800, the weld thermal cycle simulation achieved a uniform length of simulated microstructure of 20mm.
- The microstructure achieved by the weld thermal cycle simulation shows refinement of the PAGBs with the existing PAGBs remaining and the new PAGBs forming.
- A decrease in Vicker's hardness and hot tensile strength resulted after the application of the weld thermal cycle simulation and PWHT.

6. Recommendations

- Interrupted long term creep tests can be carried out on weldments 1 and 2 to investigate the behaviour/formation of voids in the FGHAZ of creep aged repair welded joints
- Long term creep tests can be carried out on the creep aged base material (X20_MD and X20_HD) to compared the creep strength of the weldments to the base material
- Investigate the effect of varying PWHT temperatures on mechanical properties of FGHAZ simulated samples
- Conduct long term creep tests on FGHAZ simulated samples

7. Appendices

Appendix 1 **As-received Base Material**

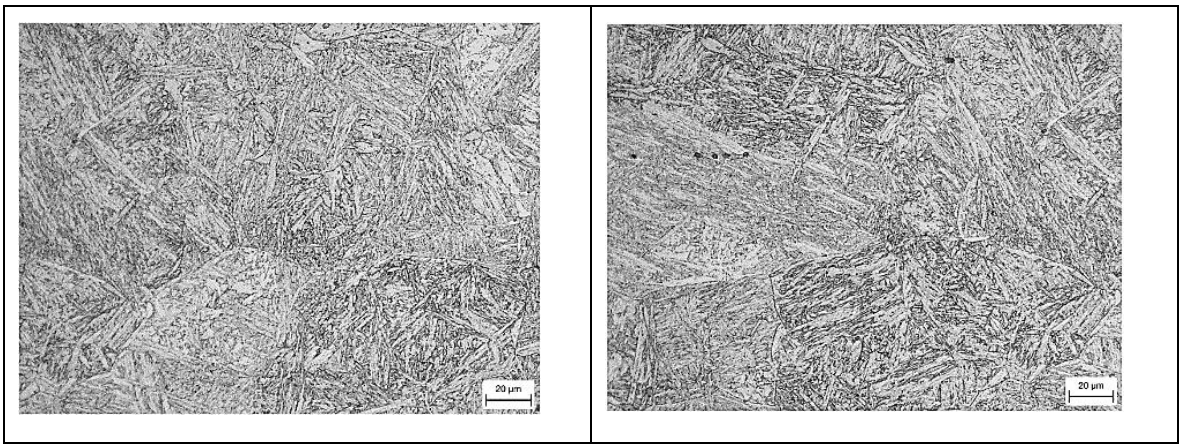

Figure 107: Base material X20_ND

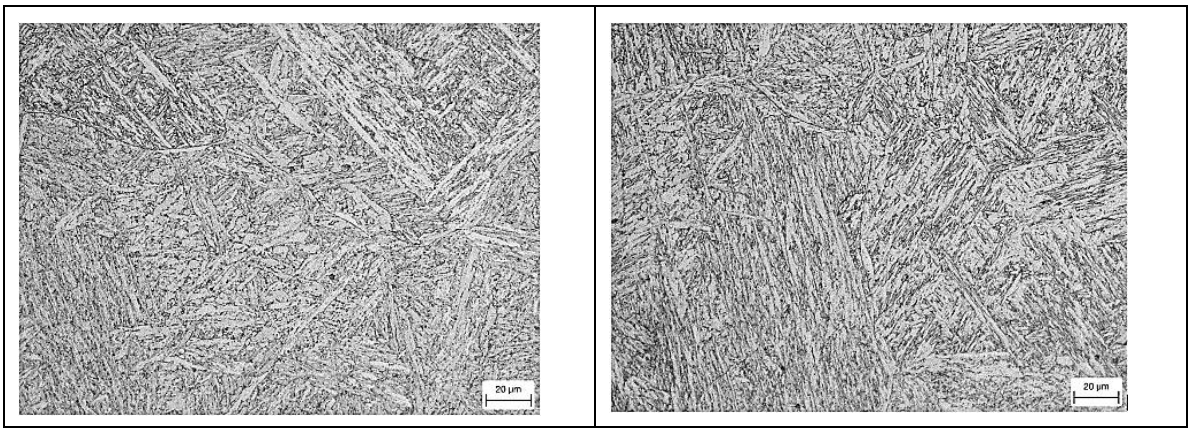

Figure 108: Base material X20_MD

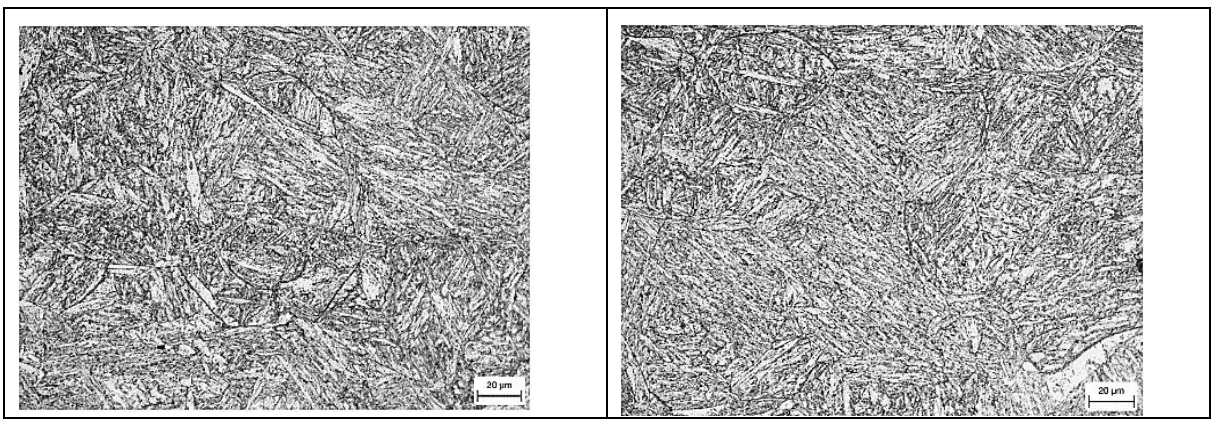

Figure 109: Base material X20_HD

Appendix 2 **Fracture Surfaces**

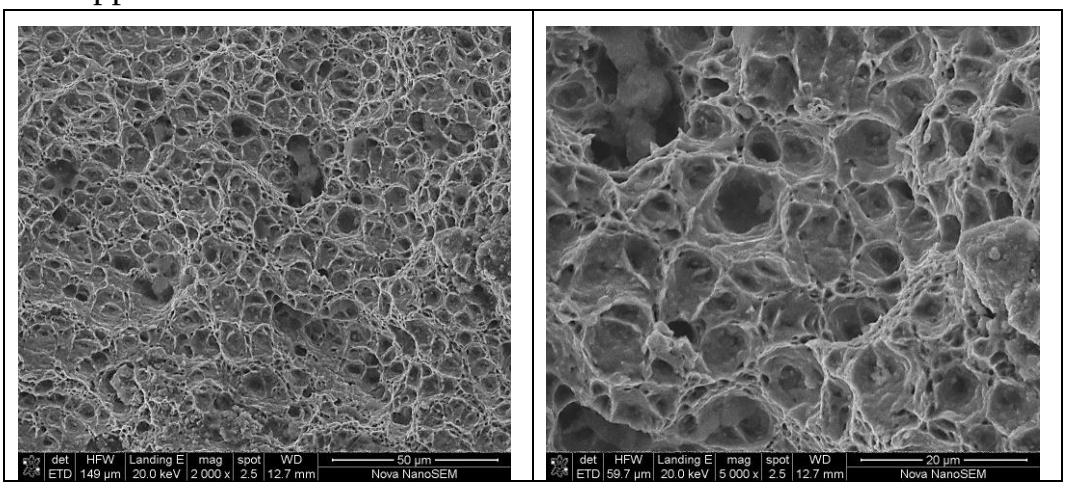

Figure 110: Fracture surfaces of test 1 A GS at magnifications of 2000x (left) and 5000x (right)

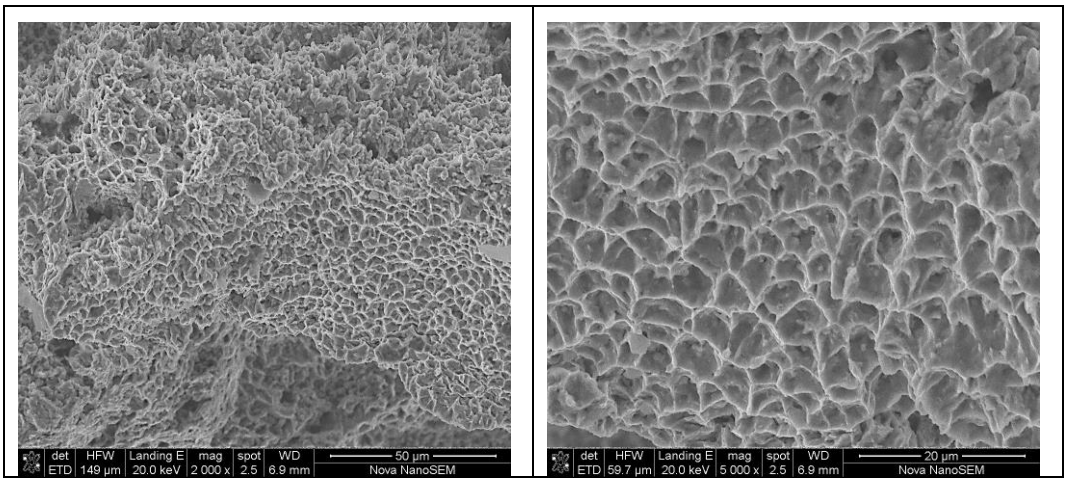

Figure 111: Fracture surfaces of test 1 B GL at magnifications of 2000x (left) and 5000x (right)

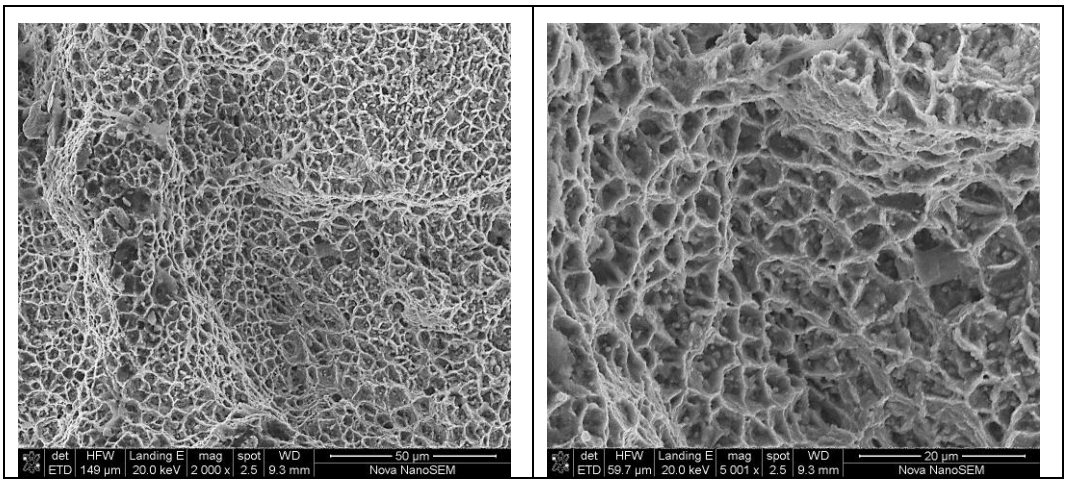

Figure 112: Fracture surfaces of test 1 B GS at magnifications of 2000x (left) and 5000x (right)

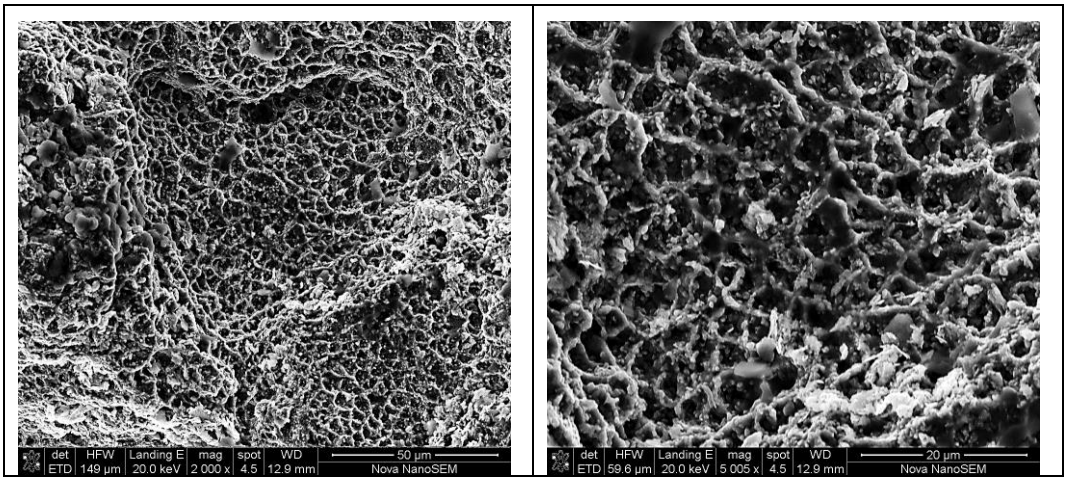

Figure 113: Fracture surfaces of test 2 A GL at magnifications of 2000x (left) and 5000x (right)

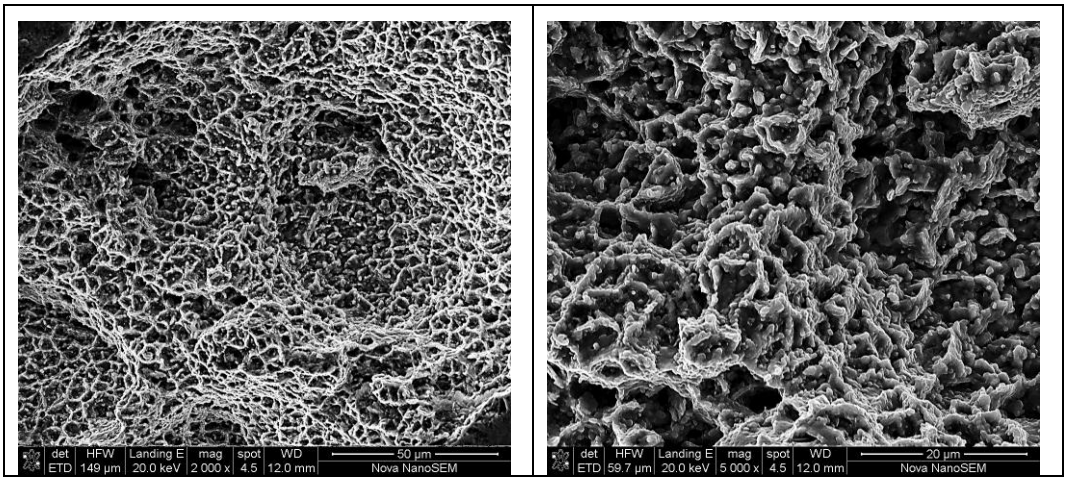

Figure 114: Fracture surfaces of test 2 A GS at magnifications of 2000x (left) and 5000x (right)

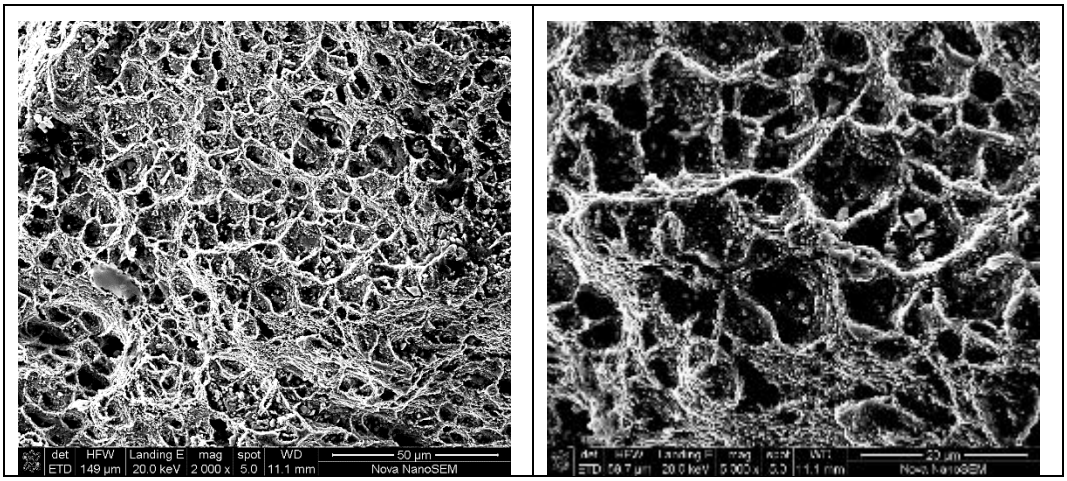

Figure 115: Fracture surfaces of test 2 B GL at magnifications of 2000x (left) and 5000x (right)

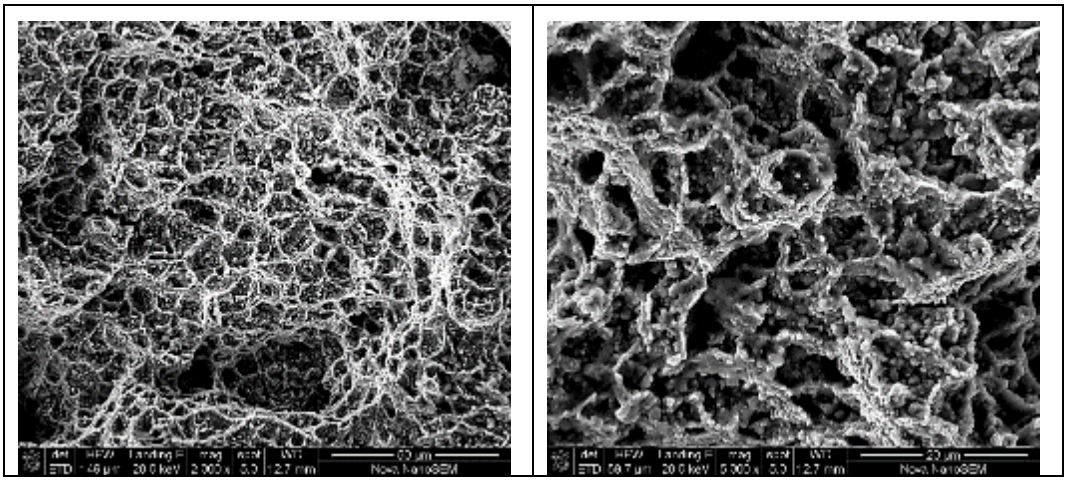

Figure 116: Fracture surfaces of test 2 B GS at magnifications of 2000x (left) and 5000x (right)

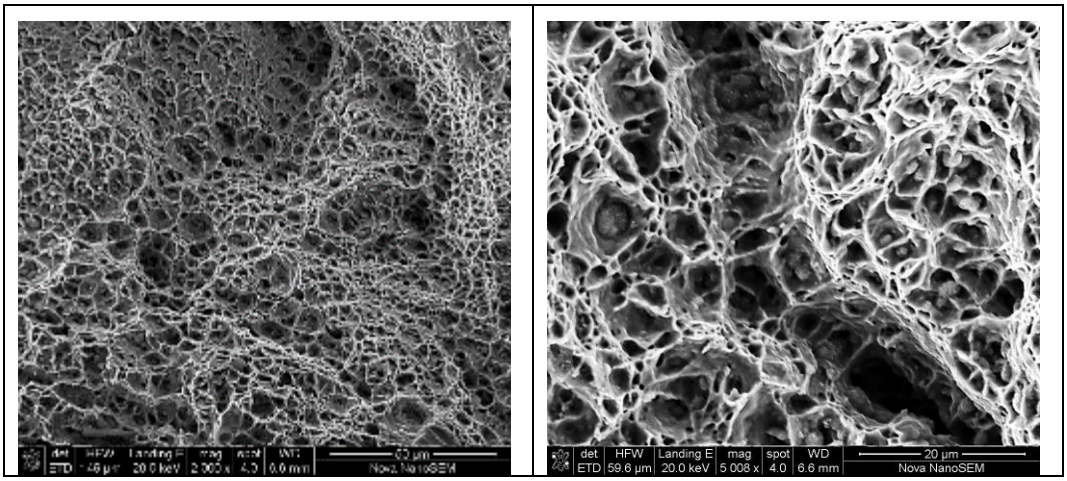

Figure 117: Fracture surfaces of test 3 A GL at magnifications of 2000x (left) and 5000x (right)

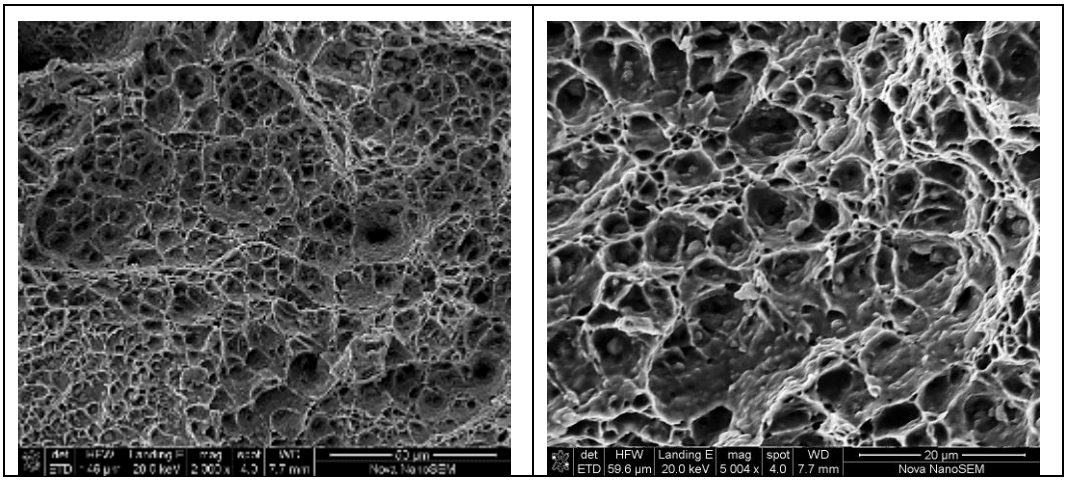

Figure 118: Fracture surfaces of test 3 A GS at magnifications of 2000x (left) and 5000x (right)

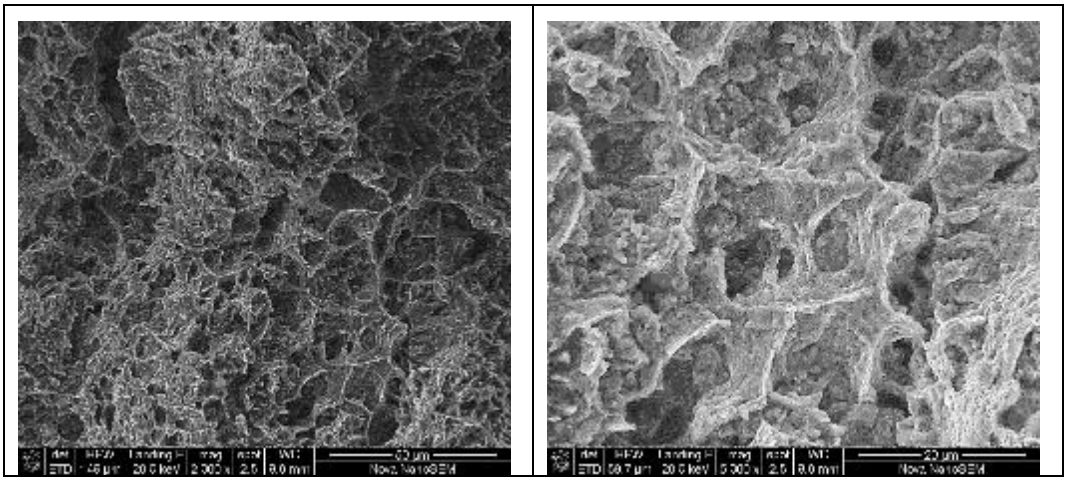

Figure 119: Fracture surfaces of test 4 A GL at magnifications of 2000x (left) and 5000x (right)

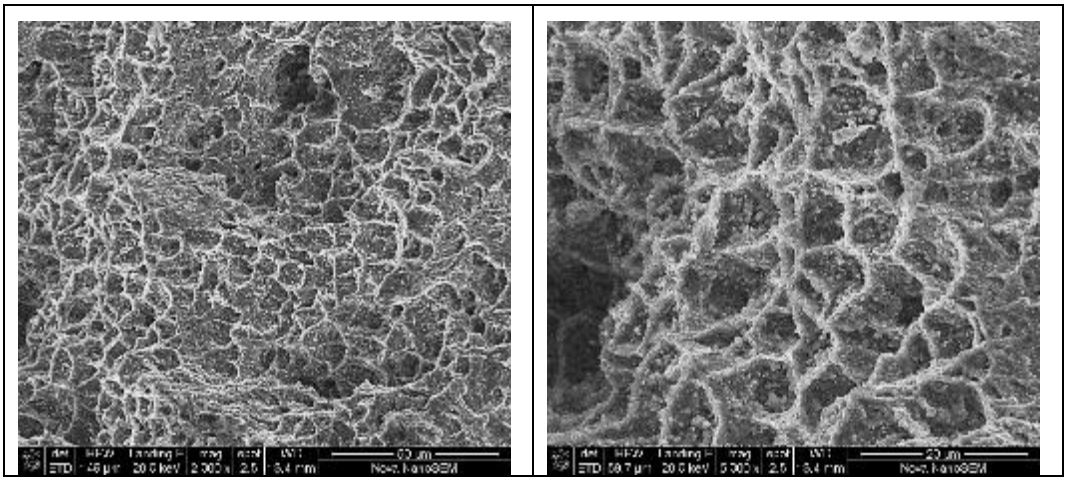

Figure 120: Fracture surfaces of test 4 A GS at magnifications of 2000x (left) and 5000x (right)

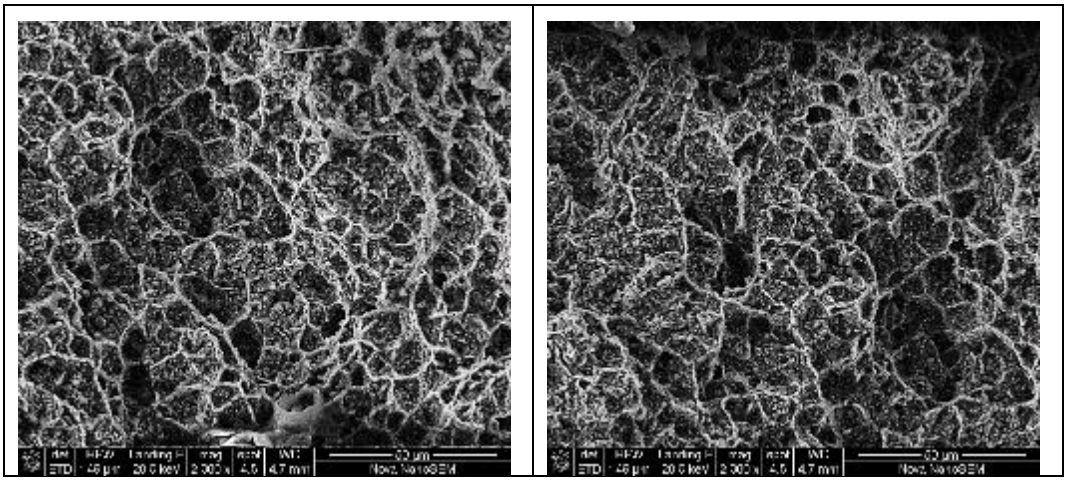

Figure 121: Fracture surfaces of test 4 B GL at a magnification of 2000x

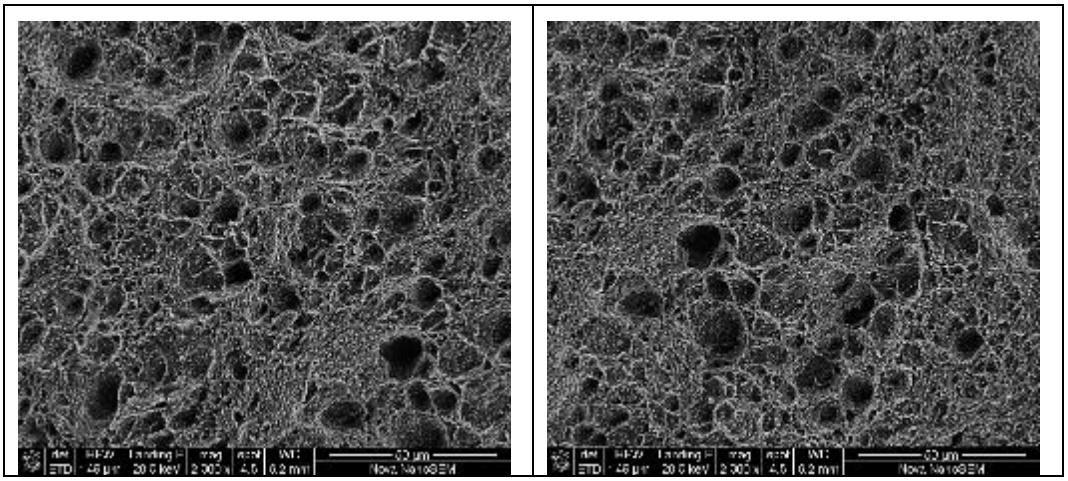

Figure 122: Fracture surfaces of test 4 B GS at a magnification of 2000x

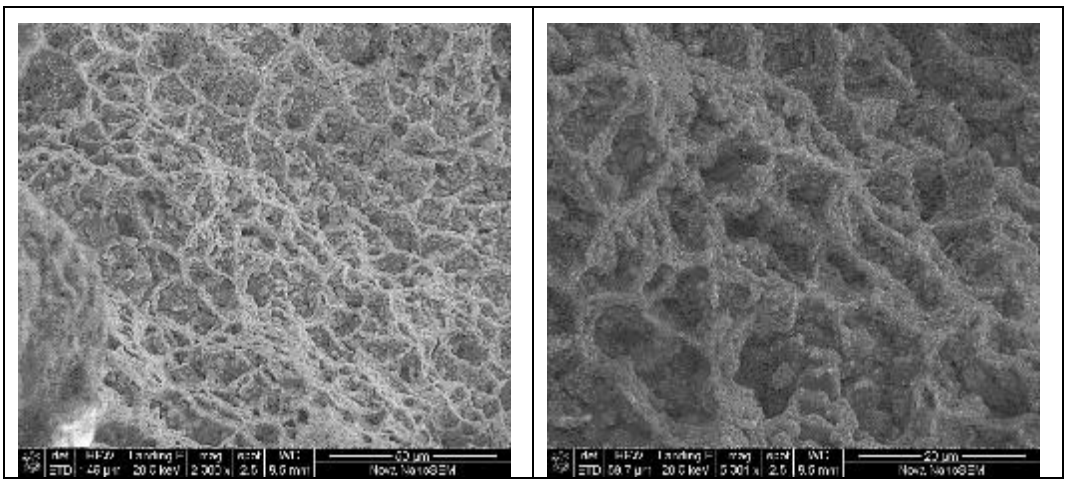

Figure 123: Fracture surfaces of test 5 A GL at magnifications of 2000x (left) and 5000x (right)

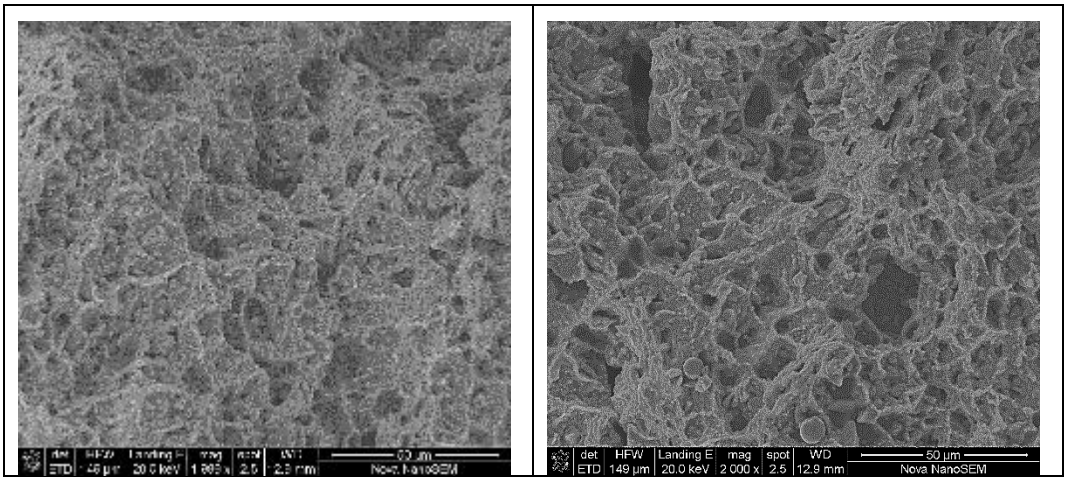

Figure 124: Fracture surfaces of test 5 A GS at a magnification of 2000x

Appendix 3 **Void Occurrences**

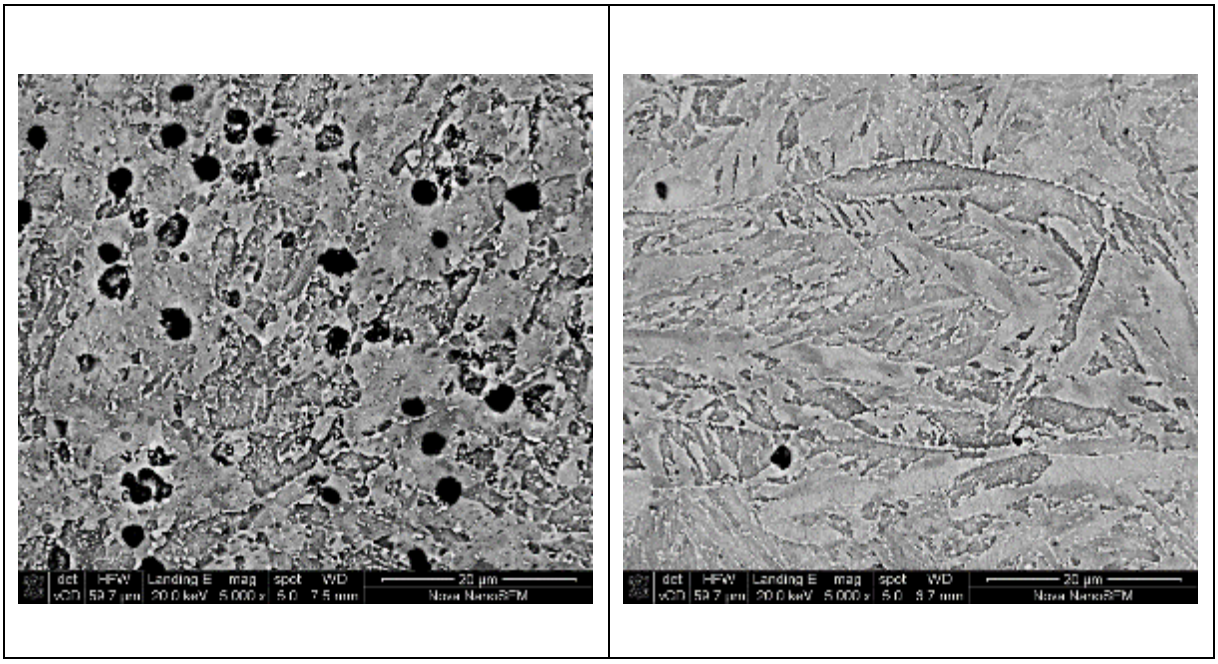

Figure 125: Backscatter SEM images of the rupture surface (left) and base/weld material (right) for test 1 A

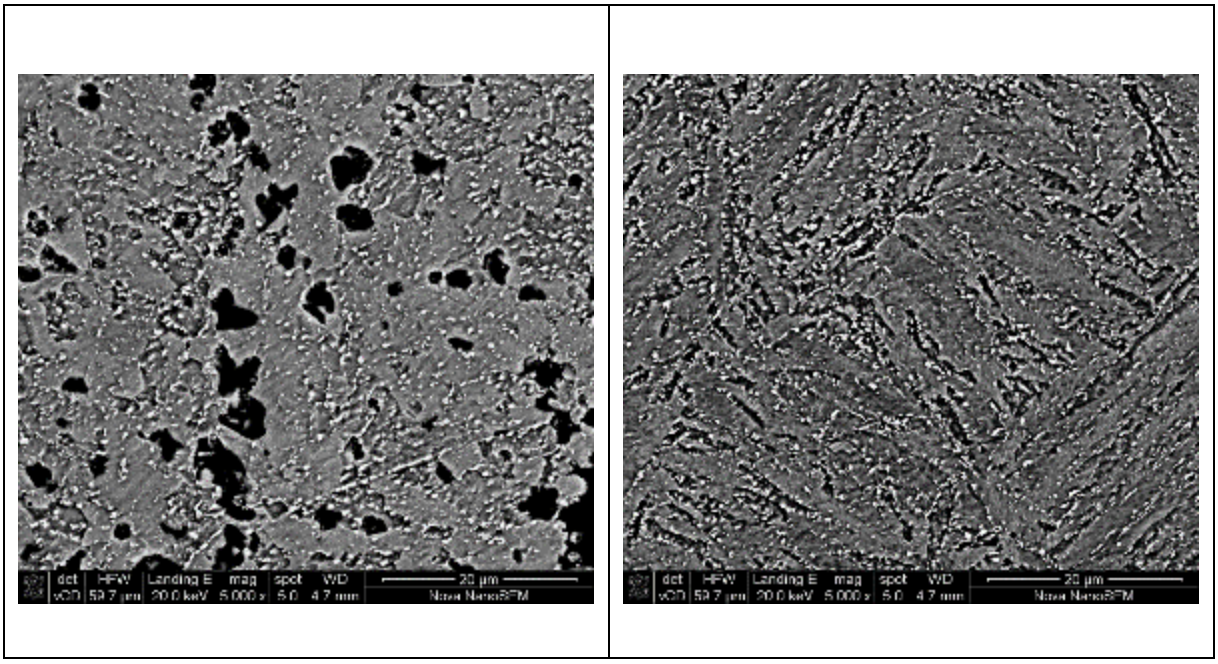

Figure 126: Backscatter SEM images of the rupture surface (left) and base/weld material (right) for test 1 B

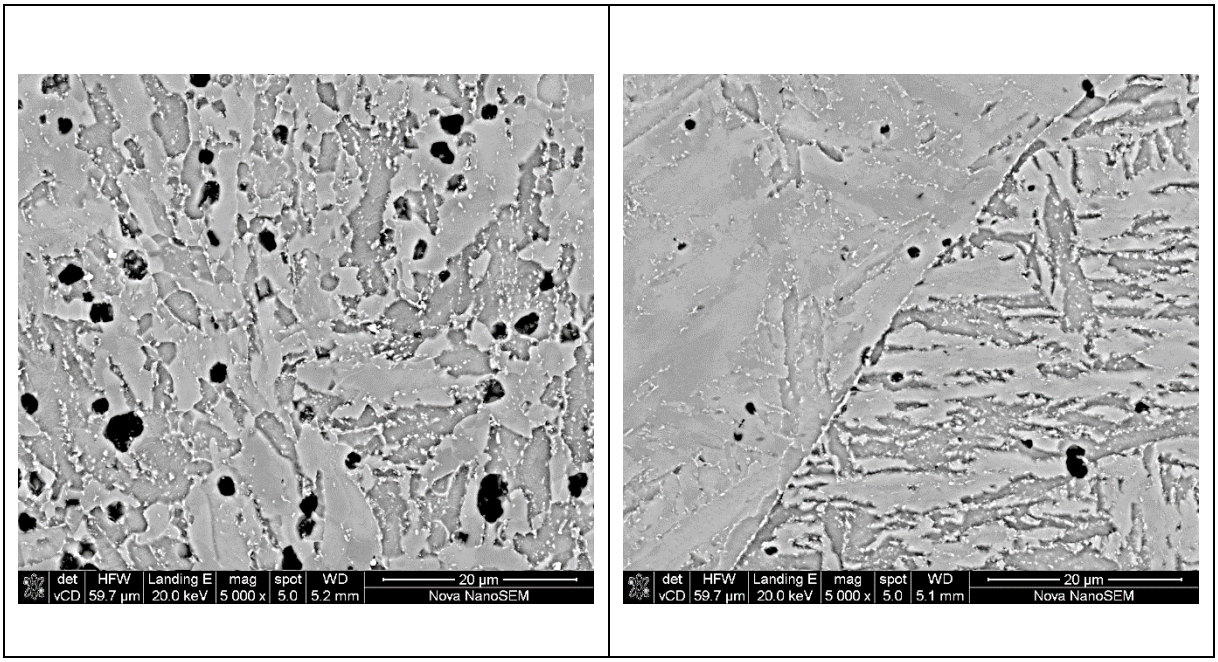

Figure 127: Backscatter SEM images of the rupture surface (left) and base/weld material (right) for test 2 A

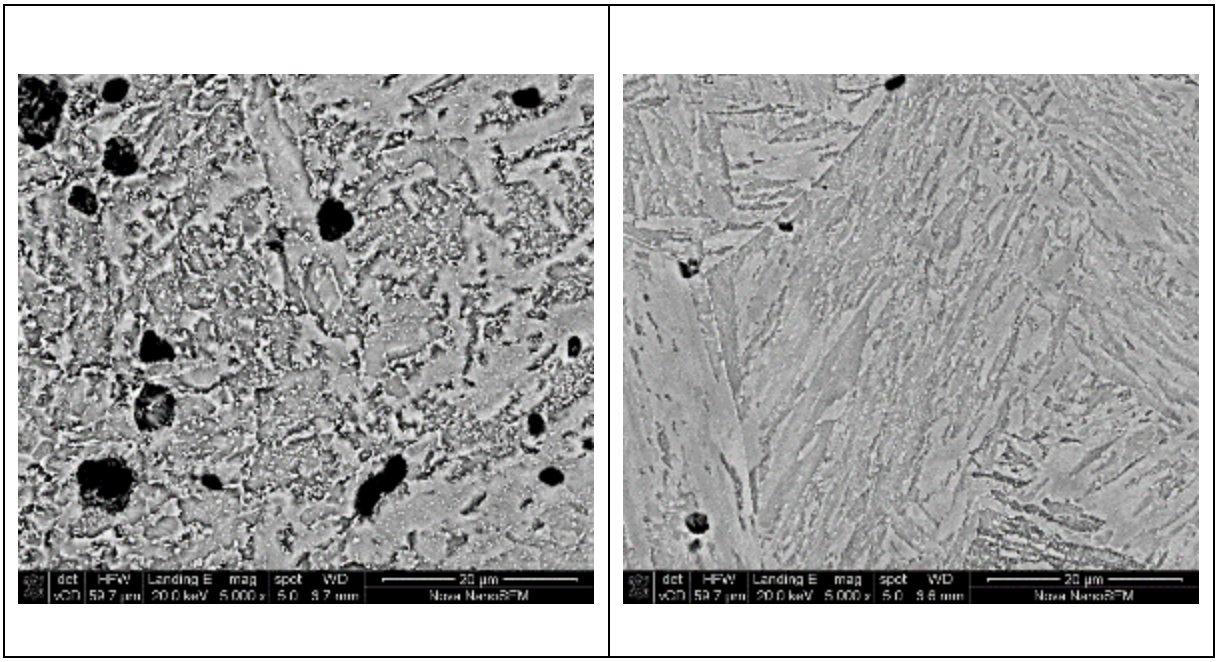

Figure 128: Backscatter SEM images of the rupture surface (left) and base/weld material (right) for test 2 B

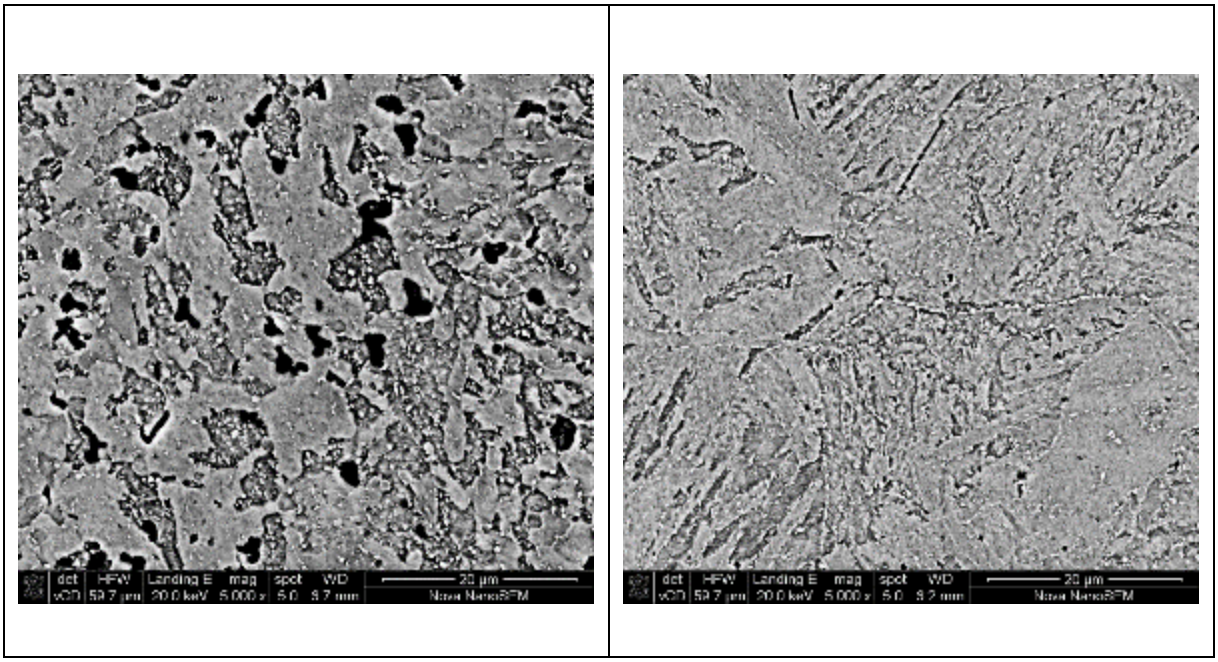

Figure 129: Backscatter SEM images of the rupture surface (left) and base/weld material (right) for test 3 A

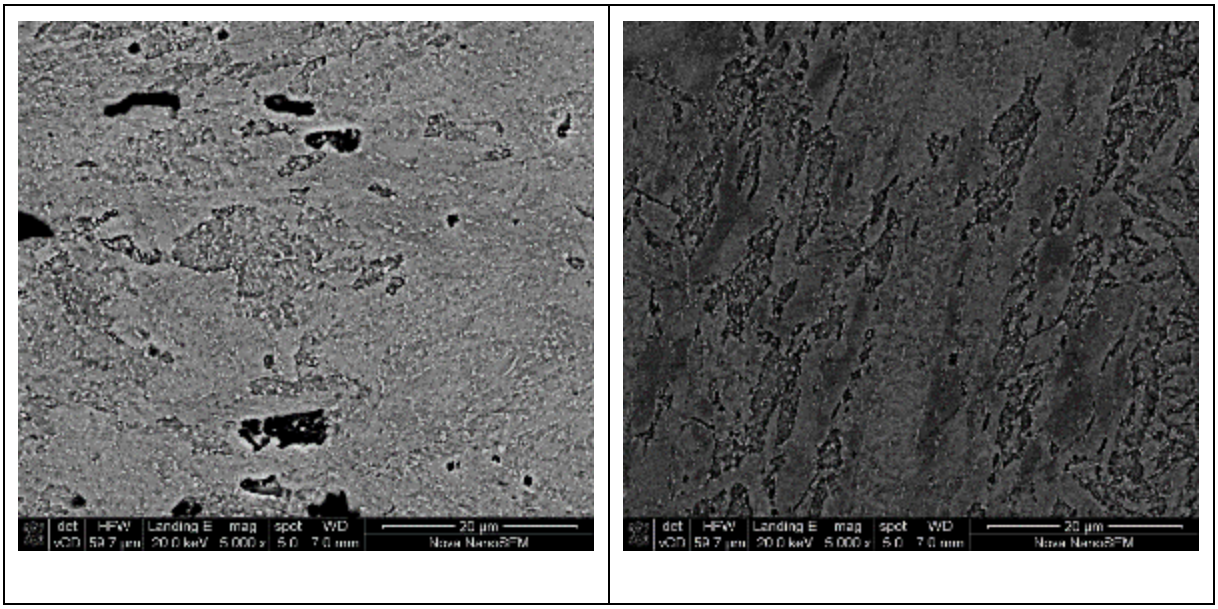

Figure 130: Backscatter SEM images of the rupture surface (left) and base/weld material (right) for test 4 A

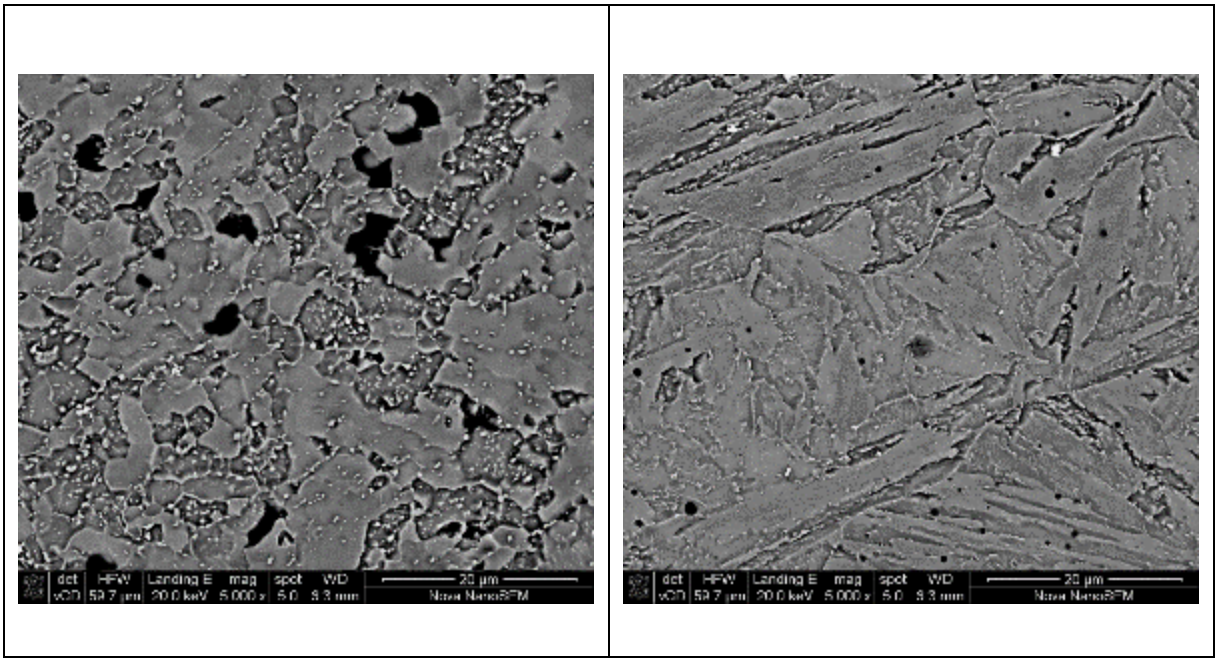

Figure 131: Backscatter SEM images of the rupture surface (left) and base/weld material (right) for test 4 B

Appendix 4 **Void Density Profile**

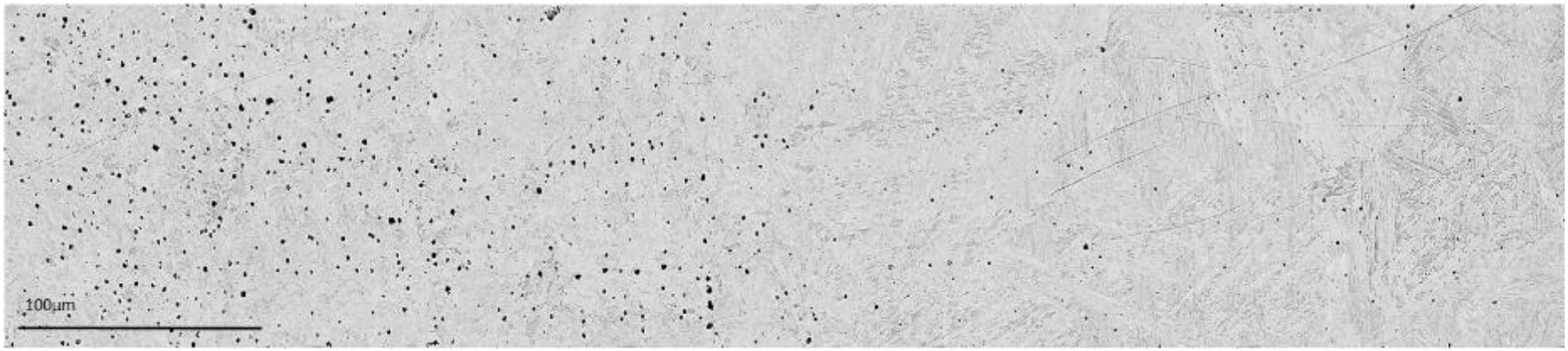

Figure 132: Backscatter SEM stitched image of test 1 A GS sample

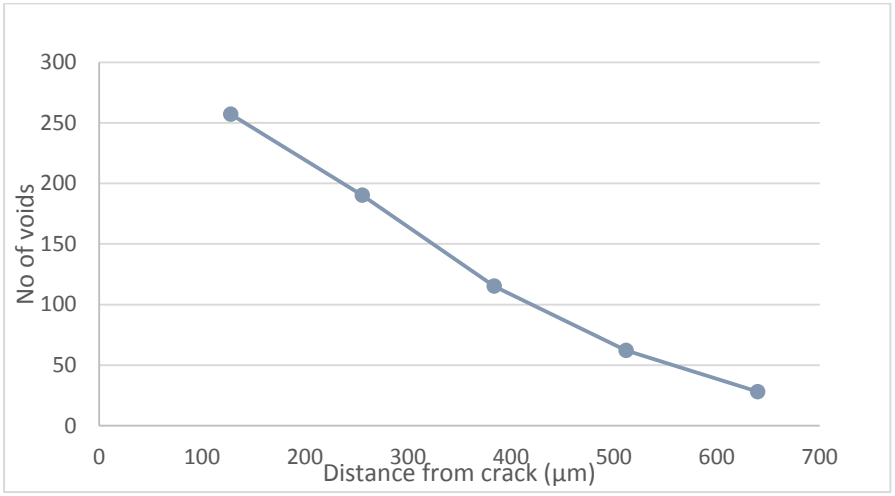

Figure 133: Graph showing the void density as a function of the distance from the fracture surface in sample test 1 A GS

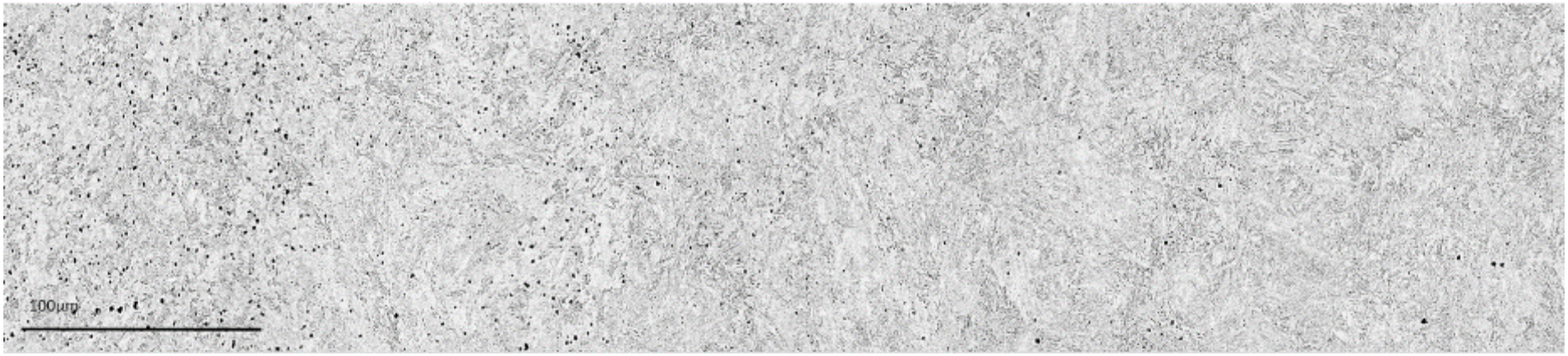

Figure 134: Backscatter SEM stitched image of test 1 B GL sample

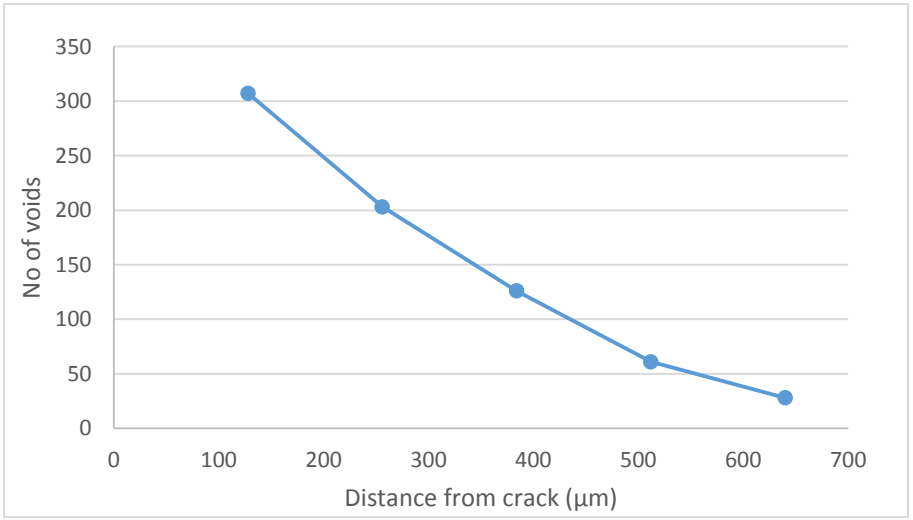

Figure 135: Graph showing the void density as a function of the distance from the fracture surface in sample test 1 B GL

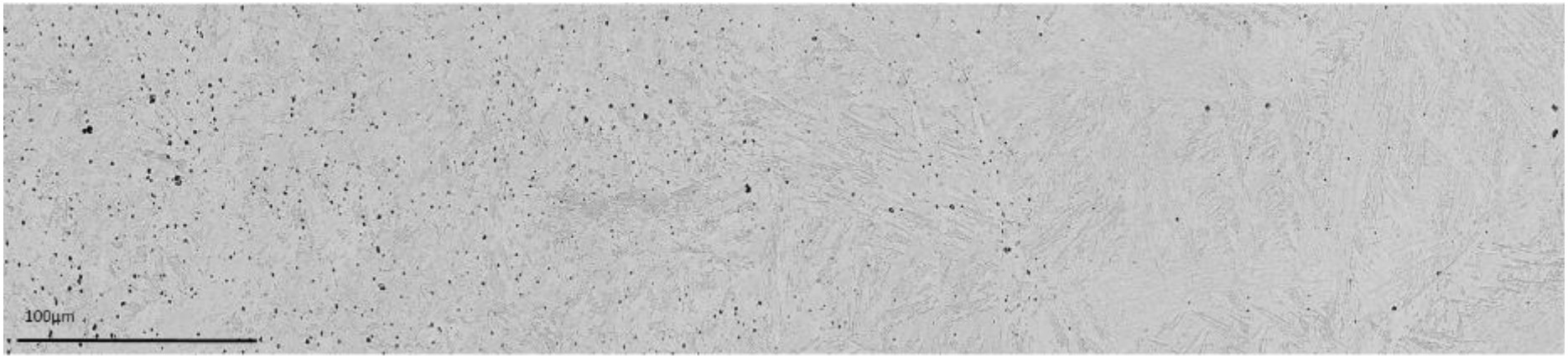

Figure 136: Backscatter SEM stitched image of test 1 B GS sample

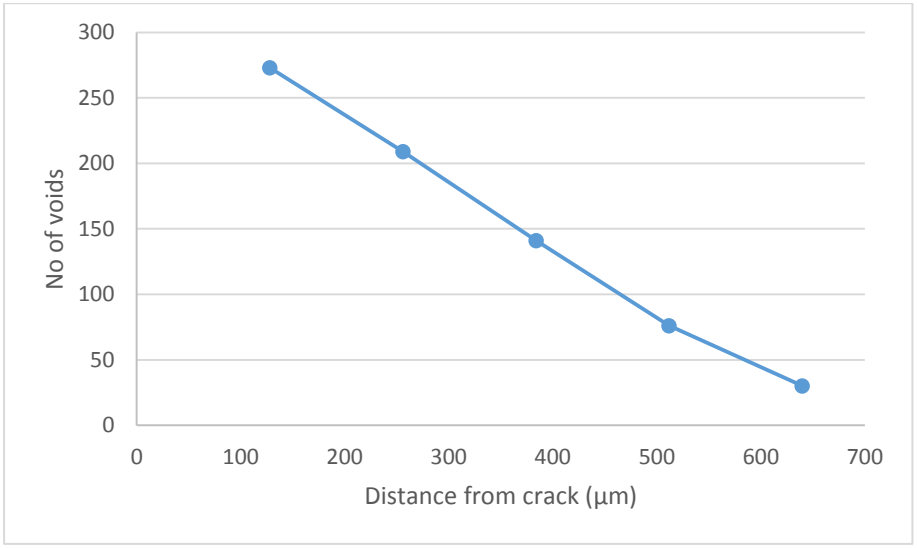

Figure 137: Graph showing the void density as a function of the distance from the fracture surface in sample test 1 B GS

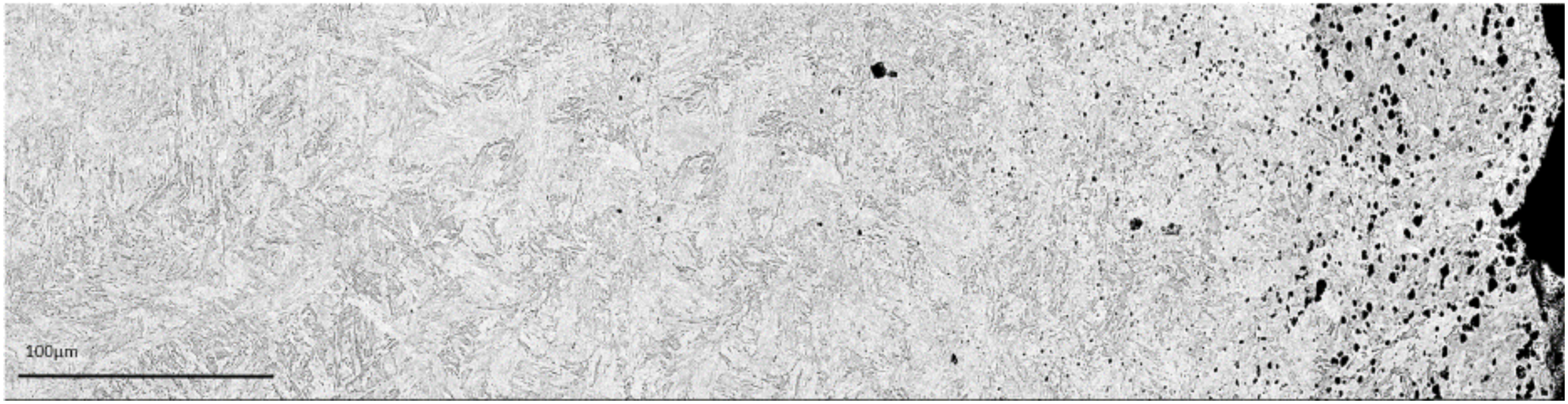

Figure 138: Backscatter SEM stitched image of test 2 A GL sample

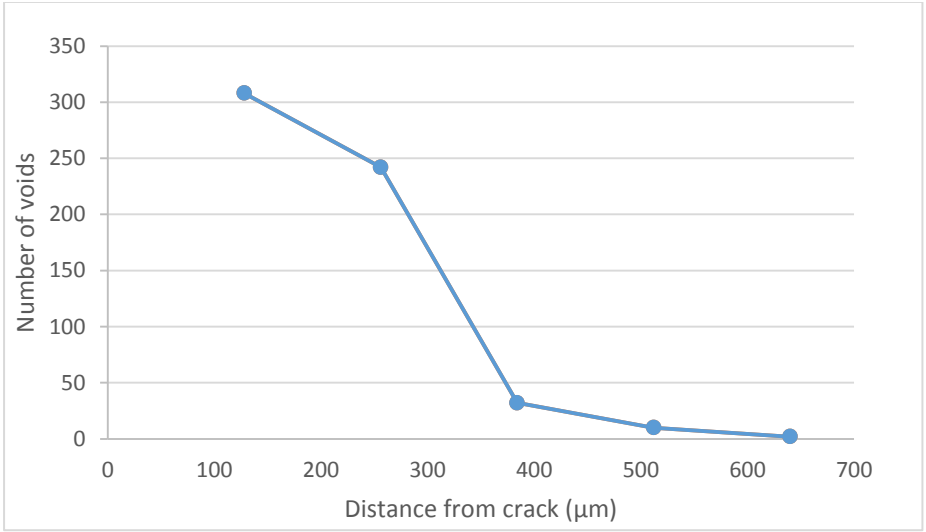

Figure 139: Graph showing the void density as a function of the distance from the fracture surface in sample test 2 A GL

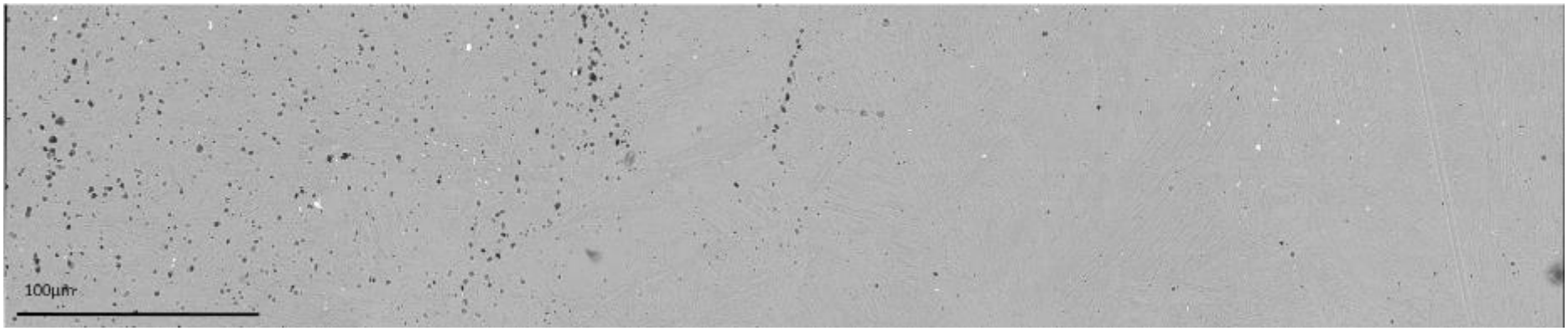

Figure 140: Backscatter SEM stitched image of test 2 A GS sample

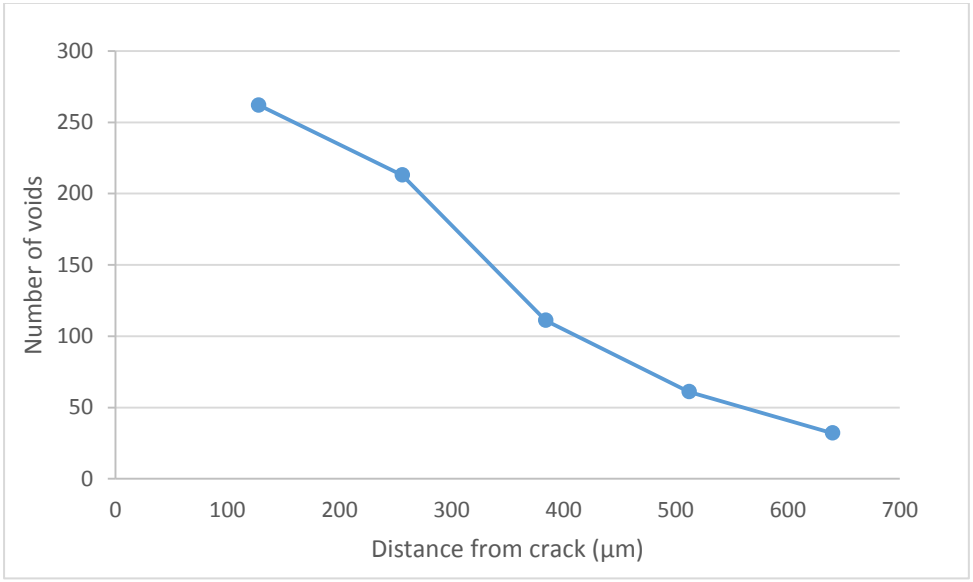

Figure 141: Graph showing the void density as a function of the distance from the fracture surface in sample test 2 A GS

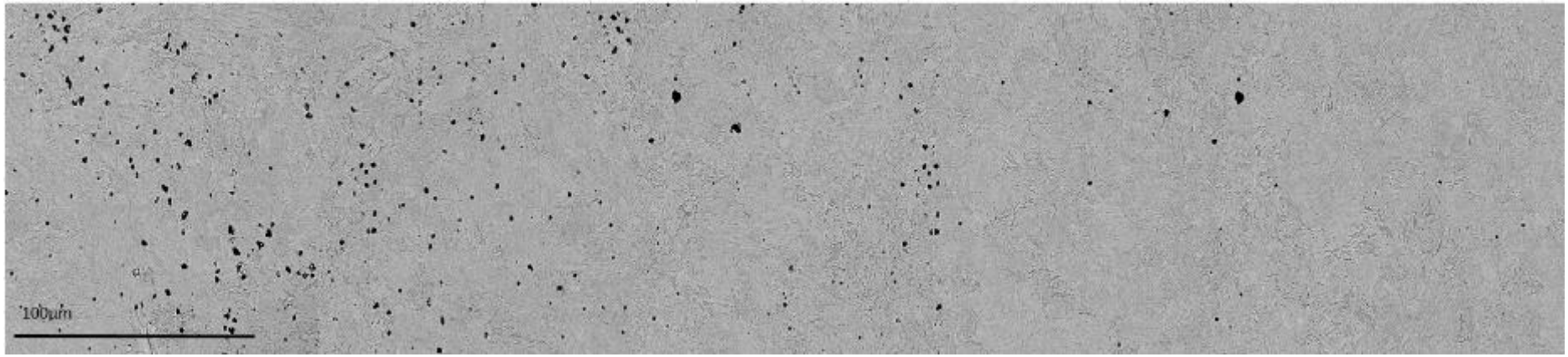

Figure 142: Backscatter SEM stitched image of test 2 B GL sample

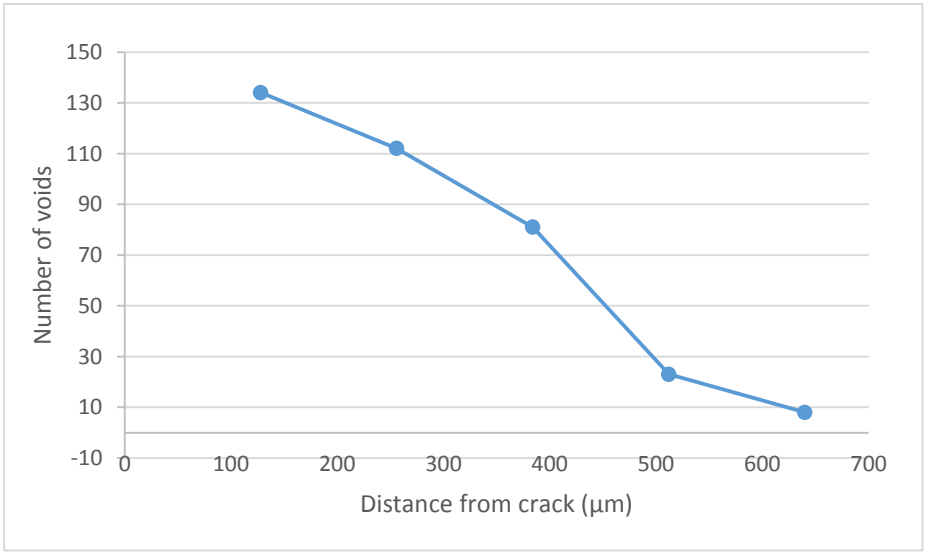

Figure 143: Graph showing the void density as a function of the distance from the fracture surface in sample test 2 B GL

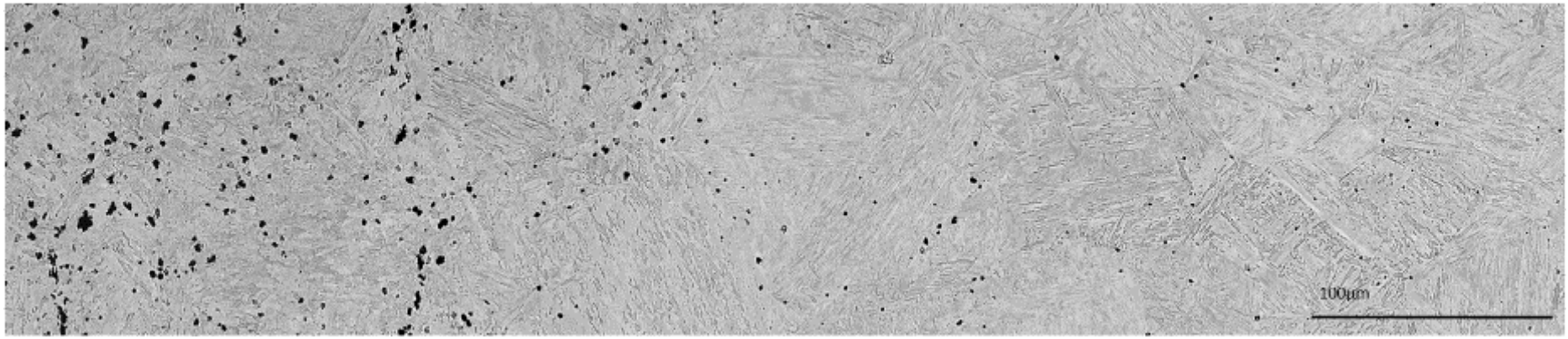

Figure 144: Backscatter SEM stitched image of test 2 B GS sample

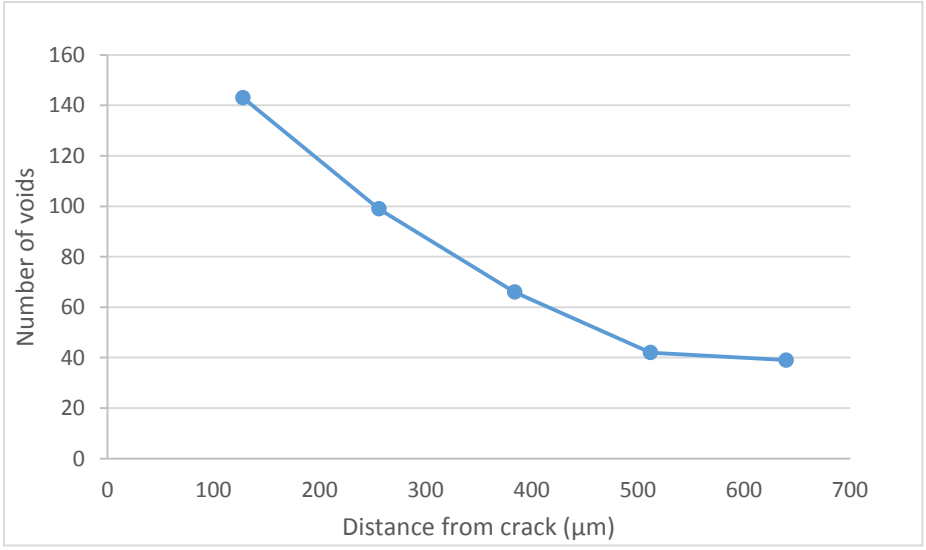

Figure 145: Graph showing the void density as a function of the distance from the fracture surface in sample test 2 B GS

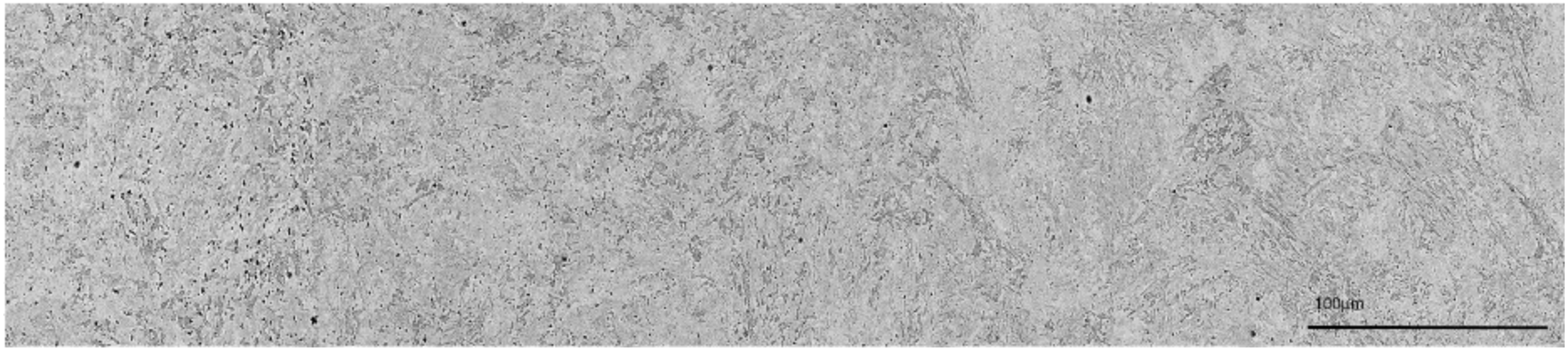

Figure 146: Backscatter SEM stitched image of test 3 A GL sample

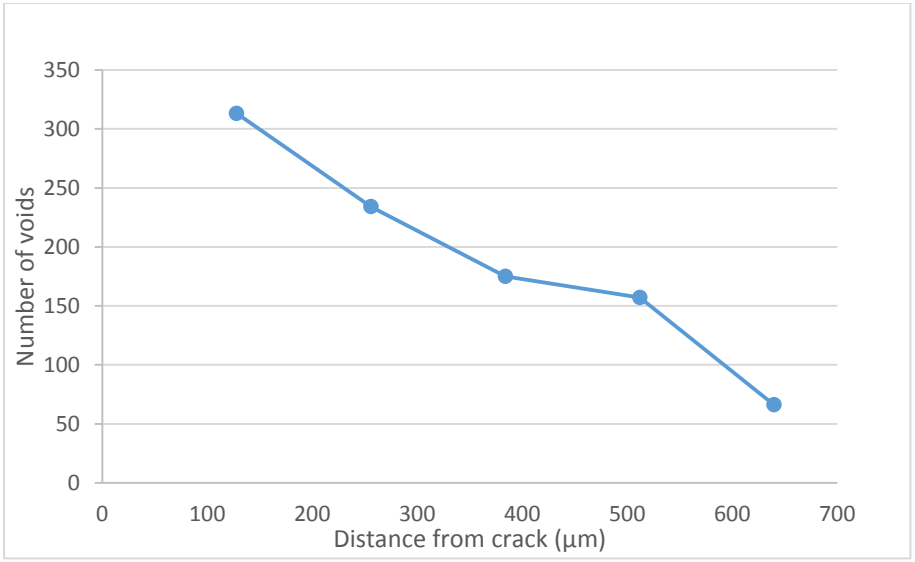

Figure 147: Graph showing the void density as a function of the distance from the fracture surface in sample test 3 A GL

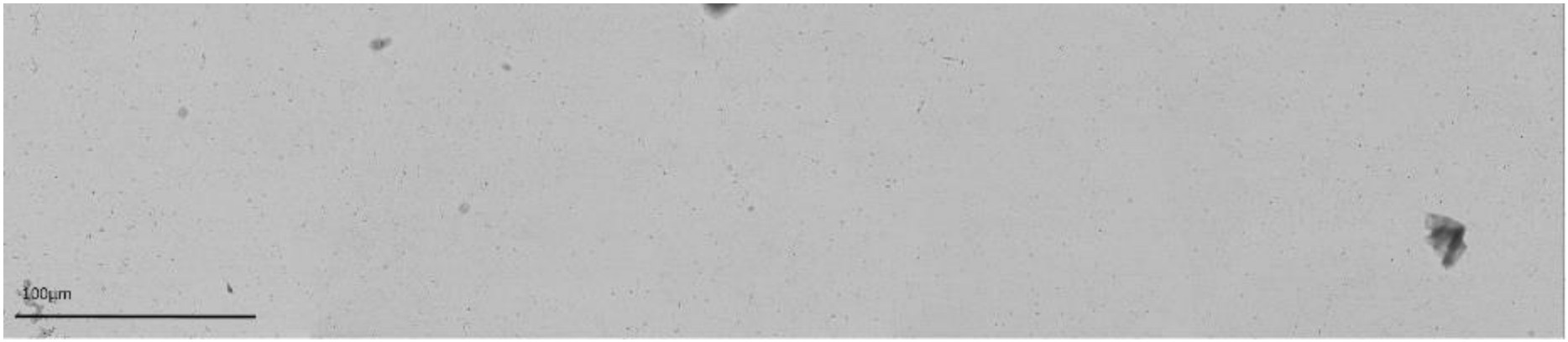

Figure 148: Backscatter SEM stitched image of test 3 A GS sample

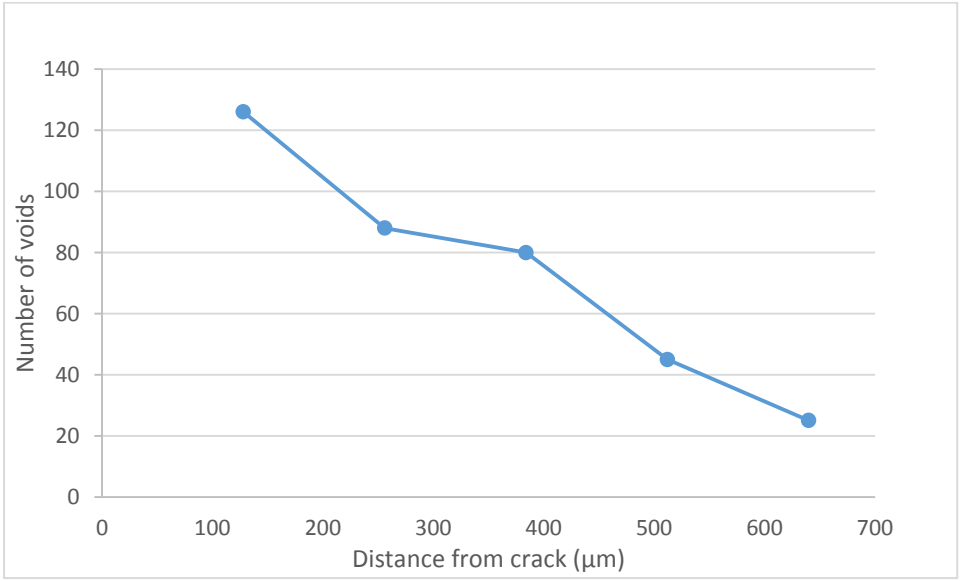

Figure 149: Graph showing the void density as a function of the distance from the fracture surface in sample test 3 A GS

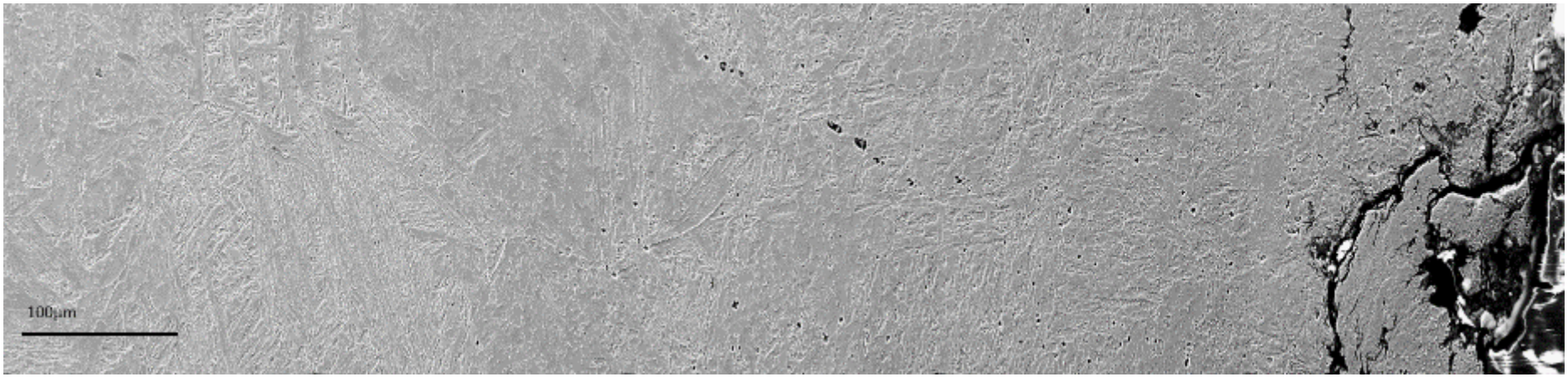

Figure 150: Backscatter SEM stitched image of test 4 A GL sample

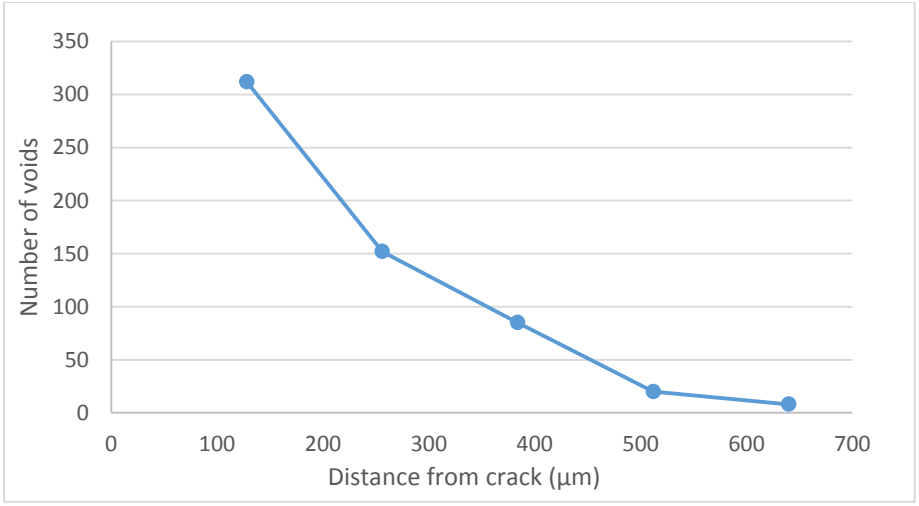

Figure 151: Graph showing the void density as a function of the distance from the fracture surface in sample test 4 A GL

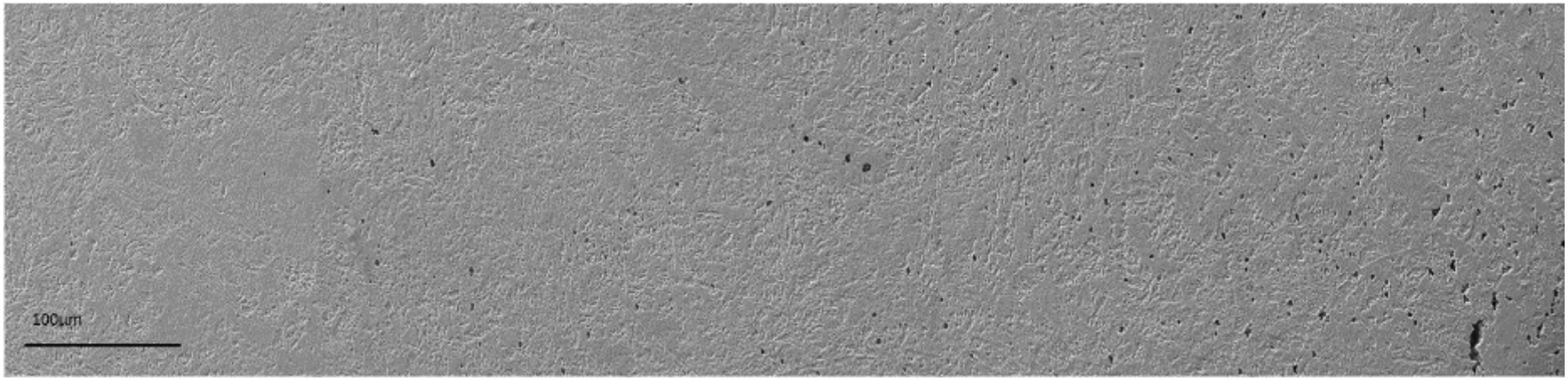

Figure 152: Backscatter SEM stitched image of test 4 A GS sample

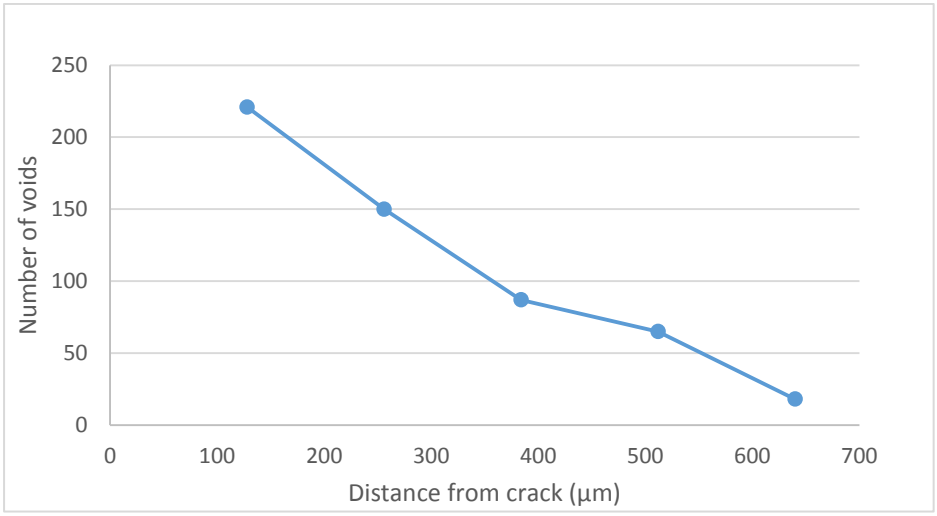

Figure 153: Graph showing the void density as a function of the distance from the fracture surface in sample test 4 A GS

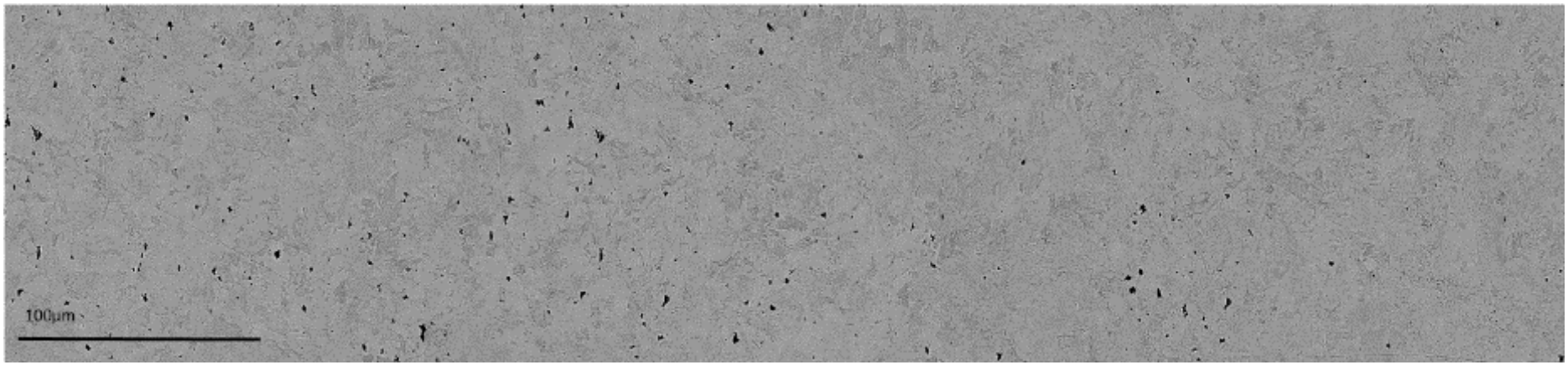

Figure 154: Backscatter SEM stitched image of test 4 B GL sample

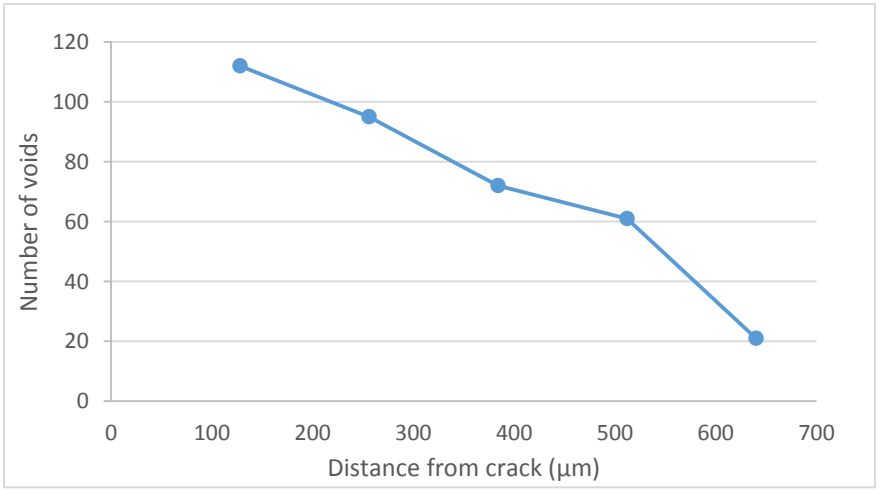

Figure 155: Graph showing the void density as a function of the distance from the fracture surface in sample test 4 B GL

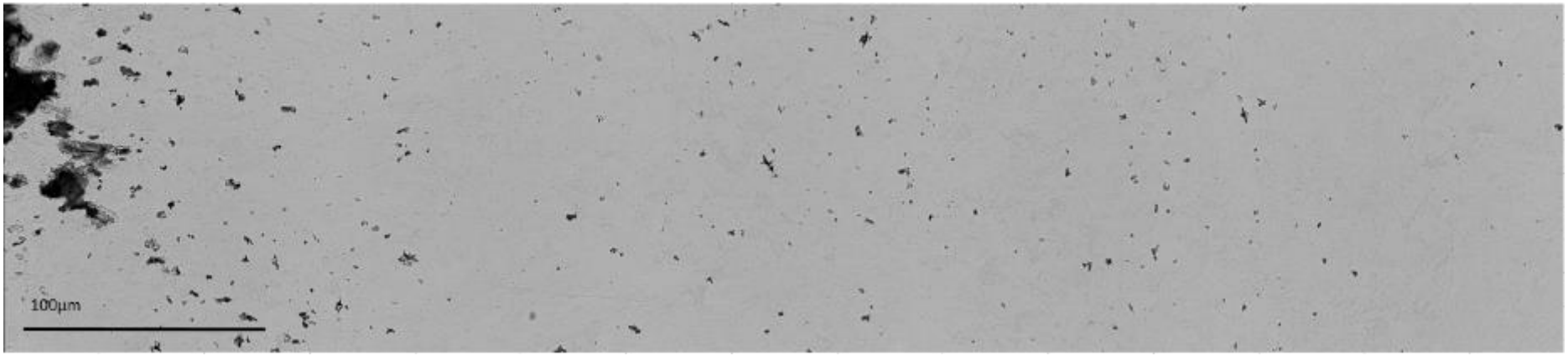

Figure 156: Backscatter SEM stitched image of test 4 B GS sample

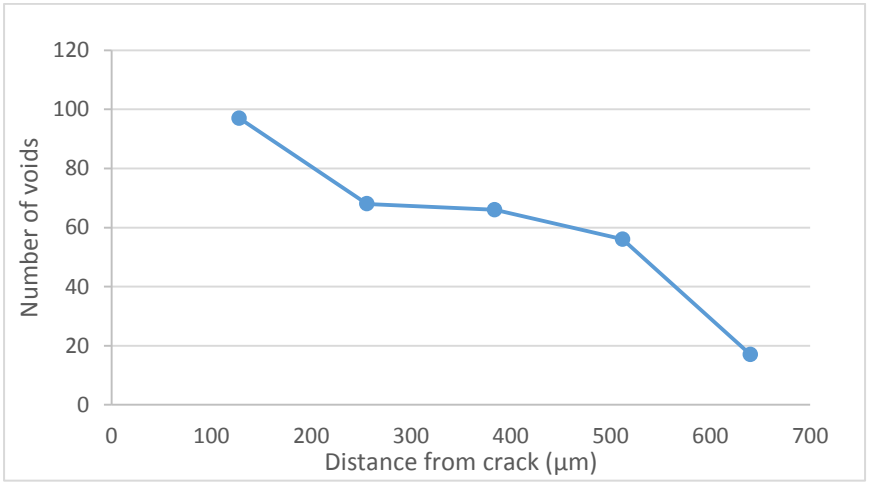

Figure 157: Graph showing the void density as a function of the distance from the fracture surface in sample test 4 B GS

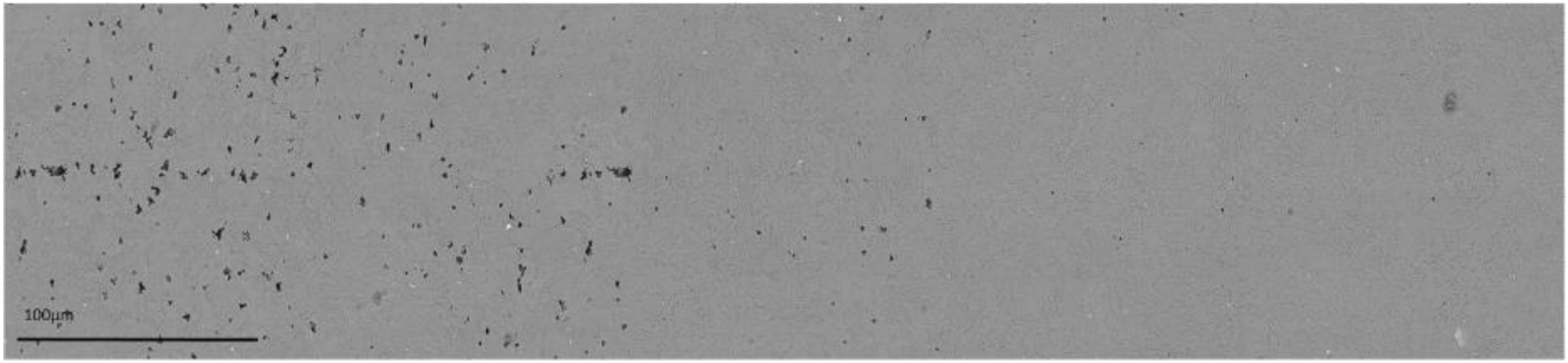

Figure 158: Backscatter SEM stitched image of test 5 A GL sample

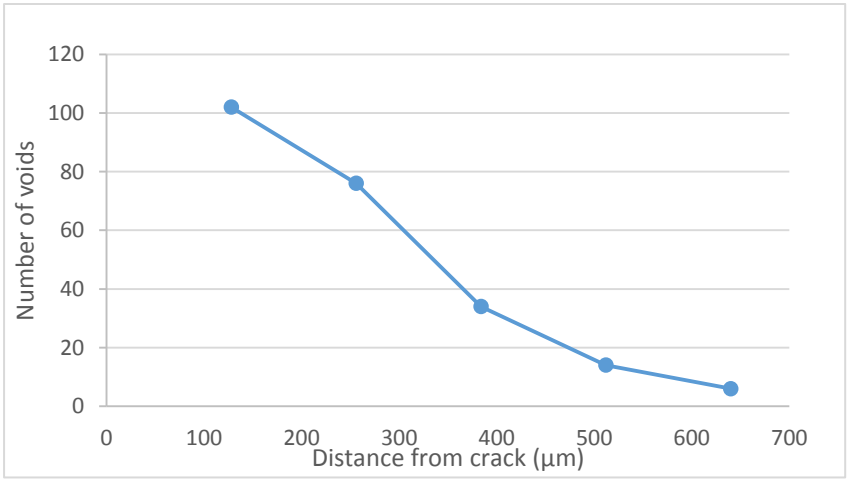

Figure 159: Graph showing the void density as a function of the distance from the fracture surface in sample test 5 A GL

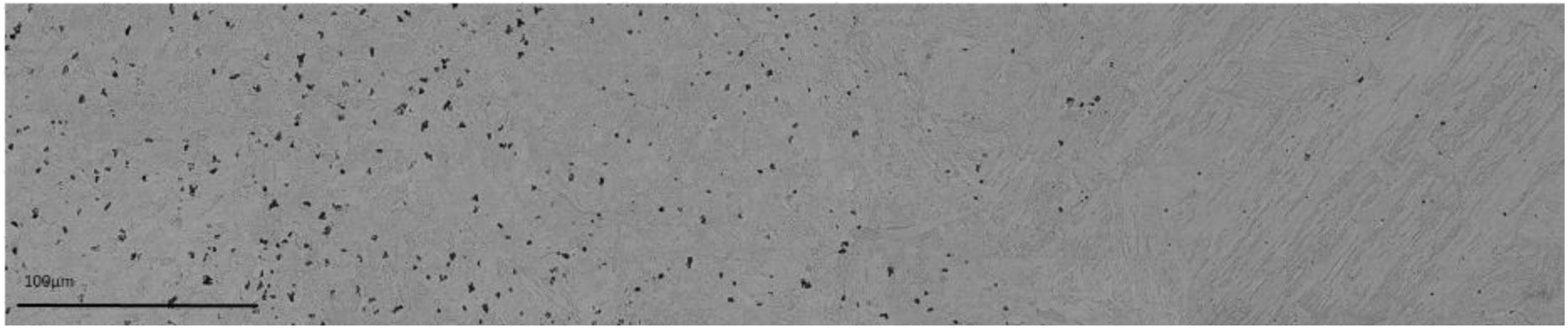

Figure 160: Backscatter SEM stitched image of test 5 A GS sample

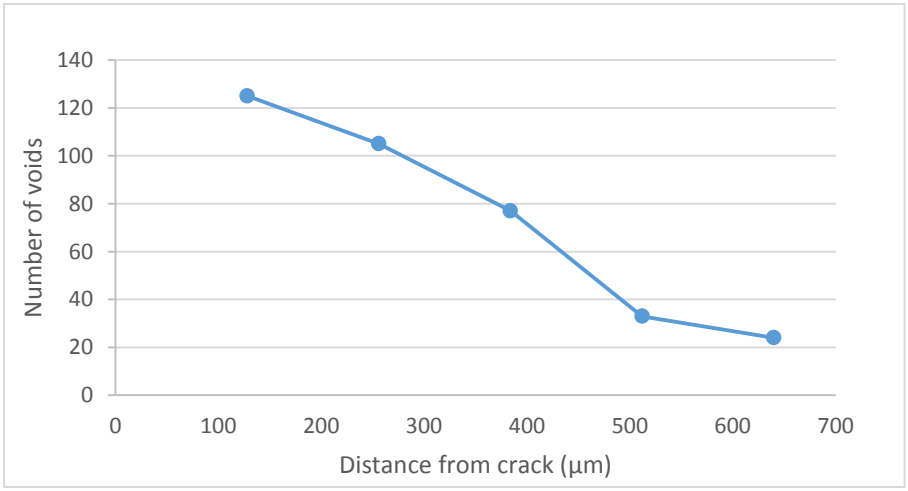

Figure 161: Graph showing the void density as a function of the distance from the fracture surface in sample test 5 A GL

Appendix 5 **Creep Strain Curves**

Applied stress: 80MPa

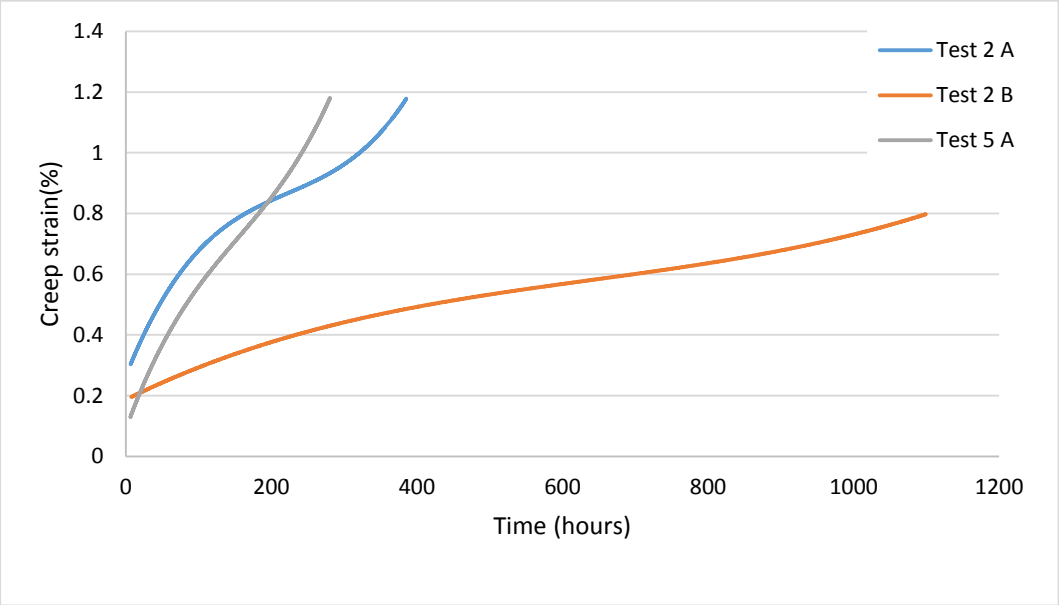

Figure 162: Creep strain curve versus testing time for weldment 1 and 2 at 610°C and 80 MPa

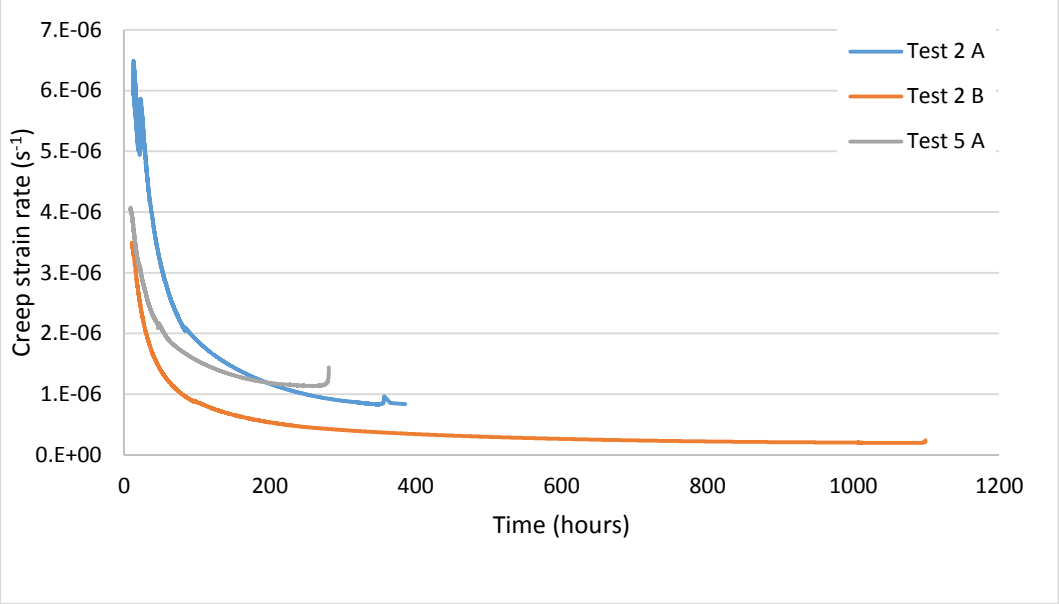

Figure 163: Creep strain rate versus testing time for weldment 1 and 2 at 610°C and 80 MPa

Applied stress: 90MPa

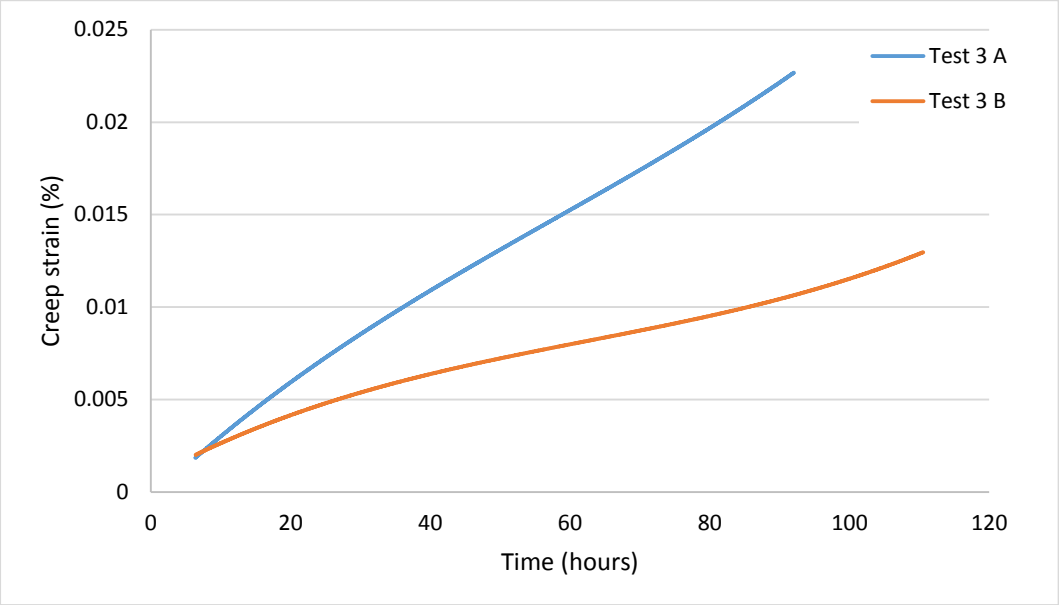

Figure 164: Creep strain curve versus testing time for weldment 1 and 2 at 610°C and 90 MPa

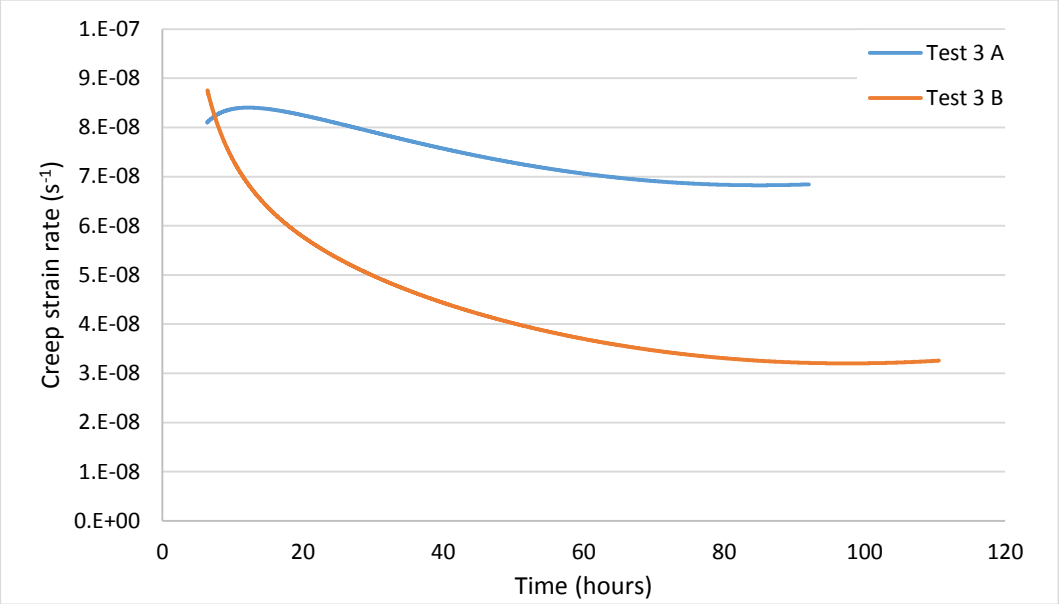

Figure 165: Creep strain rate versus testing time for weldment 1 and 2 at 610°C and 90 MPa

8. References

[1] M. Hino, Y. He, K. Li, J. Chang, and K. Shin, "Microstructural Evolution of X20CrMoV12 . 1 Steel upon Short-term Creep Rupture Test," *Appl. Microsc.*, vol. 43, no. 4, pp. 164–172, 2013.

[2] T. J. Molokwane, "Weldability Limits for X20 CrMoV12-1 steel," *HP pipework forum*, pp. 3–4, 2014.

[3] E. van Zyl, "Remnant Life Monitoring," *Eskom Gr. Technol. Eng.*, vol. 1, no. 38–702, pp. 1–21, 2011.

[4] P. van der Meer, "Effect of Geometry on the Microstructural Ageing of a 1CrMoV Turbine Rotor Steel," University of Cape Town, 2013.

[5] J. Storesund, K. Borggreen, and W. Zang, "Creep behaviour and lifetime of large welds in X 20 CrMOV 12 1-results based on simulation and inspection," *Int. J. Press. Vessel. Pip.*, vol. 83, pp. 875–883, 2006.

[6] Y.-K. Chung, C.-H. Joo, J.-J. Park, I.-M. Park, and H.-J. Kim, "Quantification of creep cavitation in welded joint and evaluation of material characteristics of simulated heat-affected zone in X 20 CrMoV 12 1 steel," *J. Press. Vessel Technol.*, vol. 123, no. 1, pp. 112–117, 2001.

[7] F. Abe, "Introduction," in *Creep-resistant steels*, F. Abe, T.-U. Kern, and R. Viswanathan, Eds. Cambridge: Woodhead Publishing Limited, 2008, pp. 3–14.

[8] A. A. Bazazi, "Evolution of Microstructure during Long - term Creep of a Tempered Martensite Ferritic Steel," Ruhr-Universitat Bochum, 2009.

[9] R. W. Evans and B. Wilshire, *Introduction to creep*. Michigan: Institute of Materials, 1993.

[10] R. E. Smallman and A. H. W. Ngan, *Modern Physical Metallurgy*. Elsevier, 2014.

[11] Gene Mathers, "Creep and creep testing." [Online]. Available: http://www.twi-global.com/technical-knowledge/job-knowledge/creep-and-creep-testing-081/. [Accessed: 11-Jun-2014].

[12] F. Abe, T.-U. Kern, and R. Viswanathan, *Creep-resistant steels*. Cambridge: Woodhead Publishing Limited, 2008.

[13] F. Abe, "Creep rates and strengthening mechanisms in tungsten-strengthened 9Cr steels," *Mater. Sci. Eng. A*, vol. 319–321, pp. 770–773, 2001.

[14] P. J. Ennis, A. Zielinska-Lipiec, O. Wachter, and A. Czyrska-Filemonowicz, "of the Martensitic Steel P92 for," *Acta Mater.*, vol. 45, no. 12, 1997.

[15] K. Maruyama, K. Sawada, and J. Koike, "Strengthening mechanisms of creep resistant tempered martensitic steel," *Isij Int.*, vol. 41, no. 6, pp. 641–653, 2001.

[16] F. Abe, "Strengthening mechanisms in steel for creep and creep rupture," in *Creep-resistant steels*, F. Abe, T.-U. Kern, and R. Viswanathan, Eds. Cambridge: Woodhead Publishing Limited, 2008, pp. 279–304.

[17] K. Sawada, K. Kubo, and F. Abe, "Creep behavior and stability of MX precipitates at high temperature in 9Cr–0.5Mo–1.8W–VNb steel," *Mater. Sci. Eng. A*, vol. 319–321, pp. 784–787, Dec. 2001.

[18] H. Oikawa and Y. Iijima, “Diffusion behaviour or creep-resistant steels,” in *Creep-resistant steels*, F. Abe, T.-U. Kern, and R. Viswanathan, Eds. Cambridge: Woodhead Publishing Limited, 2008, pp. 241–264.

[19] M. . Ashby, “A first report on deformation-mechanism maps,” *Acta Metall.*, vol. 20, no. 7, pp. 887–897, Jul. 1972.

[20] K. Maruyama, “Fundamental aspects of creep deformation and deformation mechanism map,” in *Creep-resistant steels*, F. Abe, T.-U. Kern, and R. Viswanathan, Eds. Cambridge: Woodhead Publishing Limited, 2008, pp. 265–278.

[21] M. E. Kassner and M. E. Kassner, *Fundamentals of Creep in Metals and Alloys*. Elsevier, 2008.

[22] R. E. Smallman and A. H. W. Ngan, *Modern Physical Metallurgy*. Elsevier, 2014.

[23] EPRI, “X20 CrMoV12-1 Steel Handbook,” Palo Alto, CA, 2006.

[24] H. Jesper and H. R. Kautz, “Eigenschaften, Verarbeitung und Bewährung des Stahles X20CrMo(W)V12-1 im Kraftwerk,” *VGB Conf. Werkstatte und Schweisstechnik im Kraftw.*, vol. 9, pp. 274–316, 1985.

[25] K. Baumann, “Erfahrungen Mit Werkstoffen Fuer Gegendruck Dampfanlagen Ueber 560°C,” *Int. Energiekonferenz Laussane*, vol. 26, pp. 81–91, 1968.

[26] R. L. Klueh and D. R. Harries, *High Chromium Ferritic and Martensitic Steels for Nuclear Applications*. .

[27] VGB-Empfehlung, “Hinweise für die Verarbeitung des Warmfesten Stahles X20 CrMoV12-1,” *VGB Kraftwerkstechnik GmbH*. Essen, Germany.

[28] G. Eggeler, N. Nilsvang, and B. Iishner, “Microstructural changes in a 12% chromium steel during creep,” *Steel Res.*, vol. 58, no. 2, pp. 97–103, 1987.

[29] J. Hald, “Metallurgy and Creep Properties of New 9-12%Cr Steels,” *Steel Res.*, vol. 67, no. 9, pp. 369–374, 1996.

[30] S. Straub, M. Meier, J. Ostermann, and W. Blum, “Entwicklung der Mikrostruktur und der Festigkeit des Stahles X20 CrMoV 121 bei 823 K während Zeitstandbeanspruchung und Glühung,” *VGB Kraftwerkstechnik*, vol. 73, no. 8, pp. 744–752.

[31] H. Weber and F. Bruhl, “Determination of the Residual Service Life of Hot Media Piping Systems in Power Stations,” *Pip. Syst. Valves*, pp. 848–880.

[32] T. C. C. 267 "Industrial piping and Pipelines", “BSI Standards Publication Metallic materials — Metallic industrial piping Part 4: Fabrication and installation,” 2012.

[33] H. Cerjak, “Welding of steam turbine components,” Brussels, 1992.

[34] P. Mayr, “Evolution of microstructure and mechanical properties of the heat affected zone in B-containing 9 % chromium steels,” Graz University of Technology, 2007.

[35] D. J. Smith, N. S. Walker, and S. T. Kimmins, “Type IV creep cavity accumulation and failure in steel welds,” *Int. J. Press. Vessel. Pip.*, vol. 80, no. 9, pp. 617–627, 2003.

[36] J. A. Francis, W. Mazur, and H. K. D. H. Bhadeshia, “Type IV cracking in ferritic power plant steels,” vol. 22, no. 12, pp. 1387–1395, 2006.

[37] M. Tabuchi, “Evaluation of Creep Damage and Fracture in High Cr Steel Welds,” in

13th International Conference on Fracture, 2013, pp. 1–7.

[38] K. Haarmann, J. C. Vaillant, B. Vandenberge, W. Bendick, and A. Arbab, *The T91/P91 book*. 2002.

[39] P. Mayr, "Evoultion of microstructure and mechanical properties of the heat affected zone in 9Cr steels," *Weld. World*, vol. 54, pp. R1–R11, 2010.

[40] Y. Takagi and S. Otsuki, "Creep-fatigue characteristics of partial repair welds and full repair welds on aged 2.25Cr-1Mo steel," *OMMI*, vol. 3, no. 1, pp. 1–12, 2004.

[41] D. Halici, "Microstructural Evolution of the Heat-affected Zone in 9%Cr steels," Graz University of Technology, 2011.

[42] H. J. Shuller, L. Hagn, and A. Woitscheck, "Risse im Schweißnahtbereich von Formstücken aus Heißdampfleitungen - Werkstoffuntersuchungen," *Der Maschinenschaden*, vol. 47, no. 1, pp. 1–13, 1974.

[43] P. Auerkari, D. Barraclough, B. Buchmayr, C. Coussement, J. Granacher, S. R. Holdsworth, S. Holmström, A. Klenk, H. Konig, P. F. Morris, G. Merckling, N. K, J. Orr, H. Rantala, D. G. Robertson, W. Rohde, R. Sandström, I. A. Shibli, H. Theofel, and A. Vanderschaeghe, "Data acceptability criteria and data generation: creep data for welds," *ECCC Recomm.*, vol. 3, no. 3, 2011.

[44] J. Rothwell and P. Mayr, "The cross-weld performance of 9%Cr creep-resistant steels, and the influence of welding parameters."

[45] C. J. Middleton and E. Metcalfe, "A review of laboratory type IV cracking data in high chromium ferritic steels," in *Steam plants for the 1990s*, 1990, pp. 275–282.

[46] K. Laha, K. S. Chandravathi, P. Parameswaran, K. B. S. Rao, and S. L. Mannan, "Characterization of Microstructures across the Heat-Affected Zone of the Modified 9Cr-1Mo Weld Joint to Understand Its Role in Promoting Type IV Cracking," *Metall. Mater. Trans. A*, vol. 38, no. 1, pp. 58–68, 2007.

[47] F. Abe, "R&D of advanced ferritic steels for 650uC USC boilers," in *The innovative structural materials for infrastructure in 21st century*, 2000, pp. 119–129.

[48] M. Tabuchi, T. Watanabe, K. Kubo, M. Matsui, J. Kinugawa, and F. Abe, "Creep crack growth behavior in the HAZ of weldments of W containing high Cr steel," *Int. J. Press. Vessel. Pip.*, vol. 78, no. 11–12, pp. 779–784, 2001.

[49] K. Shinozaki, D.-J. Li, H. Kuroki, H. Harada, and K. Ohishi, "Analysis of Degradation of Creep Strength in Heat-affected Zone of Weldment of High Cr Heat-resisting Steels Based on Void Observation.," *ISIJ Int.*, vol. 42, no. 12, pp. 1578–1584, 2002.

[50] F. Abe, M. Tabuchi, S. Tsukamoto, and T. Shirane, "Microstructure evolution in HAZ and suppression of Type IV fracture in advanced ferritic power plant steels," *Int. J. Press. Vessel. Pip.*, vol. 87, no. 11, pp. 598–604, Nov. 2010.

[51] C. R. Chen, H. G. Armaki, and K. Maruyama, "Microstructural Degradation During High Temperature Exposure Up To 105 H And Its Effects On Creep Of Gr . 91 Steel Microstructural," in *Sixth International Conference on Advances in Materials Technology for Fossil Power Plants*, 2010.

[52] F. Abe, "Precipitate design for creep strengthening of 9% Cr tempered martensitic steel for ultra-supercritical power plants," *Sci. Technol. Adv. Mater.*, vol. 9, no. 1, p.

013002, 2008.

[53] Y. Hasegawa, T. Muraki, and M. Ohgami, “Metallurgical Investigation of a Type IV Damage at the Heat Affected Zone of Weld for Tungsten Containing Martensitic Heat Resistant Steels,” in *ASME/JSME 2004 Pressure Vessels and Piping Conference*, 2004, pp. 45–56.

[54] A. Klenk and M. Stuttgart, “Creep testing of weldments: practices and investigations into the effects of sampling and size on creep test results for weldments,” *ECCC Recomm. Data Accept. criteria data Gener. creep data welds*, vol. 3, no. 3, p. Appendix 1, 2011.

[55] B. Buchmayr, “Characterisation of the creep behaviour of weldments by HAZ-simulation,” *ECCC Recomm. Data Accept. criteria data Gener. creep data welds*, vol. 3, no. 3, p. Appendix 2, 2011.

[56] T. J. Molokwane, “Microstructural and Property Assessment of Creep Aged 12Cr Steel After Welding,” University of Cape Town, 2013.

[57] “Calphad.” [Online]. Available: http://www.calphad.org/. [Accessed: 24-Aug-2016].

[58] J. Koukal, M. Sondel, and D. Schwarz, “Correlation of Creep Properties of Simulated and Real Weld Joints in Modified 9 %Cr Steels,” *Weld. World*, vol. 54, no. 1–2, pp. R27–R34, Jan. 2013.

[59] P. Trimby, Y. Cao, and S. Samudrala, “EBSD Explained,” *Oxford Instruments plc*, 2015. .

[60] F. J. Humphreys, “Quantitative metallography by electron backscattered diffraction,” *J. Microsc.*, vol. 195, no. November 1998, pp. 170–185, 1999.

[61] T. Maitland and S. Sitzman, “Backscattering detector and EBSD in Nanomaterials characterization,” in *Scanning Microscopy for Nanotechnology*, 2007, pp. 41–75.

[62] “Welcome to ImageJ,” 2015. [Online]. Available: http://imagej.net/Welcome. [Accessed: 27-Jul-2015].

[63] A. R. Marder, “Replication Microscopy Techniques for NDE,” *ASM Handb. Nondestruct. Eval. Qual. Control*, vol. 17, pp. 52–56, 1989.

[64] F. H. Van Zyl, M. E. J. Bezuidenhout, P. Doubell, F. C. Havinga, D. A. H. Pegler, and M. Newby, “Life Assessment and Creep Damage Monitoring of High Temperature Pressure Components in South Africa ’ s,” in *ECCC*, 2005, no. September, pp. 12–14.

[65] J. Storesund, R. Wu, and K. Borggreen, “Creep properties of weld repaired low alloy heat resistant CrMo and Mo steels at,” in *ECCC Creep Conference*, 2009, no. April, pp. 21–23.